National Technical University of Athens

School of Mechanical Engineering

Fluids Section

Biofluids and Biomedical Engineering Laboratory

Computational Simulation of Flow Control with the Immersed Boundary Method

A thesis submitted for the degree of
Doctor of Philosophy

Iosif C. Moulinos

Supervisor: Sokrates Tsangaris
Professor NTUA, Em.

Athens 2022

National Technical University of Athens
School of Mechanical Engineering
Fluids Section
Biofluids and Biomedical Engineering Laboratory

Computational simulation of flow control with the immersed boundary method

Ph.D. Thesis

Iosif C. Moulinos

Supervisor: Sokrates Tsangaris, Professor,
School of Mechanical Engineering, NTUA, Em.

Examination committee:

1. Spyridon Voutsinas, Professor, School of Mechanical Engineering, NTUA, Member of the advisory committee
2. Ioannis Anagnostopoulos, Professor, School of Mechanical Engineering, NTUA, Member of the advisory committee
3. Dimitrios Mathioulakis, Professor, School of Mechanical Engineering, NTUA
4. Kyriakos Giannakoglou, Professor, School of Mechanical Engineering, NTUA
5. Demetri Bouris, Professor, School of Mechanical Engineering, NTUA
6. Vasilis Riziotis, Associate Professor, School of Mechanical Engineering, NTUA
7. Christos Manopoulos, Assistant Professor, School of Mechanical Engineering, NTUA

Athens 2022

Computational simulation of flow control with the immersed boundary method

Iosif C. Moulinos

Ph.D. Thesis

Advisor: Sokrates Tsangaris, Professor NTUA, Em.

Abstract

Flow control constitutes the utmost objective of fluid dynamics. In a multitude of techniques used for regulating the flow parameters and characteristics, moving solid parts are involved, either rigid or deformable. The computation of this kind of flows by means of the classical body fitted methods, demands the regeneration of the computational mesh for every new step in the discretized time domain. On the contrary, immersed boundary methods achieve integration of flow equations in time, even for time varying fluid domain geometry, using invariant underlying grid throughout the computation.

In the structured grid setting, the class of geometrical domains in which a curvilinear grid can be fitted, strictly includes and is overwhelmingly larger of the class of domains discretizable by Cartesian grids. The adaptation of the underlying mesh to the steady part of the boundary of the fluid domain is a desired feature as it enables the direct imposition of the boundary conditions. Thus, leads to reduced complexity and increased accuracy for immersed boundary methods that implement approximation schemes on the immersed surfaces.

In the present dissertation, a structured curvilinear immersed boundary method, extended with fluid-structure interaction features for deformable solid bodies, is employed for the analysis of flow control with several techniques:

- Steady and unsteady separated flow by interaction with actively and passively moving surfaces
- Peristaltic motion of generalized Newtonian fluids
- Oscillating membrane pulsatile flow.

The investigation is oriented in the direction of the questions:

- How the streamwise length of the detached flow can be reduced by a moving portion of the surface over which the boundary layer is separated?
- How efficient is the control of the recirculation by a passive membrane?
- What is the effect of the speed, the amplitude and the modality of the peristaltic wave in transport efficiency?
- How do shear thinning fluids behave under peristalsis in comparison with Newtonian fluids?

- How does the membrane's oscillation amplitude affect the outlet pressure of a balloon pump?
- On which factors does the angle shift between the waves of balloon volume change rate and outflow pressure depend?

The immersed boundary method (IBM) used, is recommended as adequate for the simulation of the flow manipulation methods studied, as shown by the agreement of its output with existing results by body fitted algorithms. Extended for generalized Newtonian fluids, the IBM estimations show high grade of coincidence with that of classical methods. The elastic membrane is introduced for the control of the confined detached flow and the fluid-structure interaction of the steady and the unsteady flow with the passive means is analyzed. Parametric investigation of the number of replicas of the wave of contraction for straight peristaltic pumps, highlights the advantages of the multi-cylinder setting. Many fluids of interest, such as blood, are non-Newtonian. Shear thinning behavior impact in the peristaltic pumping characteristics is also pointed out. Pressure performance and the time varying flow field is illustrated for balloon pumping in a straight artery.

Keywords: Computational fluid dynamics, Navier - Stokes equations, Curvilinear immersed boundary method, Fluid-structure interaction, Active - passive flow control, Generalized curvilinear coordinates, Elastic membrane, Peristalsis, Non-Newtonian fluids, Pulsatile flow, Intra-aortic balloon pump, Counterpulsation, Biomedical engineering

Acknowledgements

I would like to thank my advisor, Sokrates Tsangaris, for giving me the opportunity to work with him and for his guidance during the period of my doctoral studies. His enthusiasm, insight, enlightening remarks, persistence and rigorous approach paved the way for the completion of this thesis. I am indebted to him for constant availability and regular discussions, often on a daily basis.

I am grateful to the members of the advisory committee, Spyridon Voutsinas and Ioannis Anagnostopoulos. Their valuable suggestions improved crucially the present dissertation and its oral and written presentation. They were continuously interested in the progress of my doctorate and at each of our meetings gave me advice on how to proceed.

I am thankful to my undergraduate advisor, Kyriakos Giannakoglou, who has also been supportive to me after graduation. All that I learned from him at the period of my diploma studies was essential for the present PhD dissertation. Moreover, the offer of computational resources and support from the Parallel CFD and Optimization Unit enabled demanding processing.

I would like to thank the professors, members of the examination committee, Dimitrios Mathioulakis, whose class stimulation is still profound to me, Demetri Bouris and Vasilis Riziotis, with whom I had the chance to interact as an assistant, and Christos Manopoulos, who was very helpful at various aspects of my PhD studies.

I am thankful to the alumni member of the Aerodynamics Laboratory, Dionysis Angelidis, and the alumni members of the Biofluids and Biomedical Engineering Laboratory, Theodora Pappou, Socrates Vrachliotis and Konstantinos Stokos, with whom I had the opportunity and the pleasure to collaborate.

I would also like to thank the members of the PCOpt, Varvara Asouti, for introducing me to the HPC cluster, and, Marina Kontou, for the platform support.

Finally, I want to thank my parents, Constantinos and Artemis, for being a lifelong source of inspiration, along with my wider family, for setting an example and for their abundant support.

Contents

List of Figures

List of Tables

Chapter 1

Introduction

1.1 Flow control

Fluid flow control is a branch of fluid dynamics attracting vast attention by researchers because of the abundance and the significance of its applications. The work of Prandtl presented at the third international congress of mathematicians in 1904, introducing the boundary layer and a way of controlling it, was a breakthrough in the field [Pra04; Eck17]. Major targets of flow control are volume rate determination, drag reduction, lift enhancement, mixing augmentation, noise suppression, heat transfer enhancement and pressure determination. The control methods aim often at the suppression or the provocation of flow separation, the spatial determination of the transition from laminar to turbulent flow and the positive or negative gain added to turbulence [Hak01]. For the achievement of these goals either passive or active or reactive control can be implemented. Multiple flow control techniques have been applied such as suction-blowing flow, vortex generators, membranes, flaps, heating sources and electromagnetic fields [WF18; BBC17; MMN22; Hak00; Sto+15; BLW08; MSM04].

Optimization of control has been proposed through sensitivity derivatives calculation, namely the adjoint method [GKM00; Kia+15; Zym+13; McN+04; KTH13; Bou21; RZ10] or by means of stochastic methods such as evolutionary algorithms [Bin+18; AG09; Tro+12].

Machine learning algorithms have been adapted for the optimization of flow control characteristics. The discounted reward maximization in deep reinforcement learning [SB18] is implemented as

$$v^*(s) = \max_{\pi} \lim_{T \to \infty} \mathbb{E}_{\pi} \left[\sum_{k=0}^{T} \gamma^k R_{t+k+1} \,\middle|\, S_t = s \right], \forall s \in S, \tag{1.1}$$

where v^* is the optimal reward, π is the policy of the network i.e. the probability that an action is taken at a given state, R_{t+k+1} is the reward at step $t+k+1$, S_t is the current state, and S is the set of states often perceived as states of a Markov decision process [RK19; Rab+20; RHT20; Fan+20; RRT21; Vin+22]. For the manipulation of Equation (1.1), Bellman decomposition is applied [Bel58].

1.2 The immersed boundary method

The immersed boundary method was introduced by Viecelli [Vie69] to treat the fluid boundary as a free surface to which a pressure is exerted. Soon after, Peskin computed flow around heart valves via this method [Pes72]. The main idea of the method is the decoupling between the shape of the fluid domain and the grid for the description of the flow dynamics [TVI14]. In the immersed boundary setting, the need for the regeneration of the mesh, for the discretization of the flow field at cases involving moving bodies, vanishes.

A crucial and characteristic point for the method, is the way the boundary conditions on the immersed surface are taken into account. A proposed technique for the imposition of the conditions is by modifying the governing equations with the addition of an external force accounting for the presence of the boundary [LP00; MY97; Fad+00]. An alternative to the continuous forcing method is the discrete forcing one, where the external force representing the immersed body is introduced at the discretized equations. In order to circumvent the diffusion of the external force to multiple neighboring boundary nodes, direct forcing approaches have been developed. By the cut-cell method, cells that are cut by the immersed surface, are reshaped. In case the volume center is in the fluid region, the respective cell is sustained, truncated to the fluid portion of it. Otherwise, the cell is absorbed by the cells on its vicinity [CSH86; AB99; CL00; Ana07; VSG21]. The ghost-cell method takes into account the solid nodes neighboring to fluid. The values imposed at these nodes are such, so that the resulting values, after interpolation at the immersed surface, are the demanded [IV03; TF03; YB19]. The hybrid Cartesian/immersed boundary methods define the values of the variables at fluid nodes adjacent to solid nodes by interpolating the value at the immersed boundary and the antipodal, with respect to the node of interest, fluid points [Fad+00; GS05; SY14].

1.3 Thesis outline

Chapter 2: The equations governing the flow phenomena examined are presented. The Navier-Stokes equations are introduced in integral and differential form and in convective and conservation configurations. The derivation process of the momentum conservation law for Newtonian and generalized Newtonian fluids is prescribed. Nondimensionalization of the equations follows, which allows for the simulations to address to a family of similar problems rather than a single one. Generalized curvilinear meshes provide better structured adaptability to random boundaries than their Cartesian counterparts. The generalized curvilinear coordinate system is presented along with the metric tensor, the covariant derivative and the Christoffel symbols. The differential operators are expressed in the introduced coordinate system and are used to write the equations of the flow in it. Subsequently, large eddy simulation for turbulence prediction is demonstrated. The law of motion of an elastic membrane of negligible mass is employed for the interaction with the flow.

Chapter 3: The combined staggered and non-staggered mesh formulation is employed for the discretization of the flow field. The Crank-Nicolson scheme is applied for the time integration of the flow equations. Updates for the velocity field computed by the momentum equations, emerge from the projection method. A Newton scheme and the generalized minimal residual method are used for the solution of the resulting algebraic systems. An advanced version of the ray tracing algorithm dubs the nodes of the underlying grid and runs the ray - triangle intersection procedure as a subroutine. The method is firstly implemented for benchmark flow fields, such as the flow around a sphere and an airfoil. The integration of the membrane motion partial derivatives equation is performed by a combination of fifth and fourth order Runge-Kutta methods enabling adaptive step size.

Chapter 4: The steady flow over a backward facing step (BFS) is computed as a warm up for the validation of the procedure to the geometry of interest. This flow is thereafter controlled by an elastic membrane. Subsequently, the free unsteady flow over the BFS is simulated. Active control is introduced in the next section, where the separation bubble is controlled by an oscillating portion of the backstep bottom. Elastic membrane control is also implemented for the unsteady flow [MMT22].

Chapter 5: The effect of the relative occlusion, the roller speed and the generalized Newtonian fluids power index on the peristalsis efficiency are clarified for a straight peristaltic pump. Multiple pair of rollers peristaltic pumps are found to exhibit advantages over those with one pair. Pumping characteristics for various relative occlusion pumps and various power index fluids are drawn [MMT21].

Chapter 6: Pulsatile flow, imposed by a periodically dilating-contracting balloon of spheroid shape, under steady inlet flow is studied. The phase difference between the balloon volume waveform and the pressure waveform is found to depend only on the Womersley number and to be independent from the point of equilibrium and the amplitude of the oscillation of the minor axis length of the ellipsoidal balloon [MMT23].

Chapter 7: Concluding remarks are noted and directions for further research are proposed.

Chapter 2

Governing equations

The basic governing equations of fluid motion are the equation of mass conservation, along with the Navier–Stokes equations of momentum conservation, named after Claude-Louis Navier and George Gabriel Stokes.

2.1 Derivation of the basic equations of fluid motion

Under the continuum hypothesis for fluids, the continuity equation originates from the Lomonosov-Lavoisier principle, defining that under classical physics assumptions, mass is not created nor destroyed or in other words is conserved. Momentum equations arise from Newton's second law, stating that the net force acting on an infinitesimal section of fluid equals the rate by which its momentum changes and points to the direction of that change.

2.1.1 Integral form of continuity equation

Let the control volume CV be surrounded by a closed control surface CS with outer normal vector $\boldsymbol{n}$. The conservation of mass is given as

$$\frac{d}{dt}\iiint_{CV}\rho dV + \oiint_{CS}\rho\boldsymbol{u}\cdot\boldsymbol{n}dS = \sum_{i=1}^{n}\dot{m}_i, \tag{2.1}$$

where t is time, $\rho(\boldsymbol{x},t)$ is the density of the fluid, $\boldsymbol{u}(\boldsymbol{x},t)$ is the velocity field and $\sum_{i=1}^{n}\dot{m}_i$ is the rate by which mass included in CS changes in time due to concentrated mass sources or sinks $\dot{m}_i,\ i\in\{1,..,n\}$ in the interior of the control volume. The left-hand side terms stand for the mass change in the control volume due to the temporal change in the density ρ of the fluid and the mass entering or leaving the control volume through its boundary CS.

2.1.2 Derivative form of continuity equation

Using Gauss's theorem

$$\iiint_{CV} (div\boldsymbol{b})dV = \oiint_{CS} (\boldsymbol{b} \cdot \boldsymbol{n})dS, \tag{2.2}$$

Equation (2.1) becomes

$$\iiint_{CV} \frac{\partial \rho}{\partial t} dV + \iiint_{CV} div(\rho \boldsymbol{u})dV = \sum_{i=1}^{n} \dot{m}_i. \tag{2.3}$$

In cases where $\sum\limits_{i=1}^{n} \dot{m}_i = 0$ we deduce that almost everywhere, i.e. except of regions with measure zero, in CV

$$\frac{\partial \rho}{\partial t} + div(\rho \boldsymbol{u}) = 0. \tag{2.4}$$

Assuming incompressible flow, namely that the variation of the density in the whole fluid domain is small, the continuity equation becomes

$$div(\rho \boldsymbol{u}) = div(\boldsymbol{u}) = 0 \tag{2.5}$$

or

$$\frac{\partial u_i}{\partial x_i} = 0. \tag{2.6}$$

2.1.3 Integral form of the Navier–Stokes equations

Let again CS be a closed surface surrounding volume CV. The momentum equation in integral form is

$$\frac{d}{dt} \iiint_{CV} \rho \boldsymbol{u} dV + \oiint_{CS} \rho \boldsymbol{u}(\boldsymbol{u} \cdot \boldsymbol{n})dS = \sum_{i=1}^{n} F_i, \tag{2.7}$$

where F_i, $i \in \{1, .., n\}$, are the forces exerted on the fluid in CV. The integrals at the left-hand side denote the change in time of the momentum of the fluid contained in the control volume and the momentum that crosses the control surface. The forces acting on the fluid are

- Mass or volume forces acting on a mass dm or volume dV element of the fluid. For example gravitational forces are given as $\boldsymbol{G} = \iiint_{CV} \boldsymbol{g} \rho dV$.
- Forces acting on the element dS of surface CS, written as $\boldsymbol{F}_{CS} = \oiint_{CS} \boldsymbol{t} dS$ with $\boldsymbol{t}$ the stresses vector given from $\boldsymbol{t} = \boldsymbol{\sigma}^{\intercal} \boldsymbol{n}$. The symbol $\boldsymbol{\sigma}$ stands for the Cauchy stress tensor

$$\boldsymbol{\sigma} = \begin{bmatrix} \sigma_{xx} & \sigma_{xy} & \sigma_{xz} \\ \sigma_{yx} & \sigma_{yy} & \sigma_{yz} \\ \sigma_{zx} & \sigma_{zy} & \sigma_{zz} \end{bmatrix}. \tag{2.8}$$

- Forces from solid body with outer surface S_κ that are of the same nature with the surface forces and can be written as $-\boldsymbol{K} = \iint_{S_\kappa} \boldsymbol{t} dS$.

Concluding, the integral form of the momentum theorem is

$$\frac{d}{dt}\iiint_{CV}\rho\boldsymbol{u}dV+\oiint_{CS}\rho\boldsymbol{u}(\boldsymbol{u}\cdot\boldsymbol{n})dS=\iiint_{CV}\boldsymbol{g}\rho dV+\oiint_{CS}\boldsymbol{t}dS-\boldsymbol{K}. \tag{2.9}$$

Lemma 1 is introduced for simplification.

Lemma 1. *Given closed surface S and the corresponding surrounded volume V*

$$\oiint_{S}\boldsymbol{\alpha}(\boldsymbol{b}\cdot\boldsymbol{n})dS=\iiint_{V}div(\boldsymbol{b}\otimes\boldsymbol{a})dV=\iiint_{V}(\boldsymbol{b}\cdot grad\boldsymbol{\alpha}+div\boldsymbol{b}\boldsymbol{\alpha})dV$$

The symbol $\otimes$ is let to denote the dyadic or tensor product.

Proof. $\oiint_S \boldsymbol{\alpha}(\boldsymbol{b}\cdot\boldsymbol{n})dS=\iiint_V(div(\alpha_1\boldsymbol{b})\boldsymbol{e}_1+div(\alpha_2\boldsymbol{b})\boldsymbol{e}_2+div(\alpha_3\boldsymbol{b})\boldsymbol{e}_3)dV=\iiint_V div(\boldsymbol{b}\otimes\boldsymbol{a})dV$

$$div(\boldsymbol{b}\otimes\boldsymbol{a})=div(\alpha_1\boldsymbol{b})\boldsymbol{e}_1+div(\alpha_2\boldsymbol{b})\boldsymbol{e}_2+div(\alpha_3\boldsymbol{b})\boldsymbol{e}_3=$$

$$(grad\alpha_1\cdot\boldsymbol{b}+div\boldsymbol{b}\alpha_1)\boldsymbol{e}_1+(grad\alpha_2\cdot\boldsymbol{b}+div\boldsymbol{b}\alpha_2)\boldsymbol{e}_2+(grad\alpha_3\cdot\boldsymbol{b}+div\boldsymbol{b}\alpha_3)\boldsymbol{e}_3=$$

$$(grad\alpha_1\cdot\boldsymbol{b})\boldsymbol{e}_1+(grad\alpha_2\cdot\boldsymbol{b})\boldsymbol{e}_2+(grad\alpha_3\cdot\boldsymbol{b})\boldsymbol{e}_3+div\boldsymbol{b}\boldsymbol{\alpha}=$$

$$\boldsymbol{b}\cdot grad\boldsymbol{\alpha}+div\boldsymbol{b}\boldsymbol{\alpha}=grad^{\mathsf{T}}\boldsymbol{\alpha}\cdot\boldsymbol{b}+div\boldsymbol{b}\boldsymbol{\alpha},$$

where we made use of Gauss's theorem. □

By employing Lemma 1 we get

$$\oiint_{CS}\rho\boldsymbol{u}(\boldsymbol{u}\cdot\boldsymbol{n})dS=\iiint_{CV}(div(\rho\boldsymbol{u})\boldsymbol{u}+\rho\boldsymbol{u}\cdot grad\boldsymbol{u})dV=\iiint_{CV}(div(\rho\boldsymbol{u})\boldsymbol{u}+grad^{\mathsf{T}}\boldsymbol{u}\cdot\rho\boldsymbol{u})dV \tag{2.10}$$

and the integral form of the momentum equation becomes

$$\iiint_{CV}\frac{\partial(\rho\boldsymbol{u})}{\partial t}dV+\iiint_{CV}(div(\rho\boldsymbol{u})\boldsymbol{u}+grad^{\mathsf{T}}\boldsymbol{u}\cdot\rho\boldsymbol{u})dV=\iiint_{CV}\boldsymbol{g}\rho dV+\iiint_{CV}div\boldsymbol{\sigma}^{\mathsf{T}}dV-\boldsymbol{K}, \tag{2.11}$$

where we additionally used the divergence theorem for tensor fields to express the surface forces term and

$$div\,\boldsymbol{\sigma}^{\mathsf{T}}=\nabla\cdot\boldsymbol{\sigma}=\begin{bmatrix}\dfrac{\partial\sigma_{xx}}{\partial x}+\dfrac{\partial\sigma_{yx}}{\partial y}+\dfrac{\partial\sigma_{zx}}{\partial z}\\ \dfrac{\partial\sigma_{xy}}{\partial x}+\dfrac{\partial\sigma_{yy}}{\partial y}+\dfrac{\partial\sigma_{zy}}{\partial z}\\ \dfrac{\partial\sigma_{xz}}{\partial x}+\dfrac{\partial\sigma_{yz}}{\partial y}+\dfrac{\partial\sigma_{zz}}{\partial z}\end{bmatrix}. \tag{2.12}$$

2.1.4 Derivative convective form of the Navier–Stokes equations

Assuming the absence of body forces exerted on the fluid, the derivative form of the momentum equation is derived from Equation (2.11)

$$\frac{\partial(\rho \boldsymbol{u})}{\partial t} + div(\rho \boldsymbol{u})\boldsymbol{u} + grad^{\mathsf{T}}\boldsymbol{u} \cdot \rho \boldsymbol{u} = \rho \boldsymbol{g} + div\boldsymbol{\sigma}^{\mathsf{T}}, \tag{2.13}$$

except for a set $A \subset CV$ with measure $m(A) = 0$. Rearranging the terms of the left-hand side at the momemtum equation we get

$$\frac{\partial(\rho \boldsymbol{u})}{\partial t} + div(\rho \boldsymbol{u})\boldsymbol{u} + grad^{\mathsf{T}}\boldsymbol{u} \cdot \rho \boldsymbol{u} = \left[\frac{\partial \rho}{\partial t} + div(\rho \boldsymbol{u})\right]\boldsymbol{u} + \rho\left(\frac{\partial \boldsymbol{u}}{\partial t} + \boldsymbol{u} \cdot grad\boldsymbol{u}\right). \tag{2.14}$$

Using the continuity equation we get the simplified Lagrangian form of the momentum equation

$$\rho \frac{D\boldsymbol{u}}{Dt} = \rho \boldsymbol{g} + div\boldsymbol{\sigma}^{\mathsf{T}}, \tag{2.15}$$

where the material derivative for the flow field is given as

$$\frac{D}{Dt} = \frac{\partial}{\partial t} + u\frac{\partial}{\partial x} + \mathrm{v}\frac{\partial}{\partial y} + w\frac{\partial}{\partial z} = \frac{\partial}{\partial t} + \boldsymbol{u} \cdot grad, \tag{2.16}$$

where u, v, w are the Cartesian velocity components of the flow field $\boldsymbol{u}$.

2.1.5 Derivative conservation form of the Navier–Stokes equations

Considering the identity $\nabla \cdot (\rho u \boldsymbol{u}) = u\nabla \cdot (\rho \boldsymbol{u}) + \rho \boldsymbol{u} \cdot \nabla u$ for say the x-component of Equation (2.13) we derive the Eulerian form for the x equation

$$\frac{D(\rho u)}{Dt} = \frac{\partial(\rho u)}{\partial t} + \nabla \cdot (\rho u \boldsymbol{u}) = \rho g_x + \frac{\partial \sigma_{xx}}{\partial x} + \frac{\partial \sigma_{yx}}{\partial y} + \frac{\partial \sigma_{zx}}{\partial z}. \tag{2.17}$$

Working analogously for the equations in y, z directions, we get the Navier-Stokes equations in conservation form

$$\frac{\partial(\rho \boldsymbol{u})}{\partial t} + \nabla \cdot (\rho \boldsymbol{u} \otimes \boldsymbol{u}) = \rho \boldsymbol{g} + \nabla \cdot \boldsymbol{\sigma}. \tag{2.18}$$

2.1.6 Newtonian fluids

The system of Equations (2.4), (2.18) is incomplete, therefore a material constitutive equation is required. The tensor $\boldsymbol{D}$ is the rate of deformation given by

$$D_{ij} = \frac{1}{2}\left(\frac{\partial u_i}{\partial x_j} + \frac{\partial u_j}{\partial x_i}\right) \tag{2.19}$$

or in matrix notation

$$\boldsymbol{D} = \frac{1}{2}(grad^{\mathsf{T}}\boldsymbol{u} + grad\boldsymbol{u}) = \frac{1}{2}((\nabla\boldsymbol{u})^{\mathsf{T}} + \nabla\boldsymbol{u}) = \begin{bmatrix} u_x & \frac{1}{2}(u_y + \mathrm{v}_x) & \frac{1}{2}(u_z + w_x) \\ \frac{1}{2}(u_y + \mathrm{v}_x) & \mathrm{v}_y & \frac{1}{2}(w_y + \mathrm{v}_z) \\ \frac{1}{2}(w_x + u_z) & \frac{1}{2}(w_y + \mathrm{v}_z) & w_z \end{bmatrix}. \tag{2.20}$$

Materials which obey to the equation

$$\boldsymbol{\sigma} = -p\boldsymbol{I} + \boldsymbol{\tau}, \tag{2.21}$$

where $\boldsymbol{I}$ is the identity tensor, are called Stokes materials. If additionally the shear stresses are proportional to the rate of strain (which is found experimentally for the most common fluids as air and water)

$$\boldsymbol{\tau} = f(D_{ij}), \tag{2.22}$$

where f is linear, or

$$\tau_{ij} = \alpha_{ijkm} D_{ij}, \;\; i,j,k,m = 1,2,3 \tag{2.23}$$

for a fourth rank tensor α_{ijkm}, the fluids are called Newtonian. By demanding the tensor elements to be independent of axis rotation, α_{ijkm} should be isotropic

$$\alpha_{ijkm} = \mu' \delta_{ij}\delta_{km} + \mu(\delta_{ik}\delta_{jm} + \delta_{im}\delta_{jk}) + \mu''(\delta_{ik}\delta_{jm} - \delta_{im}\delta_{jk}). \tag{2.24}$$

Hence,

$$\begin{aligned} \tau_{ij} &= \left[\mu' \delta_{ij}\delta_{km} + \mu(\delta_{ik}\delta_{jm} + \delta_{im}\delta_{jk}) + \mu''(\delta_{ik}\delta_{jm} - \delta_{im}\delta_{jk})\right] D_{km} \\ &= \mu'\delta_{ij}D_{kk} + \mu\left(D_{ij} + D_{ji}\right) + \mu''\left(D_{ij} - D_{ji}\right) \\ &= \mu'\delta_{ij}D_{kk} + \mu\left(\frac{\partial u_i}{\partial x_j} + \frac{\partial u_j}{\partial x_i}\right), \end{aligned} \tag{2.25}$$

where the symmetry $D_{ij} = D_{ji}$ is taken into account. Using matrices

$$\boldsymbol{\tau} = 2\mu\boldsymbol{D} + \mu'\, tr\boldsymbol{D}\boldsymbol{I}, \tag{2.26}$$

where μ is the (coefficient of) dynamic viscosity, μ' is the bulk viscosity or second coefficient of viscosity and

$$tr\boldsymbol{D} = \frac{\partial u}{\partial x} + \frac{\partial \mathrm{v}}{\partial y} + \frac{\partial w}{\partial z} = div\boldsymbol{u}. \tag{2.27}$$

Therefore the entries of tensor $\boldsymbol{\sigma}$ are

$$\sigma_{xx} = -p + 2\mu\frac{\partial u}{\partial x} + \mu' div\boldsymbol{u} \tag{2.28}$$

$$\sigma_{yy} = -p + 2\mu \frac{\partial \mathrm{v}}{\partial y} + \mu' div\boldsymbol{u} \tag{2.29}$$

$$\sigma_{zz} = -p + 2\mu \frac{\partial w}{\partial z} + \mu' div\boldsymbol{u} \tag{2.30}$$

$$\sigma_{xy} = \sigma_{yx} = \mu \left(\frac{\partial u}{\partial y} + \frac{\partial \mathrm{v}}{\partial x} \right) \tag{2.31}$$

$$\sigma_{xz} = \sigma_{zx} = \mu \left(\frac{\partial u}{\partial z} + \frac{\partial w}{\partial x} \right) \tag{2.32}$$

$$\sigma_{yz} = \sigma_{zy} = \mu \left(\frac{\partial \mathrm{v}}{\partial z} + \frac{\partial w}{\partial y} \right). \tag{2.33}$$

Substituting these equations in Equation (2.15) we get

$$\begin{aligned}
\rho \frac{Du}{Dt} &= \rho g_x - \frac{\partial p}{\partial x} + \frac{\partial}{\partial x}\left[2\mu \frac{\partial u}{\partial x} + \mu' div\boldsymbol{u}\right] + \frac{\partial}{\partial y}\left[\mu\left(\frac{\partial u}{\partial y} + \frac{\partial \mathrm{v}}{\partial x}\right)\right] + \frac{\partial}{\partial z}\left[\mu\left(\frac{\partial u}{\partial z} + \frac{\partial w}{\partial x}\right)\right] \\
\rho \frac{D\mathrm{v}}{Dt} &= \rho g_y - \frac{\partial p}{\partial y} + \frac{\partial}{\partial x}\left[\mu\left(\frac{\partial \mathrm{v}}{\partial x} + \frac{\partial u}{\partial y}\right)\right] + \frac{\partial}{\partial y}\left[2\mu \frac{\partial \mathrm{v}}{\partial y} + \mu' div\boldsymbol{u}\right] + \frac{\partial}{\partial z}\left[\mu\left(\frac{\partial \mathrm{v}}{\partial z} + \frac{\partial w}{\partial y}\right)\right] \\
\rho \frac{Dw}{Dt} &= \rho g_z - \frac{\partial p}{\partial z} + \frac{\partial}{\partial x}\left[\mu\left(\frac{\partial w}{\partial x} + \frac{\partial u}{\partial z}\right)\right] + \frac{\partial}{\partial y}\left[\mu\left(\frac{\partial w}{\partial y} + \frac{\partial \mathrm{v}}{\partial z}\right)\right] + \frac{\partial}{\partial z}\left[2\mu \frac{\partial w}{\partial z} + \mu' div\boldsymbol{u}\right].
\end{aligned} \tag{2.34}$$

So these are the Navier-Stokes equations for Newtonian fluids. Using the assumption that μ is constant and by employing Schwarz 's theorem for commutation of partial derivatives in second partial derivatives, we derive the simplified form for Newtonian fluids

$$\begin{aligned}
\rho \frac{Du}{Dt} &= \rho \left(\frac{\partial u}{\partial t} + u\frac{\partial u}{\partial x} + \mathrm{v}\frac{\partial u}{\partial y} + w\frac{\partial u}{\partial z} \right) \\
&= \rho g_x - \frac{\partial p}{\partial x} + \mu\left(\frac{\partial^2 u}{\partial x^2} + \frac{\partial^2 u}{\partial y^2} + \frac{\partial^2 u}{\partial z^2} \right) + \mu \frac{\partial (div\boldsymbol{u})}{\partial x} + \frac{\partial (\mu' div\boldsymbol{u})}{\partial x} \\
\rho \frac{D\mathrm{v}}{Dt} &= \rho \left(\frac{\partial \mathrm{v}}{\partial t} + u\frac{\partial \mathrm{v}}{\partial x} + \mathrm{v}\frac{\partial \mathrm{v}}{\partial y} + w\frac{\partial \mathrm{v}}{\partial z} \right) \\
&= \rho g_y - \frac{\partial p}{\partial y} + \mu\left(\frac{\partial^2 \mathrm{v}}{\partial x^2} + \frac{\partial^2 \mathrm{v}}{\partial y^2} + \frac{\partial^2 \mathrm{v}}{\partial z^2} \right) + \mu \frac{\partial (div\boldsymbol{u})}{\partial y} + \frac{\partial (\mu' div\boldsymbol{u})}{\partial y} \\
\rho \frac{Dw}{Dt} &= \rho \left(\frac{\partial w}{\partial t} + u\frac{\partial w}{\partial x} + \mathrm{v}\frac{\partial w}{\partial y} + w\frac{\partial w}{\partial z} \right) \\
&= \rho g_z - \frac{\partial p}{\partial z} + \mu\left(\frac{\partial^2 w}{\partial x^2} + \frac{\partial^2 w}{\partial y^2} + \frac{\partial^2 w}{\partial z^2} \right) + \mu \frac{\partial (div\boldsymbol{u})}{\partial z} + \frac{\partial (\mu' div\boldsymbol{u})}{\partial z}
\end{aligned} \tag{2.35}$$

in scalar form. In a more succinct way, the above system can be written in vector notation as

$$\begin{aligned} \rho\frac{D\boldsymbol{u}}{Dt} =&\rho\frac{\partial \boldsymbol{u}}{\partial t}+\rho\left(u\frac{\partial \boldsymbol{u}}{\partial x}+\mathrm{v}\frac{\partial \boldsymbol{u}}{\partial y}+w\frac{\partial \boldsymbol{u}}{\partial z}\right)= \\ &\rho\boldsymbol{g}-\nabla p+\mu\left(\frac{\partial^2\boldsymbol{u}}{\partial x^2}+\frac{\partial^2\boldsymbol{u}}{\partial y^2}+\frac{\partial^2\boldsymbol{u}}{\partial z^2}\right)+\mu\nabla\cdot(\nabla\cdot\boldsymbol{u})\boldsymbol{I}+\nabla\cdot(\mu'\nabla\cdot\boldsymbol{u})\boldsymbol{I} \end{aligned} \tag{2.36}$$

or

$$\frac{D\boldsymbol{u}}{Dt}=\frac{\partial\boldsymbol{u}}{\partial t}+\boldsymbol{u}\cdot\nabla\boldsymbol{u}=\boldsymbol{g}-\frac{1}{\rho}\nabla p+\nu\nabla^2\boldsymbol{u}+\frac{\mu}{\rho}\nabla\cdot(\nabla\cdot\boldsymbol{u})\boldsymbol{I}+\frac{1}{\rho}\nabla\cdot(\mu'\nabla\cdot\boldsymbol{u})\boldsymbol{I}, \tag{2.37}$$

where the kinematic viscosity $\nu=\frac{\mu}{\rho}$, is introduced. By substituting Equation (2.5) in Equation (2.37), we get for incompressible flows

$$\frac{D\boldsymbol{u}}{Dt}=\frac{\partial\boldsymbol{u}}{\partial t}+\boldsymbol{u}\cdot\nabla\boldsymbol{u}=\boldsymbol{g}-\frac{1}{\rho}\nabla p+\nu\nabla^2\boldsymbol{u} \tag{2.38}$$

or in tensor notation

$$\frac{Du_i}{Dt}=\frac{\partial u_i}{\partial t}+u_j\frac{\partial u_i}{\partial x_j}=g_i-\frac{1}{\rho}\frac{\partial p}{\partial x_i}+\nu\frac{\partial^2 u_i}{\partial x_j\partial x_j}. \tag{2.39}$$

Furthermore, by substituting Equations (2.28-2.33) in Equation (2.18) and by working in the same manner we get the conservation form of the Navier-Stokes equations for Newtonian incompressible flows

$$\frac{\partial\boldsymbol{u}}{\partial t}+\nabla\cdot(\boldsymbol{u}\otimes\boldsymbol{u})=\boldsymbol{g}-\frac{1}{\rho}\nabla p+\nu\nabla\cdot[(\nabla\boldsymbol{u})^{\intercal}+\nabla\boldsymbol{u}] \tag{2.40}$$

or in tensor notation

$$\frac{\partial u_i}{\partial t}+\frac{\partial}{\partial x_j}(u_iu_j)=g_i-\frac{1}{\rho}\frac{\partial p}{\partial x_i}+\nu\frac{\partial}{\partial x_j}\left(\frac{\partial u_i}{\partial x_j}+\frac{\partial u_j}{\partial x_i}\right) \tag{2.41}$$

and by introducing the continuity equation

$$\frac{\partial\boldsymbol{u}}{\partial t}+\nabla\cdot(\boldsymbol{u}\otimes\boldsymbol{u})=\boldsymbol{g}-\frac{1}{\rho}\nabla p+\nu\nabla^2\boldsymbol{u} \tag{2.42}$$

or

$$\frac{\partial u_i}{\partial t}+\frac{\partial}{\partial x_j}(u_iu_j)=g_i-\frac{1}{\rho}\frac{\partial p}{\partial x_i}+\nu\frac{\partial^2 u_i}{\partial x_j\partial x_j}. \tag{2.43}$$

2.1.7 Generalized Newtonian fluids

Time-independent non-Newtonian fluids with the constitutive law of the form of a generalized first-grade Rivlin–Ericksen fluid are considered. The shear-dependent viscosity is given as

$$\sigma(v)=-p\boldsymbol{I}+2\mu(\dot{\gamma})\boldsymbol{D}, \tag{2.44}$$

where $\boldsymbol{D}$ stands for the strain rate tensor ($2\boldsymbol{D}$ is the first Rivlin–Ericksen tensor) (Equation (2.19)) and $\dot{\gamma}$ stands for the shear rate (i.e., the strain rate tensor norm):

$$\begin{aligned}\dot{\gamma} =&\sqrt{2(\boldsymbol{D}:\boldsymbol{D})} = \sqrt{2tr(\boldsymbol{D}^2)}\\ =&\sqrt{2\left(\frac{\partial u}{\partial x}\right)^2+2\left(\frac{\partial \mathrm{v}}{\partial y}\right)^2+2\left(\frac{\partial w}{\partial z}\right)^2+\left(\frac{\partial u}{\partial y}+\frac{\partial \mathrm{v}}{\partial x}\right)^2+\left(\frac{\partial u}{\partial z}+\frac{\partial w}{\partial x}\right)^2+\left(\frac{\partial w}{\partial y}+\frac{\partial \mathrm{v}}{\partial z}\right)^2}.\end{aligned} \tag{2.45}$$

The symbol : represents the colon product of dyads.

Starting from Equation (2.34) and assuming shear dependent dynamic viscosity, the incompressible flow Navier–Stokes equations for the class of generalized Newtonian fluids that have a rheological equation of state as in Equation (2.44), are

$$\rho\frac{\partial \boldsymbol{u}}{\partial t}+\rho(\boldsymbol{u}\cdot\nabla)\boldsymbol{u}=\rho\boldsymbol{g}-\nabla p+\nabla\cdot(2\mu(\dot{\gamma})\boldsymbol{D}). \tag{2.46}$$

The category of generalized Newtonian fluids examined, is characterized by rheology predicted from the Bird–Carreau equation for the shear dependent dynamic viscosity :

$$\mu(\dot{\gamma})=\mu_{\mathrm{inf}}+(\mu_0-\mu_{\mathrm{inf}})(1+(\lambda\dot{\gamma})^2)^{\frac{n-1}{2}}. \tag{2.47}$$

In the above equation, μ_{inf} is the viscosity at infinite shear rate, μ_0 is the viscosity at zero shear rate, λ is the relaxation time and n is the Bird–Carreau power index. Fluids with $n<1$ exhibit shear-thinning or pseudoplastic behavior, whereas $n>1$ shows shear-thickening or dilatant behavior, while fluids with $n=1$ degenerate to Newtonian.

2.2 Non dimensional form of the Navier-Stokes equations for incompressible flows

In order to solve families of similar flows by giving a single solution to the system of partial differential equations which describes them, the nondimensionalization technique is used. For each flow, characteristic scales of the variables involved are chosen and the system is nondimensionalized as follows

- Length $\mathcal{L}$
- Flow velocity U
- Time $\mathcal{T}$
- Characteristic pressure difference $\mathcal{P}-\mathcal{P}_\infty$
- External field $\mathcal{G}$.

The nondimensional variables arise as $v' = \dfrac{v}{U}$ for $v \in \{u, \mathrm{v}, w\}$, $p' = \dfrac{p - \mathcal{P}_\infty}{\mathcal{P} - \mathcal{P}_\infty}$, $x_i' = \dfrac{x_i}{\mathcal{L}}$, for $x_i \in \{x, y, z\}$ and $x_i' \in \{x', y', z'\}$ respectively, $t' = \dfrac{t}{\mathcal{T}}$. By the differentiation rules we derive

$$\begin{aligned}
\frac{\mathcal{L}}{U\mathcal{T}}\frac{\partial u'}{\partial t'} + u'\frac{\partial u'}{\partial x'} + \mathrm{v}'\frac{\partial u'}{\partial y'} + w'\frac{\partial u'}{\partial z'} &= \frac{\mathcal{L}\mathcal{G}}{U^2}g_x' - \frac{\mathcal{P} - \mathcal{P}_\infty}{\rho U^2}\frac{\partial p'}{\partial x'} + \frac{\nu}{U\mathcal{L}}\left(\frac{\partial^2 u'}{\partial x'^2} + \frac{\partial^2 u'}{\partial y'^2} + \frac{\partial^2 u'}{\partial z'^2}\right) \\
\frac{\mathcal{L}}{U\mathcal{T}}\frac{\partial \mathrm{v}'}{\partial t'} + u'\frac{\partial \mathrm{v}'}{\partial x'} + \mathrm{v}'\frac{\partial \mathrm{v}'}{\partial y'} + w'\frac{\partial \mathrm{v}'}{\partial z'} &= \frac{\mathcal{L}\mathcal{G}}{U^2}g_y' - \frac{\mathcal{P} - \mathcal{P}_\infty}{\rho U^2}\frac{\partial p'}{\partial y'} + \frac{\nu}{U\mathcal{L}}\left(\frac{\partial^2 \mathrm{v}'}{\partial x'^2} + \frac{\partial^2 \mathrm{v}'}{\partial y'^2} + \frac{\partial^2 \mathrm{v}'}{\partial z'^2}\right) \\
\frac{\mathcal{L}}{U\mathcal{T}}\frac{\partial w'}{\partial t'} + u'\frac{\partial w'}{\partial x'} + \mathrm{v}'\frac{\partial w'}{\partial y'} + w'\frac{\partial w'}{\partial z'} &= \frac{\mathcal{L}\mathcal{G}}{U^2}g_z' - \frac{\mathcal{P} - \mathcal{P}_\infty}{\rho U^2}\frac{\partial p'}{\partial z'} + \frac{\nu}{U\mathcal{L}}\left(\frac{\partial^2 w'}{\partial x'^2} + \frac{\partial^2 w'}{\partial y'^2} + \frac{\partial^2 w'}{\partial z'^2}\right) \\
\frac{\partial u'}{\partial x'} + \frac{\partial \mathrm{v}'}{\partial y'} + \frac{\partial w'}{\partial z'} &= 0.
\end{aligned} \tag{2.48}$$

At this point, the following nondimensional parameters are introduced

- Strouhal number $St = \dfrac{\mathcal{L}}{U\mathcal{T}}$
- Froude number $Fr = \dfrac{U}{\sqrt{\mathcal{G}\mathcal{L}}}$
- Reynolds number $Re = \dfrac{U\mathcal{L}}{\nu}$
- Euler number $Eu = \dfrac{\mathcal{P} - \mathcal{P}_\infty}{\rho U^2}$.

Hence the nondimensional equations become

$$\begin{aligned}
St\frac{\partial u}{\partial t} + u\frac{\partial u}{\partial x} + \mathrm{v}\frac{\partial u}{\partial y} + w\frac{\partial u}{\partial z} &= \frac{1}{Fr^2}g_x - Eu\frac{\partial p}{\partial x} + \frac{1}{Re}\left(\frac{\partial^2 u}{\partial x^2} + \frac{\partial^2 u}{\partial y^2} + \frac{\partial^2 u}{\partial z^2}\right) \\
St\frac{\partial \mathrm{v}}{\partial t} + u\frac{\partial \mathrm{v}}{\partial x} + \mathrm{v}\frac{\partial \mathrm{v}}{\partial y} + w\frac{\partial \mathrm{v}}{\partial z} &= \frac{1}{Fr^2}g_y - Eu\frac{\partial p}{\partial y} + \frac{1}{Re}\left(\frac{\partial^2 \mathrm{v}}{\partial x^2} + \frac{\partial^2 \mathrm{v}}{\partial y^2} + \frac{\partial^2 \mathrm{v}}{\partial z^2}\right) \\
St\frac{\partial w}{\partial t} + u\frac{\partial w}{\partial x} + \mathrm{v}\frac{\partial w}{\partial y} + w\frac{\partial w}{\partial z} &= \frac{1}{Fr^2}g_z - Eu\frac{\partial p}{\partial z} + \frac{1}{Re}\left(\frac{\partial^2 w}{\partial x^2} + \frac{\partial^2 w}{\partial y^2} + \frac{\partial^2 w}{\partial z^2}\right) \\
\frac{\partial u}{\partial x} + \frac{\partial \mathrm{v}}{\partial y} + \frac{\partial w}{\partial z} &= 0,
\end{aligned} \tag{2.49}$$

where the nondimensional variables are represented for simplicity without the prime $'$. In vector notation, the nondimensional Navier-Stokes system in convective form is

$$St\frac{\partial \boldsymbol{u}}{\partial t} + u\frac{\partial \boldsymbol{u}}{\partial x} + \mathrm{v}\frac{\partial \boldsymbol{u}}{\partial y} + w\frac{\partial \boldsymbol{u}}{\partial z} = \frac{1}{Fr^2}\boldsymbol{g} - Eu\nabla p + \frac{1}{Re}\left(\frac{\partial^2 \boldsymbol{u}}{\partial x^2} + \frac{\partial^2 \boldsymbol{u}}{\partial y^2} + \frac{\partial^2 \boldsymbol{u}}{\partial z^2}\right). \tag{2.50}$$

In an analogous manner Equations (2.42) become nondimensional as

$$St\frac{\partial \boldsymbol{u}}{\partial t} + \nabla \cdot (\boldsymbol{u} \otimes \boldsymbol{u}) = \frac{1}{Fr^2}\boldsymbol{g} - Eu\nabla p + \frac{1}{Re}\nabla^2 \boldsymbol{u}. \tag{2.51}$$

2.3 Navier-Stokes equations in a curvilinear coordinate system

2.3.1 The generalized curvilinear coordinate system

A curvilinear coordinate system is a coordinate chart on the differentiable manifold E^n (Euclidean space in n dimensions) which is isomorphic to the Cartesian coordinate chart on the manifold.

We introduce the one to one and differentiable mapping from $\mathbb{R}^3$ to $\mathbb{R}^3$: $(x, y, z) \to (\xi, \eta, \zeta)$. The values of functions (ξ, η, ζ) are called curvilinear coordinates of the point with Cartesian coordinates (x, y, z) in the Euclidean space.

Next, we consider the covariant and the contravariant bases i.e. the one which changes directly proportionally with the change of the axes, $(\boldsymbol{g}_1, \boldsymbol{g}_2, \boldsymbol{g}_3)$ and the one which changes inversely proportionally with the axes, $(\boldsymbol{g}^1, \boldsymbol{g}^2, \boldsymbol{g}^3)$, respectively. These bases are given by the relations

$$\begin{aligned}
\boldsymbol{g}_1 &= \frac{\partial \boldsymbol{x}}{\partial \xi} = \left(\frac{\partial x}{\partial \xi}, \frac{\partial y}{\partial \xi}, \frac{\partial z}{\partial \xi} \right) = (x_\xi, y_\xi, z_\xi) \\
\boldsymbol{g}_2 &= \frac{\partial \boldsymbol{x}}{\partial \eta} = \left(\frac{\partial x}{\partial \eta}, \frac{\partial y}{\partial \eta}, \frac{\partial z}{\partial \eta} \right) = (x_\eta, y_\eta, z_\eta) \\
\boldsymbol{g}_3 &= \frac{\partial \boldsymbol{x}}{\partial \zeta} = \left(\frac{\partial x}{\partial \zeta}, \frac{\partial y}{\partial \zeta}, \frac{\partial z}{\partial \zeta} \right) = (x_\zeta, y_\zeta, z_\zeta)
\end{aligned} \tag{2.52}$$

$$\begin{aligned}
\boldsymbol{g}^1 &= \nabla \xi = \left(\frac{\partial \xi}{\partial x}, \frac{\partial \xi}{\partial y}, \frac{\partial \xi}{\partial z} \right) = (\xi_x, \xi_y, \xi_z) \\
\boldsymbol{g}^2 &= \nabla \eta = \left(\frac{\partial \eta}{\partial x}, \frac{\partial \eta}{\partial y}, \frac{\partial \eta}{\partial z} \right) = (\eta_x, \eta_y, \eta_z) \\
\boldsymbol{g}^3 &= \nabla \zeta = \left(\frac{\partial \zeta}{\partial x}, \frac{\partial \zeta}{\partial y}, \frac{\partial \zeta}{\partial z} \right) = (\zeta_x, \zeta_y, \zeta_z).
\end{aligned} \tag{2.53}$$

The vectors $\boldsymbol{g}_i$ are tangent to the respective ξ^i grid lines and the vectors $\boldsymbol{g}^i$ are perpendicular to the respective constant ξ^i lines. In order to use Einstein's notation, we call (x, y, z) as $(x_1, x_2, x_3) = \boldsymbol{r}$ and (ξ, η, ζ) as (ξ^1, ξ^2, ξ^3). Consequently the former bases can be written more succinctly as

$$\boldsymbol{g}_i = \frac{\partial \boldsymbol{r}}{\partial \xi^i} = \left(\frac{\partial x_1}{\partial \xi^i}, \frac{\partial x_2}{\partial \xi^i}, \frac{\partial x_3}{\partial \xi^i} \right) \tag{2.54}$$

$$\boldsymbol{g}^i = \nabla \xi^i = \left(\frac{\partial \xi^i}{\partial x_1}, \frac{\partial \xi^i}{\partial x_2}, \frac{\partial \xi^i}{\partial x_3} \right). \tag{2.55}$$

By definition of the gradient operator, we get for the function ξ^i

$$d\xi^i = \nabla \xi^i \cdot d\boldsymbol{r} \tag{2.56}$$

and because $\boldsymbol{r} = \boldsymbol{r}(\xi^1, \xi^2, \xi^3)$, from the chain rule follows that

$$d\boldsymbol{r} = \frac{\partial \boldsymbol{r}}{\partial \xi^j} d\xi^j = \boldsymbol{g}_j d\xi^j. \tag{2.57}$$

Therefore, by Equation (2.56) we derive

$$d\xi^i = \nabla \xi^i \cdot \boldsymbol{g}_j d\xi^j. \tag{2.58}$$

Consequently,

$$\begin{aligned} \nabla \xi^i \cdot \boldsymbol{g}_j &= \delta^i_j \\ \boldsymbol{g}^i \cdot \boldsymbol{g}_j &= \delta^i_j. \end{aligned} \tag{2.59}$$

Thus, the two bases $\boldsymbol{g}_i$ and $\boldsymbol{g}^i$ which share the same index set $i = \{1, 2, 3\}$ are reciprocal to each other and to produce the vectors $\boldsymbol{g}^i, i = \{1, 2, 3\}$ from its dual $\boldsymbol{g}_i, i = \{1, 2, 3\}$ we use the transformations

$$\boldsymbol{g}^1 = \frac{\boldsymbol{g}_2 \times \boldsymbol{g}_3}{\boldsymbol{g}_1 \cdot (\boldsymbol{g}_2 \times \boldsymbol{g}_3)}, \ \boldsymbol{g}^2 = \frac{\boldsymbol{g}_3 \times \boldsymbol{g}_1}{\boldsymbol{g}_2 \cdot (\boldsymbol{g}_3 \times \boldsymbol{g}_1)}, \ \boldsymbol{g}^3 = \frac{\boldsymbol{g}_1 \times \boldsymbol{g}_2}{\boldsymbol{g}_3 \cdot (\boldsymbol{g}_1 \times \boldsymbol{g}_2)} \tag{2.60}$$

and vice versa

$$\boldsymbol{g}_1 = \frac{\boldsymbol{g}^2 \times \boldsymbol{g}^3}{\boldsymbol{g}^1 \cdot (\boldsymbol{g}^2 \times \boldsymbol{g}^3)}, \ \boldsymbol{g}_2 = \frac{\boldsymbol{g}^3 \times \boldsymbol{g}^1}{\boldsymbol{g}^2 \cdot (\boldsymbol{g}^3 \times \boldsymbol{g}^1)}, \ \boldsymbol{g}_3 = \frac{\boldsymbol{g}^1 \times \boldsymbol{g}^2}{\boldsymbol{g}^3 \cdot (\boldsymbol{g}^1 \times \boldsymbol{g}^2)}. \tag{2.61}$$

A vector $\boldsymbol{a}$ is expressed in respect of the Cartesian basis $(\boldsymbol{x}_1, \boldsymbol{x}_2, \boldsymbol{x}_3)$ as

$$\boldsymbol{a} = a_{x_1}\boldsymbol{x}_1 + a_{x_2}\boldsymbol{x}_2 + a_{x_3}\boldsymbol{x}_3,$$

while in respect of the basis $(\boldsymbol{g}_1, \boldsymbol{g}_2, \boldsymbol{g}_3)$, is written as

$$\boldsymbol{a} = A^1\boldsymbol{g}_1 + A^2\boldsymbol{g}_2 + A^3\boldsymbol{g}_3. \tag{2.62}$$

The components of a vector written in a covariant basis are contravariant. On the other hand, the expression concerning the contravariant basis $(\boldsymbol{g}^1, \boldsymbol{g}^2, \boldsymbol{g}^3)$ is

$$\boldsymbol{a} = A_1\boldsymbol{g}^1 + A_2\boldsymbol{g}^2 + A_3\boldsymbol{g}^3, \tag{2.63}$$

namely, it employs covariant components. By employing Equation (2.59) we get the relation between contravariant and Cartesian coordinates as

$$\begin{aligned} A^i =& \boldsymbol{g}^i \cdot a_{x_j}\boldsymbol{x}_j \\ =& \left(\frac{\partial \xi^i}{\partial x_1}, \frac{\partial \xi^i}{\partial x_2}, \frac{\partial \xi^i}{\partial x_3}\right) \cdot (1,0,0)a_{x_1} + \left(\frac{\partial \xi^i}{\partial x_1}, \frac{\partial \xi^i}{\partial x_2}, \frac{\partial \xi^i}{\partial x_3}\right) \cdot (0,1,0)a_{x_2} \\ & + \left(\frac{\partial \xi^i}{\partial x_1}, \frac{\partial \xi^i}{\partial x_2}, \frac{\partial \xi^i}{\partial x_3}\right) \cdot (0,0,1)a_{x_3} \\ =& \frac{\partial \xi^i}{\partial x_1}a_{x_1} + \frac{\partial \xi^i}{\partial x_2}a_{x_2} + \frac{\partial \xi^i}{\partial x_3}a_{x_3} \qquad = \frac{\partial \xi^i}{\partial x_j}a_{x_j}. \end{aligned} \tag{2.64}$$

By the same manner, the Cartesian components are given as function of the contravariant ones as

$$a_{x_i} = \frac{\partial x_j}{\partial \xi^i} A^j. \tag{2.65}$$

The volume element in curvilinear coordinates is

$$dV = \left| \frac{\partial(x_1, x_2, x_3)}{\partial(\xi^1, \xi^2, \xi^3)} \right| d\xi^1 d\xi^2 d\xi^3. \tag{2.66}$$

The jacobian matrix is

$$\frac{\partial(x_1, x_2, x_3)}{\partial(\xi^1, \xi^2, \xi^3)} \tag{2.67}$$

and its determinant has the form

$$\begin{aligned} J = \left| \frac{\partial(x_1, x_2, x_3)}{\partial(\xi^1, \xi^2, \xi^3)} \right| = & \begin{vmatrix} \frac{\partial x_1}{\partial \xi^1} & \frac{\partial x_1}{\partial \xi^2} & \frac{\partial x_1}{\partial \xi^3} \\ \frac{\partial x_2}{\partial \xi^1} & \frac{\partial x_2}{\partial \xi^2} & \frac{\partial x_2}{\partial \xi^3} \\ \frac{\partial x_3}{\partial \xi^1} & \frac{\partial x_3}{\partial \xi^2} & \frac{\partial x_3}{\partial \xi^3} \end{vmatrix} \\ = & \boldsymbol{g}_1 \cdot (\boldsymbol{g}_2 \times \boldsymbol{g}_3). \end{aligned} \tag{2.68}$$

2.3.2 The metric tensor

Assuming the invariant base $\boldsymbol{e}_1 = (1, 0, 0)$, $\boldsymbol{e}_2 = (0, 1, 0)$, $\boldsymbol{e}_3 = (0, 0, 1)$ of the Cartesian coordinate system, the distance between two points P and Q with coordinates x_i and $x_i + dx_i$ is ds

$$ds^2 = \sum_{i=1}^{3} dx_i dx_i. \tag{2.69}$$

We can write the differential of x_i as

$$dx_k = \frac{\partial x_k}{\partial \xi^i} d\xi^i \tag{2.70}$$

and the equation for ds becomes

$$ds^2 = \sum_{k=1}^{3} \left(\frac{\partial x_k}{\partial \xi^i} d\xi^i \right) \left(\frac{\partial x_k}{\partial \xi^j} d\xi^j \right) = g_{ij} d\xi^i d\xi^j. \tag{2.71}$$

The quantity

$$g_{ij} = \sum_{k=1}^{3} \frac{\partial x_k}{\partial \xi^i} \frac{\partial x_k}{\partial \xi^j} = \boldsymbol{g}_i \cdot \boldsymbol{g}_j \tag{2.72}$$

that arises at the right-hand side, is called the metric tensor and is the factor of proportionality between the product of the differentials of the curvilinear coordinates and that of the length.

Because bases $\boldsymbol{g}_i$ and $\boldsymbol{g}^j$ span the same space,

$$span\{\boldsymbol{g}_1, \boldsymbol{g}_2, \boldsymbol{g}_3\} = span\{\boldsymbol{g}^1, \boldsymbol{g}^2, \boldsymbol{g}^3\}, \tag{2.73}$$

coefficients $\mathcal{M}_{ij}$ should exist, such that

$$\begin{aligned} \boldsymbol{g}_i &= \mathcal{M}_{ij}\boldsymbol{g}^j \\ \boldsymbol{g}_i \cdot \boldsymbol{g}_j &= \mathcal{M}_{ij}\boldsymbol{g}^j \cdot \boldsymbol{g}_j \\ g_{ij} &= \mathcal{M}_{ij}. \end{aligned}$$

Therefore,

$$\boldsymbol{g}_i = g_{ij}\boldsymbol{g}^j. \tag{2.74}$$

Similarly, coefficients $\mathcal{N}_{ij}$ should exist such that

$$\begin{aligned} \boldsymbol{g}^i &= \mathcal{N}_{ij}\boldsymbol{g}_j \\ \boldsymbol{g}^i \cdot \boldsymbol{g}^j &= \mathcal{N}_{ij}\boldsymbol{g}_j \cdot \boldsymbol{g}^j \\ g^{ij} &= \mathcal{N}_{ij} \end{aligned}$$

or

$$\boldsymbol{g}^i = g^{ij}\boldsymbol{g}_j \tag{2.75}$$

and

$$\boldsymbol{g}^i \cdot \boldsymbol{g}^j = g^{ij}. \tag{2.76}$$

The determinant of the matrix with elements g_{ij} is

$$det[g_{ij}] = |g| = (\boldsymbol{g}_1 \cdot (\boldsymbol{g}_2 \times \boldsymbol{g}_3))(\boldsymbol{g}_1 \cdot (\boldsymbol{g}_2 \times \boldsymbol{g}_3)) = J^2. \tag{2.77}$$

2.3.3 Riemannian connection - Covariant derivative

For a vector field $\boldsymbol{Y}$, the partial derivative with respect to the ith coordinate is

$$\boldsymbol{Y}_{,i} = Y^j_{,i}\,\boldsymbol{g}_j + Y^j\boldsymbol{g}_{j,i}. \tag{2.78}$$

A vector field is expanded as

$$\boldsymbol{X} = X^\mu \frac{\partial}{\partial x^\mu}, \tag{2.79}$$

for X^μ smooth functions on manifold M.

Assuming the differential vector fields $\boldsymbol{X}, \boldsymbol{Y}$, a connection or covariant derivative, on a Riemannian manifold M, equipped with an inner product h, is a map $(\boldsymbol{X}, \boldsymbol{Y}) \mapsto \nabla_{\boldsymbol{X}}\boldsymbol{Y}$ satisfying the following axioms

- Additivity in the direction $\nabla_{\boldsymbol{X}_1+\boldsymbol{X}_2}\boldsymbol{Y} = \nabla_{\boldsymbol{X}_1}\boldsymbol{Y} + \nabla_{\boldsymbol{X}_2}\boldsymbol{Y}$

- Linearity in the direction $\nabla_{f\boldsymbol{X}}\boldsymbol{Y} = f \cdot \nabla_{\boldsymbol{X}}\boldsymbol{Y}$
- Additivity of the differentiated field $\nabla_{\boldsymbol{X}}(\boldsymbol{Y}_1 + \boldsymbol{Y}_2) = \nabla_{\boldsymbol{X}}\boldsymbol{Y}_1 + \nabla_{\boldsymbol{X}}\boldsymbol{Y}_2$
- Product rule in the differentiated field $\nabla_{\boldsymbol{X}}(f\boldsymbol{Y}) = f \cdot \nabla_{\boldsymbol{X}}\boldsymbol{Y} + \nabla_{\boldsymbol{X}} f \cdot \boldsymbol{Y}$

If additionally the following two axioms hold, for $\boldsymbol{Z}$ a vector field, the connection is Riemannian or Levi-Civita

- Compatibility with the metric $\nabla_{\boldsymbol{X}}\, h(\boldsymbol{Y}, \boldsymbol{Z}) = h(\nabla_{\boldsymbol{X}}\boldsymbol{Y}, \boldsymbol{Z}) + h(\boldsymbol{Y}, \nabla_{\boldsymbol{X}}\boldsymbol{Z})$
- Symmetry - torsion freeness $\nabla_{\boldsymbol{X}}\boldsymbol{Y} - \nabla_{\boldsymbol{Y}}\boldsymbol{X} = [\boldsymbol{X}, \boldsymbol{Y}]$,

where the Lie bracket is defined as $[\boldsymbol{X}, \boldsymbol{Y}](f) = \boldsymbol{X}(\boldsymbol{Y}(f)) - \boldsymbol{Y}(\boldsymbol{X}(f))$ and $f : M \to \mathbb{R}$ is a differentiable function.

By the product rule for $\boldsymbol{X} = \boldsymbol{g}_i$

$$\nabla_{\boldsymbol{X}}\boldsymbol{Y} = \nabla_{\boldsymbol{g}_i}(Y^j \boldsymbol{g}_j) = \frac{\partial Y^j}{\partial \xi^i}\boldsymbol{g}_j + Y^j \frac{\partial \boldsymbol{g}_j}{\partial \xi^i}. \tag{2.80}$$

The derivative $\boldsymbol{g}_{i,j}$ is

$$\boldsymbol{g}_{i,j} = \Gamma^1_{ij}\,\boldsymbol{g}_1 + \Gamma^2_{ij}\,\boldsymbol{g}_2 + ... + \Gamma^n_{ij}\,\boldsymbol{g}_n = \Gamma^k_{ij}\,\boldsymbol{g}_k, \tag{2.81}$$

where the coefficients Γ^k_{ij} are called Christoffel symbols and because of the symmetry $g_{i,j} = g_{j,i}$, $\Gamma^k_{ij} = \Gamma^k_{ji}$ follows. Substituting in (2.80) we get

$$\boldsymbol{Y}_{,i} = Y^j_{,i}\,\boldsymbol{g}_j + Y^j \Gamma^k_{ij}\,\boldsymbol{g}_k = (Y^k_{,i} + \Gamma^k_{ij} Y^j)\boldsymbol{g}_k, \tag{2.82}$$

where the quantity $Y^k_{,i} + \Gamma^k_{ij} Y^j$ is called covariant derivative of Y^k and is symbolized as $\nabla_i Y^k$. The inner product of Equation (2.81) by $\boldsymbol{g}^p$ yields

$$\boldsymbol{g}^p \boldsymbol{g}_{i,j} = \Gamma^k_{ij}\,\boldsymbol{g}^p \cdot \boldsymbol{g}_k = \Gamma^k_{ij}\delta^p_k = \Gamma^p_{ij}. \tag{2.83}$$

2.3.4 Christoffel symbols

A change of coordinates is introduced from the system ξ^j to η^k. Writing the elements of the new basis $\tilde{\boldsymbol{g}}_j$ as a linear combination of the elements of the starting, $\boldsymbol{g}_i$, we get

$$\tilde{\boldsymbol{g}}_1 = A^1_1\,\boldsymbol{g}_1 + A^2_1\,\boldsymbol{g}_2 + A^3_1\,\boldsymbol{g}_3$$

$$\tilde{\boldsymbol{g}}_2 = A^1_2\,\boldsymbol{g}_1 + A^2_2\,\boldsymbol{g}_2 + A^3_2\,\boldsymbol{g}_3$$

$$\tilde{\boldsymbol{g}}_3 = A^1_3\,\boldsymbol{g}_1 + A^2_3\,\boldsymbol{g}_2 + A^3_3\,\boldsymbol{g}_3$$

or more succinctly

$$\tilde{\boldsymbol{g}}_j = A^i_j\,\boldsymbol{g}_i \tag{2.84}$$

and in matrix notation

$$\widetilde{G} = G\,A. \tag{2.85}$$

Because $|\widetilde{G}| = |G||A|$ and $\{\boldsymbol{g}_i\}$, $\{\widetilde{\boldsymbol{g}}_i\}$, span their space each, it follows that $|A| \neq 0$ and A is invertible. Thus we derive

$$G = \widetilde{G} A^{-1} \tag{2.86}$$

or in index notation $\boldsymbol{g}_j = (A^{-1})^i_j \, \widetilde{\boldsymbol{g}}_i$. By inverting, the relation for $\widetilde{\boldsymbol{g}}^i$ is

$$\widetilde{\boldsymbol{g}}^i = (A^{-1})^i_j \, \boldsymbol{g}^j. \tag{2.87}$$

Starting from the definition of the Christoffel symbols in Equation (2.83), we have

$$\widetilde{\Gamma}^i_{jk} = \widetilde{\boldsymbol{g}}^i \cdot \frac{\partial \widetilde{\boldsymbol{g}}_j}{\partial \eta^k}. \tag{2.88}$$

The base vectors of the new system are written also as

$$\begin{aligned} \widetilde{\boldsymbol{g}}_j &= \left(\frac{\partial \boldsymbol{x}}{\partial \xi^1}\right) \frac{\partial \xi^1}{\partial \eta^j} + \left(\frac{\partial \boldsymbol{x}}{\partial \xi^2}\right) \frac{\partial \xi^2}{\partial \eta^j} + \left(\frac{\partial \boldsymbol{x}}{\partial \xi^3}\right) \frac{\partial \xi^3}{\partial \eta^j} \\ &= \frac{\partial \xi^i}{\partial \eta^j} \boldsymbol{g}_i. \end{aligned} \tag{2.89}$$

Comparing with (2.84), the coefficients A^i_j are given as

$$\begin{aligned} A^i_j &= \frac{\partial \xi^i}{\partial \eta^j} \\ (A^{-1})^i_j &= \frac{\partial \eta^i}{\partial \xi^j}. \end{aligned} \tag{2.90}$$

By (2.87) and (2.90), the two sets of base vectors are related as

$$\widetilde{\boldsymbol{g}}^i = \frac{\partial \eta^i}{\partial \xi^p} \boldsymbol{g}^p. \tag{2.91}$$

Differentiation of (2.89) yields

$$\frac{\partial \widetilde{\boldsymbol{g}}_j}{\partial \eta^k} = \frac{\partial}{\partial \eta^k} \left(\frac{\partial \xi^i}{\partial \eta^j} \boldsymbol{g}_i \right) = \frac{\partial^2 \xi^i}{\partial \eta^j \partial \eta^k} \boldsymbol{g}_i + \frac{\partial \xi^i}{\partial \eta^j} \frac{\partial \boldsymbol{g}_i}{\partial \eta^k}. \tag{2.92}$$

By the chain rule

$$\frac{\partial \boldsymbol{g}_i}{\partial \eta^k} = \frac{\partial \boldsymbol{g}_i}{\partial \xi^l} \frac{\partial \xi^l}{\partial \eta^k} = \frac{\partial \xi^l}{\partial \eta^k} \Gamma^m_{il} \boldsymbol{g}_m, \tag{2.93}$$

where we have used the definition of the Christoffel symbol (2.82). Thus, by substituting and using the definition of Kronecker delta, (2.88) takes the form

$$\widetilde{\Gamma}^i_{jk} = \frac{\partial \eta^i}{\partial \xi^p}\left(\frac{\partial^2 \xi^p}{\partial \eta^j \partial \eta^k} + \frac{\partial \xi^i}{\partial \eta^j}\frac{\partial \xi^l}{\partial \eta^k}\Gamma^p_{il}\right). \tag{2.94}$$

Starting from a Cartesian base $\xi^i = x^i$, and transforming to coordinates $\eta^i = \xi^k$, we notice that the Christoffel symbols are equal to zero for the starting system, so

$$\Gamma^i_{jk} = \frac{\partial \xi^i}{\partial x^p}\frac{\partial^2 x^p}{\partial \xi^j \partial \xi^k}. \tag{2.95}$$

By differentiating Equation (2.72) we get

$$g_{ij,k} = (\boldsymbol{g}_i \cdot \boldsymbol{g}_j)_{,k} = \boldsymbol{g}_{i,k} \cdot \boldsymbol{g}_j + \boldsymbol{g}_i \cdot \boldsymbol{g}_{j,k}. \tag{2.96}$$

Substituting by Equation (2.81) yields

$$g_{ij,k} = \Gamma^l_{ik}\boldsymbol{g}_l \cdot \boldsymbol{g}_j + \boldsymbol{g}_i \cdot (\Gamma^l_{jk}\boldsymbol{g}_l), \tag{2.97}$$

in addition, analogously,

$$g_{kj,i} = \Gamma^l_{ki} g_{lj} + \Gamma^l_{ji} g_{kl} \tag{2.98}$$

$$g_{ik,j} = \Gamma^l_{ij} g_{lk} + \Gamma^l_{kj} g_{il}. \tag{2.99}$$

Therefore, by adding the last equations with proper coefficients, multiplying with $\frac{1}{2}g^{mj}$ both sides and taking into account the symmetry of the Christoffel symbols concerning the lower indices

$$\Gamma^m_{ik} = \frac{1}{2} g^{mj}(g_{ij,k} + g_{kj,i} - g_{ik,j}), \tag{2.100}$$

where it is also made use of the fact that $[g^{ij}]$ and $[g_{ij}]$ are both symmetric and their product is the unitary matrix I

$$g^{ik} g_{kj} = g^{ki} g_{kj} = g^{ik} g_{jk} = g^{ki} g_{jk} = \delta^i_j. \tag{2.101}$$

2.3.5 Differential operators in curvilinear coordinates

The del operator in curvilinear coordinates is

$$\nabla = \boldsymbol{g}^i \frac{\partial}{\partial \xi^i}. \tag{2.102}$$

The divergence of a vector field $\boldsymbol{Y}$ is the inner product of the del operator with $\boldsymbol{Y}$ i.e.

$$\begin{aligned}\nabla \cdot \boldsymbol{Y} =& \boldsymbol{g}^i \cdot \frac{\partial (Y^j \boldsymbol{g}_j)}{\partial \xi^i} = \boldsymbol{g}^i \cdot \boldsymbol{g}_j \nabla_i Y^j \\ =& \nabla_i Y^i = Y^i_{,i} + \Gamma^i_{ij} Y^j.\end{aligned} \tag{2.103}$$

Lemma 2.

$$\Gamma^i_{ij} = J^{-1} J_{,i}. \tag{2.104}$$

Proof. Starting from Equation (2.100) we have

$$\Gamma^i_{ij} = \frac{1}{2} g^{im} (g_{im,j} + g_{jm,i} - g_{ij,m}). \tag{2.105}$$

We observe that in the expansion of the determinant of the matrix $[g_{im}]$, according to the row or the column including g_{im}, the coefficient of that element is $(-1)^{i+m} A_{mi}$, thus,

$$\frac{\partial |g|}{\partial g_{im}} = (-1)^{i+m} A_{mi}. \tag{2.106}$$

Using the chain rule we get

$$\frac{\partial |g|}{\partial \xi^j} = \frac{\partial |g|}{\partial g_{im}} \frac{\partial g_{im}}{\partial \xi^j}. \tag{2.107}$$

So the derivative $g_{im,j}$ is

$$g_{im,j} = \frac{\partial |g|}{\partial \xi^j} \frac{1}{(-1)^{i+m} A_{mi}}. \tag{2.108}$$

Moreover, the element g^{-1}_{im} of the inverse matrix of $[g_{im}]$ is

$$\begin{aligned} g^{-1}_{im} &= \frac{1}{|g|} [(-1)^{i+m} A_{mi}] \\ (-1)^{i+m} A_{mi} &= J^2 g^{-1}_{im} = J^2 g^{im}.\end{aligned} \tag{2.109}$$

Hence,

$$g_{im,j} = 2 J J_{,j} \frac{1}{J^2 g^{im}} = 2 J_{,j} \frac{g_{im}}{J}. \tag{2.110}$$

Combining with Equation (2.105) and taking into account Equation (2.101) we get

$$\begin{aligned}\Gamma^i_{ij} =& \frac{1}{2} g^{im} \left(2 J_{,j} \frac{g_{im}}{J} + 2 J_{,i} \frac{g_{jm}}{J} - 2 J_{,m} \frac{g_{ij}}{J} \right) \\ =& g^{im} g_{im} \frac{J_{,j}}{J} = J_{,j} J^{-1}.\end{aligned} \tag{2.111}$$

□

Use of Lemma 2 yields

$$\begin{aligned}\nabla \cdot \boldsymbol{Y} =& Y^i_{,i} + \Gamma^i_{ij} Y^j = Y^i_{,i} + J_{,j} J^{-1} Y^j \\ =& Y^i_{,i} + J_{,i} J^{-1} Y^i = J^{-1} (J Y^i)_{,i} = \frac{1}{J} (J \boldsymbol{g}^i \cdot \boldsymbol{Y})_{,i}.\end{aligned} \tag{2.112}$$

Similarly, for the gradient operator applied on a scalar field

$$\nabla \phi = \boldsymbol{g}^j \frac{\partial \phi}{\partial \xi^j} = \frac{1}{J} \frac{\partial}{\partial \xi^j} (J \boldsymbol{g}^j \phi). \tag{2.113}$$

Consequently, the Laplacian operator is

$$\nabla^2 \phi = \frac{1}{J} \frac{\partial}{\partial \xi^j} \left(J \boldsymbol{g}^j \cdot \boldsymbol{g}^k \frac{\partial \phi}{\partial \xi^k} \right). \tag{2.114}$$

Thus, by combining the results of Subsection 2.3.5 with Equation (2.5) we get that for the continuity equation the index contravariant form is

$$\frac{1}{J} \frac{\partial}{\partial \xi^j} (J U^j) = 0 \tag{2.115}$$

and by using the differential operators in curvilinear coordinates for Equation (2.46), the momentum conservation equation is

$$\rho \frac{\partial \left(J U^k \right)}{\partial t} + \rho \frac{\partial \xi^k}{\partial x_i} \frac{\partial}{\partial \xi^j} (J \; U^j u_i) = - \frac{\partial \xi^k}{\partial x_i} \frac{\partial}{\partial \xi^j} \left(J \; \frac{\partial \xi^j}{\partial x_i} p \right) + \frac{\partial \xi^k}{\partial x_i} \frac{\partial}{\partial \xi^j} \left(J \; \mu(\dot{\gamma}) g^{jm} \frac{\partial u_i}{\partial \xi^m} \right). \tag{2.116}$$

Assuming dynamic viscosity independent from the shear rate

$$\frac{\partial \left(J U^k \right)}{\partial t} + \frac{\partial \xi^k}{\partial x_i} \frac{\partial}{\partial \xi^j} (J \; U^j u_i) = - \frac{\partial \xi^k}{\partial x_i} \frac{\partial}{\partial \xi^j} \left(J \; \frac{\partial \xi^j}{\partial x_i} \frac{p}{\rho} \right) + \nu \frac{\partial \xi^k}{\partial x_i} \frac{\partial}{\partial \xi^j} \left(J \; g^{jm} \frac{\partial u_i}{\partial \xi^m} \right). \tag{2.117}$$

2.4 Large eddy simulation

In large-eddy simulation the space and time fluctuations of the flow are resolved to a length Δ which is orders of magnitude larger than the Kolmogorov scale η_k. The scales of the flow variable ϕ are separated by using a low frequency pass filter G on them. The convolution of ϕ with the filter function provides the filtered variable $\overline{\phi}$

$$\overline{\phi}(\boldsymbol{x}, t) = \phi(\boldsymbol{x}, t) * G(\boldsymbol{x}, t) = \int_{-\infty}^{+\infty} \phi(\boldsymbol{u}, t) G(\boldsymbol{x} - \boldsymbol{u}) d\boldsymbol{u}, \tag{2.118}$$

For convenience, the filters applied satisfy the properties of conservation of constants, linearity and commutation with derivation namely

1. $\overline{c} = c$

2. $\overline{\phi + \psi} = \overline{\phi} + \overline{\psi}$

3. $\overline{\dfrac{\partial \phi}{\partial \boldsymbol{x}}} = \dfrac{\partial \overline{\phi}}{\partial \boldsymbol{x}}$ and $\overline{\dfrac{\partial \phi}{\partial t}} = \dfrac{\partial \overline{\phi}}{\partial t}$.

2.4.1 Cartesian coordinates

By applying spatial filtering to Equations 2.6 and 2.41 respectively, the filtered continuity equation is derived as

$$\frac{\partial \overline{u}_i}{\partial x_i} = 0 \tag{2.119}$$

and the filtered Navier-Stokes equations as

$$\frac{\partial \overline{u}_i}{\partial t} + \frac{\partial}{\partial x_j}(\overline{u_i u_j}) = \overline{g}_i - \frac{1}{\rho}\frac{\partial \overline{p}}{\partial x_i} + \nu \frac{\partial}{\partial x_j}\left(\frac{\partial \overline{u}_i}{\partial x_j} + \frac{\partial \overline{u}_j}{\partial x_i}\right). \tag{2.120}$$

Addition and subtraction of the quantity $\overline{v}_i\overline{v}_j$ at the second term of Equation 2.120 and manipulation yields

$$\frac{\partial \overline{u}_i}{\partial t} + \frac{\partial}{\partial x_j}(\overline{u}_i \overline{u}_j) = \overline{g}_i - \frac{1}{\rho}\frac{\partial \overline{p}}{\partial x_i} + \nu \frac{\partial}{\partial x_j}\left(\frac{\partial \overline{u}_i}{\partial x_j} + \frac{\partial \overline{u}_j}{\partial x_i}\right) - \frac{\partial \tau_{ij}}{\partial x_j}, \tag{2.121}$$

where the subgrid tensor τ has the form $\tau_{ij} = \overline{u_i u_j} - \overline{u}_i \overline{u}_j$. Using the Boussinesq 's hypothesis of eddy viscosity, the subgrid scale stress tensor is modeled as

$$\tau_{ij} = -2\nu_t \overline{S}_{ij} + \frac{1}{3}\delta_{ij}\tau_{kk}, \tag{2.122}$$

where ν_t is the eddy viscosity, $\overline{S}_{ij} = \dfrac{1}{2}\left(\dfrac{\partial \overline{u}_i}{\partial x_j} + \dfrac{\partial \overline{u}_j}{\partial x_i}\right)$ is the filtered strain rate tensor and δ_{ij} is the Kronecker delta. The Smagorinsky model proposes

$$\nu_t = (C_s \Delta)^2 (2\overline{S}_{ij}\overline{S}_{ij})^{1/2}, \tag{2.123}$$

for C_s the Smagorinsky constant, $\overline{\Delta}$ the characteristic lower threshold length of the eddy size and $(2\overline{S}_{ij}\overline{S}_{ij})^{1/2}$ the norm of the tensor $\overline{S}_{ij}$.

The Smagorinsky constant is determined as

$$(C_s)^2 = \frac{\langle L_{ij} M_{ij} \rangle}{\langle M_{lm} M_{lm} \rangle}, \tag{2.124}$$

where $L_{ij} = \widehat{\overline{u}_i \overline{u}_j} - \widehat{\overline{u}}_i \widehat{\overline{u}}_j$ is the resolved stress tensor (or Leonard stress tensor), $M_{ij} = 2\widehat{\overline{\Delta}^2 \overline{S}_{ij} |\overline{S}|} - 2\widehat{\overline{\Delta}}^2 \widehat{\overline{S}}_{ij} |\widehat{\overline{S}}|$. The angled brackets represent averaging around a node and the hat is for test filtering.

2.4.2 Generalized curvilinear coordinates

By applying spatial filtering to Equations 2.115 and 2.117, respectively, the filtered Navier-Stokes equations are derived as

$$\frac{1}{\bar{\bar{J}}}\frac{\partial}{\partial \xi^j}(\overline{J U^j}) = 0 \tag{2.125}$$

$$\frac{\partial\left(\overline{JU^k}\right)}{\partial t} + \overline{\frac{\partial \xi^k}{\partial x_i}}\frac{\partial}{\partial \xi^j}(\overline{J\ U^j u_i}) = -\overline{\frac{\partial \xi^k}{\partial x_i}}\frac{\partial}{\partial \xi^j}\left(\bar{J}\ \overline{\frac{\partial \xi^j}{\partial x_i}}\frac{\overline{p}}{\rho}\right) + \nu\overline{\frac{\partial \xi^k}{\partial x_i}}\frac{\partial}{\partial \xi^j}\left(\bar{J}\ \overline{g^{jm}}\frac{\partial \overline{u}_i}{\partial \xi^m}\right) \tag{2.126}$$

or

$$\frac{\partial\left(\overline{JU^k}\right)}{\partial t} + \overline{\frac{\partial \xi^k}{\partial x_i}}\frac{\partial}{\partial \xi^j}(\bar{J}\ \overline{U}^j\overline{u_i}) = -\overline{\frac{\partial \xi^k}{\partial x_i}}\frac{\partial}{\partial \xi^j}\left(\bar{J}\ \overline{\frac{\partial \xi^j}{\partial x_i}}\frac{\overline{p}}{\rho}\right) + \nu\overline{\frac{\partial \xi^k}{\partial x_i}}\frac{\partial}{\partial \xi^j}\left(\bar{J}\ \overline{g^{jm}}\frac{\partial \overline{u}_i}{\partial \xi^m}\right) - \frac{\partial \sigma_i^j}{\partial \xi^j} \tag{2.127}$$

with

$$\sigma_i^j = \overline{J\ U^j u_i} - \bar{J}\ \overline{U}^j\overline{u_i} = \bar{J}\overline{\frac{\partial \xi^k}{\partial x_i}}\left(\overline{u_i u_j} - \overline{u}_i\overline{u}_j\right) = \bar{J}\overline{\frac{\partial \xi^k}{\partial x_i}}\tau_{ij}. \tag{2.128}$$

The Smagorinsky constant is given as

$$(C_s)^2 = \frac{\langle L_{ij}M_{ik}g_{jk}\rangle}{\langle M_{lm}M_{ln}g_{mn}\rangle}. \tag{2.129}$$

2.5 Elastic membrane equation of motion

The dynamics of an elastic membrane are predicted by the following equation, under the assumptions of small displacement and small inertia

$$T_m\frac{\partial^2 g(x,t)}{\partial x^2} = -(p_e(x,t) - p_i(x,t)),\ \left|\frac{\partial g(x,t)}{\partial x}\right| \ll 1,\ b\rho_0 \to 0,\ 0 \le x \le l. \tag{2.130}$$

The constant tension of the membrane (force per width) is T_m, the pressure applied on its negative side is $p_e(x,t)$ and the pressure applied at its positive side is $p_i(x,t)$. The membrane thickness is b, its length is l and its density is ρ_0. Assuming known position functions $c_0(t)$, $c_l(t)$ for the membrane's both ends,

$$\begin{aligned} g(0,t) &= c_0(t) \\ g(l,t) &= c_l(t), \end{aligned} \tag{2.131}$$

a boundary value problem, with Dirichlet boundary conditions, is defined for the membrane shape function $g(x,t)$.

Chapter 3

Numerical methods for solving the governing equations

3.1 Immersed boundary method

Immersed boundary methods [Pes72] possess the advantage of simulating the flow around moving bodies, deformable structures and shapes of complicated geometry, using steady underlying computational meshes of limited complexity accompanied with a routine to handle the moving, deforming or complex part of the solid-fluid interfaces. Such solid regions of interest are represented by the corresponding closed surface of their outer boundary, which, in hybrid Cartesian-immersed boundary methods usually is tessellated [GS05; GB98]. In such variants, every additional solid region considered as immersed body, incurs an initial overhead for triangulating its boundary and for interface tracking (Subsection 3.1.1) and increases the complexity of imposing the boundary conditions on it and computing quantities of interest on its surface. Therefore, the minimization of the part of the solid region considered as immersed is pursued. On this purpose, the grade of fitting of the background mesh to fluid domain is a crucial factor. In the present thesis, the immersed boundary method as formulated by Ge and Sotiropoulos [GS07] is employed. A curvilinear, volume structured mesh is fitted at a surface containing the fluid domain during the whole period of time. Much higher fitting capability is offered by the set of curvilinear meshes comparing to the Cartesian one.

3.1.1 Classification of computational grid nodes

The background mesh nodes are categorized as solid, immersed boundary or fluid. Solid nodes are those to the interior of the closed surface triangular mesh describing the immersed boundary, immersed boundary nodes are those which are less than a cell away and at the outer of the triangular mesh and fluid nodes are the rest, where the flow equations are solved [BGS08].

For each immersed body, a bounding box is firstly created around it. The bounding box is an orthogonal parallelepiped which extends more than a cell out of the immersed body in every direction. All nodes out of the bounding box are categorized as fluid cells.

For the rest of the background mesh points, in order for the procedure to be faster, the bounding box is divided into $n_i \times n_j \times n_k$ orthogonal blocks for x, y, z Cartesian directions respectively. Every block is given an ″empty″ or ″full″ flag, depending on whether there are elements of the surface mesh in the block. The ray tracing algorithm is then implemented using rays within a solid angle such that only blocks with same *i,j*, as that of the point examined, are intersected by the ray. Thus, for a surface grid with N triangular elements, the subroutine which for the naive approach (without block partitioning) repeats N times for each point of the underlying mesh, repeats approximately $\frac{N}{n_i \times n_j}$ times. In extracting the previous estimation, a uniform distribution of the triangular elements in space is assumed. The triangle ray intersection algorithm checks whether the ray is parallel to the triangle's plane, in which case returns negatively. Subsequently, expresses the point of intersection of the ray with the triangle's plane as a linear combination of the triangle's vertices and certifies intersection in case where all the normalized coefficients of the expression are in the range $[0, 1]$.

The computational geometry procedure for the classification of an underlying grid node is described in Algorithm 1 [BGS08] (Figure 3.1) whereas the subroutine for the ray tracing algorithm of Möller and Trumbore [MT97] is given in Algorithm 2 (Figure 3.2).

Algorithm 1 Decide underlying grid point P flag

```
• Given parameters: Points $N$ and elements $E$ of surface triangular mesh of immersed boundary.
if P is inside the bounding box
    compute the block of the bounding box $(i_x, i_y, i_z)$ surrounding P as
        $i_x = \lfloor x_p - min\{x_{IB}\} \rfloor + 1$        ▷ $x_{IB} = \{x | \{\exists Q \in N | x_Q = x\}\}$
        $i_y = \lfloor y_p - min\{y_{IB}\} \rfloor + 1$        ▷ $y_{IB} = \{y | \{\exists Q \in N | y_Q = y\}\}$
        $i_z = \lfloor z_p - min\{z_{IB}\} \rfloor + 1$        ▷ $z_{IB} = \{z | \{\exists Q \in N | z_Q = z\}\}$
    if block $(i_x, i_y, i_z)$ contains no surface mesh triangular elements
        if block $(i_x, i_y, i_z)$ is a fluid block
            flag of P = 'fluid'
        else
            flag of P = 'solid'
    else
        choose ray PS in random direction, such that PS intersects only with blocks $(i_x, i_y, k > i_z)$
        #intersections = 0
        for $k = i_z$ to $n_k$        ▷ $n_k$: number of blocks in $z$ direction
            $\forall$ triangle $\Delta$ intersecting with $(i_x, i_y, k)$
                if PS intersects with $\Delta$
                    #intersections ← #intersections + 1
        if #intersections $\equiv 0 \pmod 2$
            flag of P = 'fluid'
        else
            flag of P = 'solid'
```

```
else flag of P = 'fluid'
```

Eventually, every vertex with 'fluid' flag is checked for whether there is at its vicinity a 'solid' node. If this is the case, the 'fluid' vertex is marked as 'immersed boundary' node (Figure 3.3).

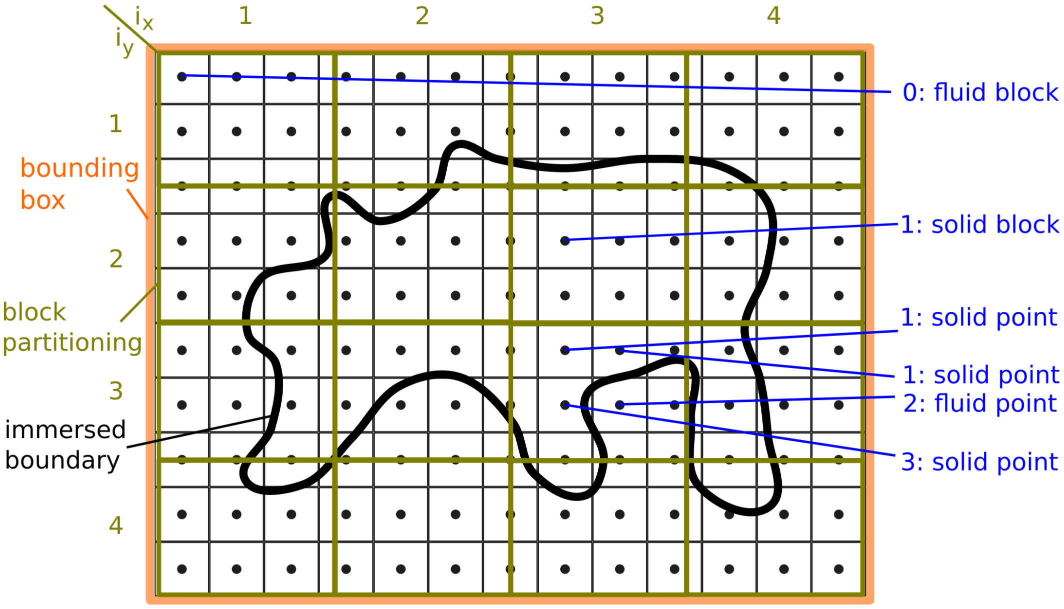

Figure 3.1: Decision of relative position of closed surface and underlying grid points in two dimensional projection. A single ray is emitted from blocks (i_x, i_y) without intersection with the immersed boundary and a ray for each point of a block is emitted otherwise. The number of ray - immersed boundary intersections is noted in exemplary rays. Block (1,1): fluid, block (3,2): solid.

Algorithm 2 Decide intersection of ray with triangle

```
• Given parameters: ray $\boldsymbol{PS}$ (where P: ray origin, S: ray target), triangle $ABC$ ($\boldsymbol{A}$, $\boldsymbol{B}$, $\boldsymbol{C}$ are the position vectors of the triangle's vertices), constant $\epsilon \ll 1$
compute triangle edge vectors $\boldsymbol{AB}$, $\boldsymbol{AC}$ as
    $\boldsymbol{AB} = \boldsymbol{B} - \boldsymbol{A}$
    $\boldsymbol{AC} = \boldsymbol{C} - \boldsymbol{A}$
$\boldsymbol{pvec} = \boldsymbol{PS} \times \boldsymbol{AC}$
$det = \boldsymbol{AB} \cdot \boldsymbol{pvec}$
if $|det| < \epsilon$
    return 'ray does not intersect with triangle'
$invdet = 1/det$
$\boldsymbol{tvec} = \boldsymbol{P} - \boldsymbol{A}$
$u = (\boldsymbol{tvec} \cdot \boldsymbol{pvec})invdet$
if $|u - 0.5| > 0.5$
    return 'ray does not intersect with triangle'
```

```
$\boldsymbol{qvec} = \boldsymbol{tvec} \times \boldsymbol{AB}$
$v = (\boldsymbol{PS} \cdot \boldsymbol{qvec}) invdet$
if $v < 0$ or $u + v > 1$
    return 'ray does not intersect with triangle'
$t = (\boldsymbol{AB} \cdot \boldsymbol{qvec}) invdet$
    return 'ray does intersect with triangle', u, v, t
```

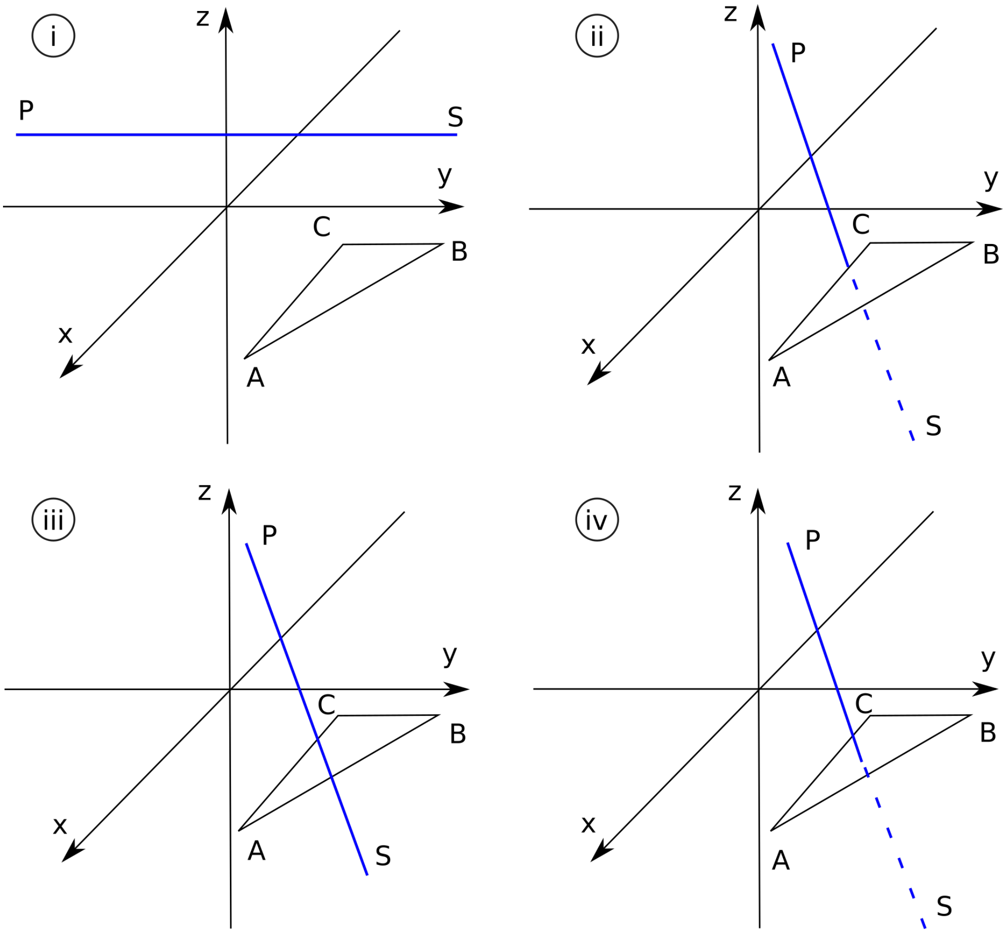

Figure 3.2: Möller - Trumbore algorithm. Triangle ABC lies on plane $x - y$. Ray PS is parallel to plane $x - y$ in (i) and intersects with plane $x - y$ under angle $0 < \phi \leq \pi/2$ in cases (ii), (iii) and (iv). i) $|det| < \epsilon$ ii, iii) $|u - 0.5| > 0.5$ or $v < 0$ or $u + v > 1$ cases iv) Ray intersects with triangle.

Flow equations are solved at every fluid node with flag 'fluid'.

3.1.2 Navier - Stokes equations discretization on curvilinear mesh

The nondimensional Navier-Stokes equations are solved in three dimensions, on a curvilinear coordinate system $\boldsymbol{\xi} = \{\xi^1, \xi^2, \xi^3\}$. The Jacobian of the transformation from the Cartesian to the curvilinear

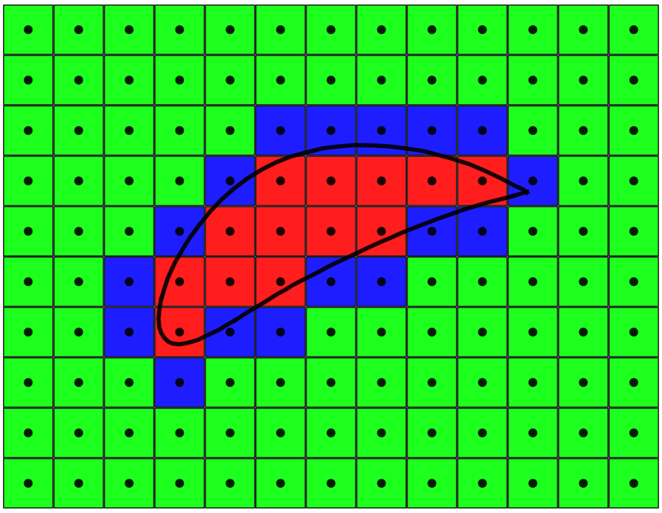

Figure 3.3: Categorization of underlying grid nodes for an immersed airfoil. Red: solid body nodes, blue: immersed boundary nodes, green: fluid nodes. (Coarse discretization for illustrative purposes.)

base is expressed as

$$J = det\left(\frac{\partial x_i}{\partial \xi^j}\right). \tag{3.1}$$

The mass continuity law is (Equation (2.115))

$$\frac{1}{J}\frac{\partial}{\partial \xi^j}(J\mathrm{U}^j) = 0 \tag{3.2}$$

and the linear momentum conservation law (Equation (2.116)) is written in the form

$$\frac{\partial\left(JU^k\right)}{\partial t} + \frac{\partial \xi^k}{\partial x_i}\frac{\partial}{\partial \xi^j}(J\ U^j u_i) = -\frac{\partial \xi^k}{\partial x_i}\frac{\partial}{\partial \xi^j}\left(J\ \frac{\partial \xi^j}{\partial x_i}\frac{p}{\rho}\right) + \frac{\partial \xi^k}{\partial x_i}\frac{\partial}{\partial \xi^j}\left(J\ \nu(\dot{\gamma}) g^{jm}\frac{\partial u_i}{\partial \xi^m}\right). \tag{3.3}$$

In tensor notation, the symbols employed are U^i for the contravariant velocity component, u_i for the Cartesian velocity component, x_i for the Cartesian coordinate, p for the pressure, $\nu(\dot{\gamma})$ for the shear rate dependent kinematic viscosity and $\boldsymbol{g}^i$ for the contravariant base vector

$$\boldsymbol{g}^i = \{g^i_1, g^i_2, g^i_3\},\ \ g^i_j = \frac{\partial \xi^i}{\partial x_j}. \tag{3.4}$$

For the discretization on the curvilinear mesh, the flow variables (u_1, u_2, u_3, p) are defined at volume centers while the variables (U^1, U^2, U^3) are defined at the computational cell face centers leading to a staggered/non-staggered approach. The momentum equations are solved at surface centers, using values for the convective and viscous terms interpolated by the cell centers. Thus, the evaluation of the covariant derivatives of the base vectors i.e. the Christoffel symbols, is avoided, leading to computational cost reduction [GS07]. In the present study, linear interpolation is used for the derivation of the convective and viscous quantities of the momentum equations at the surface centers [Kan10].

For the $i+\frac{1}{2}, j, k$ surface (Figure 3.4), this is written as

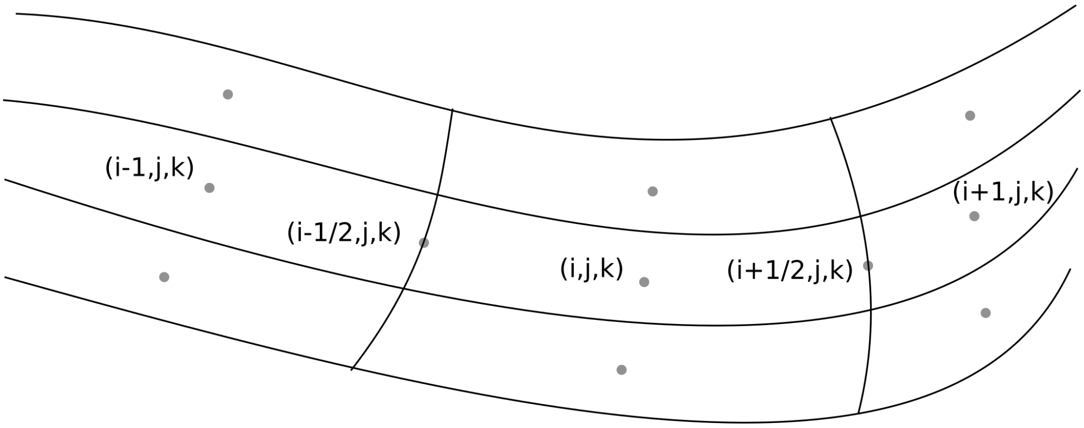

Figure 3.4: Indexing of curvilinear underlying grid cell centers and faces.

$$\mathbf{F}|_{i+\frac{1}{2},j,k} = J|_{i+\frac{1}{2},j,k}\left(0.5\cdot\frac{\mathbf{F}|_{i,j,k}}{J|_{i,j,k}} + 0.5\cdot\frac{\mathbf{F}|_{i+1,j,k}}{J|_{i+1,j,k}}\right), \tag{3.5}$$

where

$$\begin{gathered} F^k(\mathbf{U},\mathbf{u}) = -\frac{\partial\xi^k}{\partial x_i}\frac{\partial}{\partial\xi^j}(JU^j u_i) + \frac{\partial\xi^k}{\partial x_i}\frac{\partial}{\partial\xi^j}\left(J\nu(\dot{\gamma})\boldsymbol{g}^j\cdot\boldsymbol{g}^m\frac{\partial u_i}{\partial\xi^m}\right), \\ \mathbf{F} = \{F^1, F^2, F^3\}, \quad \mathbf{U} = \{U^1, U^2, U^3\}, \quad \mathbf{u} = \{u_1, u_2, u_3\}. \end{gathered} \tag{3.6}$$

The first term of F^r is discretized using second order accuracy as

$$\begin{aligned} &\left[\frac{\partial\xi^r}{\partial x_p}\frac{\partial}{\partial\xi^q}(JU^q u_p)\right]_{i,j,k} = \\ &\quad \left.\frac{\partial\xi^r}{\partial x_p}\right|_{i,j,k}\left(\frac{\left(JU^1\right)\Big|_{i+\frac{1}{2},j,k}\dfrac{u_p|_{i+1,j,k}+u_p|_{i,j,k}}{2} - \left(JU^1\right)\Big|_{i-\frac{1}{2},j,k}\dfrac{u_p|_{i,j,k}+u_p|_{i-1,j,k}}{2}}{\Delta\xi^1}\right. \\ &\qquad + \frac{\left(JU^2\right)\Big|_{i+\frac{1}{2},j,k}\dfrac{u_p|_{i+1,j,k}+u_p|_{i,j,k}}{2} - \left(JU^2\right)\Big|_{i-\frac{1}{2},j,k}\dfrac{u_p|_{i,j,k}+u_p|_{i-1,j,k}}{2}}{\Delta\xi^2} \\ &\qquad \left. + \frac{\left(JU^3\right)\Big|_{i+\frac{1}{2},j,k}\dfrac{u_p|_{i+1,j,k}+u_p|_{i,j,k}}{2} - \left(JU^3\right)\Big|_{i-\frac{1}{2},j,k}\dfrac{u_p|_{i,j,k}+u_p|_{i-1,j,k}}{2}}{\Delta\xi^3}\right). \end{aligned} \tag{3.7}$$

The viscous term of F^r is discretized as

$$
\begin{aligned}
&\left[\frac{\partial\xi^r}{\partial x_p}\frac{\partial}{\partial\xi^q}\left(J\nu(\dot{\gamma})\boldsymbol{g}^q\cdot\boldsymbol{g}^m\frac{\partial u_p}{\partial\xi^m}\right)\right]_{i,j,k} = \\
&\qquad \left.\frac{\partial\xi^r}{\partial x_p}\right|_{i,j,k}\left(\frac{\left.\left(J\nu(\dot{\gamma})\boldsymbol{g}^1\cdot\boldsymbol{g}^m\frac{\partial u_p}{\partial\xi^m}\right)\right|_{i+\frac{1}{2},j,k}-\left.\left(J\nu(\dot{\gamma})\boldsymbol{g}^1\cdot\boldsymbol{g}^m\frac{\partial u_p}{\partial\xi^m}\right)\right|_{i-\frac{1}{2},j,k}}{\Delta\xi^1}\right. \\
&\qquad\qquad +\frac{\left.\left(J\nu(\dot{\gamma})\boldsymbol{g}^2\cdot\boldsymbol{g}^m\frac{\partial u_p}{\partial\xi^m}\right)\right|_{i+\frac{1}{2},j,k}-\left.\left(J\nu(\dot{\gamma})\boldsymbol{g}^2\cdot\boldsymbol{g}^m\frac{\partial u_p}{\partial\xi^m}\right)\right|_{i-\frac{1}{2},j,k}}{\Delta\xi^2} \\
&\qquad\qquad \left.+\frac{\left.\left(J\nu(\dot{\gamma})\boldsymbol{g}^3\cdot\boldsymbol{g}^m\frac{\partial u_p}{\partial\xi^m}\right)\right|_{i+\frac{1}{2},j,k}-\left.\left(J\nu(\dot{\gamma})\boldsymbol{g}^3\cdot\boldsymbol{g}^m\frac{\partial u_p}{\partial\xi^m}\right)\right|_{i-\frac{1}{2},j,k}}{\Delta\xi^3}\right),
\end{aligned}
\tag{3.8}
$$

with truncation errors $\Theta\left((\Delta\xi^1)^2\right)$, $\Theta\left((\Delta\xi^2)^2\right)$ and $\Theta\left((\Delta\xi^3)^2\right)$ for the three terms in parentheses respectively, where

$$
\begin{aligned}
\left.\frac{\partial u_p}{\partial\xi^1}\right|_{i+\frac{1}{2},j,k} &= \frac{u_p|_{i+1,j,k}-u_p|_{i,j,k}}{\Delta\xi^1} \\
\left.\frac{\partial u_p}{\partial\xi^2}\right|_{i+\frac{1}{2},j,k} &= \frac{\dfrac{u_p|_{i+1,j+1,k}-u_p|_{i+1,j-1,k}}{2\Delta\xi^2}+\dfrac{u_p|_{i,j+1,k}-u_p|_{i,j-1,k}}{2\Delta\xi^2}}{2} \\
\left.\frac{\partial u_p}{\partial\xi^3}\right|_{i+\frac{1}{2},j,k} &= \frac{\dfrac{u_p|_{i+1,j,k+1}-u_p|_{i+1,j,k-1}}{2\Delta\xi^3}+\dfrac{u_p|_{i,j,k+1}-u_p|_{i,j,k-1}}{2\Delta\xi^3}}{2}.
\end{aligned}
\tag{3.9}
$$

The pressure term

$$
\mathbf{G}=\{G^1,G^2,G^3\},\quad G^k(p)=-\frac{\partial\xi^k}{\partial x_i}\frac{\partial}{\partial\xi^j}\left(J\,\frac{\partial\xi^j}{\partial x_i}p\right), \tag{3.10}
$$

is discretized e.g. at the surface center $i+\frac{1}{2},j,k$, as

$$
\left[\frac{\partial\xi^r}{\partial x_p}\frac{\partial}{\partial\xi^q}\left(J\,\frac{\partial\xi^q}{\partial x_p}p\right)\right]_{i+\frac{1}{2},j,k}=\left[J\left(g^{11}\frac{\partial p}{\partial\xi^1}+g^{12}\frac{\partial p}{\partial\xi^2}+g^{13}\frac{\partial p}{\partial\xi^3}\right)\right]_{i+\frac{1}{2},j,k}, \tag{3.11}
$$

where

$$
\begin{aligned}
\left.\frac{\partial p}{\partial\xi^1}\right|_{i+\frac{1}{2},j,k} &= \frac{p|_{i+1,j,k}-p|_{i,j,k}}{\Delta\xi^1}+\Theta\big((\Delta\xi^1)^2\big) \\
\left.\frac{\partial p}{\partial\xi^2}\right|_{i+\frac{1}{2},j,k} &= \frac{\dfrac{p|_{i+1,j+1,k}-p|_{i+1,j-1,k}}{2\Delta\xi^2}+\dfrac{p|_{i,j+1,k}-p|_{i,j-1,k}}{2\Delta\xi^2}}{2}+\Theta\big((\Delta\xi^2)^2\big) \\
\left.\frac{\partial p}{\partial\xi^3}\right|_{i+\frac{1}{2},j,k} &= \frac{\dfrac{p|_{i+1,j,k+1}-p|_{i+1,j,k-1}}{2\Delta\xi^3}+\dfrac{p|_{i,j,k+1}-p|_{i,j,k-1}}{2\Delta\xi^3}}{2}+\Theta\big((\Delta\xi^3)^2\big)
\end{aligned}
\tag{3.12}
$$

and analogously at the surfaces $i, j+\frac{1}{2}, k$ and $i, j, k+\frac{1}{2}$. Overall, the procedure is second order accurate.

For the velocity values at an immersed boundary node P, the normal from P to the immersed surface is taken, which intersects the immersed surface at point C. By extending the half line CP, the first intersection with a triangle of fluid points is found, point A. The velocity of P arises as the linear interpolation between the values for C and A [GS05] (Figure 3.5).

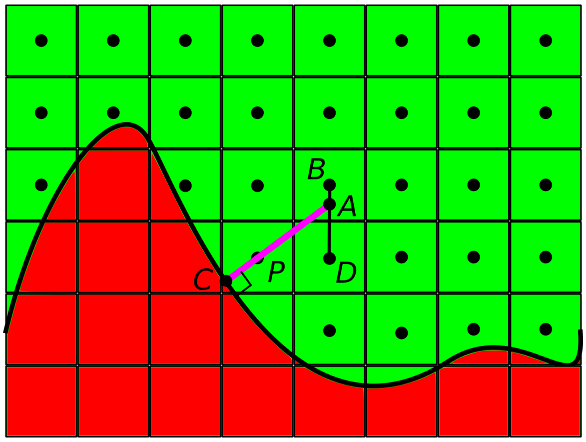

Figure 3.5: Satisfaction of boundary condition on an immersed boundary node P. Velocity for P is estimated by linear interpolation between the velocity of the closest element C of the immersed surface and point A. Point A arises by extending the half line CP and finding its closest to P intersection with a triangle of fluid nodes. The example is presented in two dimensions for visual reasons i.e. the triangle of fluid nodes is represented by the line segment BD.

The time integration of the system of equations is performed via a Crank-Nicolson second order scheme of the form [CN47; CKS14]

$$J\frac{\mathbf{U}^m - \mathbf{U}^n}{\Delta t} = 0.5 \cdot \mathbf{F}(\mathbf{U}^m, \mathbf{u}^m) + 0.5 \cdot \mathbf{F}(\mathbf{U}^n, \mathbf{u}^n) + \mathbf{G}(p^n). \tag{3.13}$$

The superscript (m) is employed to refer to the velocity field derived from the solution of the momentum equations and before the projection step for the solution of the continuity equation, while the (n) superscript refers to the last time step at which the flow is already fully computed.

The pressure field is computed so as for the incompressibility constraint to be satisfied. For this aim, the divergence of Equation (3.3) is considered and Equation (3.2) is used to derive the condition that is demanded to be satisfied by the pressure correction field

$$\phi^{n+1} = \frac{p^{n+1}}{\rho} - \frac{p^n}{\rho}, \tag{3.14}$$

leading to zero divergence of the velocity field at the next time step [PS72]. The superscript $(n+1)$ refers to the next time step to which the computation is targeting.

Owing to the linearity of the operator acting on pressure and using the expression of Equation

(2.112), the Poisson equation for the corrections on the pressure field arises [Kan+11]

$$\frac{1}{\Delta t}\frac{\partial(J^2\boldsymbol{g}^j\cdot U^{i,m}\boldsymbol{g}_i)}{\partial\xi^j} = -\frac{\partial}{\partial\xi^i}\left(J\boldsymbol{g}^i\cdot\frac{\partial\xi^k}{\partial x_l}\frac{\partial}{\partial\xi^j}\left(J\frac{\partial\xi^j}{\partial x_l}\phi^{n+1}\boldsymbol{g}_k\right)\right) \tag{3.15}$$

or

$$\frac{1}{\Delta t}\frac{\partial(J^2U^{j,m})}{\partial\xi^j} = -\frac{\partial}{\partial\xi^i}\left(J\frac{\partial\xi^i}{\partial x_l}\frac{\partial}{\partial\xi^j}\left(J\frac{\partial\xi^j}{\partial x_l}\phi^{n+1}\right)\right). \tag{3.16}$$

Using spatial finite differences, the LHS is taken as

$$\frac{1}{\Delta t}\left[\frac{\partial(JU^{j,m})}{\partial\xi^j}\right]_{i+\frac{1}{2},j,k} = \frac{1}{\Delta t}J|_{i+\frac{1}{2},j,k}\left(\frac{U^{1,m}}{\partial\xi^1}+\frac{U^{2,m}}{\partial\xi^2}+\frac{U^{3,m}}{\partial\xi^3}\right)_{i+\frac{1}{2},j,k}, \tag{3.17}$$

where

$$\left.\frac{U^{p,m}}{\partial\xi^p}\right|_{i+\frac{1}{2},j,k} = \frac{U^{p,m}|_{i+1,j,k}-U^{p,m}|_{i,j,k}}{\Delta\xi^p}. \tag{3.18}$$

The discrete Laplacian (RHS) takes the form

$$\left[\frac{\partial}{\partial\xi^p}\left(\frac{\partial\xi^p}{\partial x_l}\frac{\partial}{\partial\xi^q}\left(J\frac{\partial\xi^q}{\partial x_l}\phi^{n+1}\right)\right)\right]_{i,j,k} = \left[\frac{\partial}{\partial\xi^p}\left(Jg^{p1}\frac{\partial\phi^{n+1}}{\partial\xi^1}+Jg^{p2}\frac{\partial\phi^{n+1}}{\partial\xi^2}+Jg^{p3}\frac{\partial\phi^{n+1}}{\partial\xi^3}\right)\right]_{i,j,k}, \tag{3.19}$$

where the first term is computed using a second order central difference as

$$\left[\frac{\partial}{\partial\xi^p}\left(Jg^{p1}\frac{\partial\phi^{n+1}}{\partial\xi^1}\right)\right]_{i,j,k} = \frac{\left(Jg^{p1}\frac{\partial\phi^{n+1}}{\partial\xi^1}\right)_{i+\frac{1}{2},j,k}-\left(Jg^{p1}\frac{\partial\phi^{n+1}}{\partial\xi^1}\right)_{i-\frac{1}{2},j,k}}{\Delta\xi^p} \tag{3.20}$$

and similarly the other two terms.

The spatial derivative of the pressure correction e.g. at the $i+\frac{1}{2},j,k$ facet is approximated as

$$\begin{aligned}
\left.\frac{\partial\phi^{n+1}}{\partial\xi^1}\right|_{i+\frac{1}{2},j,k} &= \frac{\phi^{n+1}|_{i+1,j,k}-\phi^{n+1}|_{i,j,k}}{\Delta\xi^1}\\
\left.\frac{\partial\phi^{n+1}}{\partial\xi^2}\right|_{i+\frac{1}{2},j,k} &= \frac{\dfrac{\phi^{n+1}|_{i+1,j+1,k}-\phi^{n+1}|_{i+1,j-1,k}+\phi^{n+1}|_{i,j+1,k}-\phi^{n+1}|_{i,j-1,k}}{2\Delta\xi^2}}{2}\\
\left.\frac{\partial\phi^{n+1}}{\partial\xi^3}\right|_{i+\frac{1}{2},j,k} &= \frac{\dfrac{\phi^{n+1}|_{i+1,j,k+1}-\phi^{n+1}|_{i+1,j,k+1}+\phi^{n+1}|_{i,j,k+1}-\phi^{n+1}|_{i,j,k-1}}{2\Delta\xi^3}}{2}.
\end{aligned} \tag{3.21}$$

Consequently, the velocity component at the new time step $U^{i,n+1}$ is derived from the equation

$$\frac{JU^{i,n+1}-JU^{i,m}}{\Delta t} = -\frac{\partial\xi^i}{\partial x_l}\frac{\partial}{\partial\xi^j}\left(J\frac{\partial\xi^j}{\partial x_l}\phi^{n+1}\right). \tag{3.22}$$

The discrete momentum equations are handled by means of a Newton based nonlinear iterative solver that uses a trust region [Mor+84]. The resulting linear systems are solved by the generalized minimal residual method (GMRES) [Kan10; SS86; KK04](Algorithm 3), with the (block) Jacobi preconditioner. The discretized Poisson equation on the background mesh, that arises for pressure correction field [GS07], is also solved with the GMRES method, using the algebraic multigrid method as a preconditioner [RS87].

Algorithm 3 Generalized minimal residual (GMRES)(m)

```
 • Given parameters: Linear system $A\boldsymbol{x} = \boldsymbol{b}$, with $A$ an $N \times N$ matrix, tolerance $\delta$
 1: choose $\boldsymbol{x}_0$
 2: compute $\boldsymbol{r}_0 = \boldsymbol{b} - A\boldsymbol{x}_0$
 3: compute $\boldsymbol{v}_1 = \frac{\boldsymbol{r}_0}{\|\boldsymbol{r}_0\|}$
 4: for $j = 1$ to $m$ do
 5:         compute $h_{i,j} = \boldsymbol{v}_i^{\intercal} A\boldsymbol{v}_j,\ i = 1,2,...j$
 6:         compute $\tilde{\boldsymbol{v}}_{j+1} = A\boldsymbol{v}_j - \sum_{i=1}^{j}(h_{i,j}\boldsymbol{v}_i)$
 7:         $h_{j+1,j} \leftarrow \|\tilde{\boldsymbol{v}}_{j+1}\|_2$
 8:         compute $\boldsymbol{v}_{j+1} = \frac{\tilde{\boldsymbol{v}}_{j+1}}{h_{j+1,j}}$
 9: $V_m \leftarrow (\boldsymbol{v}_0, \boldsymbol{v}_1, ..., \boldsymbol{v}_m)$    ▷ Orthonormal base $V_m$ spans the Krylov space $K_m(A, b)$
10: compute $\boldsymbol{y}_m = \min_{\boldsymbol{y} \in \mathbb{R}^m} \|\beta \boldsymbol{e}_1 - H_m \boldsymbol{y}\|_2$    ▷ Using QR decomposition $H_m = QR$, $H_m$: $m \times m$ upper Hessenberg matrix, $Q$ orthogonal matrix, $R$ upper triangular matrix, $\beta = \|\boldsymbol{r}_0\|$, $\boldsymbol{e}_1 = (1,0,0,...,0)^{\intercal}$
11: compute $\boldsymbol{x}_m = \boldsymbol{x}_0 + V_m \boldsymbol{y}_m$
12: compute $\boldsymbol{r}_m = \boldsymbol{b} - A\boldsymbol{x}_m$
13: if $\|\boldsymbol{r}_m\|_2 \geq \delta$
14:         $\boldsymbol{x}_0 \leftarrow \boldsymbol{x}_m$
15:         $\boldsymbol{v}_1 \leftarrow \frac{\boldsymbol{r}_m}{\|\boldsymbol{r}_m\|}$
16:         repeat from 4
17: else
18:         return $\boldsymbol{x}_m$
```

The implementation of the immersed boundary method and the solution of the Navier-Stokes equations are performed with the Virtual Flow Simulator software [Cal+15; Vfs].

3.1.3 Solid to fluid transition

The time step of the computation advancement is bounded as a consequence of the constraint of no sublimation of solid nodes of the underlying mesh. A solid node that converts to a fluid node at the succeeding discrete time instance possesses inconsistent flow variables values. Therefore, it is mandatory that the conversion is evolved in two steps. The solid node in time instance i converts to immersed boundary node at time instance $i+1$ so that its velocity is reconstructed by the effect of the combination of the boundary conditions and flow values of nearby fluid nodes. At the next time instance, $i+2$, the immersed boundary node having valid values for the flow field variables, turns into fluid node. For the limitation to be satisfied, suitably upper bounded time step is required [GS05].

$$\Delta t \leq \min_{i \in 1,2,3} \frac{\Delta \xi^i(\boldsymbol{x})}{U^i(\boldsymbol{x})}, \;\; \boldsymbol{x} \in \{solid\ points\ converting\ to\ fluid\} \tag{3.23}$$

where $\boldsymbol{x}$ is the position vector of a solid node, which converts to fluid and $\Delta\xi^i(\boldsymbol{x})$ is the grid spacing at ξ^i direction at position $\boldsymbol{x}$.

3.2 Turbulence model

The LES method described in Section 2.4 is used along with the dynamic Smagorinsky model for the computation of turbulent viscosity. The filter applied is the mean filter (box filter) with $\Delta = J^{1/3}$ in each direction [Kan+11], described in one dimension by the function

$$G(r) = \frac{1}{\Delta} H\left(\frac{1}{2}\Delta - |r|\right), \tag{3.24}$$

where H is the Heaviside step function and r is the distance from the filter center [Pop00]. The transfer function of the filter is derived as the Fourier transform of the filter function in the physical space [PM06]

$$G(\kappa) = \frac{sin\left(\frac{1}{2}\kappa\Delta\right)}{\frac{1}{2}\kappa\Delta} = Sa\left(\frac{1}{2}\kappa\Delta\right), \tag{3.25}$$

with κ the wavenumber (spatial frequency). The test filter is also a top-hat filter and its width is twice as the primary filter width in each direction [Kan+11].

3.3 Curvilinear immersed boundary method test cases

3.3.1 Steady sphere in laminar and in turbulent fluid stream

A sphere of unitary diameter is put in a stream of unitary speed at Reynolds number 100. In Figure 3.6a the surface mesh of the immersed boundary is presented and in Figure 3.6b a detail of it. The unstructured mesh of uniform density, consists of $236,321$ nodes and $472,638$ triangular elements.

The underlying structured grid consists of $294 \times 244 \times 244$ in x, y and z directions respectively. The flow direction of the free stream attacking the sphere identifies with the positive x axis. It spans the area $15D \times 10D \times 10D$, where D is the sphere's diameter. Mesh nodes are distributed with inter-

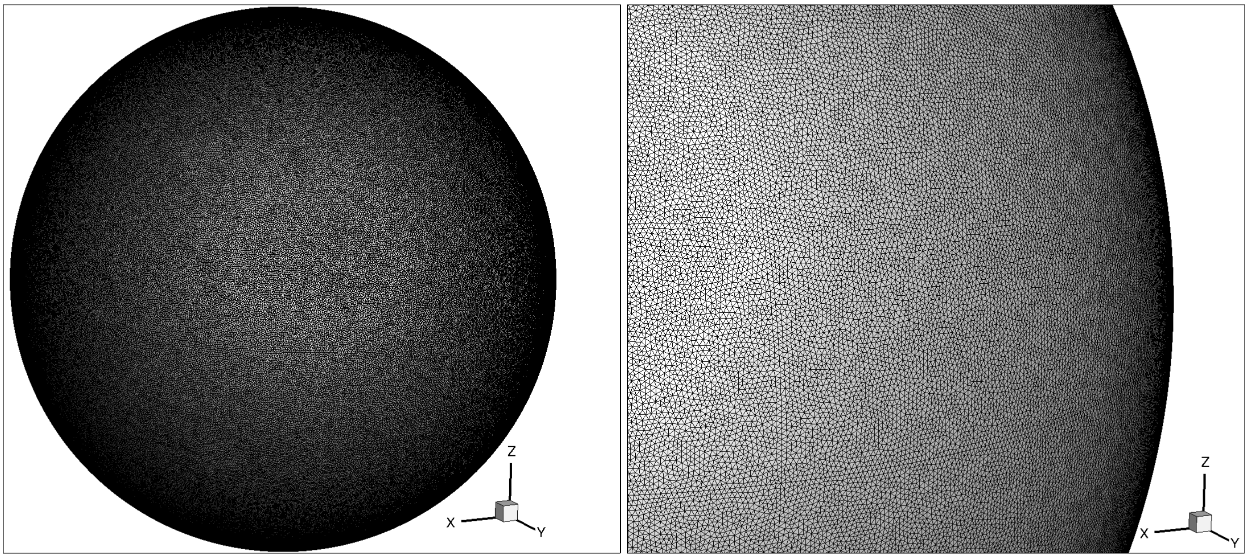

(a) The whole surface mesh.

(b) Detail of the surface mesh.

Figure 3.6: Immersed boundary mesh of unitary diameter sphere.

val $\delta\phi$ as:

$$\delta\phi = \begin{cases} 0.02D, & |\phi - \phi_c| < 1.46D \\ 0.04D, & 1.46D < |\phi - \phi_c| < 1.92D \\ 0.08D, & 1.92D < |\phi - \phi_c|, \end{cases}$$

where $\phi \in \{x, y, z\}$ and ϕ_c is the respective coordinate of the sphere center.

The streamwise velocity field, for Reynolds number 100 is presented in Figure 3.7 and the pressure contours in Figure 3.8.

The length of the recirculation bubble behind the sphere is reported in Table 3.1.

Table 3.1: Recirculation length and detachment angle for a sphere in a free stream at Reynolds number 100. Comparison with results of [ACS16], [MRF95] and [VPT12].

Metrics	Present results	Angelidis et al. [ACS16]	Magnaudet et al. [MRF95]	Vrachliotis et al. [VPT12]
Recirculation length	0.85D	0.88D	0.88D	0.87D
Detachment angle	126.1°	126.2°	126.1°	-

The pressure coefficient around the sphere, which is computed as:

$$C_p = \frac{P - P_\infty}{\frac{1}{2}\rho V_\infty^2}. \tag{3.26}$$

is presented in Figure 3.9. The streamlines of the flow are given in Figure 3.10.

Following a line of research for supercritical turbulent flow around a sphere [Ach72; CS04; Jin+04], such a simulation is performed at Reynolds number 1,140,000, by predicting turbulence using large eddy simulation with the dynamic Smagorinsky subgrid scale (SGS) model [Sma63; Ger+91; Kan+11]

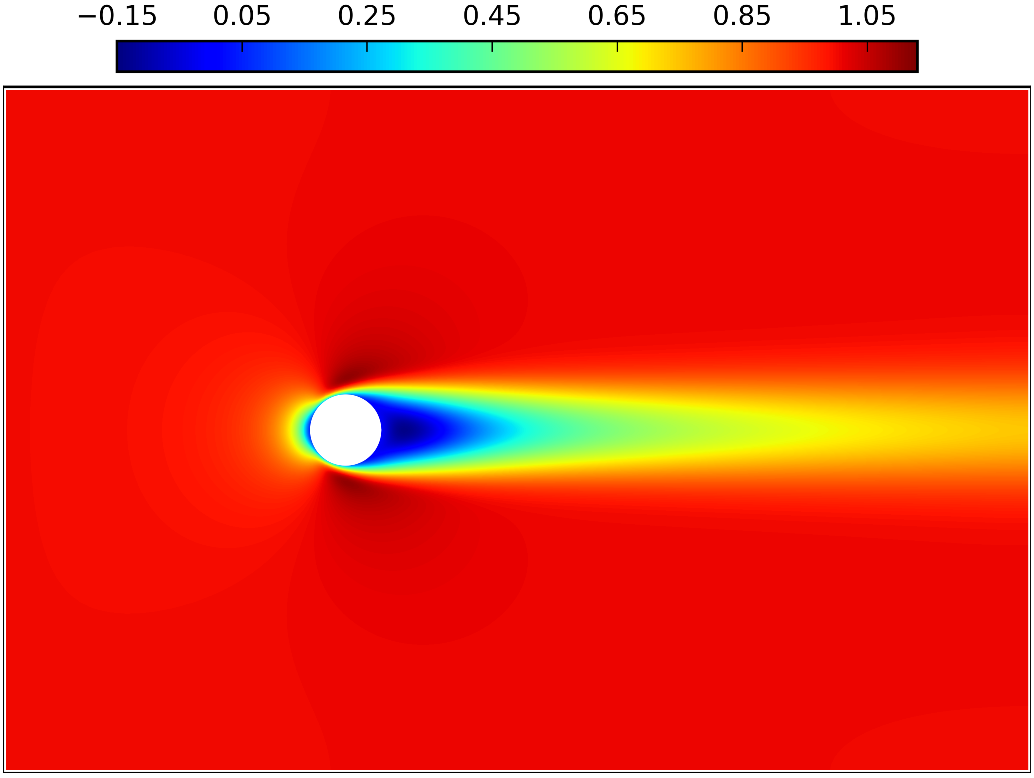

Figure 3.7: The longitudinal velocity field around a sphere at Reynolds number 100.

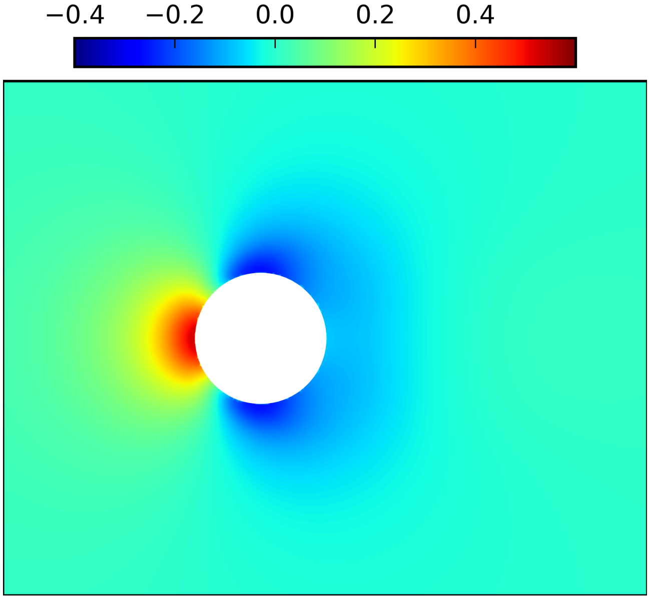

Figure 3.8: The pressure field around a sphere at Reynolds number 100.

(Sections 2.4 and 3.2) and by using the underlying and surface grids used for the laminar case. The pressure coefficient (Equation (3.26)) is computed and presented in Figure 3.11. The calculated coefficient downstream of the separation point does not coincide with the experimental values. The

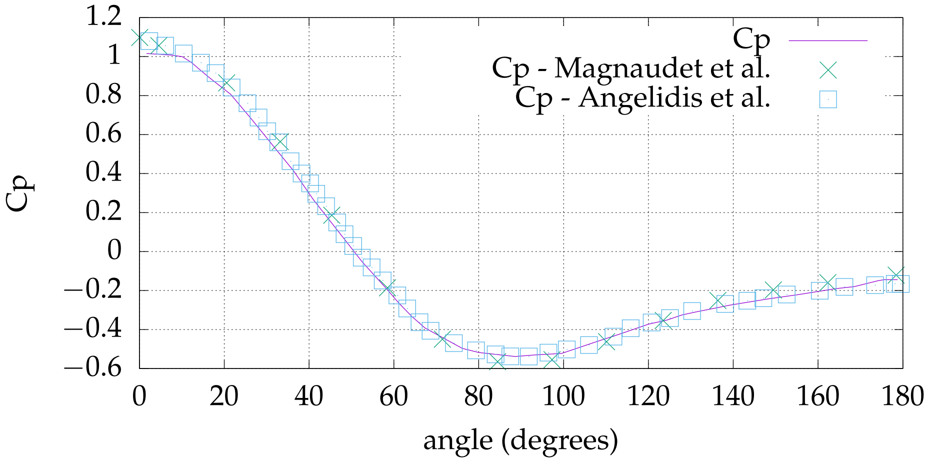

Figure 3.9: Pressure coefficient C_p for a sphere at Reynolds number 100. Comparison with results of [MRF95] and [ACS16].

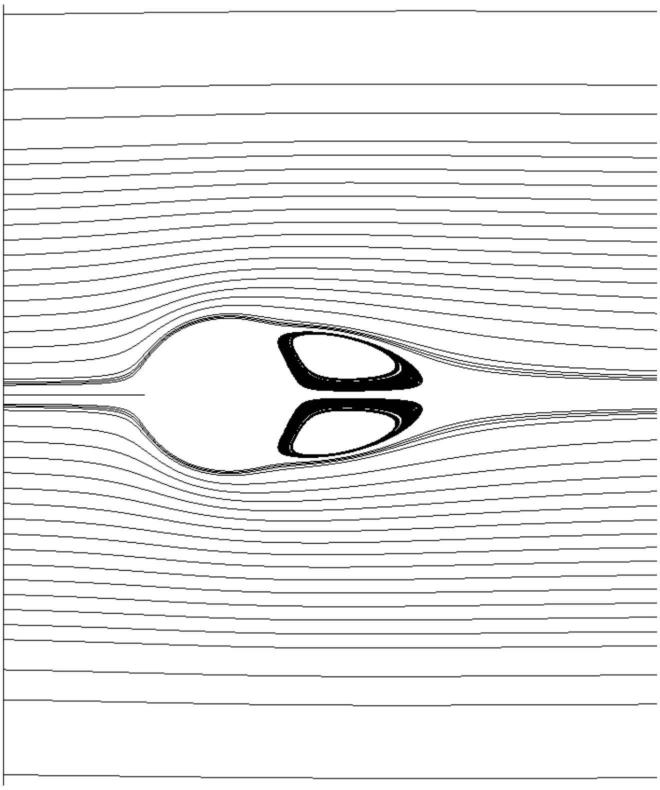

Figure 3.10: Streamlines around sphere at Reynolds number 100.

transition from laminar to turbulent flow on the separated region may affect the flow downstream of the separation. The weakness of the turbulence model to capture the complex boundary layer transition pattern is a potential factor for the divergent computational results from the measured quantities [CS04].

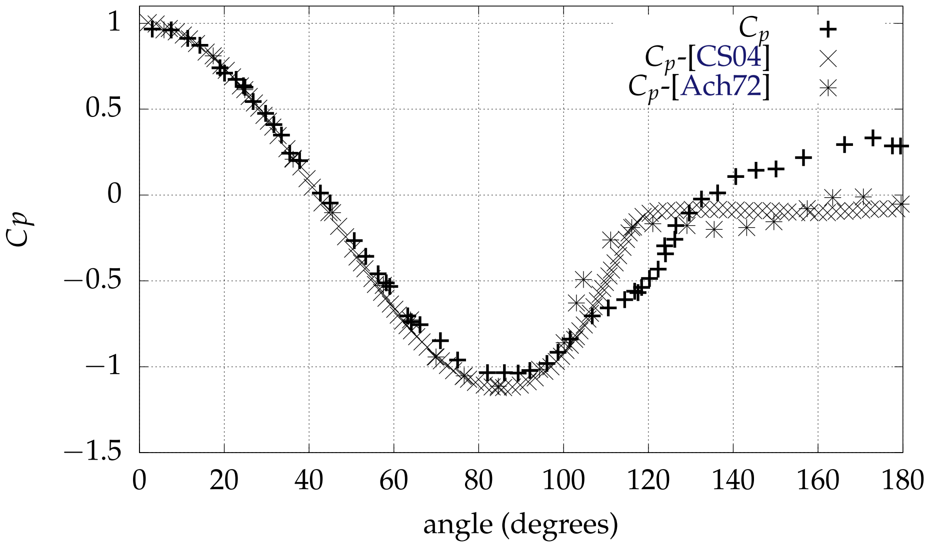

Figure 3.11: Pressure coefficient C_p for a sphere at Reynolds number $1,140,000$. Comparison with results of [CS04] and [Ach72]

.

3.3.2 Flow around airfoil

In this subsection, the flow around a NACA 4702 airfoil for Reynolds number 1000 and angle of attack 7°, is simulated. The underlying mesh is Cartesian, consisting of 3050 × 315 nodes. A local refinement region of the computational mesh imposes denser discretization at the x-range and y-range of the aerodynamic shape with $\delta x = \delta y = 0.0008$. The starting and ending position of the suction side recirculation region of the airfoil as a percentage of the airfoil chord, are given in Table 3.2.

Table 3.2: Detachment and reattachment positions for NACA 4702 airfoil in uniform flow. Comparison with results of [MA10].

	angle of attack $a = 7°$			
	Present		**[MA10]**	
Reynolds number	***Detachment***	***Reattachment***	***Detachment***	***Reattachment***
1000	0.9282	0.9697	0.9356	0.9712

3.4 Membrane equation of motion

The boundary value problem of Section 2.5 is solved by means of the shooting method. The integration of the partial differential equation for a given time instance $t = t_0$, starts at one boundary, assuming the value of the derivative at the same point. By applying the Newton-Raphson method, the correct value of the derivative on the boundary where the integration begins is found, aiming at the satisfaction of the boundary condition on the boundary where integration concludes (Algorithm 4) [Pre+07].

Algorithm 4 Boundary Value Problem solution algorithm

```
• Initialization parameters: time instance $t = t_0$, tolerance $\delta$, iteration number $n = 0$, initial
  membrane inclination at step position $g'(0, t_0) = \mu^1$
1: define $e(\mu) = g(l, t_0; \mu)$                         ▷ Error function, depicting divergence from 2nd BV
2: $n \leftarrow n + 1$                                       ▷ Next integration index
3: solve initial value problem of Equation (2.130), $g(0, t_0) = 0$ and $g'(0, t_0) = \mu^n$
4: if $|e(\mu^n)| > \delta$                                    ▷ If error greater than tolerance
5:     compute $e'(\mu^n)$                         ▷ Derivative of error with respect to inclination at $x = 0$
6:     compute $\mu^{n+1}$ from Newton-Raphson method          ▷ Zero error desired at next step $n + 1$

           $e'(\mu^n) = -\frac{e(\mu^n)}{\mu^{n+1} - \mu^n}$          (3.27)

7:     repeat from 2
8: else                                                       ▷ BVP problem is satisfied
9:     return $g(x, t_0)$                                      ▷ Return BVP solution
```

For the integration of the ordinary second order differential equation produced by Equation (2.130) for fixed time $t = t_0$, a transformation to a system of first order ODEs is performed as

$$\begin{aligned} \frac{dg(x, t_0)}{dx} &= y_1 \\ \frac{dy_1}{dx} &= \frac{-(p_e(x, t_0) - p_i(x, t_0))}{T_m} = f_1(x). \end{aligned} \tag{3.28}$$

The pair of ODEs is solved by the Cash-Karp method [CK90] combining a fifth and a fourth order Runge-Kutta methods [Kut01] with common intermediate points for each step. For a differential equation of the form

$$\frac{dy(x)}{dx} = f(x, y(x)) \tag{3.29}$$

the slopes

$$k_i = hf(x_n + \alpha_i h, y_n + \sum_{j=1}^{RK-order} b_{i,j} k_j), \;\; i \in \{1, .., RK - order\} \tag{3.30}$$

are calculated, where h is the adaptive step. An integration step is given as

$$y(x_{n+1}, t_0) = y_1 + \sum_{i=1}^{RK-order} c_i k_i. \tag{3.31}$$

Coefficients a_i, $b_{i,j}$, c_i are given in Butcher Table 3.3.

For each ODE, the difference of the estimations via the fifth and fourth order methods for $y(x_{n+1}, t_0)$

Table 3.3: Butcher tableau for Runge-Kutta coefficients of the Cash-Karp method.

α_i							
0	0						
$\frac{1}{5}$	$\frac{1}{5}$	0					
$\frac{3}{10}$	$\frac{3}{40}$	$\frac{9}{40}$	0				
$\frac{3}{5}$	$\frac{3}{10}$	$-\frac{9}{10}$	$\frac{6}{5}$	0			
1	$-\frac{11}{54}$	$\frac{5}{2}$	$-\frac{70}{27}$	$\frac{35}{27}$	0		
$\frac{7}{8}$	$\frac{1631}{55296}$	$\frac{175}{512}$	$\frac{575}{13824}$	$\frac{44275}{110592}$	$\frac{253}{4096}$	0	
	$\frac{37}{378}$	0	$\frac{250}{621}$	$\frac{125}{594}$	0	$\frac{512}{1771}$	c_i RK-5
	$\frac{2825}{27648}$	0	$\frac{18575}{48384}$	$\frac{13525}{55296}$	$\frac{277}{14336}$	$\frac{1}{4}$	c_i RK-4

are calculated

$$e = y_5(x_{n+1}, t_0) - y_4(x_{n+1}, t_0), \tag{3.32}$$

where $y_5(x_{n+1}, t_0)$ and $y_4(x_{n+1}, t_0)$ are the estimations of $y(x_{n+1}, t_0)$ with Runge-Kutta fifth and fourth order respectively. In case the maximum, over the ODEs, error

$$em_{i,x_s=x_0} = \max_{eq\ \in\ ODE\ system} e_{i,x_s=x_0}, \tag{3.33}$$

is below a tolerance (tol), the step i starting at $x_s = x_0$ is considered successful. Otherwise $em_{i,x_s=x_0}$ is used to decide step size ($h_{i+1,x_s=x_0}$) for iteration $i+1$ of the interval starting at $x_s = x_0$ as

$$h_{i+1,x_s=x_0} = \max\left(0.9 \cdot h_{i,x_s=x_0} \cdot \left(\frac{em_{i,x_s=x_0}}{tol}\right)^{-\frac{1}{5}}, \frac{h_{i,x_s=x_0}}{10}\right), \ \ em_{i,x_s=x_0} > tol. \tag{3.34}$$

The first argument of max function aims at ensuring an error close to the value $em_{i,x_s=x_0} = 0.9 \cdot tol$. The second guarantees that the next step ($h_{i+1,x_s=x_0}$) tested will be at least a given fraction of the former ($h_{i,x_s=x_0}$). In case the maximum error of a completed step (starting at $x_s = x_0$ and ending at $x_e = x_0 + h_{i,x_s=x_0}$) is less than a threshold th, the starting value of the next integration step is set twice as large as the former

$$h_{0,x_s=x_0+h_{i,x_s=x_0}} = 2 \cdot h_{i,x_s=x_0}, \ \ em_{i,x_s=x_0} < th. \tag{3.35}$$

By virtue of these adaptations of the integration step, the required accuracy is achieved even in demanding intervals, without the procedure in relatively smoother regions to be prolonged.

3.5 Flow - membrane equations coupling

Fluid - structure interaction between the main flow and the elastic membrane is assumed. The fluid dynamics equations are loosely coupled with the boundary value problem (BVP) of the membrane motion equation (Equation (2.130)) in conjunction with the boundary conditions defined by Equation (2.131). Following the computation of the flow field, the new surface of the membrane is determined.

In order for the no sublimation constraint (Subsection 3.1.3) to be satisfied, binary search is applied for the selection of an apposite time step.

The computation for an advancement step in time is presented in Figure 3.12.

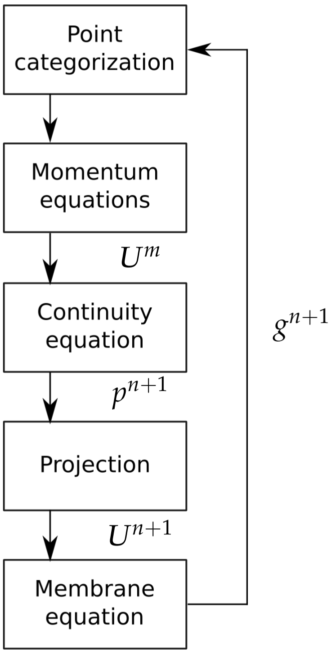

Figure 3.12: Flow chart of the FSI computation.

Chapter 4

Flow separation control over a backward-facing step

Synopsis

The internal steady and oscillating flows are examined through a backward facing step (expansion ratio 2), for low Reynolds numbers ($Re = 400$, $Re = 800$). A lower part of the backward facing step is oscillating with the same frequency as the unsteady flow. The effect of the frequency, the amplitude, and the length of this oscillation is investigated. By suitable active control regulation, the recirculation lengths are reduced, and, for a percentage of the time period, no upper wall, negative velocity, region occurs. Moreover, by substituting the prescriptively moving surface by a pressure responsive homogeneous membrane, the fluid–structure interaction is examined. We show that, by selecting proper values for the membrane parameters, such as membrane tension and applied external pressure, the upper wall flow separation bubble vanishes, while the lower one diminishes significantly in both the steady and the unsteady cases. Furthermore, for the time varying case, the length fluctuation of the lower wall reversed flow region is fairly contracted. The findings of the study have applications at the control of confined and external flows where separation occurs.

4.1 Introduction

Flow separation arises innately in internal and external flows, incurring losses. The suppression of the effects of the detached flow, such as pressure drop or drag, is a common goal of fluid dynamics analysis and design. The inner flow past a backward facing step (BFS) constitutes a benchmark problem for the analysis of recirculation owing to its simplicity, along with the fixation of the lower wall detachment position at the step location [EN+05; SFS04]. Backward facing step flow applications abound in everyday life. Bubble zones at the wake of vehicles, separated flow over airfoils at large attack angles, spoiler flows, detachment of inflow in an engine, and bubble downstream of flows around constructions/ships are common cases of backward facing step flow applications occurring in modern practices [Che+18]. For the control of the flow, various methods have been applied, such as plasma actuation, electromagnetic actuation, synthetic jet, oscillating flap, inlet pulsation, periodic perturbation, vortex generators, local forcing, visual feedback [Che+18; WL16; YM08; MS17; TPP10; KM14; MH04; CS96; GA13].

The oscillating flow past a BFS having the same frequency as the moving portion of the bottom wall is simulated by Mateescu and Venditti [MV01] and Mateescu et al. [MMnS10]. Under several values of the periodical inflow amplitude, the positions where detachment or reattachment occurs are calculated for various surface oscillation amplitude and frequency values for a range of low and intermediate inflow Reynolds numbers (400–1000). The Navier–Stokes equations are discretized with a second order backward implicit scheme and an artificial compressibility scheme is employed for the coupling of the equations. The pseudotime discretization is performed using a first order implicit scheme. It is concluded that for increasing wall oscillation amplitude, the upper wall bubble length increases and its presence percentage during the period decreases. The authors also find that the lower wall bubble length fluctuation increases. For higher Reynolds number values, the length of the separation regions increase significantly, a secondary lower wall separation region emerges and the upper wall separation region is present the whole period. By increasing the oscillation frequency, the fluctuation amplitude of the lower wall closed streamlines length increases, while the upper wall bubble remains nearly unchanged.

Fluid structure interaction (FSI) involving elastic membranes [Gra75] has been extensively studied in biomedical cases and other settings [TP00; LP95; GAL21; MGW08]. The steady flow in a 2D channel with one rigid plate, and another with a part of it replaced by an elastic membrane, is perturbed and the resulting flow is studied by Luo and Pedley [LP96]. It is shown that the steady solutions become unstable as membrane tension falls below a threshold value and self-excited oscillations emerge. The interaction of Poiseuille flow with a tensioned membrane portion of one of the walls with structural damping, is addressed by Huang [Hua01]. The oscillation of the membrane is found to strongly depend on inlet and outlet boundary conditions.

The immersed boundary method [Pes72] has been applied for the computation of the flow over a BFS by Saleel et al. for low Reynolds numbers (0.0001–100) [SSJ13]. The authors implement the momentum forcing and the mass source/sink to satisfy, at the solid boundaries, zero flow velocity relative to the boundaries. They employ a finite volume method on a staggered grid with a fractional step in time. Yang et al. apply an LES-immersed boundary approach for the flow over a backward facing step for Reynolds numbers in the turbulent region (5100) [Yan+21]. Agreement is found between the results from the IB method coupled with LES and those from DNS and experiments.

The curvilinear immersed boundary method of Ge and Sotiropoulos has been applied for the computation of unsteady incompressible flows [GS07], such as that in a 2D driven cavity, an impulsively started flow at a square cross-section duct, the pulsatile flow at a circular-section pipe bend and the pulsatile flow in a bileaflet mechanical heart valve (BMHV). Moreover, it has been applied by Borazjani et al. [BGS08] for the research on FSI pertaining to rigid bodies, such as an elastic mounted cylinder in the free stream and the blood flow through a BMHV. Gilmanov et al. [GLS15] extended the method and simulated FSI with thin flexible shells.

In this work, the immersed boundary method [MI05], in the form proposed by Ge and Sotiropoulos [GS07], is employed to simulate the control of the confined, viscous, steady, and unsteady, incompressible flow over a backward facing step. The proposed control methods and the findings of the present study for the separation of the flow at the standard case of the flow over a backward facing step, can have a plethora of applications to external and internal industrial and biomedical flows. The implementation of the method of Ge and Sotiropoulos [GS07] for the computation of the fluid structure interaction with a deformable body, where the total fluid volume of the computational domain changes in time, is a novelty aspect of this work.

Initially, the flow characteristics for the BFS under steady and unsteady inflow conditions are presented. Imposing forced oscillatory movement at a portion of its bottom wall, the unsteady flow over the BFS is simulated, examining the effect of the amplitude and the frequency of the oscillating surface. Moreover, the role of the length of the oscillating surface is examined, for which results do not exist in bibliography. Substituting the moving oscillating part of the bottom wall with an elastic membrane, the FSI with the steady and unsteady flow is analyzed. To the best of our knowledge, control of the flow by means of an elastic membrane with direct interaction with the main periodical flow, has not been implemented so far for the BFS. An elastic membrane has the advantage over the rigid passive control means, of adaptability within a range of different inflow conditions, without tuning demanded.

4.2 Problem Setup and discretization

4.2.1 Geometry and boundary conditions of BFS with partly moving bottom wall

The geometry of the problem on the x-y plane is shown in Figure 4.1.

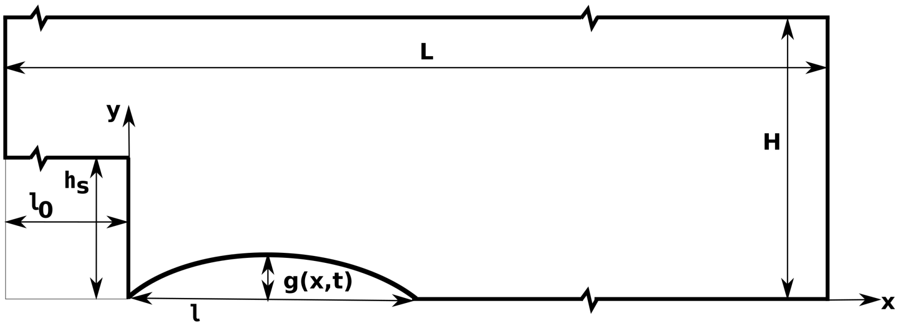

Figure 4.1: Backward facing step with portion l of moving bottom wall. The inlet lies at $x = -l_0$ and the outlet at $x = L - l_0$.

A backward facing step with expansion ratio two i.e. $H/(H - h_s) = 2$, length upstream of the step $l_0 = 2H$ and length downstream $L - l_0 = 30H$ is examined, following a large part of existing research [Arm+83; KM85; Gar90; Soh88; PT97].

Dirichlet boundary condition for the velocity in the inlet ($x = -l_0$) is given as [Gar90; MMnS10]

$$u(x = -l_0, y, t) = U_0(1 - \alpha sin(\omega t))6(y - h_s)\frac{H - y}{(H - h_s)^2}, \;\; v(x = -l_0, y, t) = 0, \;\; y \in [h_s, H], \tag{4.1}$$

where αU_0 is the inflow velocity oscillation amplitude, u, v are the longitudinal and transverse Cartesian velocity components, respectively, ω is the angular frequency of the oscillation and t is time. At the outlet ($x = L - l_0$) the Neumann boundary conditions

$$\left.\frac{\partial \psi}{\partial x}\right|_{x=L-l_0} = 0, \;\; \psi \in \{u, v\} \tag{4.2}$$

are imposed.

We examine two cases for the function $g(x, t)$ of the position of the moving part of the bottom wall of length l.

(a) Forced motion with frequency same as the frequency of the inflow, according to the equation [MV01]

$$g(x, t) = Acos(\omega t)sin(\frac{\pi x}{l}), \;\; 0 \leq x \leq l, \tag{4.3}$$

where A is the amplitude of the oscillation and l is the length of the oscillating portion of the bottom wall.

(b) Fluid-structure interaction between the flow and the moving part of the bottom wall which is considered an elastic membrane. The structure couples with the flow according to the equation of a membrane, under the assumptions of small displacement and small inertia (Equation (2.130)). The equation of motion of the membrane is constrained with the boundary conditions of membrane's both streamwise ends ($x = 0$ and $x = l$) being fixed at $y = 0$,

$$g(0, t) = g(l, t) = 0. \tag{4.4}$$

At every wall S_w, including the immersed boundary, no slip boundary conditions are imposed

$$\psi(S_w) = \psi_{S_w}, \;\; \psi \in \{u, v\}, \tag{4.5}$$

where ψ_{S_w} is the respective velocity component of the wall.

For the derivation of pressure at the immersed boundary, the following Neumann boundary condition which is deduced by the momentum conservation applies [FFSR04; ACS16]

$$-\nabla p(\mathbf{x}, t) \cdot \mathbf{n} = \frac{\partial \mathbf{U}_{wall}(\mathbf{x}, t)}{\partial t} \cdot \mathbf{n}, \tag{4.6}$$

where $\mathbf{x}$ is the position vector, $\mathbf{n}$ is the normal vector to the immersed surface and $\mathbf{U}_{wall}$ is the velocity of the immersed surface.

A three dimensional methodology is used for the implementation of the immersed boundary method (Subsection 3.1.2), therefore a small depth d of the uniform flow field in the z direction is considered, specifically $d = 0.024H$. On the third dimension, z, slip boundary conditions are applied

$$\left.\frac{\partial \psi}{\partial z}\right|_{z=z_{min}} = \left.\frac{\partial \psi}{\partial z}\right|_{z=z_{max}} = 0, \;\; \psi \in \{u, v\}, \;\; w|_{z=z_{min}} = w|_{z=z_{max}} = 0, \tag{4.7}$$

where w is the depthwise Cartesian velocity component.

Nondimensionalization of the geometrical and flow quantities is done with H for the length, U_0 for the velocity, $\rho {U_0}^2$ for the pressure and $H\rho {U_0}^2$ for the membrane tension T_m. In the following, the nondimensional version of the involved variables is considered, keeping the same symbol for each physical quantity i.e.

$$H = 1, \;\; l_0 = 2, \;\; L = 32, \;\; u(x = -2, y = 0.75, z, t = 0) = 1.5 \;\; etc.$$

From hereon we consider the nondimensional problem and all referenced quantities are normalized.

4.2.2 Computational grids and discretization steps

Space and time discretization independence study is performed for each case in order for the underlying grids and time steps to be selected. For the steady case with $l_0 = 0$ of Subsection 4.3.1, the fine mesh used (2019 × 149 grid points) shows a maximum difference of 0.088% in detachment-reattachment positions results in comparison to the next coarser mesh (2019 × 134 grid points) that was implemented.

The underlying mesh used in Subsection 4.3.1 for the $l_0 = 0$ case has 2019 points in x direction and 121 points in y direction. Inflation for x partitioning is applied in the region $x \in [0, 19]$ with step size $\delta x = 0.01$ and for y direction partitioning in the region $y \in [0.45, 0.55]$ with step size $\delta y = 0.005$. Additionally, local inflation near the upper and lower walls is employed. For the $l_0 = 2$ case, a 3025 × 182 dense grid is employed for the discretization of the computational domain with $\delta x = 0.006$ for $x \in [0, 19]$ and uniform y partitioning with near wall inflation. The flow computation grid consists for the $l_0 = 0$ case of $\approx 732,897$ nodes and for the $l_0 = 2$ case of $\approx 1,617,486$ nodes.

For Subsections 4.3.2 - 4.3.5, the background grid has 1721 nodes for x discretization. The minimum x interval, $min\ \delta x$ is 0.01 for $x = 0$ to $x = 12.5$. From $x = 12.5$ to $x = 30$, δx increases geometrically to the value 0.08. For the y discretization 149 and 113 nodes are used for the active and passive control cases computations, respectively. In the forced oscillation case the minimum y interval, $min\ \delta y$ is 0.005 for y in the region from -0.22 to 0.25 and increases geometrically in the interval $y \in [0.25, 0.98]$ to the value 0.03. From $y = 0.98$ to $y = 1$ three more grid lines are located. In the membrane case the interval with y discretization step $\delta y = 0.005$ is $[0, 0.25]$. The rest of y discretization, for $y \in [0.25, 1]$, is identical to the oscillating surface case. For the 3d fluid computational domain the calculation grid consists of approximately $600,000$ nodes. For the immersed boundary surface mesh used for the moving part of the bottom wall in Subsections 4.3.2, 4.3.4, 4.3.5, the streamwise partitioning is performed with step $\delta x = 0.1$.

The time step used in Subsections 4.3.3 and 4.3.4 is 0.002 while in Subsection 4.3.5, where the motion of the solid boundary is less intensive in comparison with the active control case, the nondimensional time is sampled every 0.01.

Fluid and structure discretization steps should be similar in size to facilitate data exchange through their interface. To ensure that the integration step for the membrane equation is not of higher order of magnitude than that of space discretization, an upper bound $h \leq h_{max} = 0.02$ is set for the ordinary differential equation integration marching step.

4.3 Results

In this section, the results for the steady and unsteady flows over the backward facing step without and with control are presented and discussed. The in both walls separated, steady flow of Subsection 4.3.1 is passively controlled using an elastic membrane and the results are presented in Subsection 4.3.2. The forced control of the unsteady, separated flow of Subsection 4.3.3 by an oscillating portion of the bottom wall, is shown in Subsection 4.3.4 and the management by an elastic membrane of the same flow is described in Subsection 4.3.5.

4.3.1 Steady flow

In Table 4.1, the characteristic recirculation lengths are presented, for the steady case over the BFS, for Reynolds number

$$Re = \frac{U_0 H}{\nu} = 800, \tag{4.8}$$

where ν is the kinematic viscosity of the fluid.

Table 4.1: Position of the upper wall detachment and reattachment and lower wall recirculation length for the backward facing step under steady, parabolic inflow with Reynolds number 800 and without control. Comparison with results from body fitted methods.

	$l_0 = 0$				$l_0 = 2$	
	Present	[MV01]	[Gar90]	[Soh88]	Present	[MV01]
Grid density	2019 × 121	1201 × 241	600 × 30		3025 × 182	2193 × 401
Upper wall detach.	4.82	4.85	4.85	-	4.4	4.66
Upper wall reattach.	10.46	10.47	10.48	-	10.38	10.31
Lower wall reattach.	6.06	6.09	6.1	5.8	5.61	5.9

The results, for the validation of the method, are in close agreement with the results obtained via body-fitted methods.

For Reynolds number 400 and $l_0 = 2$ we find the lower wall reattachment at $x = 4.065$ and no upper wall separation of the flow.

4.3.2 Control of steady flow using an elastic membrane

The portion of the rigid bottom wall starting at the step position and having length $l = 10$ is substituted with an elastic membrane with tension $T_m = 55$. The external pressure exerted on the outer surface of the membrane is taken to be steady and uniform with value $p_e(x, t) = p_e = 0.525$. The criterion for selecting the combination of membrane's parameters, is the deformation of the membrane to be small and positive and the external pressure to be close to the internal pressure exerted by the flow. Solving the FSI between the steady flow and the membrane for Reynolds number 400, the velocity vectors are depicted at Figures 4.2 and 4.3.

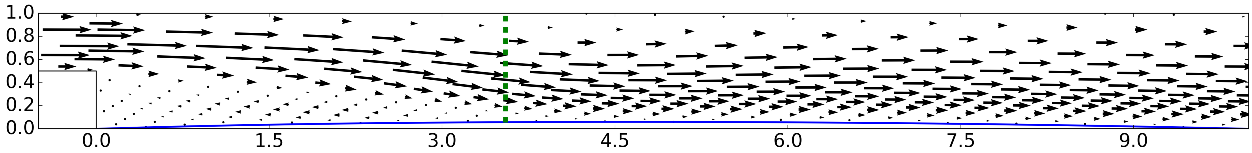

Figure 4.2: The backward facing step under steady inflow, with control portion $l = 10$ of elastic membrane bottom wall with $T_m = 55$ and $p_e = 0.525$, for $-0.5 \leq x \leq 10$. The maximum membrane displacement arrow emerges at $x = 4.655$ and has the value $g(x = 4.655) = 0.06$. Reattachment of the flow occurs at $x = 3.55$ (indicated by the dashed line).

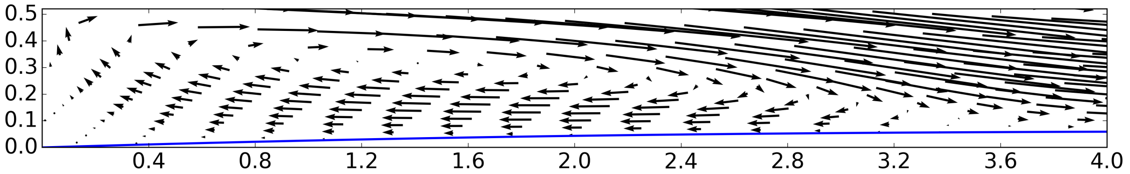

Figure 4.3: Backward facing step under steady inflow, with control portion $l = 10$ of elastic membrane bottom wall with $T_m = 55$ and $p_e = 0.525$. Detail of the lower wall recirculation region for $0 \leq x \leq 4$ and $0 \leq y \leq 0.5$.

Due to the inertia of the flow, the expansion of the mainstream of the flow after the step position, is not immediate as shown by the longitudinal velocity contours of Figure 4.4 and the longitudinal velocity profiles of Figure 4.5. It develops downstream of the step and exhibits its major intensity approximately at the region $2 \leq x \leq 3.5$, as shown in the transverse velocity contours of Figure 4.6 and the transverse velocity profiles of Figure 4.7.

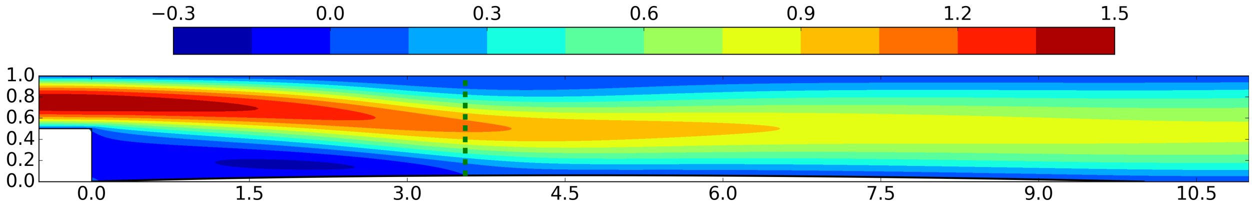

Figure 4.4: Backward facing step under steady inflow, with control portion $l = 10$ of elastic membrane bottom wall with $T_m = 55$ and $p_e = 0.525$. Longitudinal velocity contour plot for $-0.5 \leq x \leq 11$. The lower reattachment position is emphasized by the dashed line.

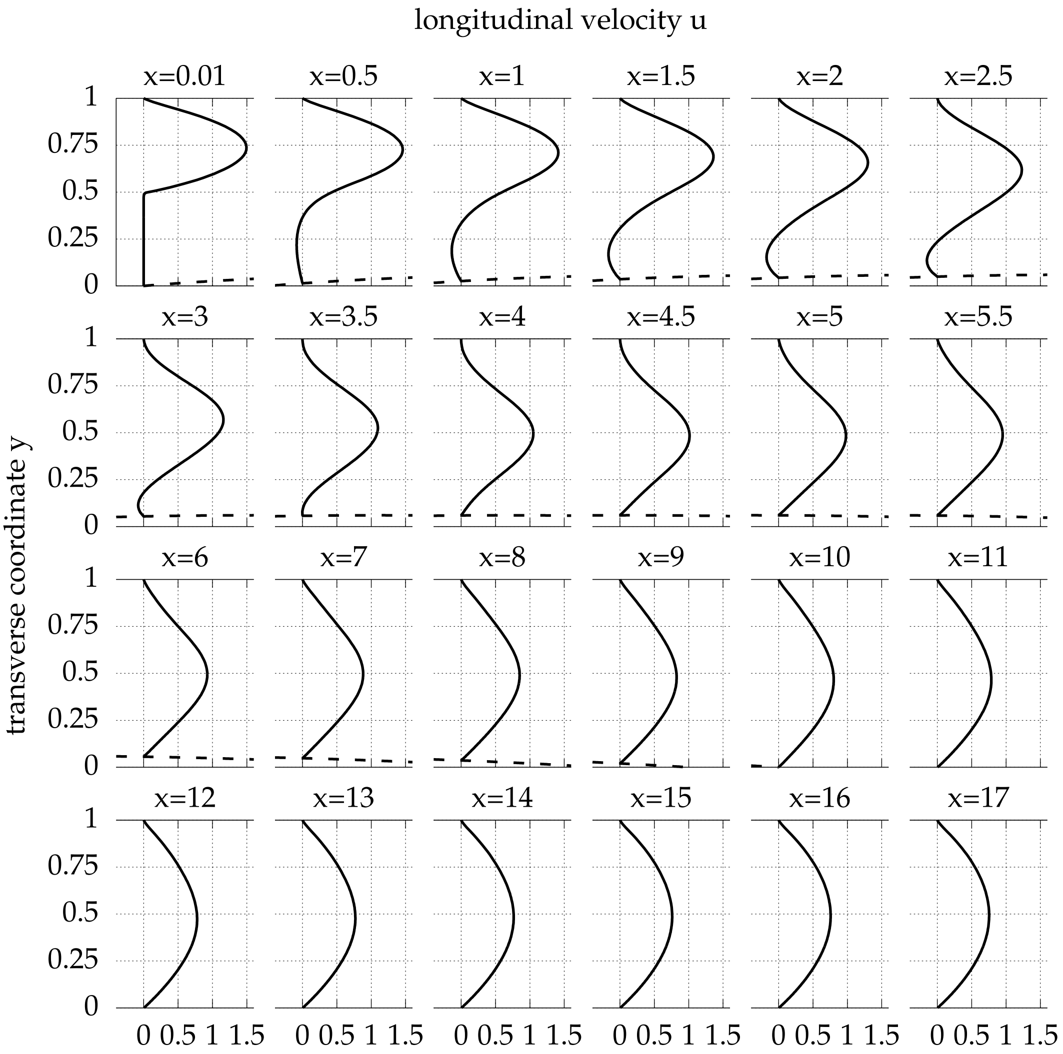

Figure 4.5: Longitudinal velocity profiles for successive positions x downstream of the step, for BFS with control portion $l = 10$ of elastic membrane bottom wall, with $T_m = 55$ and $p_e = 0.525$, under steady inflow at $Re = 400$ $(0 \leq x \leq 17)$. The membrane shape is depicted also in nondimensional units at the bottom (dashed line).

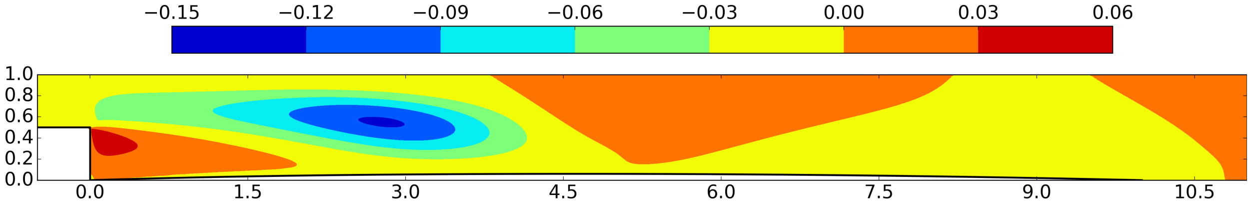

Figure 4.6: Backward facing step under steady inflow, with control portion $l = 10$ of elastic membrane bottom wall with $T_m = 55$ and $p_e = 0.525$. Transverse velocity contour plot for $-0.5 \leq x \leq 11$.

The lower wall closed streamlines extend as far as $x = 3.55$, reducing by 12.7% the uncontrolled separation length of magnitude 4.065 (Subsection 4.3.1). The upper wall separation region vanishes.

The transverse velocity profile is zeroed out at $x = 17$, indicating that the flow is developed at this point. Longitudinal velocity profiles of Figure 4.5 confirm the observation, as at this position are parabolic.

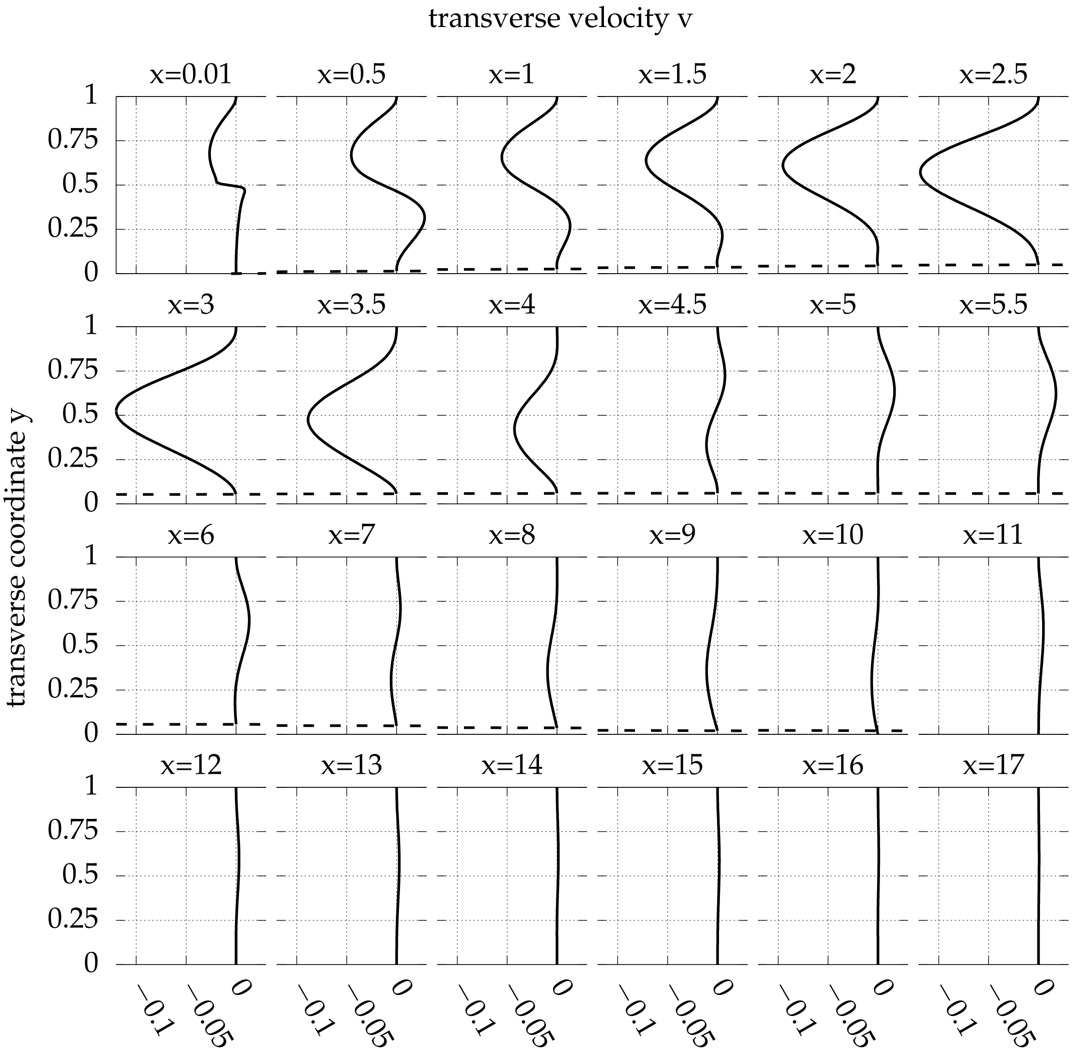

Figure 4.7: Transverse velocity profiles for successive positions x downstream of the step, for BFS with control portion of length $l = 10$ of elastic membrane bottom wall, with $T_m = 55$ and $p_e = 0.525$, at steady flow with $Re = 400$ $(0 \leq x \leq 17)$. The membrane shape is depicted also in nondimensional units at the bottom (dashed line).

Due to the low velocity of the fluid under the inlet flow, at the lower wall bubble, the curvature of the streamlines is small. Hence, the pressure distribution is nearly uniform for each cross-section (Figure 4.8) [GTG07]. At the region $2.9 \leq x \leq 5.3$ the streamlines are slightly convex down. At this segment the lower wall pressure is higher than the upper wall pressure with maximum surplus value $\max_{0 \leq x \leq l}(p(x, y = g(x)) - p(x, y = 1)) = 0.04$ as shown in Figure 4.9. Pressure raises streamwise after the step, by the combined application of momentum and continuity equations and reaches its maximum close to the position where the major low recirculation region reaches its end [SA08].

After this position, the pressure drops streamwise due to the action of viscosity. These remarks are in accordance with the results of [Gar90] for the analogous case for $Re = 800$.

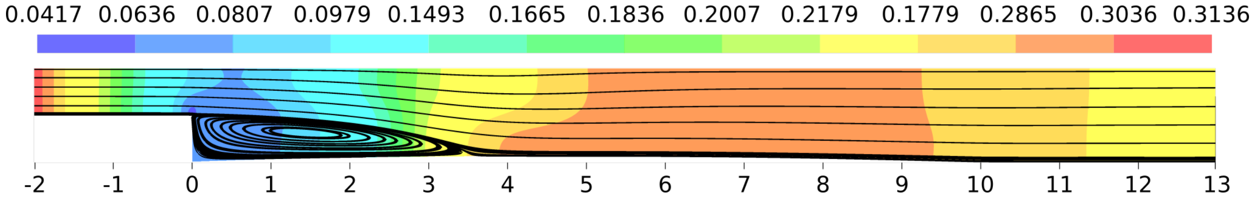

Figure 4.8: Pressure contours and streamlines for BFS with control portion $l = 10$ of elastic membrane bottom wall, with $T_m = 55$ and $p_e = 0.525$, at steady flow with $Re = 400$ for $-2 \leq x \leq 13$.

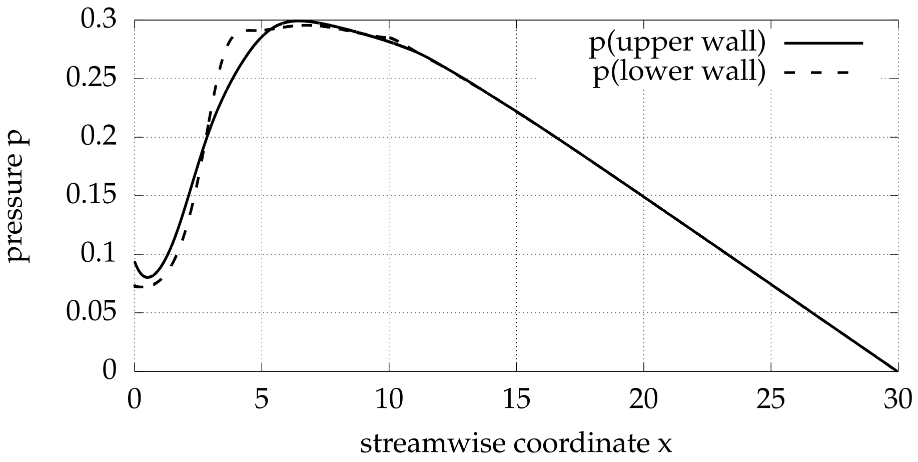

Figure 4.9: Pressure distribution at lower and upper walls downstream of the step for BFS with control portion $l = 10$ of elastic membrane bottom wall, with $T_m = 55$ and $p_e = 0.525$, at steady flow with $Re = 400$.

4.3.3 Unsteady periodic flow

The periodic flow under the inflow velocity defined in Subsection 4.2.1, is computed as the subject of control of the next subsections. The amplitude of the flow oscillation is taken $\alpha = 0.05$ and the respective frequency of the flow is $\omega = 0.05$ following previous research [MMnS10]. The time varying parabolic inlet velocity profile for oscillation amplitude $a = 0.05$ is depicted at Figure 4.10.

The detachment and reattachment positions under unsteady flow without control are shown in Figure 4.11. As fluid volume entering the BFS shrinks because of the decrease of the inlet velocity, the upper wall detachment position is moved downstream because of the reduced viscosity effects resulting from the lower velocity values. Meanwhile, the lower wall reattachment position is moved upstream due to the reduced inertia of the flow. Finally, the upper wall reattachment position is also moved upstream due to the upstream movement of the lower wall stagnation point. In the increasing phase of the inlet velocity, where the fluid volume inserting the geometry reaches its higher values, the remarks are reversed. The results are in good agreement with those of Mateescu et al. [MMnS10].

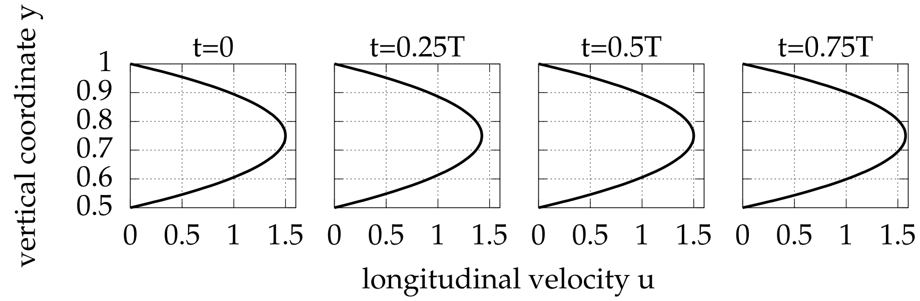

Figure 4.10: Inflow velocity profiles for four time instances during the period (Equation (4.1)). The oscillation amplitude is $\alpha = 0.05$.

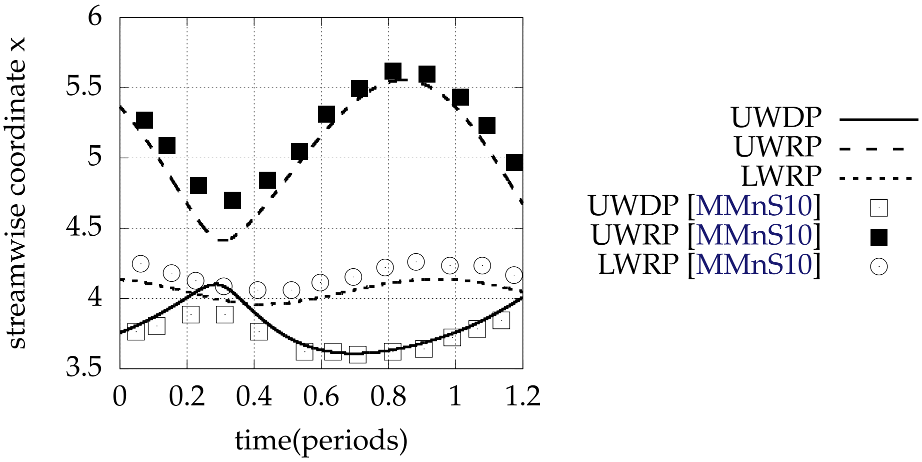

Figure 4.11: Upper wall detachment position (UWDP) and upper and lower wall reattachment positions (UWRP, LWRP), for unsteady periodic inflow with $\alpha = 0.05$, $\omega = 0.05$ and $Re = 400$, without control ($A = 0$). Comparison with results of Mateescu et al. [MMnS10] is presented.

4.3.4 Active control of unsteady periodic flow

Aiming at controlling the flow of Subsection 4.3.3, the portion of the bottom wall downstream of the step with length l is forced moving sinusoidally following Equation (4.3). For amplitude $A = 0.2$, frequency $\omega = 0.05$ and length $l = 10$ the evolution of the flow field in time is presented at Figure 4.12. The emergence and disappearance of the upper wall recirculation region and the fluctuation of the position of lower wall reattachment are visible.

As shown by evolution in time of the positions of detachment and reattachment, presented in Figure 4.13, the significant lowering of the bottom wall at the half period decreases the inclination of the lower wall stagnation line and increases its length. Therefore, pushes the lower wall reattachment position downstream. On the contrary, the maximum positive position of the oscillating portion of the bottom wall increases the inclination and decreases the length of the stagnation line, therefore causes the lower wall reattachment position to move upstream. The upper wall backflow emerges more distantly from the step position and elongates, as the control surface moves downwards. In the second half of the period, where the control surface moves upwards and the inlet velocity increases, the upper wall bubble quickly vanishes. As a consequence of the significant amplitude of the oscillation of the control surface ($A = 0.2$), which is a fifth of the expanded duct cross-section, the flow is attached at the upper wall for half of the period.

Comparing the positions of the separated zones, our results are close to those of Mateescu et al. [MMnS10]. The detachment positions computed with the immersed boundary method coincide with that computed with the body-fitted method. Upper wall reattachment positions during the cycle are in good agreement with those predicted by Mateescu et al. Lower wall reattachment position curves differ slightly before the end of the period. Current results are smoother at the time when the bottom wall bubble begins to extend downstream.

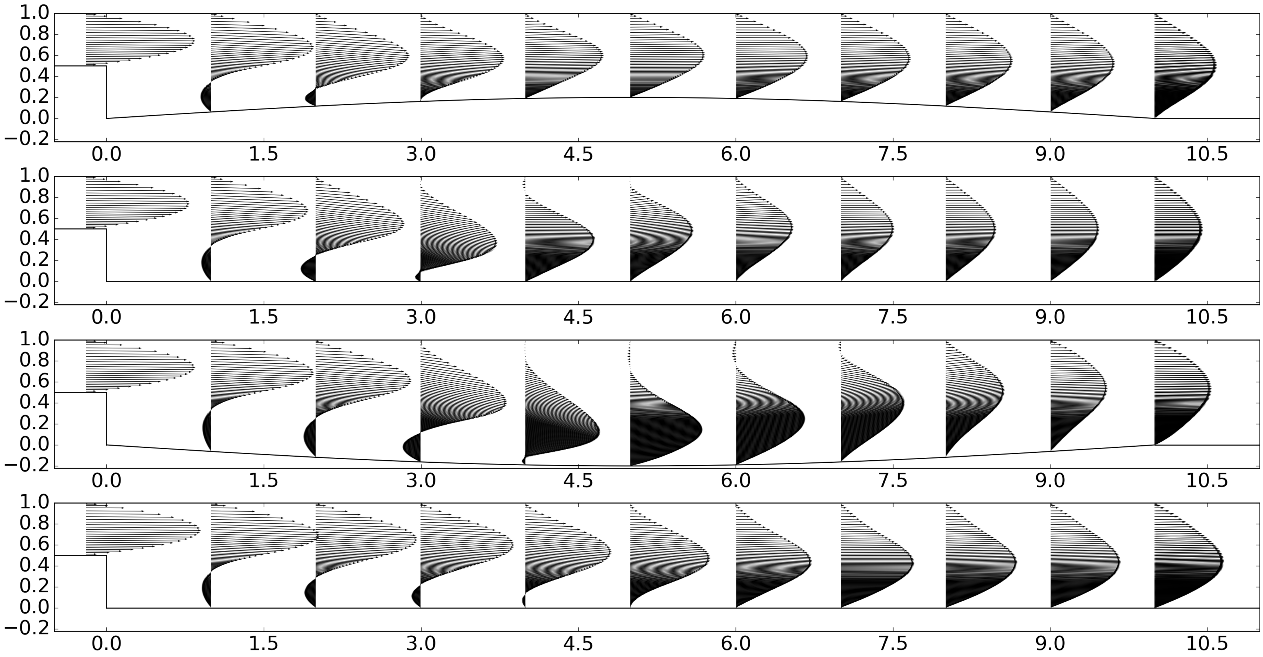

Figure 4.12: Computed velocity fields for $t = 0$, $t = T/4$, $t = T/2$, $t = 3T/4$, respectively, during a period T, for prescribed motion of the control surface with $A = 0.2$, $\omega = 0.05$, and $l = 10$. The inflow is oscillating with $\alpha = 0.05$. The Reynolds number is 400.

As seen in Figure 4.14, the increase of the frequency of the oscillation ($\omega_{high} = 0.1$, $\omega_{low} = 0.05$) pushes upstream the upper and lower wall reattachment and also the upper wall detachment, locations. The upper and lower wall recirculation oscillation amplitudes decrease with the higher frequency. Furthermore, the upper wall recirculation instantly vanishes and reappears for a small percentage of the period and also emerges earlier in the period for faster oscillating inlet velocity. This behavior arises probably due to a flow instability at the combination of higher frequency $\omega_{high} = 0.1$ and the relatively large wall oscillation amplitude $A = 0.2$. These observations are in accordance with analogous research with body fitted methods [MMnS10].

A decrease in the amplitude of oscillation of the moving portion of the bottom wall ($A_{low} = 0.15$, $A_{high} = 0.2$) causes the reduction of the upper wall separation region length. It also causes the presence of the upper wall recirculation for larger portion of the period and to the downstream

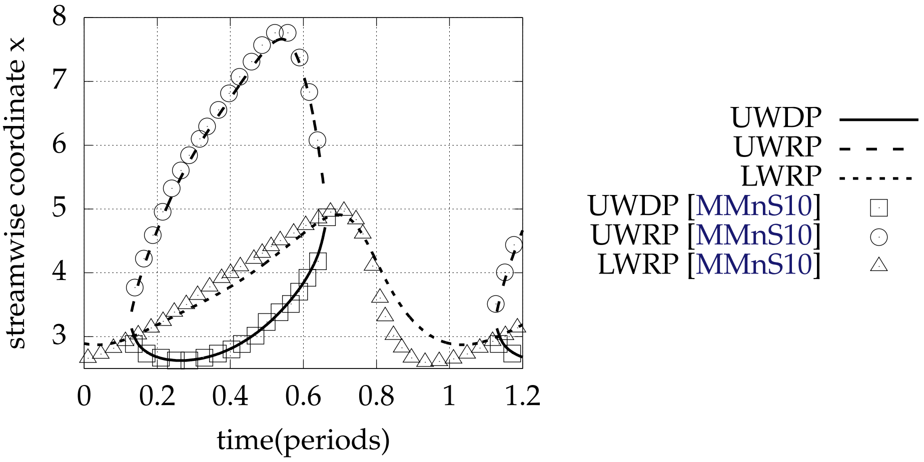

Figure 4.13: Upper wall detachment position (UWDP) and upper and lower wall reattachment positions (UWRP, LWRP) for unsteady periodic inflow with $\alpha = 0.05$ and $Re = 400$ and oscillating part of the bottom wall with $\omega = 0.05$, $A = 0.2$, $l = 10$. Comparison with results of Mateescu et al. [MMnS10] is presented.

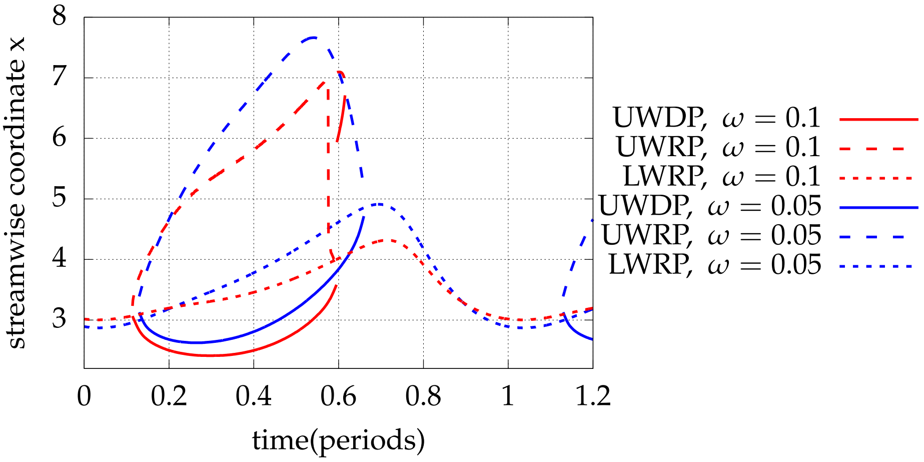

Figure 4.14: Upper wall detachment position (UWDP) and upper and lower wall reattachment positions (UWRP, LWRP), for unsteady periodic inflow with $\alpha = 0.05$ and $Re = 400$ and oscillating part of the bottom wall with $\omega = 0.1$, $A = 0.2$, $l = 10$. Comparison with results for $\omega = 0.05$.

movement of the respective detachment position. Furthermore, it leads to the reduction of lower wall reattachment position oscillation amplitude (Figure 4.15). The less upper wall and lower wall bubble length fluctuations is directly related to the reduced oscillation amplitude of the control surface. The remarks of Mateescu et al. [MMnS10] are in agreement with the aforementioned.

Finally, for the increase of the oscillating surface length ($l_{high} = 12.5$, $l_{low} = 10.0$), the fluctuation of the bottom wall recirculation length and top wall detachment position decrease, while the presence of the upper wall recirculation extends in time, as suggested by Figure 4.16. This trend is attributed to the fact, that the lower wall stagnation point is more distant to the middle point of the control surface

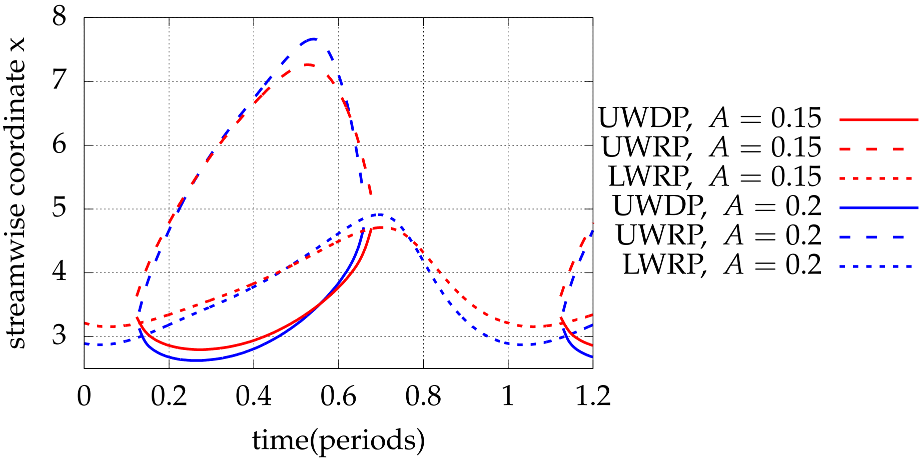

Figure 4.15: Upper wall detachment position (UWDP) and upper and lower wall reattachment positions (UWRP, LWRP), for unsteady periodic inflow, with $\alpha = 0.05$ and $Re = 400$ and oscillating part of the bottom wall, with $\omega = 0.05$, $A = 0.15$, $l = 10$. Comparison with results for $A = 0.2$.

length, which exhibits maximum amplitude. Therefore, its vertical oscillation amplitude reduces and consequently its longitudinal oscillation amplitude also reduces.

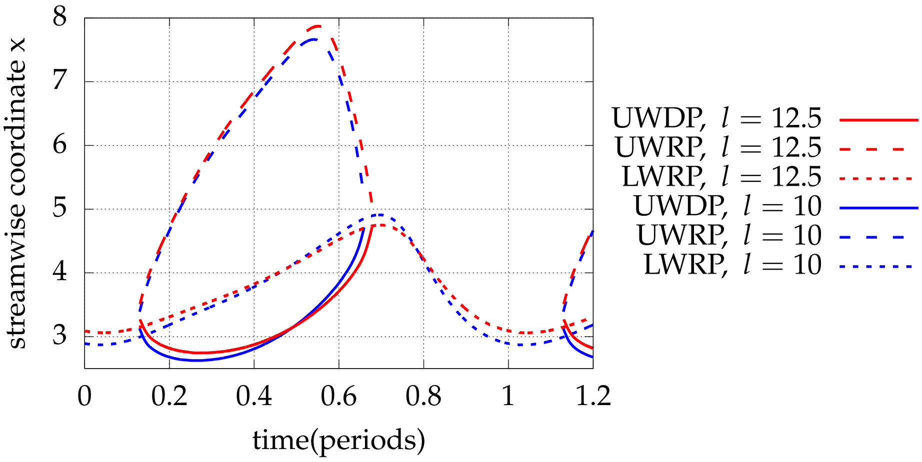

Figure 4.16: Upper wall detachment position (UWDP) and upper and lower wall reattachment positions (UWRP, LWRP), for unsteady periodic inflow, with $\alpha = 0.05$ and $Re = 400$ and oscillating part of the bottom wall, with $\omega = 0.05$, $A = 0.2$, $l = 12.5$. Comparison with results for $l = 10$.

4.3.5 Passive control of unsteady periodic flow via elastic membrane

On the purpose of controlling the flow computed in Subsection 4.3.3, we also employ an elastic membrane which follows Equation (2.130) with tension $T_m = 55$ and with steady, uniform external pressure exerted at its outer side, $p_e(x,t) = p_e = 0.55$. As for the steady case, the membrane parameters T_m and p_e are selected so that the small displacement assumption (Equation (2.131)) is satisfied

($\max_{x,t} g(x,t) < 0.1$) during the period. Additional objectives leading to the parameters' values, are the external pressure to be of the same order of magnitude with the pressure exerted by the flow and the transmural pressure $p_e - p_i(x,t)$ to be positive.

The interaction of the flow with the elastic membrane leads to the complete suppression of the upper wall recirculation as shown in the velocity profiles of Figure 4.17 and the longitudinal velocity contours of Figure 4.18. The free shear layer is identified by the set of transition points where longitudinal velocity changes sign.

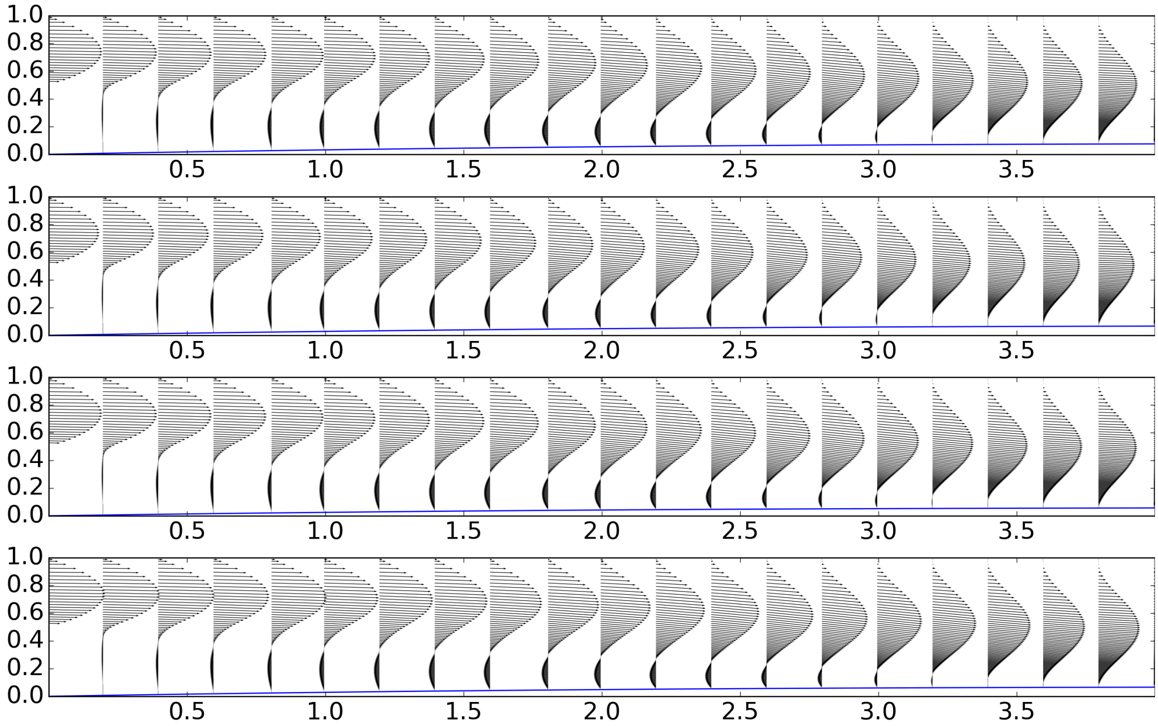

Figure 4.17: Computed velocity fields for $t = 0$, $t = T/4$, $t = T/2$, $t = 3T/4$, respectively, during an inflow period T, for FSI of the flow with a membrane with $T_m = 55$ and $p_e = 0.55$. The inflow (Equation (4.1)) is oscillating with $\alpha = 0.05$ and $\omega = 0.05$. The Reynolds number is 400.

Inasmuch as a membrane stretched in a relatively high grade is employed ($T_m = 55$), the control surface oscillation amplitude is restricted comparing to the active control of the previous subsection, as shown in Figure 4.17. In the longitudinal velocity contours exhibited in Figure 4.18, the oscillation of the inflow is observed. No negative values region is noted at the upper wall, indicating absence of upper wall flow reversal. The lower wall recirculation region extension is indicated by the negative values zone. Following the free shear layer oscillation, the lower wall reattachment position is fluctuating around $x \approx 3.5$. In Figure 4.19, the transverse velocity contours suggest more intensive downstream motion at the region $2.3 \leq x \leq 3.3$ for $t = 3T/4$, when the inlet fluid volume rate is maximum.

The induced pressure at the inner side of the membrane during the periodic inflow cycle is presented in Figure 4.20. As in the steady case (Figure 4.9), pressure recovers downstream of the step

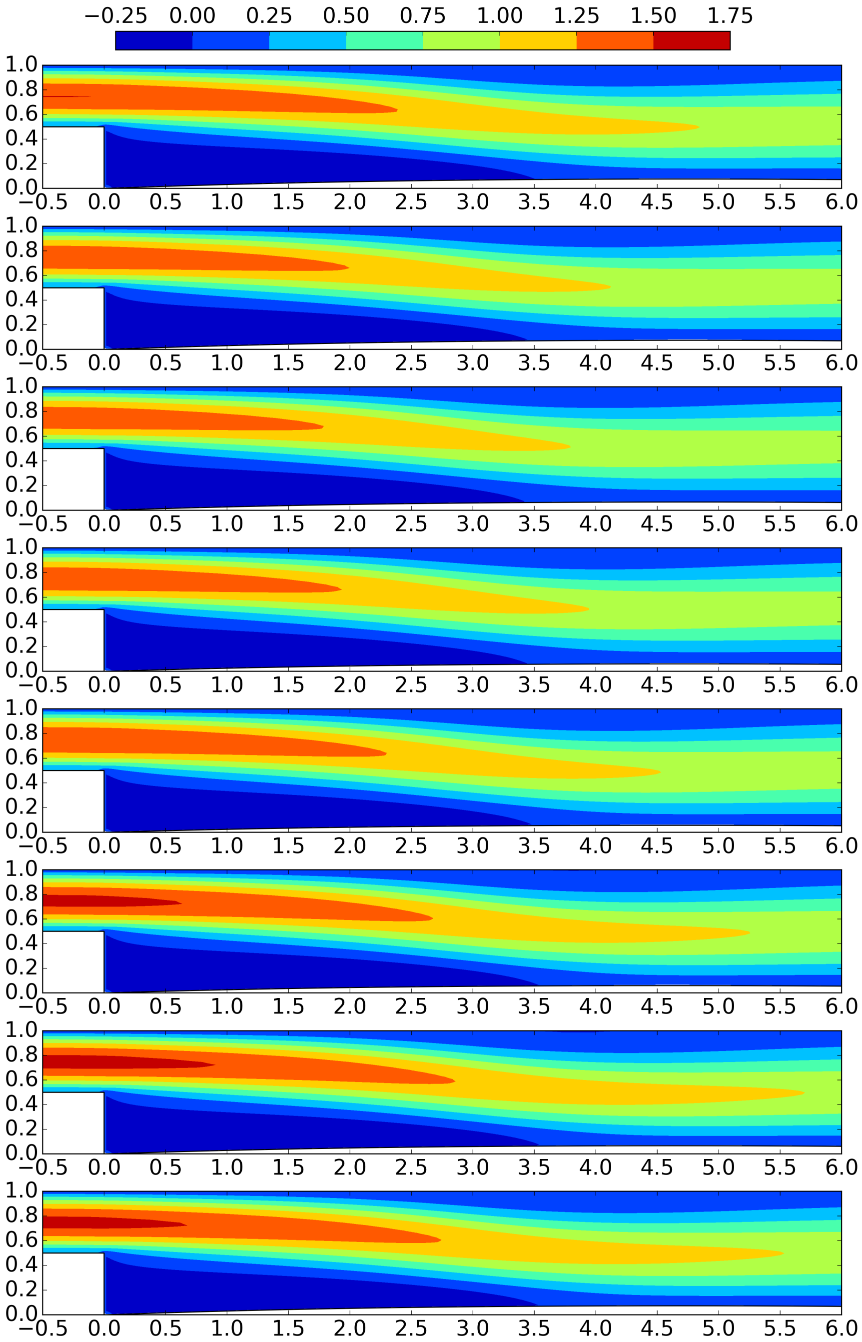

Figure 4.18: Longitudinal velocity contours for $t = 0$, $t = T/8$, $t = T/4$, $t = 3T/8$, $t = T/2$, $t = 5T/8$, $t = 3T/4$, $t = 7T/8$, respectively, during a period T, for FSI of the flow with a membrane with $T_m = 55$ and $p_e = 0.55$. The inflow (Equation (4.1)) is oscillating with $\alpha = 0.05$ and $\omega = 0.05$. The Reynolds number is 400.

and is maximized at a longitudinal position close to the lower wall reattachment cross-section [SA08]. Downstream of the stagnation point, the pressure drops streamwise due to the action of frictional forces. The maximum pressure fluctuation emerges at the region $0 \leq x \leq 1.6$ and has the value

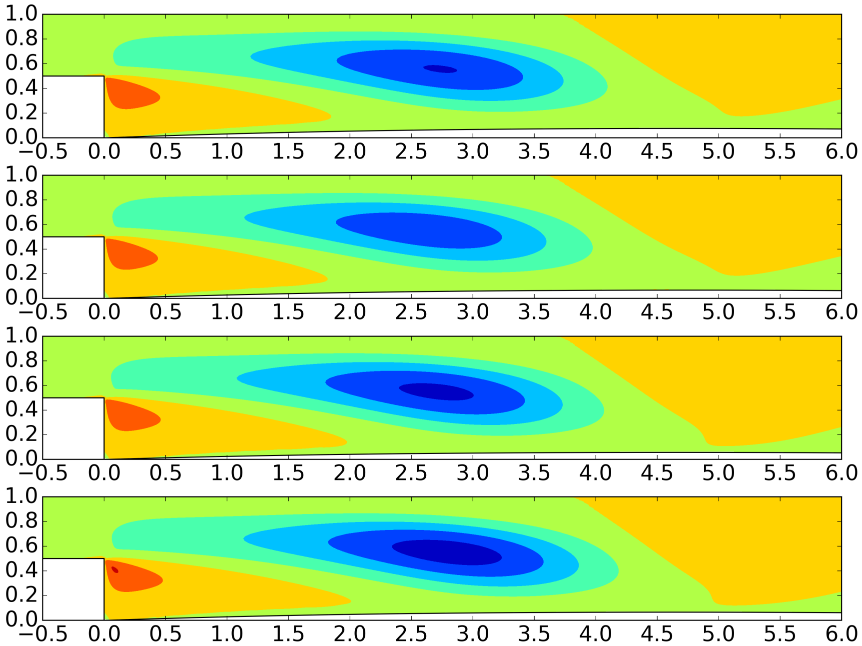

Figure 4.19: Transverse velocity contours for $t = 0$, $t = T/4$, $t = T/2$, $t = 3T/4$, respectively, during a period T, for FSI of the flow with a membrane with $T_m = 55$ and $p_e = 0.55$. The inflow (Equation (4.1)) is oscillating with $\alpha = 0.05$ and $\omega = 0.05$. The Reynolds number is 400.

$$\max_{x\in[0,l]}\left(\max_{t\in[0,T)} p(x, y = g(x,t), t) - \min_{t\in[0,T)} p(x, y = g(x,t), t)\right) = 0.093.$$

The corresponding membrane shape is presented in Figure 4.21. Membrane curve at the $x - y$ plane is approximately that of a concave down parabola due to the relatively high values of its parameters chosen (tension, external pressure). The overall membrane displacement is negatively correlated with inner pressure distribution mean value. The largest membrane displacement occurs at $x < 5$ due to the inner membrane pressure distribution, which exhibits noticeably lower mean value at the left half of its domain ($0 \leq x < 5$) and higher values at the right half ($5 < x \leq 10$). The periodical motion of the membrane is a result of its interaction with the oscillating inlet flow. Through this interaction, the membrane inner pressure distributions are decided. The work of the membrane is produced by its oscillation along with the varying membrane inner pressure distribution.

As Figure 4.22 suggests, the length of the lower wall inversed flow zone is shrank significantly (14.3%), as its maximum value drops to nearly 3.55 from 4.14 for the flow without control. Moreover, small reduction of the fluctuation of its length is observed. The peak to peak fluctuation of 0.18 for the without control case, drops to the value 0.14 for the passive control case i.e. a 22.2% reduction is noted.

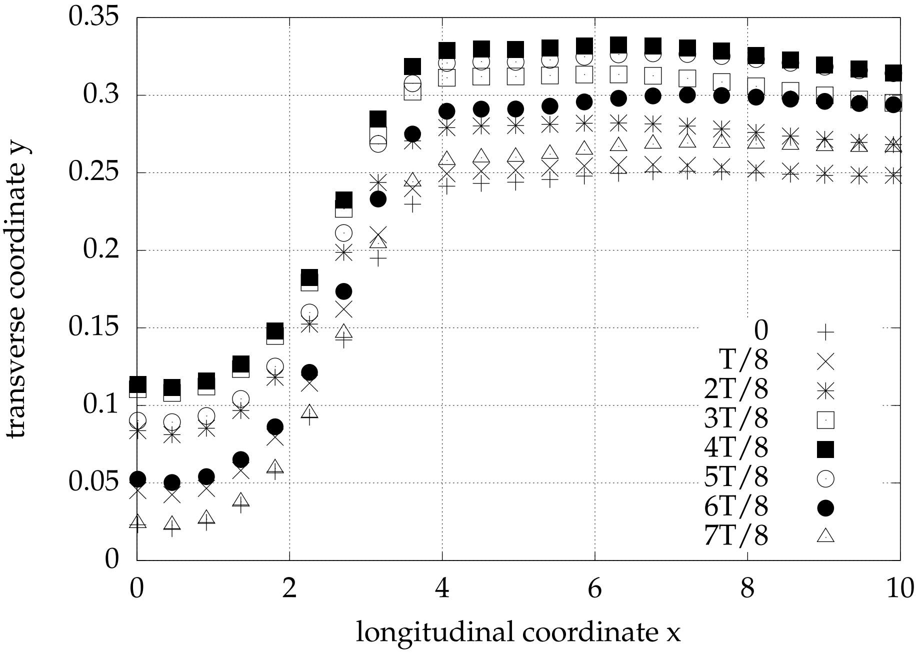

Figure 4.20: Pressure at the internal surface of an elastic control membrane with length $l = 10$, tension $T_m = 55$ and external pressure exerted at its outer side, $p_e = 0.55$, for eight instances during one inflow period T. The inflow is defined by Equation (4.1) with $\alpha = 0.05$ and $\omega = 0.05$.

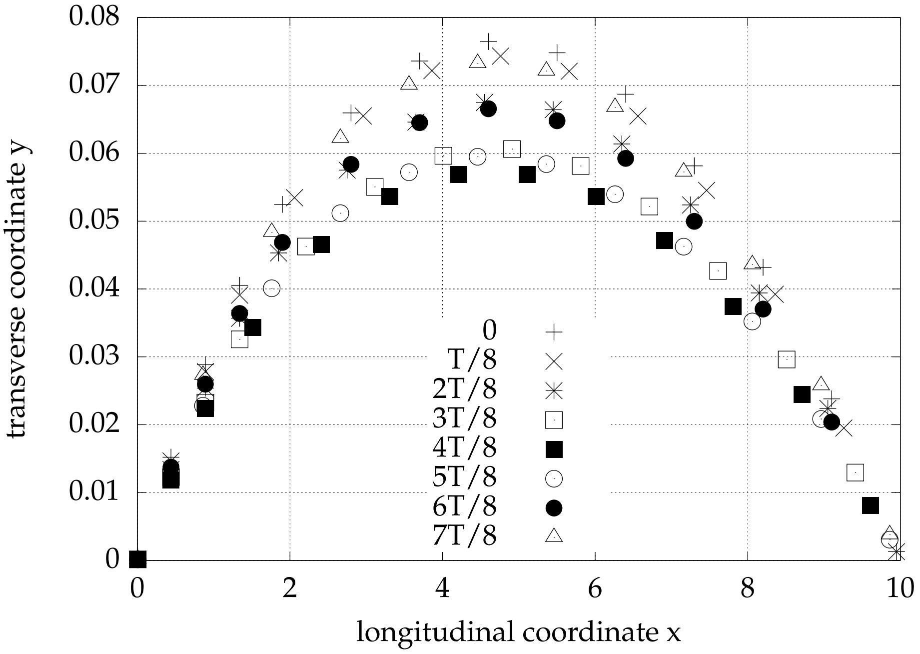

Figure 4.21: Shape of an elastic control membrane with length $l = 10$, tension $T_m = 55$ and external pressure exerted at its outer side, $p_e = 0.55$, for eight instances during one inflow period T. The inflow is defined by Equation (4.1) with $\alpha = 0.05$ and $\omega = 0.05$.

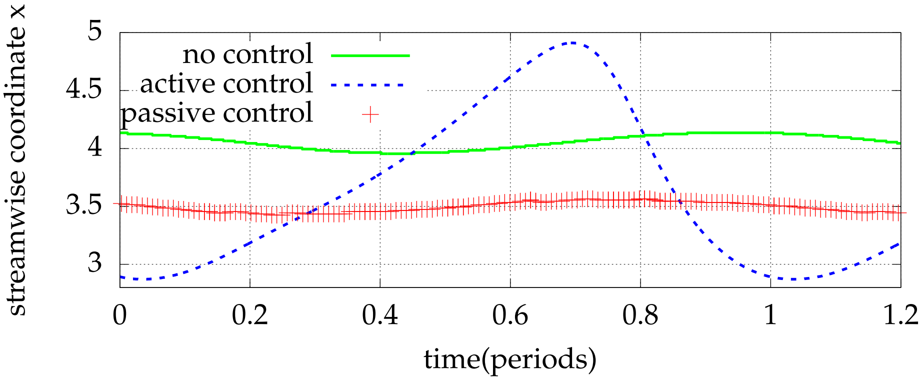

Figure 4.22: Lower wall reattachment position (LWRP) during a period for the periodic flow over a BFS controlled by an elastic membrane with $l = 10$, $T_m = 55$ and $p_e = 0.55$. The inflow is defined by Equation (4.1) with $\alpha = 0.05$ and $\omega = 0.05$. Comparison with no control and active control results.

4.4 Summary

The immersed boundary method is implemented to compute the steady and unsteady periodic laminar flow over a backward facing step, without and with control. The results are in close agreement with those of body fitted methods, for the cases where such exist. Two techniques for the control of the flow are employed.

Aiming at establishing active control, a portion of the bottom wall downstream of the step is oscillating in a prescribed sinusoidal way. The effect of the frequency, the amplitude and the length of the oscillating surface on the longitudinal detachment and attachment positions and longitudinal extension of closed streamlines are examined. The impact of the augmentation of the length of the oscillating surface to the control of the internal flow over a BFS, is investigated for the first time in the literature. Increase of the frequency shifts the occurrence of the upper wall recirculation bubble earlier during the period. A reduction of the oscillation amplitude of the surface, reduces the upper wall recirculation length. Increase of the length of the control surface compresses the range of the upper wall detachment position and decreases the fluctuation of the position of the lower wall stagnation point.

In the passive control setting, an elastic membrane substitutes for the rigid control part of the bottom wall and both the steady and unsteady fluid structure interaction problems are solved. This method of control is implemented for the first time for a flow over a backward facing step. As a result of the control, the upper wall recirculation region vanishes, while the lower one is reduced both in steady and periodic cases. The fluctuation of the lower wall separation length is also shortened for the time varying case. A study of the effect of the membrane parameter values to the separation characteristics, is a further investigation objective.

Chapter 5

Peristalsis

Synopsis

Peristaltic motion arises in many physiological, medical, pharmaceutical and industrial processes. Control of the fluid volume rate and pressure is crucial for pumping applications, such as the infusion of intravenous liquid drugs, blood transportation, etc. In this study, a simulation of peristaltic flow is presented in which occlusion is imposed by pairs of circular rollers that squeeze a deformable channel connected to a reservoir with constant fluid pressure. Naturally, this kind of flow is laminar; hence, the computation occurred in this context. The effect of the number and speed of the pairs of rollers, as well as that of the intrapair roller gap is investigated. Non-Newtonian fluids are considered, and the effect of the shear-thinning behavior degree is examined. The volumetric flow rate is found to increase with an increase in the number of rollers or in the relative occlusion. A reduction in the Bird–Carreau power index results in a small reduction in transport efficiency. The characteristic of the pumping is computed, i.e., the induced pressure as a function of the fluid volume rate. A strong positive correlation exists between relative occlusion and induced pressure. Shear-thinning behavior significantly decreases the developed pressure compared to Newtonian fluids. The immersed boundary method on curvilinear mesh is adapted and validated for non-Newtonian fluids.

5.1 Introduction

Peristaltic flow appears in many physiological processes, such as urine flow in the ureter, lymph flow in the lymphatic system, bolus and chyme flow through the gastrointestinal tract and spermatic flow in the vas deferens. Peristaltic pumping is used for industrial applications, such as food displacement in pipes, and medical applications, such as the extracorporeal pumping of blood and the infusion of pharmaceutical fluids [BB16; Gra+15b].

Elaboration of Navier–Stokes equations for two-dimensional analysis with constant viscosity (using the fact that viscous forces dominate peristaltic flow) results in good predictions for the flow [Lat66; JS71; SJW69]. The effect of the presence of an axial body on such flows has been theoretically investigated for Newtonian fluids, and the role of flow parameters in pumping characteristics was characterized by Roy et al. [RRR11]. A non-Newtonian analysis for power-law fluids is reported by Srivastava and Srivastava [SS85], which showed a peristaltic pressure rise reduction for a power index less than unity.

An analogous experimental examination of peristaltic pumping for a circular deformable tube was introduced by Latham [Lat66] and Weinberg et al. [WES71]. Flow through a straight deformable tube squeezed by three pairs of rollers is studied for non-Newtonian fluids using computer tomography and Doppler velocimetry by Nahar [Nah12].

The effects of the relative occlusion imposed by the roller, the wavenumber, the Reynolds number and the back pressure with a sinusoidal-shaped wave are investigated computationally by Tsui et al. [Tsu+14]. Sawtooth and trapezoidal wave shapes are also calculated by Tatsumi et al. [Tat+09], who found that the wave formation is less important than the wave amplitude. Additionally, shear-thinning behavior is simulated by Al-Habahbeh [AH13] and Alokaily et al. [Alo+18] for circular-segment-shaped waves produced by pairs of circular rollers squeezing the tube. U- and O-shaped pumps are simulated by Zhoo et al. [Zho+14], who showed that the O-shaped ones may produce lower levels of wall shear stress. This finding suggests that the O-shaped setting is more suitable for blood and other cell-containing fluids, as it poses less hemolysis, or cytolysis in general, risk. Backflow suppression and uniformization of roller pump outflow are addressed by Manopoulos et al. [Man+20] by introducing an appropriate inflating portion of the deformable tube. Thus, producing momentum to compensate for the negative pressure gradient at the outlet of the pump, that occurs when there is zero occlusion by a roller.

In this study, the confined flow in an elastic tube under a peristaltic wave caused by multiple (one, two and three) circular rollers moving consecutively is computed by means of the immersed boundary method (IBM). As the first step, the conclusions drawn via body-fitted methods for the effect of the roller speed, the half-gap and the Bird–Carreau power index on the peristaltic flow are confirmed. The curvilinear immersed boundary method of Ge and Sotiropoulos [GS07] is adjusted and tested for non-Newtonian fluids.

Subsequently, the resulting flow fields and the effect of the number of rollers on the output fluid volume rate are investigated. Moreover, we compute the pumping characteristics for a straight peristaltic pump considering Newtonian and non-Newtonian behavior. The role of relative occlusion and pseudoplasticity in peristalsis characteristics is analyzed.

5.2 Materials and Methods

5.2.1 Geometry

A two-dimensional symmetric model, given in Figure 5.1, is used to represent the deformable channel. The elastic tube is squeezed by two opposite circular waves that move horizontally with velocity c. Simulations were performed for channels with lengths $L = 90$ mm (Subsections 5.3.1–5.3.3 and 5.3.5) and $L = 180$ mm (Subsection 5.3.4). The half-height of the undeformed channel is taken as $H = 10$ mm, similar to that of the human esophagus. The radius of the circular sector of the roller is $r = 30$ mm (as in the experiments presented by Nahar [Nah12]). The minimum height of the deformed channel takes several values according to the compression amplitude.

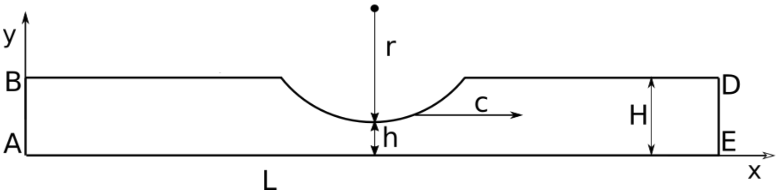

Figure 5.1: Geometry of the two-dimensional computational domain for the peristaltic pump. Mirroring this scheme with respect to the x-axis and extruding with respect to the z-axis provides the geometry of the full pump.

5.2.2 Mathematical Model

Following previous research by Nahar et al. [NJW10] and Al-Habahbeh [AH13], the density of the pumped fluid is $\rho = 1000$ kg/m^3, and its rheology is predicted from the Bird–Carreau equation for the shear dependent dynamic viscosity [Car68; BAH87] (Equation (2.47))

$$\mu(\dot{\gamma}) = \mu_{\text{inf}} + (\mu_0 - \mu_{\text{inf}})(1 + (\lambda\dot{\gamma})^2)^{\frac{n-1}{2}}. \tag{5.1}$$

The values of the constants are taken as, $\mu_{\text{inf}} = 0$, $\mu_0 = 0.1452$ Pa $\cdot$ s , $\lambda = 20$ s and $n \leq 1$.

At the centerline, symmetry boundary conditions are defined; that is, the axial velocity normal gradient and the transverse velocity are set to zero:

$$\left.\frac{\partial u}{\partial y}\right|_{y=0} = 0, \ \ \mathrm{v}(x, y = 0) = 0, \tag{5.2}$$

where u and v are the streamwise and vertical velocity components, respectively. On the upper, deformable wall, the no-slip condition is defined.

$$\phi(\text{wall}) = \phi_{\text{wall}}, \ \ \phi \in \{u, \mathrm{v}\}, \tag{5.3}$$

where ϕ_{wall} is the velocity component of the wall.

For Subsections 5.3.1–5.3.4, the boundary data for the left and right ends of the tube–cross-sections AB and DE in Figure 5.1, respectively–is the periodic condition for the velocity components:

$$\phi(x = 0, y) = \phi(x = L, y), \ \ \phi \in \{u, \mathrm{v}\}. \tag{5.4}$$

For Subsection 5.3.5, at cross-section AB of Figure 5.1, the imposed boundary condition is that of a parabolic velocity profile:

$$u(x = 0, y) = u_{max}\left(1 - \left(\frac{y}{H}\right)^2\right), \ \ \mathrm{v}(x = 0, y) = 0, \tag{5.5}$$

where u_{max} is the maximum velocity of the parabolic profile on the axis $y = 0$. At the outlet cross-section DE, for $x = L$, a zero-velocity normal gradient is set:

$$\left.\frac{\partial \phi}{\partial x}\right|_{x=L} = 0, \;\; \phi \in \{u, \mathrm{v}\}. \tag{5.6}$$

A mesh independence study was performed using a coarse (451 × 52 nodes) and a fine (1041 × 102 nodes) Cartesian grid for the 180 mm pump and analogously for the 90 mm pump. The peak difference at the axial velocity for the two grids is less than 0.25%. The maximum mesh interval of the fine mesh is 0.1 mm. A three-dimensional solution algorithm is employed; therefore, a subtle depth is considered along with slip conditions at the boundary surfaces of the third dimension. The immersed boundary surface of the roller is triangulated with 3104 nodes and 6204 elements, and the node distance is upper bounded by 0.2 mm.

We adjust the coordinate system shown in Figure 5.1 at the roller and define it as the moving frame of reference. The simulation was conducted at this moving frame of reference. Consequently, the roller does not move, whereas the surface $y = H$ moves with velocity $\boldsymbol{v} = (-c, 0)$; therefore, a steady flow field is simulated. To the computed flow field, the roller speed $\boldsymbol{v} = (c, 0)$ is added uniformly in order to return to the laboratory frame of reference.

5.3 Results and Discussion

The relative occlusion (RO) is defined as the ratio of the penetration of a pair of rollers in the deformable tube to the height of the undeformed channel, namely,

$$RO = \frac{H - h}{H}. \tag{5.7}$$

For roller speed $c = 5$ mm/s and half gap $h = 4$ mm, the flow field is shown in Figures 5.2, 5.3 and the pressure field in Figure 5.4.

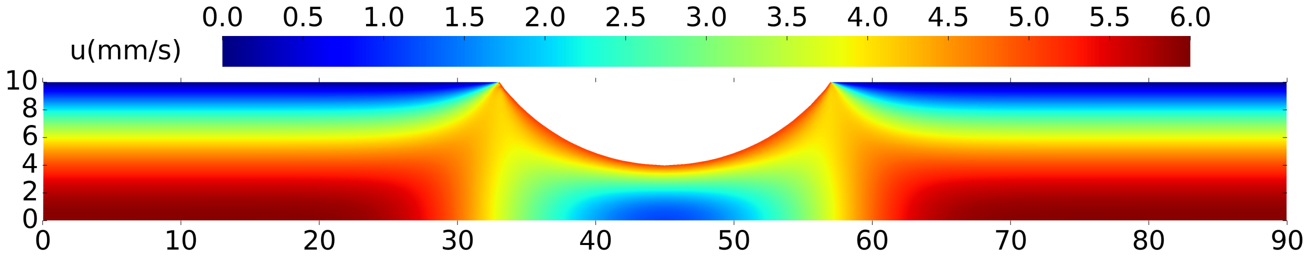

Figure 5.2: Axial velocity contours for 1 roller, $c = 5$ mm/s, $L = 90$ mm, $RO = 0.6$ and $n = 1$.

The transport efficiency (TE) is defined as the fluid volume rate over the wave speed and over the height of the complete channel, namely,

$$TE = \frac{\dot{V}}{c \cdot 2H}. \tag{5.8}$$

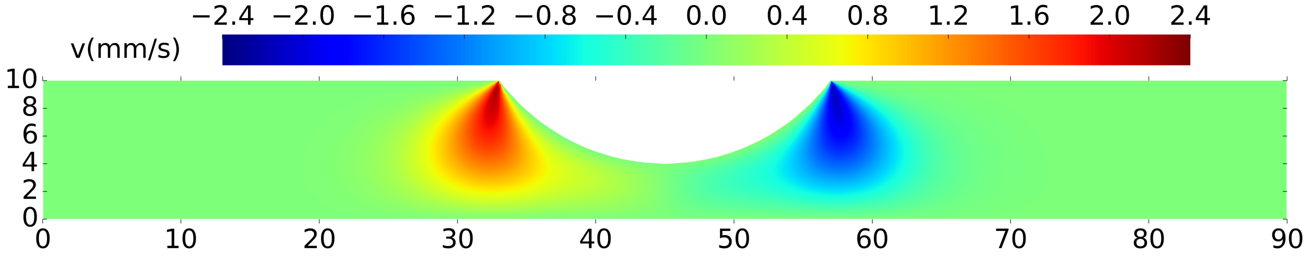

Figure 5.3: Transverse velocity contours for 1 roller, $c = 5$ mm/s, $L = 90$ mm, $RO = 0.6$ and $n = 1$.

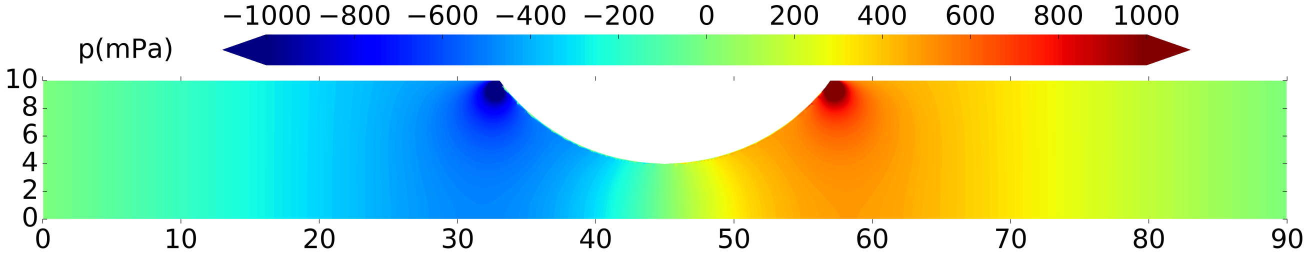

Figure 5.4: Pressure contours for 1 roller, $c = 5$ mm/s, $L = 90$ mm, $RO = 0.6$ and $n = 1$.

5.3.1 Varying Relative Occlusion

The higher the RO ceteris paribus, the higher the values of axial velocity profiles near the centerline and the higher the pressure rise after the roller, as shown in Figures 5.5 and 5.6, for $c = 5$ mm/s and $c = 10$ mm/s.

Axial velocity profiles show higher values as RO rises, as suggested by Figure 5.7. For small values of RO, retrograde flow arises in the region under the roller, as observed in Figures 5.5 and 5.7c–e.

Transport efficiency is found to be strongly dependent on relative occlusion, as is shown in Table 5.1.

Table 5.1: Transport efficiency (TE) for various pumping conditions and pump length $L = 90$ mm. Comparison with results from [AH13].

$n = 1$, $RO = 0.6$		**$c = 5$ mm/s, $n = 1$**			**$c = 10$ mm/s, $n = 1$**		**$c = 5$ mm/s, $RO = 0.6$**		
c (mm/s)	**TE (%)**	**RO**	**TE (%)**	**TE (%) [AH13]**	**RO**	**TE (%)**	**n**	**TE (%)**	**TE (%) [AH13]**
2.5	78.8	0.8	95.6	95	0.6	78.8	1	78.4	78
5	78.4	0.6	78.4	78	0.2	28.6	0.75	77.5	77
10	78.8	0.2	28.4	28			0.5	77.1	76

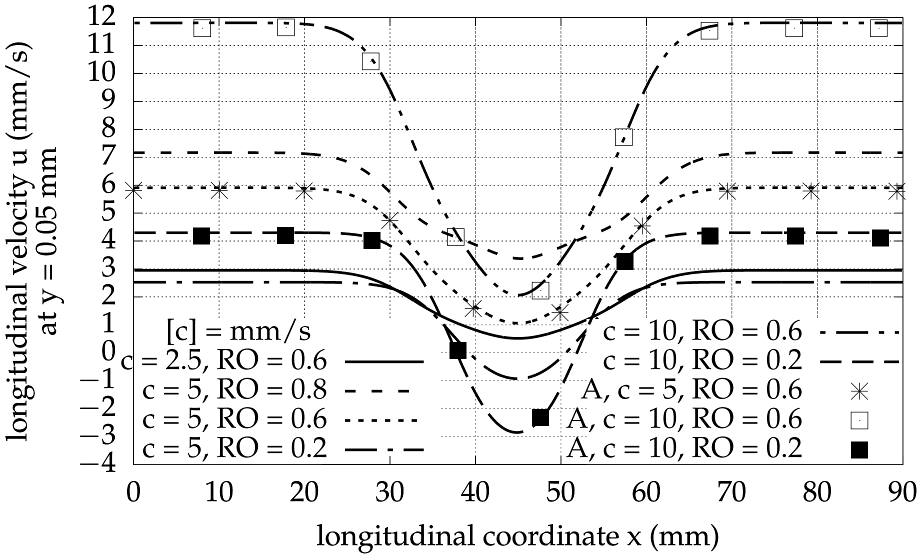

Figure 5.5: Longitudinal velocity near the central axis of the pump ($y = 0.05$ mm) for various values of *RO* and *c*, $n = 1$ and one roller. Comparison with results from [AH13] (A) is presented.

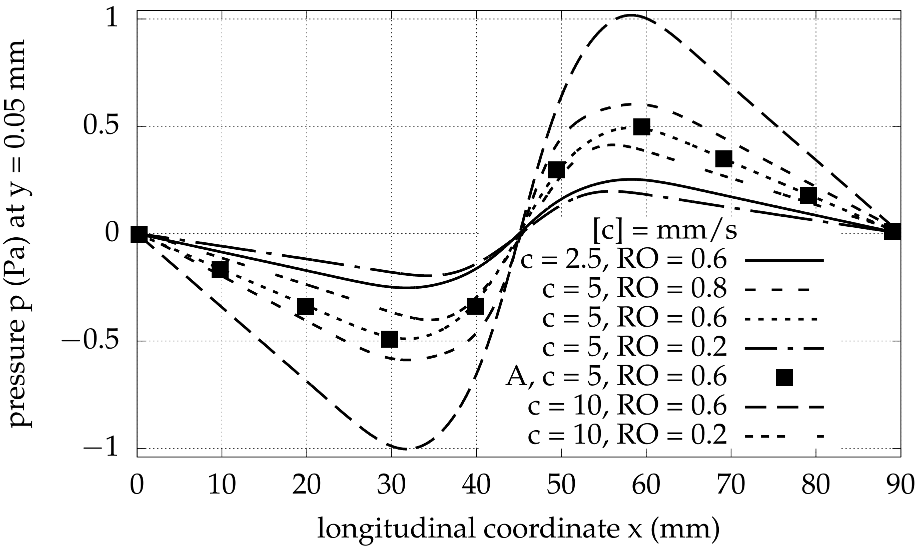

Figure 5.6: Pressure near the central axis of the pump ($y = 0.05$ mm) for various values of *RO* and *c*, $n = 1$ and one roller. Comparison with results from [AH13] (A) is presented.

5.3.2 Varying Roller Speed

Roller speed has a similar effect to that of *RO* on axial velocity and pressure. As indicated in Figure 5.5, for higher roller speed, the axial velocity near the centerline ($y = 0.05$ mm) away from the longitudinal center reaches values around 20–25% higher than *c*. Pressure fluctuation is also approximately linearly related to roller speed, as suggested by Figure 5.6. According to Figure 5.8, the shear rate near the axis has two similar skewed bell curves, which are symmetric with respect to the vertical

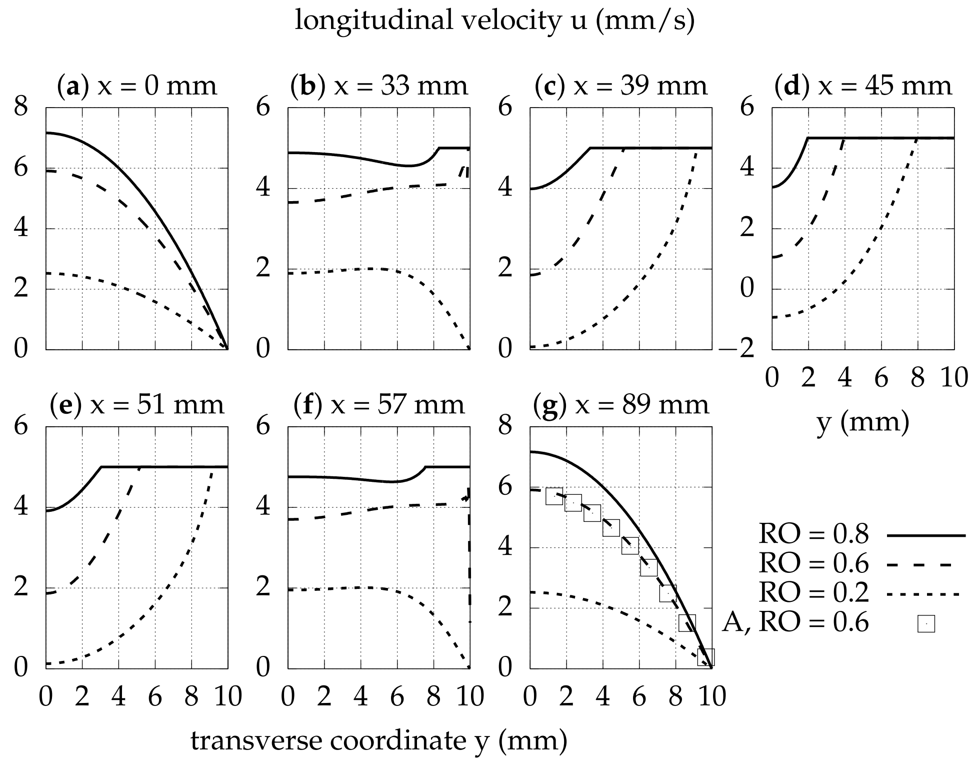

Figure 5.7: Longitudinal velocity profiles at successive longitudinal positions x (**a**–**g**) for various values of RO and for $c = 5$ mm/s, $n = 1$ and one roller. Comparison with results from [AH13] (A) is presented.

axis passing through the roller center (at $x = 45$ mm). The peak shear rate is approximately linearly related to the roller speed. For example, for $c = 2.5$ mm/s, $\max_x\{\dot{\gamma}\}$ near the axis is 0.374 s^{-1}, while for $c = 5$ mm/s, $\max_x\{\dot{\gamma}\}$ near the axis is 0.748 s^{-1}.

The transport efficiency is approximately constant with respect to changes in roller speed, so the flow volume rate through the pump is approximately linearly related to the roller speed, as shown in Table 5.1.

5.3.3 Non-Newtonian Fluids

As the value of the Bird–Carreau power index decreases, the effect of the moving roller on the axial velocity near the longitudinal axis of symmetry ($y = 0.05$ mm) slightly weakens (Figure 5.9); i.e., near the axis, the streamwise longitudinal velocity curve exhibits fairly less fluctuation, as shown in Figure 5.10. More specifically, away from the roller position, the velocity decreases, while at the position of the roller, it increases.

As suggested in Figure 5.11, near the wall, the axial velocity is higher for pseudoplastic fluids than for Newtonian fluids. Pressure shows a stronger dependence on the power index, and the force exerted on the roller decreases almost 5-fold whereas the power index decreases by a factor 0.5, as observed in Figure 5.12.

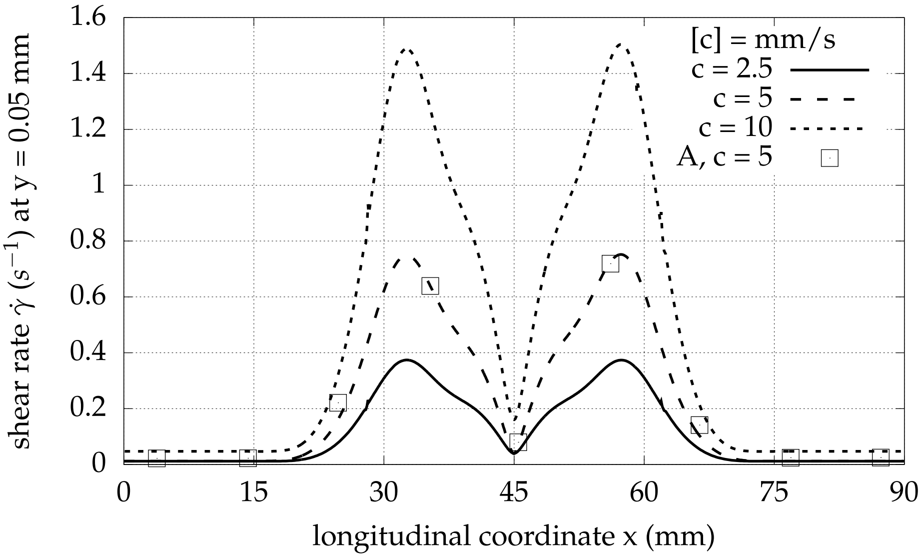

Figure 5.8: Shear rate near the central axis of the pump ($y = 0.05$ mm), for various values of c and for $RO = 0.6$, $n = 1$ and one roller. Comparison with results from [AH13] (A) is presented.

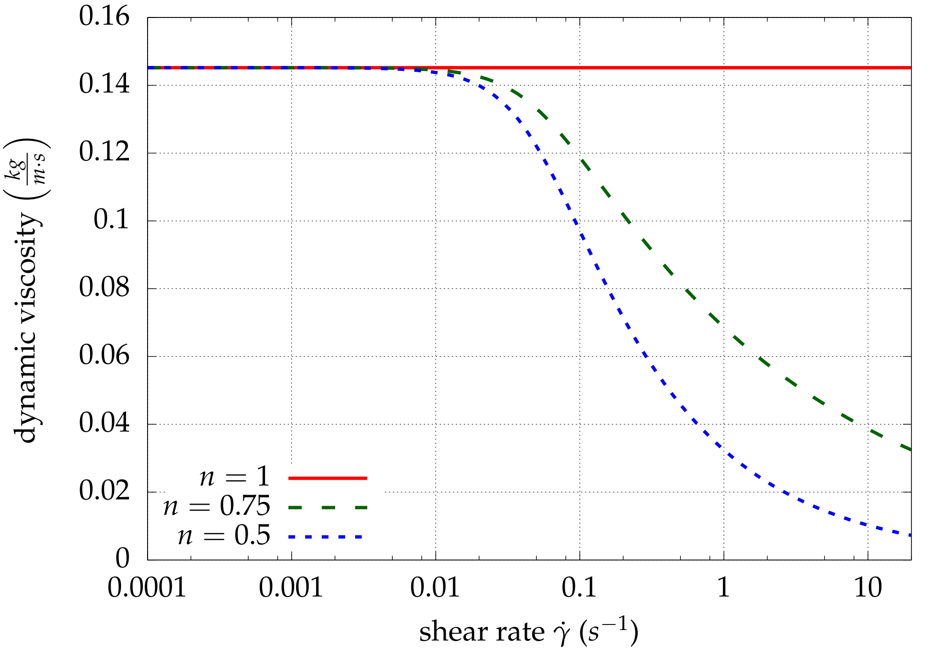

Figure 5.9: Dynamic viscosity curves for various values of the Bird-Carreau power index of shear thinning behaving fluids.

The shear rate also decreases near the x-axis for smaller values of the power index n, as Figure 5.13 shows. Near the wall, the shear rate increases for shear-thinning fluids as compared to Newtonian fluids, as shown in Figure 5.14. Transport efficiency is weakly dependent on the Bird–Carreau power index, as presented in Table 5.1.

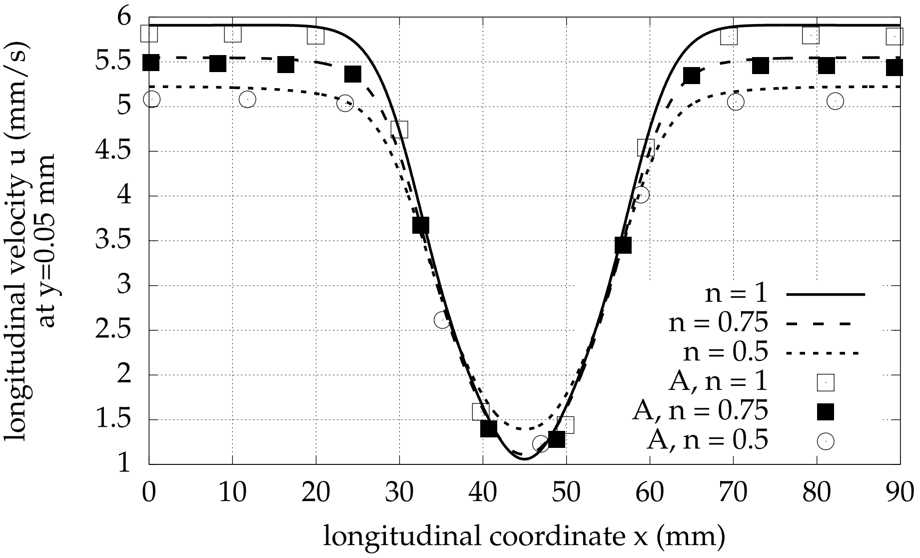

Figure 5.10: Longitudinal velocity near the central axis of the pump ($y = 0.05$ mm) for Newtonian and non-Newtonian fluids, $c = 5$ mm/s, $RO = 0.6$ and one roller. Comparison with results from [AH13] (A) is presented.

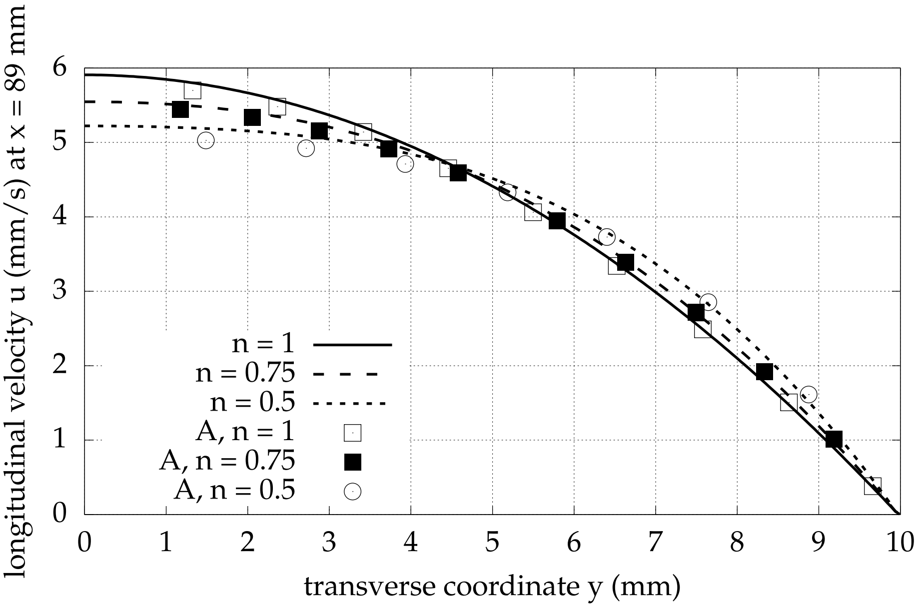

Figure 5.11: Longitudinal velocity profile at $x = 89$ mm for Newtonian and non-Newtonian fluids. The roller speed is $c = 5$ mm/s, the relative occlusion is $RO = 0.6$ and there is one roller. Comparison with results from [AH13] (A) is presented.

5.3.4 Multiple Rollers

The fluid velocity vectors for one, two and three roller pumps with $L = 180$ mm are illustrated in Figures 5.15–5.17. The axial velocity shows the highest value near the x-axis away from the roller and reaches its minimum value under the roller, as is also shown in Figure 5.18. For the case of one roller,

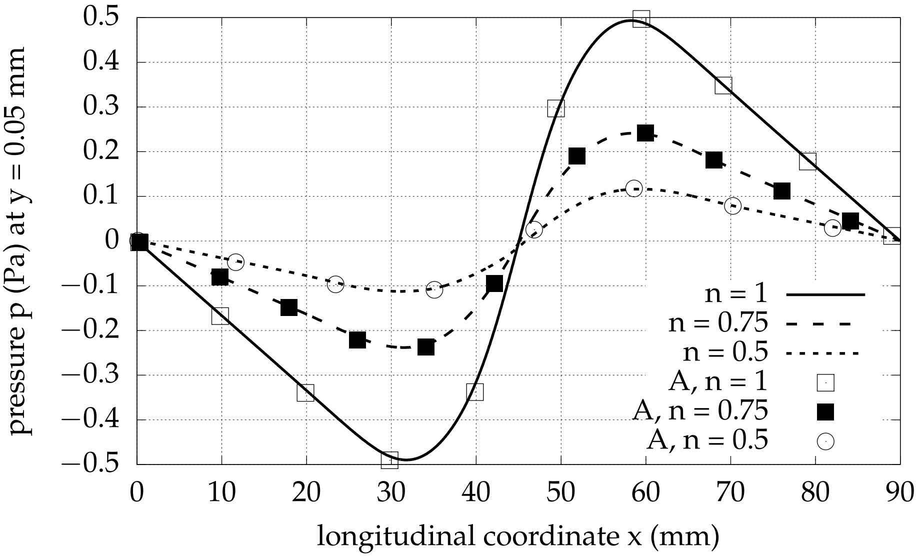

Figure 5.12: Pressure near the central axis of the pump ($y = 0.05$ mm) for Newtonian and non-Newtonian fluids, $c = 5$ mm/s, $RO = 0.6$ and one roller. Comparison with results from [AH13] (A) is presented.

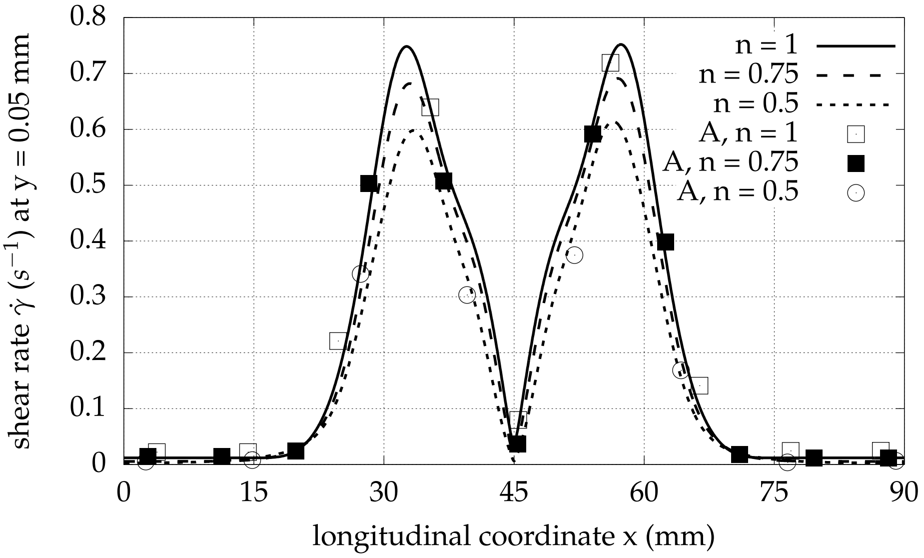

Figure 5.13: Shear rate near the central axis of the pump ($y = 0.05$ mm) for Newtonian and non-Newtonian fluids. The roller speed is $c = 5$ mm/s, the relative occlusion is $RO = 0.6$ and there is one roller. Comparison with results from [AH13] (A) is presented.

the axial velocity under the roller (82 mm $\leq x \leq$ 98 mm) and near the longitudinal axis of symmetry ($y = 0.05$ mm) is negative with a magnitude nearly half the speed of the moving roller, creating a recirculation zone. For multiple rollers, no negative axial velocity values appear.

The extrema of transverse velocity are directly before and directly after the roller(s) train for all cases. This behavior is explained by the need for the area to be vacant for the roller train to pass (e.g.,

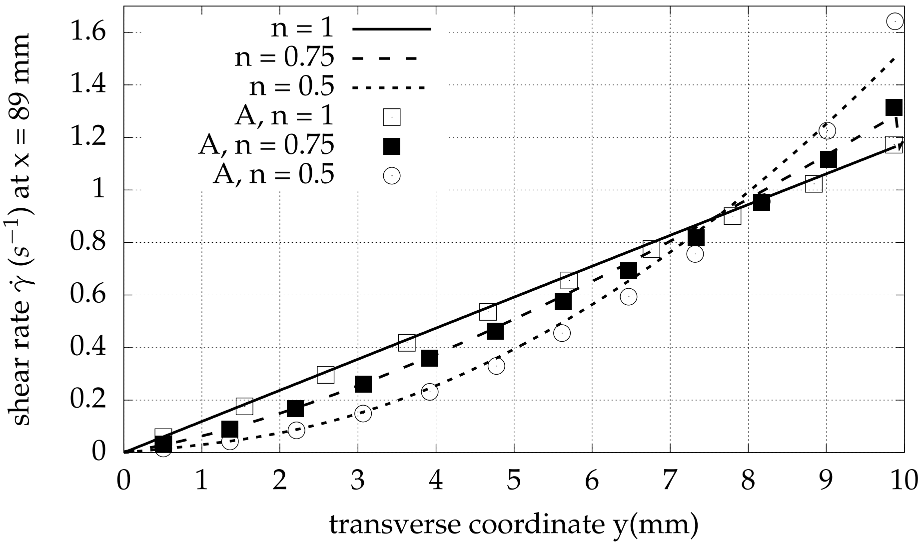

Figure 5.14: Shear rate profile at $x = 89$ mm for Newtonian and non-Newtonian fluids. The roller speed is $c = 5$ mm/s, the relative occlusion is $RO = 0.6$ and there is one roller. Comparison with results from [AH13] (A) is presented.

at $x = 114.5$ mm for two rollers) and for fluid to fill the empty space left from the departure of the roller (e.g., at $x = 65.5$ mm for two rollers).

In Figures 5.19 and 5.20, the horizontal and vertical velocity profiles, respectively, are given at the cross-sections of interest near the beginning and ending of the rollers, distributed under the rollers and at the incoming flow. The inlet longitudinal velocity profile shows higher values as the number of consecutive rollers increases. The same pattern is observed for the profiles around the middle of the length. Transverse velocity maxima are at approximately the same level, $v_{max} = 2$ mm/s, for one, two and three rollers. Under the roller center, the vertical velocity nearly vanishes, as is expected because of the symmetry of the geometry, as shown in Figure 5.20.

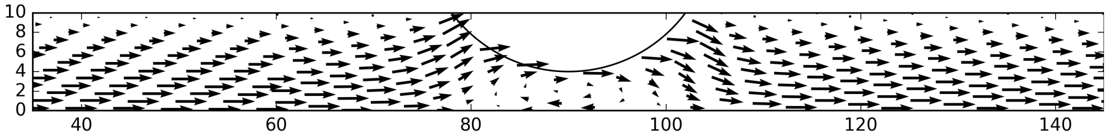

Figure 5.15: Velocity vectors for 1 roller, $c = 5$ mm/s, $L = 180$ mm, $RO = 0.6$ and $n = 1$.

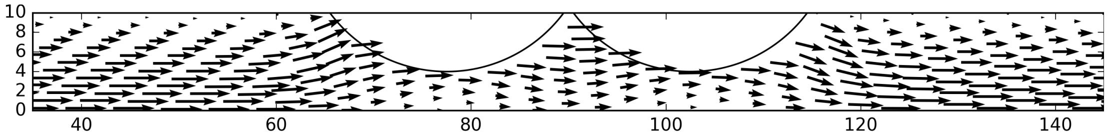

Figure 5.16: Velocity vectors for 2 rollers, $c = 5$ mm/s, $L = 180$ mm, $RO = 0.6$ and $n = 1$.

Pressure reaches its lower value right before the roller train and its higher value right downstream

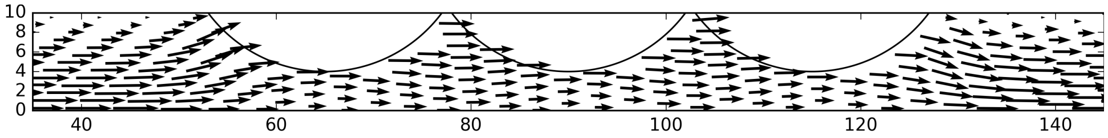

Figure 5.17: Velocity vectors for 3 rollers, $c = 5$ mm/s, $L = 180$ mm, $RO = 0.6$ and $n = 1$.

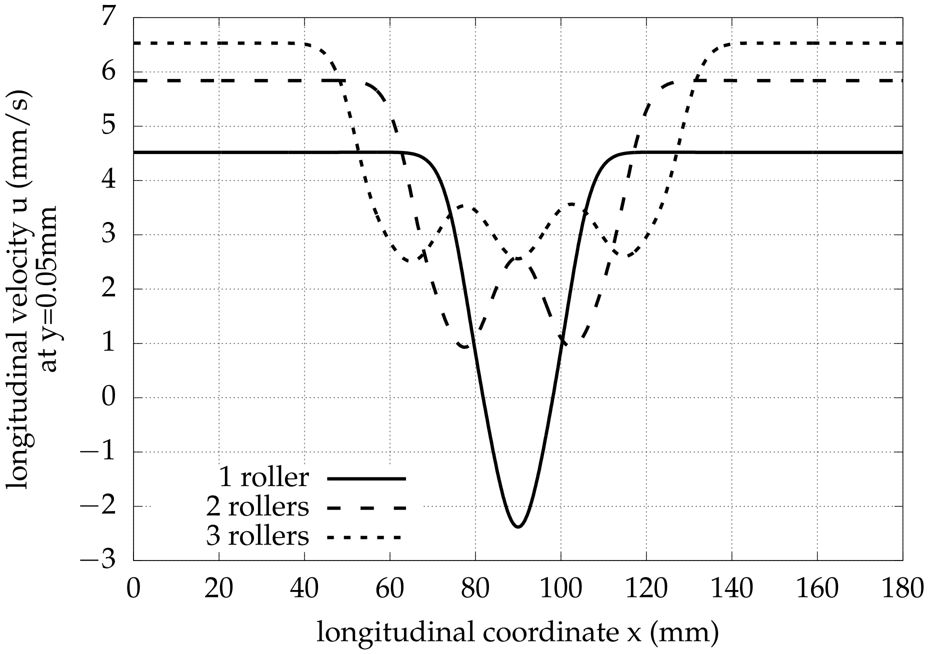

Figure 5.18: Longitudinal velocity near the central axis of the pump ($y = 0.05$ mm) for various numbers of rollers. The roller speed is $c = 5$ mm/s, the relative occlusion is $RO = 0.6$ and the Bird–Carreau power index is $n = 1$.

of it, as depicted in Figure 5.21. Moreover, the pressure function under the rollers is monotonous, with its maxima and minima having similar values, independent of the roller number. Maximum shear rate values near the axis of symmetry are considerably higher for one roller (0.98 s^{-1}) than for more than one (0.75 s^{-1} for two and 0.68 s^{-1} for three), as shown in Figure 5.22.

The shear rate profiles for a series of vertical sections are given in Figure 5.23.

Away from the rollers' positions (e.g., $x = 0$ for $n \in \{1, 2, 3\}$ or $x = 117$ for $n \in \{1\}$), the shear rate increases linearly as a function of the y-coordinate. Generally, the shear rate reaches its maximum value close to the wall, or close to the roller for streamwise positions, where a roller exists.

As tabulated in Table 5.2, transport efficiency increases sublinearly as the number of consecutive rollers rises.

5.3.5 Peristaltic Pump Characteristics

We simulated the flow of a parabolic inlet velocity profile (Equation (5.5)) through the pump geometry with one roller. Therefore, we determined the pressure rise induced by the presence of the roller

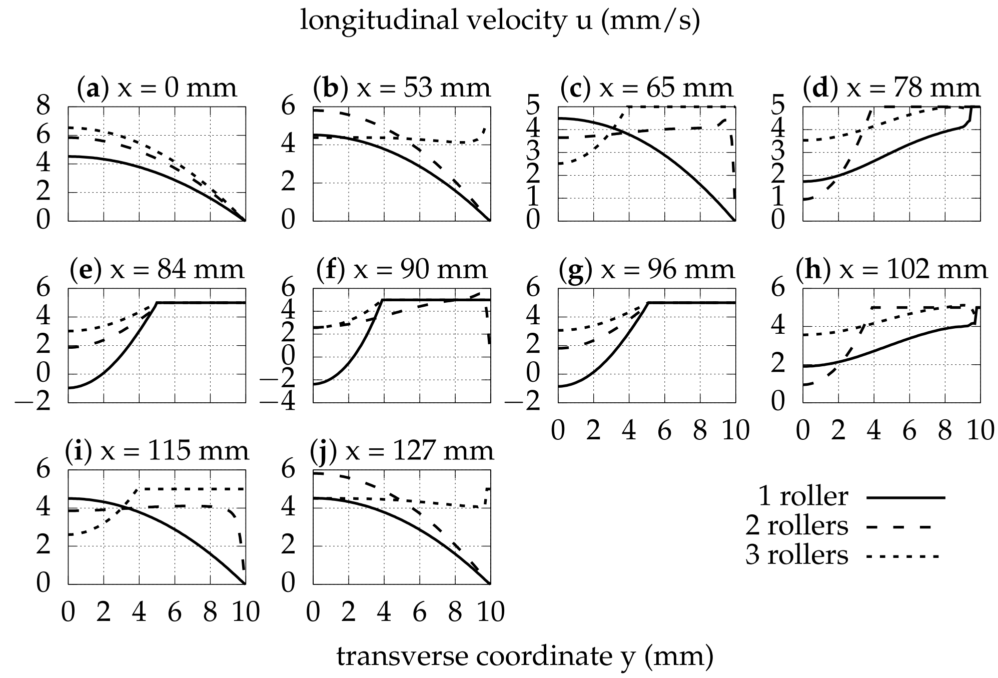

Figure 5.19: Axial velocity u profiles at successive longitudinal positions x (**a**–**j**) for various numbers of rollers, $c = 5$ mm/s, $RO = 0.6$ and $n = 1$.

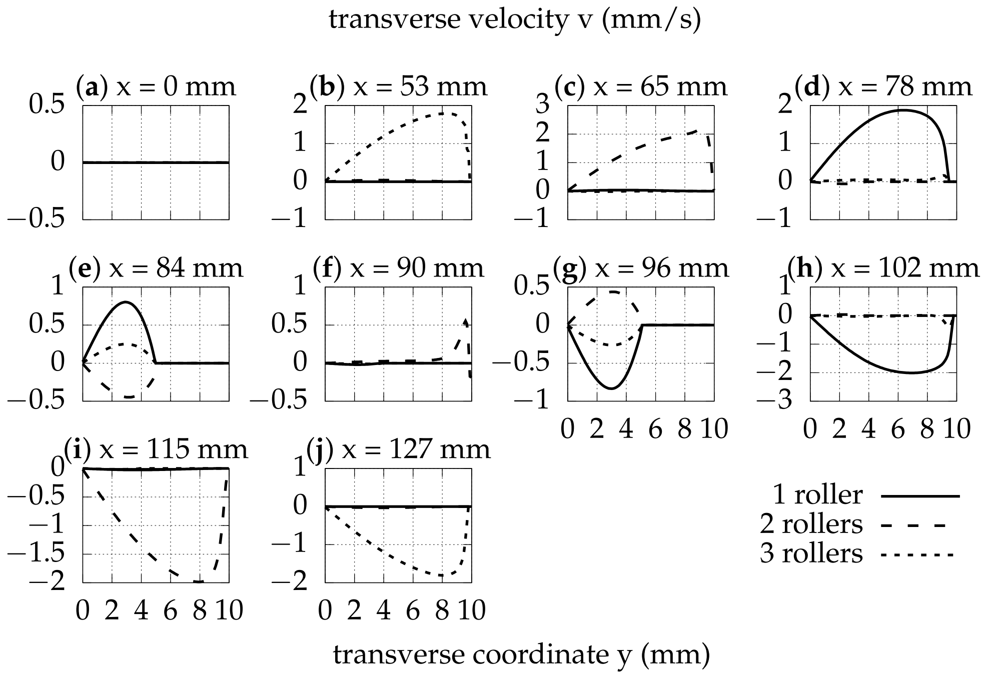

Figure 5.20: Vertical velocity v profiles at successive longitudinal positions x (**a**–**j**) for various numbers of rollers, $c = 5$ mm/s, $RO = 0.6$ and $n = 1$.

wave.

For a higher inlet flow volume rate, the pressure rise decreases, as Figure 5.24 demonstrates. The

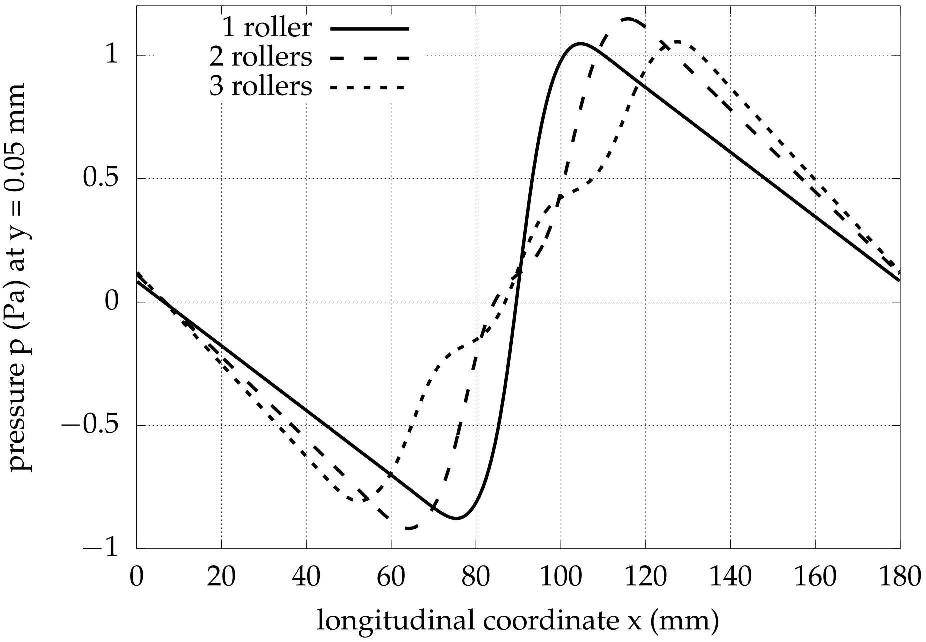

Figure 5.21: Pressure near the central axis of the pump ($y = 0.05$ mm) for various numbers of rollers, $c = 5$ mm/s, $RO = 0.6$ and $n = 1$.

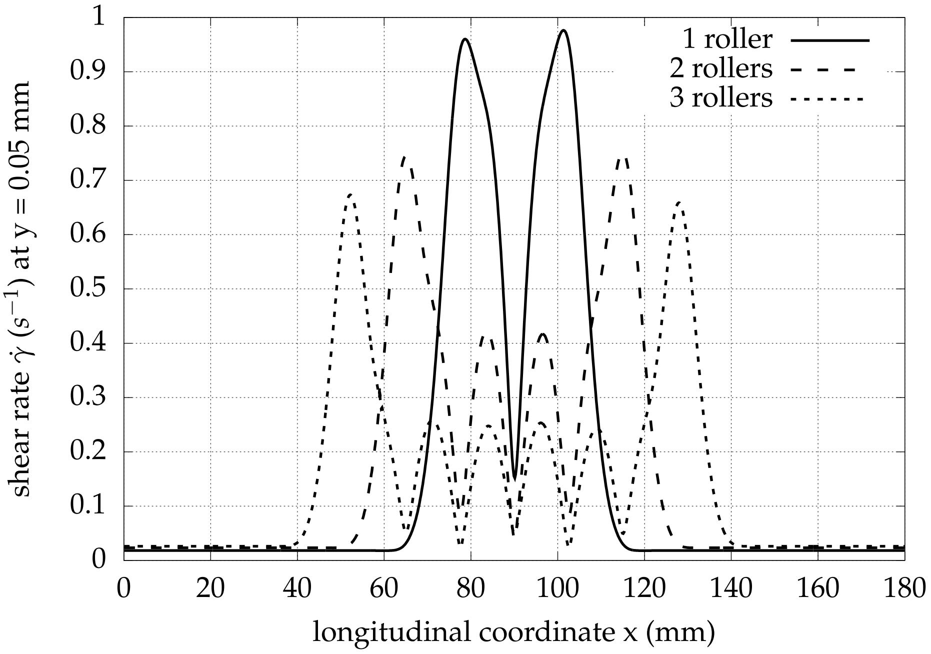

Figure 5.22: Shear rate near the central axis of the pump ($y = 0.05$ mm) for various numbers of rollers. The roller speed is $c = 5$ mm/s, the relative occlusion is $RO = 0.6$ and the Bird–Carreau power index is $n = 1$.

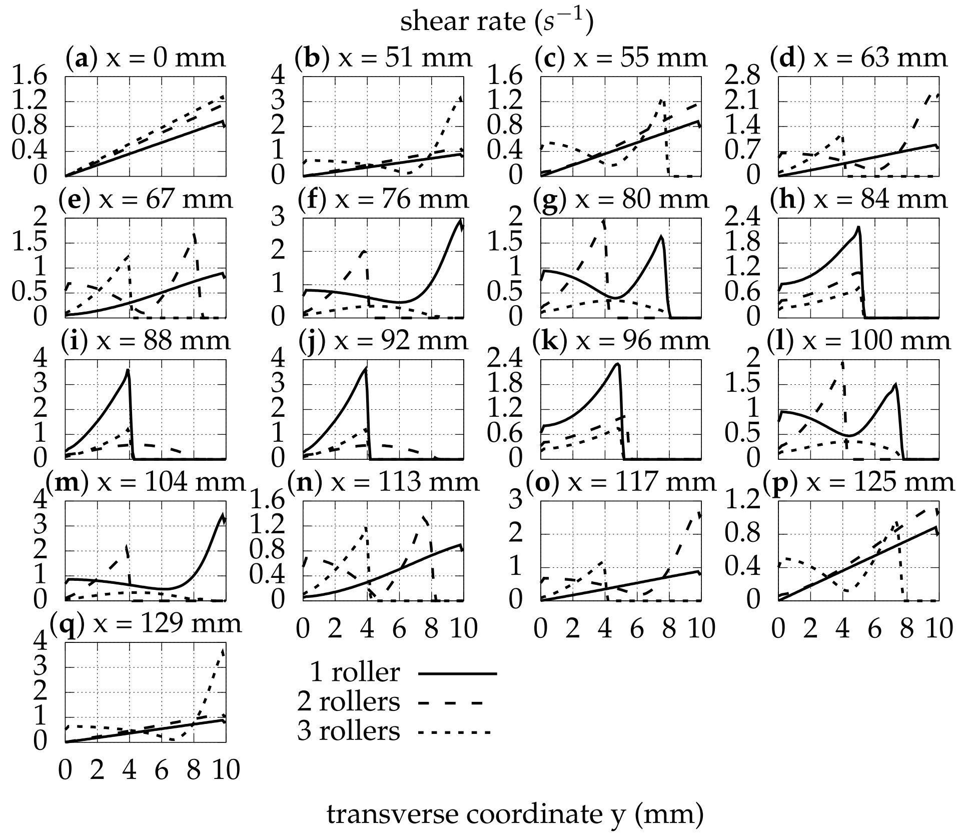

Figure 5.23: Shear rate profiles at successive longitudinal positions x (**a**–**q**) for various numbers of rollers. The roller speed is $c = 5$ mm/s, the relative occlusion is $RO = 0.6$ and the Bird–Carreau power index is $n = 1$.

Table 5.2: Transport efficiency for multiple consecutive rollers, pump length $L = 180$ mm, $c = 5$ mm/s, $RO = 0.6$ and $n = 1$.

Number of Rollers	**1**	**2**	**3**
TE (%)	60	78	87

pressure drop through the elastic channel beside the roller is reduced as the inlet fluid volume rate decreases. The pressure rise along the roller length increases dramatically as the inlet fluid volume rate decreases.

The characteristic line of the peristaltic pump is given in Figures 5.25 and 5.26 for the case of one roller, a pump with length $L = 90$ mm and roller speed $c = 5$ mm/s and for two different values of the roller gap and of the Bird–Carreau power index. The characteristics are approximately straight lines with negative slope. The inclinations of the characteristics are negatively correlated with the relative occlusion. The impact of the roller penetration on the flow becomes more noticeable when it is deeper, namely, when the half-gap is smaller. For a constant volume flux, the maximum pressure that develops on the flow is approximately six times higher for $RO = 0.8$ than for $RO =$

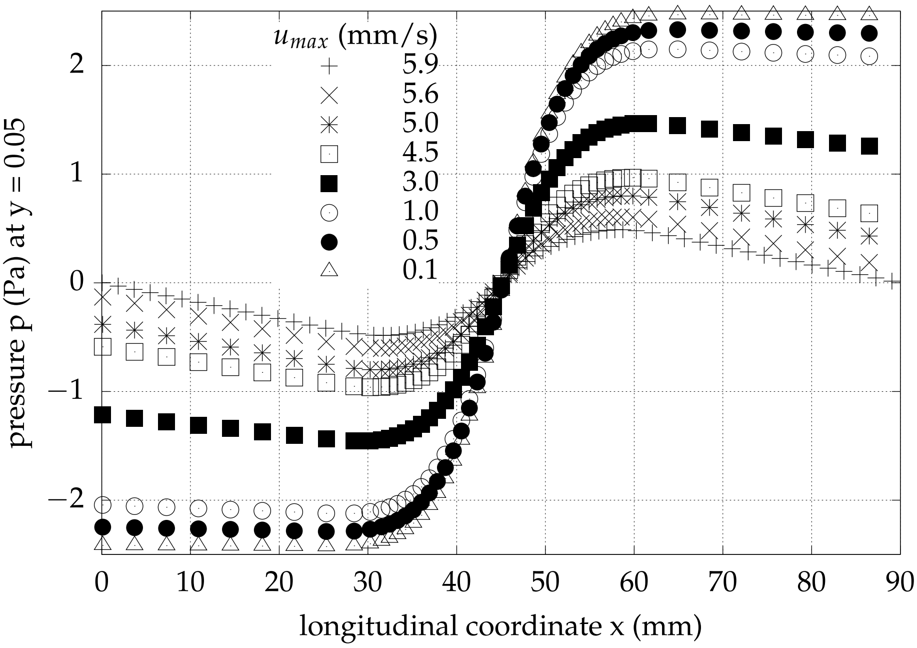

Figure 5.24: Longitudinal pressure distribution for the case of one pair roller pump, 90 mm long, $c = 5$ mm/s, $RO = 0.6$, $n = 1$ and parabolic flow inlet profile, with various values for maximum velocity of the profile.

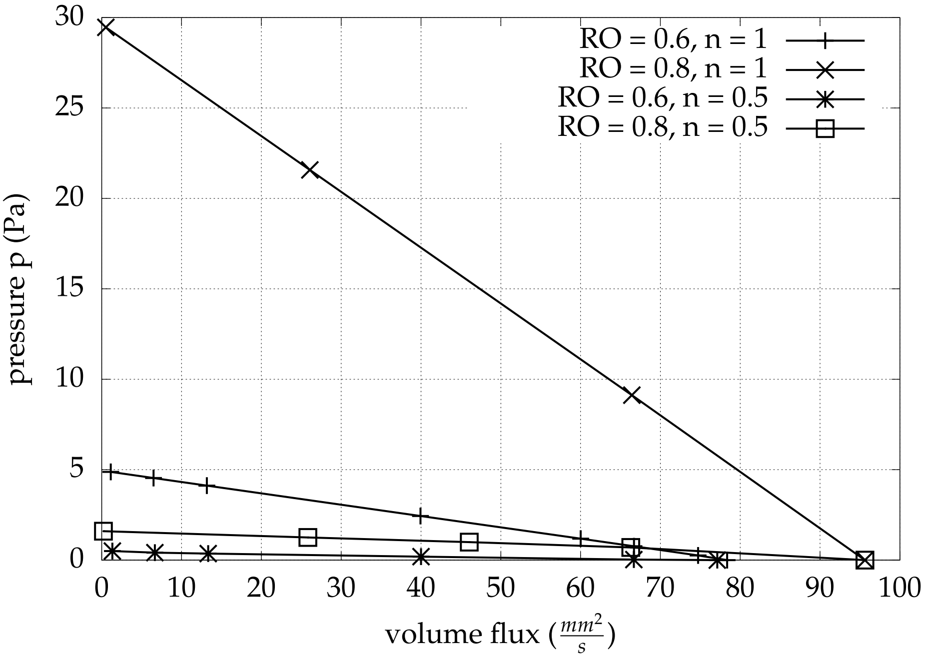

Figure 5.25: Peristalsis characteristics using linear scale for the pressure, for roller pumps 90 mm long with one roller moving at $c = 5$ mm/s.

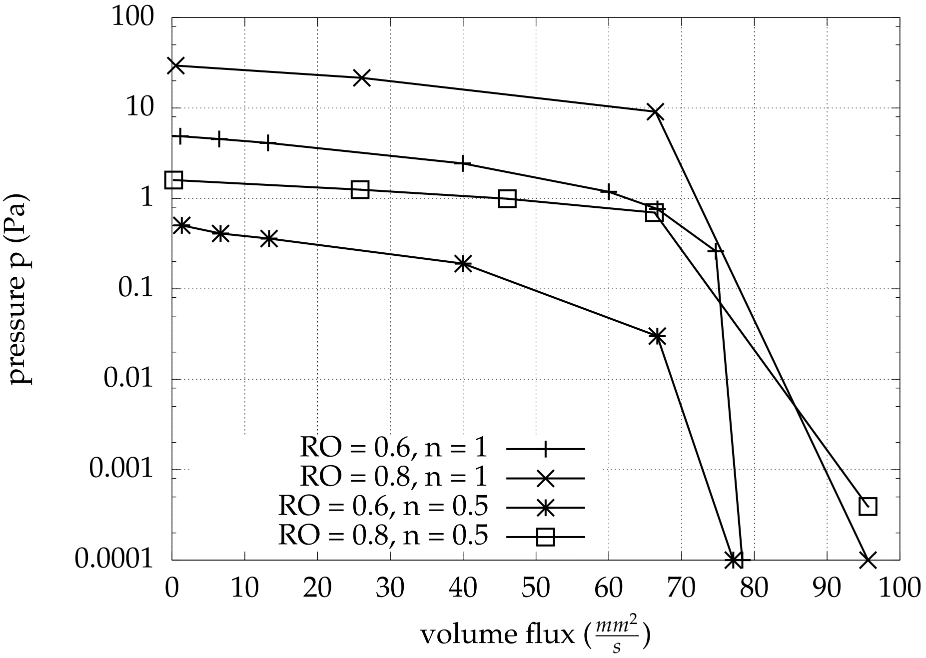

Figure 5.26: Peristalsis characteristics using logarithmic scale for pressure, for roller pumps 90 mm long, with one roller moving at $c = 5$ mm/s.

0.6. Moreover, for a constant pressure, the relative occlusion and the flow volume rate potentially observed, are positively related.

Shear-thinning fluids also exhibit approximately straight-line characteristics with negative inclination. The pressure rise potential of non-Newtonian fluids with a Bird–Carreau power index $n = 0.5$ is over an order of magnitude lower than that of the Newtonian ones. Additionally, the fluid volume rate potential decreases for shear-thinning fluids. For a non-Newtonian index $n = 0.5$, the maximum fluid volume rate that can be pumped decreases by around one-fifth in comparison to that of the Newtonian fluids.

5.4 Summary

In the present work, we studied the peristaltic flow with circular rollers for straight roller pumps. Using various values for relative occlusion RO, roller speed c, Bird–Carreau shear-thinning behavior expressed by n, number of rollers and length of the deformable tube L, simulations with the curvilinear immersed boundary method were performed.

Some of our results were compared with computational results [AH13] obtained with the OpenFOAM body-fitted algorithm [Che+14]. The validation of the curvilinear immersed boundary method for non - Newtonian fluids has a satisfying outcome, as good agreement is observed with a similar depiction of the trends of the flow versus the parameters.

Relative occlusion and the number of consecutive rollers are found to be strongly positively correlated with the transport efficiency. The Bird–Carreau shear-thinning exponent has a very slight effect, and roller speed is independent of transport efficiency. For a greater length of the deformable tube, transport efficiency decreases. Below the critical value for the relative occlusion or for the number of rollers or above a threshold for the length of the pump, backflow appears under the roller and near the longitudinal centerline. Increasing the number of identical consecutive rollers causes a lower upper bound for the shear rate, close to the longitudinal centerline, thus suggesting that multi-roller pumps are more appropriate for the extracorporeal circulation of biological, cell-containing fluids such as blood.

Peristaltic characteristics were computed for combinations of values of the input parameters. Pumping capability decreases linearly as the flow volume rate of the pumped fluid increases. The pressure rise strongly depends on relative occlusion. For shear-thinning fluids, the inclination of the characteristic rises drastically, meaning that the pumping potential decreases significantly. As an example, for a fluid with a power index $n = 0.5$, the pressure potential at the pump outflow decreases by an order of magnitude compared to that of a Newtonian fluid. The maximum volumetric flow rate that can be pumped also decreases for shear-thinning fluids.

Chapter 6

Pulsatile flow with balloon pumping

Synopsis

Balloon pumps are employed to assist cardiac function in cases of acute myocardial infarction, ventricular arrhythmias, cardiogenic shock, unstable angina, refractory ventricular failure or cardiac surgery. Counterpulsation through increasing the diastolic pressure and reducing the systolic pressure, increases coronary perfusion and assists the heart to pump more blood at each contraction. An extracting - contracting balloon modifying Poiseuille flow in a straight circular duct is examined in this study. The balloon is spheroid shaped with length of its minor axis, which is perpendicular to the flow direction, changing in time following a sinusoidal law. The inlet flow volume rate is steady while the rate, fluid volume leaves the duct, varies in time due to the presence of the balloon. For pulsation frequency 60 pulses/min, the pressure difference across the pulsating balloon exhibits significant phase lagging behind the outflow volume waveform. The outlet pressure depends on the balloon radius oscillation amplitude and is computed for a range of such. The flow field around the spheroid, periodically expanding - contracting balloon in the steady flow stream is presented.

6.1 Introduction

Blood flow in large arteries is laminar pulsatile, namely a superposition of Poiseuille flow with oscillating flows, described by a Fourier series with fundamental frequency that of the cardiac rhythm [McD55]. Womersley developed a method for calculating velocity, rate of flow, and viscous drag in arteries when the pressure gradient is known, which is commonly referred to as the ”Womersley problem” [Wom55].

The inverse Womersley problem, namely the determination of the time varying flow field given the evolution in time of flow rate through a circular pipe, is addressed by Tsangaris and Stergiopulos [TS88]. An equation expressing the developed flow velocity profile as a function of the time derivative of the flow rate is derived and integrated using finite differences. First order approximation is used for time derivatives and second order central scheme for the spatial derivatives.

The intra-aortic balloon pump (IABP) setting is used to contribute to the heart driven pulsatile flow. Treatment with intra-aortic balloon pump (IABP) is found to have positive impact if received by patients facing situations as unstable angina, acute myocardial infarction, ventricular arrhythmias, acute ischaemic mitral regurgitation, post infarct ventricular septal rupture and percutaneous coronary intervention (PCI) [Par+16]. Using an in vitro bench, the increase of cardiac output under IABP treatment is examined by Xie et al. [Xie+21]. The placement of an aortic stent at the upstream end of the balloon gives augmented product of heart rate and stroke volume.

Introduced by Moulopoulos et al, the IABP increases the diastolic blood flow in the arteries and lowers the end-diastolic arterial pressure, thus resulting in amelioration of coronary blood circulation and decreased myocardial work without taking blood out of the body [MTK62].

IABP therapy is found to exhibit very low hemolysis rate, implantation time, risk of limb ischaemia, anticoagulation and postimplantation complexity, compared to other cardial assistance devices. The surplus of left ventricle output created by the IABP is fairly low for patients with severe cardiogenic shock (CS) and the use of this kind of mechanical circulatory support assumes the absence of critical arrhythmia [OH12].

In vitro experiments and clinical study of the role of arterial stiffness in IABP therapy are presented by [Pap+02; Pap+04]. They find that augmentation of the arterial stiffness leads to the reduction of systolic and the end-diastolic aortic pressure. Arterial stiffness is found to be more important than arterial pressure for the effectiveness of IABP and is a potential additional parameter for deciding the use of IABP. Applanation tonometry is proposed for compliance measurements and stiffness gain via pharmacological interventions.

The IABP-SHOCK II trial concluded that the use of IABP had no positive effect on mortality within 30 days comparing to conventional treatment in patients suffering from cardiogenic shock following a myocardial infarction [Thi+12]. Such patients, who receive primary PCI in combination with IABP therapy, are found to exhibit lower mortality rate and better in-hospital outcome [AW+10].

The outcome of IABP-SHOCK II trial is reexamined by Mandawat and Rao [MR17]. They highlight that a larger number of patients should be included to detect the effects of IABP therapy. It is asserted that a sample where severe CS is more represented should be chosen for the effect of IABP in case of heart failure to be investigated. IABP treatment reduces death rate in conjunction with thrombolytic therapy and increases it when applied in patients undergoing primary PCI [Rom+13]. In case of severe cardiogenic shock, IABP is a candidate bridge to more adequate therapies.

The use of IABP soon after cardiogenic shock occurs, is suggested as reasonable in patients mostly in hospitals, where more suitable mechanical coronary support devices are not available [Ros+21].

A rigid duct model for the thoracic aorta with cylindrical shaped IABP is examined by Bruti [Bru15]. Pressure boundary conditions are imposed at both ends of the vessel, which are obtained by a zero dimensional model of the arterial system.

Computation of the flow field around the IABP during pulsed cardiopulmonary bypass (CPB) by Gramigna et al. [Gra+15a] showed increased perfusion during balloon inflation through the innominate, the left carotid and the left subclavian arteries. It also recorded transition from a rotational flow to an untwisted one in comparison with non-pulsatile CPB.

Different sizes and positions of the IABP are studied by Caruso et al. [CRF17]. They find that flow volume through renal, mesenteric and iliac arteries increases by decreasing the maximum balloon volume and the distance of the balloon from the left subclavian artery. The IABP therapy weaning process is calculated by Caruso et al [CGF19].

Using their zero-dimensional framework for the simulation of the cardiovascular system and mechanical circulatory and ventilation support [DL+22], De Lazzari et al. verify the measured flow patterns present in the case of hemodynamic flow with an IABP for various timing ratios [DL+20]. The blood flow through the aorta in presence of IABP or/and extracorporeal membrane oxygenation (ECMO), is studied by Gu et al. [Gu+19; Gu+22] using a finite element model.

In the present work, an expanding - contracting balloon, modulates the steady incoming flow of a circular cross-section pipe. The compliance of the containing vessel is considered negligible. The Womersley number of the flow refers to 60 pulses per minute and the Reynolds number gets value corresponding to mean blood flow through the human thoracic aorta during a cardiac cycle. The output pressure wave of the configuration is presented and the correlation with the balloon volume change rate is discussed. The presentation of the time evolving velocity and pressure fields around the prolate spheroid shaped, sinusoidally pulsating balloon is an additional contribution of this research, clarifying the flow details of balloon pumping in this setting.

6.2 Methodology

6.2.1 Vessel model

A schematic of the pump is shown in Figure 6.1. The containing the intra-aortic balloon pump vessel is modeled as a straight tube of circular cross-section. The radius of the artery is r_a and its length is l_a.

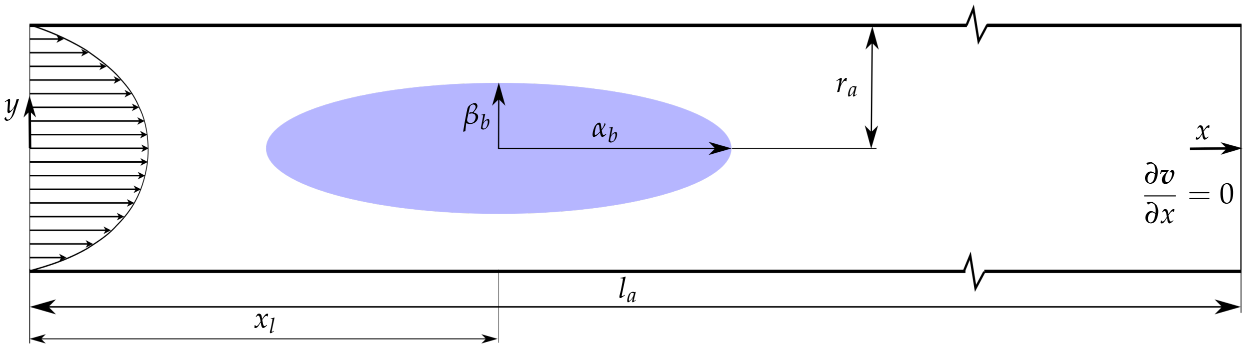

Figure 6.1: Schematic of the prolate spheroid balloon and the coaxial to it, surrounding pipe.

The balloon shape is that of a prolate ellipsoid of revolution. The spheroid major axis identifies with the artery axis of symmetry and its middle is at the longitudinal position x_l. The balloon surface in Cartesian coordinates follows the equation

$$\frac{(x-x_l)^2}{{\alpha_b}^2}+\frac{y^2}{{\beta_b}^2(t)}+\frac{z^2}{{\gamma_b}^2(t)}=1,\ \ |x-x_l|\leq a_b,\ \ \beta_b(t)<r_\alpha,\ \ \gamma_b(t)<r_\alpha \tag{6.1}$$

where $\alpha_b > \beta_b = \gamma_b$ are the corresponding semi axes. The major semi axis length is steady in time while the median and minor semi axes vary in time following a cosine law

$$\beta_b(t)=\gamma_b(t)=r_{b0}-A_b cos\left(\frac{2\pi}{T}t\right), \tag{6.2}$$

where T is the period of the oscillation.

Consequently, the balloon volume evolves in time as

$$V(t)=\frac{4}{3}\pi\cdot\alpha_b\cdot\beta_b(t)\cdot\gamma_b(t)=\frac{4}{3}\pi\cdot\alpha_b\cdot\left(r_{b0}-A_b cos\left(\frac{2\pi}{T}t\right)\right)^2. \tag{6.3}$$

Hence, the fluid volume through the outlet i.e. the pulsating flow volume rate is

$$Q_{out}(t)=Q_{in}(t)+\frac{dV(t)}{dt}=Q_{in}(t)+\frac{8}{3}\cdot\alpha_b\cdot\frac{A_b\pi^2}{T}\left(2\cdot r_{b0}\cdot sin\left(\frac{2\pi}{T}t\right)-A_b\cdot sin\left(\frac{4\pi}{T}t\right)\right). \tag{6.4}$$

The geometric values of the pump are presented in Table 6.1. The vessel radius is taken as the mean value of the aorta radius at the correspondence of the aortic arch and of renal arteries, respectively, of the work of Caruso et al. [CRF17].

Table 6.1: Values of the geometric quantities of the simulation.

Quantity	**value (cm)**
r_a	0.925
l_a	18 (for $Q_{in}=0.01L/s$), 40 (for $Q_{in}>0.01L/s$)
α_b	3
r_{b0}	0.32, 0.36, 0.44
A_b	0.02, 0.06, 0.14
x_l	7

The inlet and outlet flow volume rate curves are depicted in Figure 6.2.

The fluid properties for the simulation are as in Table 6.2.

Table 6.2: Values of the fluid properties in the CGS system of units.

Quantity	**value**
dynamic viscosity μ	0.04 $g/(cm\cdot s)$
density ρ	1.06 g/cm^3

For period $T=1s$, the nondimensional frequency parameter (Womersley number) of the pulsat-

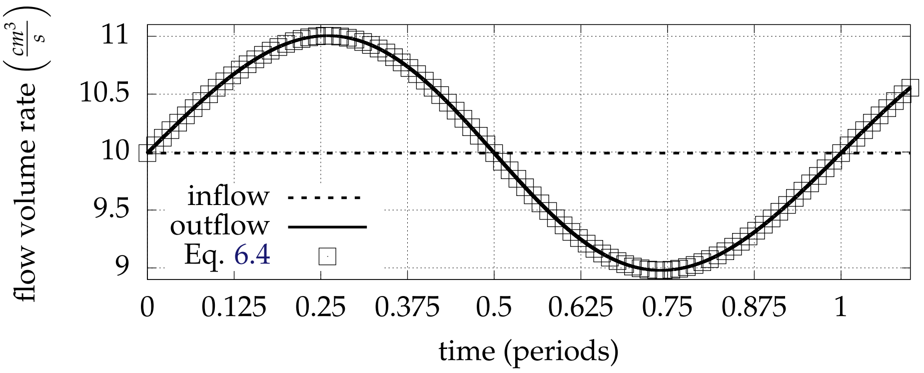

Figure 6.2: Inlet and outlet flow volume rate of the balloon pump for $Q_{in} = 0.01$ L/s, $r_{b0} = 0.32$ cm and $A_b = 0.02$ cm.

ing flow is

$$\alpha = r_{\alpha}\sqrt{\frac{\omega}{\nu}} = 11.936, \tag{6.5}$$

where $\omega = \dfrac{2\pi}{T}$ is the angular frequency of the balloon oscillation.

6.2.2 Boundary conditions

By employing cylindrical coordinates (x, r, θ) for the axial, the radial and the tangent direction respectively, the velocity is expressed as (u, U_r, U_θ), where U_r is the radial velocity component and U_θ is the peripheral velocity component.

On the inner boundary, namely on the surface of the balloon, fixed boundary conditions are imposed

$$\begin{gathered}
u\left(x, r, \theta, t \,\middle|\, \frac{(x-x_l)^2}{{\alpha_b}^2} + \frac{r^2}{{\beta_b}^2(t)} = 1\,,\ \ |x - x_l| \leq a_b\right) = 0 \\
U_r\left(x, r, \theta, t \,\middle|\, \frac{(x-x_l)^2}{{\alpha_b}^2} + \frac{r^2}{{\beta_b}^2(t)} = 1\,,\ \ |x - x_l| \leq a_b\right) = \frac{\partial r(x,t)}{\partial t} = \sqrt{a_b^2 - (x-x_l)^2} \cdot \frac{2\pi A_b}{\alpha_b T} sin\left(\frac{2\pi}{T}t\right) \\
U_\theta\left(x, r, \theta, t \,\middle|\, \frac{(x-x_l)^2}{{\alpha_b}^2} + \frac{r^2}{{\beta_b}^2(t)} = 1\,,\ \ |x - x_l| \leq a_b\right) = 0.
\end{gathered} \tag{6.6}$$

On the outer boundary of the computational domain, mixed boundary conditions are imposed. At the inlet, only the axial velocity is non-zero with a parabolic profile

$$\begin{gathered}
u(x = 0, r, \theta, t) = \frac{Q_{in}}{\pi {r_a}^2} 2\left(1 - \frac{y^2 + z^2}{{r_a}^2}\right) \\
U_r(x = 0, r, \theta, t) = 0 \\
U_\theta(x = 0, r, \theta, t) = 0.
\end{gathered} \tag{6.7}$$

At the vessel wall, no slip condition is set

$$\begin{aligned} u(x, r = r_a, \theta, t) &= 0 \\ U_r(x, r = r_a, \theta, t) &= 0 \\ U_\theta(x, r = r_a, \theta, t) &= 0. \end{aligned} \tag{6.8}$$

At the downstream end of the tube, zero longitudinal derivative of the velocity is demanded

$$\begin{aligned} \frac{\partial u}{\partial x}(x = l_\alpha, r, \theta, t) &= 0 \\ \frac{\partial U_r}{\partial x}(x = l_\alpha, r, \theta, t) &= 0 \\ \frac{\partial U_\theta}{\partial x}(x = l_\alpha, r, \theta, t) &= 0. \end{aligned} \tag{6.9}$$

Taking advantage of the symmetry of the geometry and the flow field and taking into consideration the structure of the solution algorithm, a quarter cylinder geometry is examined. Symmetry boundary conditions are imposed at the two longitudinal section planes i.e. steady meridional velocity with respect to the tangent direction and zero peripheral velocity

$$\begin{aligned} \frac{\partial u}{\partial \theta}(x, r, \theta = 0, t) &= \frac{\partial u}{\partial \theta}(x, r, \theta = \frac{\pi}{2}, t) = 0 \\ \frac{\partial U_r}{\partial \theta}(x, r, \theta = 0, t) &= \frac{\partial U_r}{\partial \theta}(x, r, \theta = \frac{\pi}{2}, t) = 0 \\ U_\theta(x, r, \theta = 0, t) &= U_\theta(x, r, \theta = \frac{\pi}{2}, t) = 0. \end{aligned} \tag{6.10}$$

6.2.3 Space and time domain discretization

Blood perfusion in large arteries can be considered Newtonian [FQV09] and with negligible compressibility [AB71] for the range of human hematocrit values, therefore, flow Equations (2.115) and (2.117) are solved on both curvilinear and Cartesian underlying mesh. In the first case the boundary conditions at the curved surface of the cylinder are set exactly while in the second, they are imposed by interpolating between the closest triangle of fluid nodes and the neighboring immersed boundary nodes as for the immersed bodies. To certify independence of the solution from the computational grid, meshes of increasing density are used. The concluding, finest curvilinear and Cartesian underlying grids utilized, are presented in Figure 6.3 and Figure 6.4 respectively, where the difference in the way the boundary conditions on the curved surface of the cylinder are assigned, is apparent.

The curvilinear consists of 80 × 80 nodes in a parallel plane to the cylinder vessel base, while the Cartesian consists of 97 × 97 nodes. Both the curvilinear and the Cartesian grids in the flow direction in the interval $3.6 \leq x \leq 10.6$ consist of cells with $\delta x = 0.02$ cm. In the region $0 \leq x \leq 3.6$, δx follows a geometric sequence starting from the value $\delta x = 0.08$ cm and concluding to $\delta x = 0.02$ cm. Finally, downstream of the balloon, within the region $10.6 \leq x \leq 18$, δx increases, following a geometric

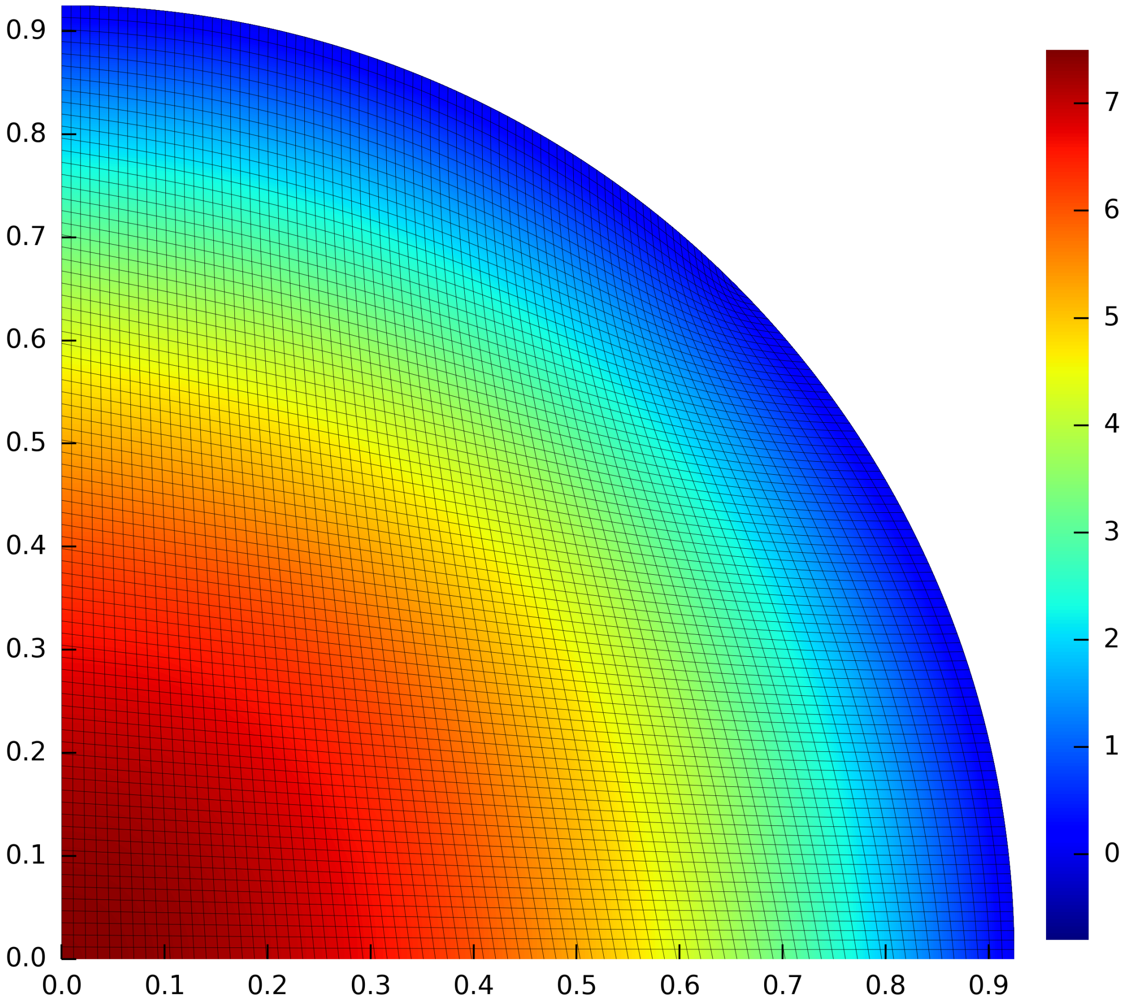

Figure 6.3: Inlet velocity contours of 3d pie-shaped wedge for $Q_{in} = 0.01$ L/s and the 80×80 curvilinear structured computational grid.

sequence with first term $\delta x = 0.02$ cm and last $\delta x = 0.12$ cm. The total number of nodes in the axial direction is 558. For a Cartesian mesh consisting of $66 \times 66 \times 410$ nodes in the transverse plane and the flow direction respectively, the maximum difference in outlet pressure comparing to the finest Cartesian mesh is 0.7 %. The respective difference in outflow velocity at the center of the pipe is 0.019 cm/s.

The pulsating balloon is triangulated by a 31206 nodes and 62408 elements grid and the aorta discretization consists of 72756 nodes and 145508 elements as shown in Figures 6.5, 6.6. Increased accuracy is required for the epsilon constant of Möller and Trumbore algorithm (Algorithm 2), used to decide whether the ray is parallel to the triangle for determining the relative position of a node and the immersed balloon ($\epsilon = 10^{-15}$).

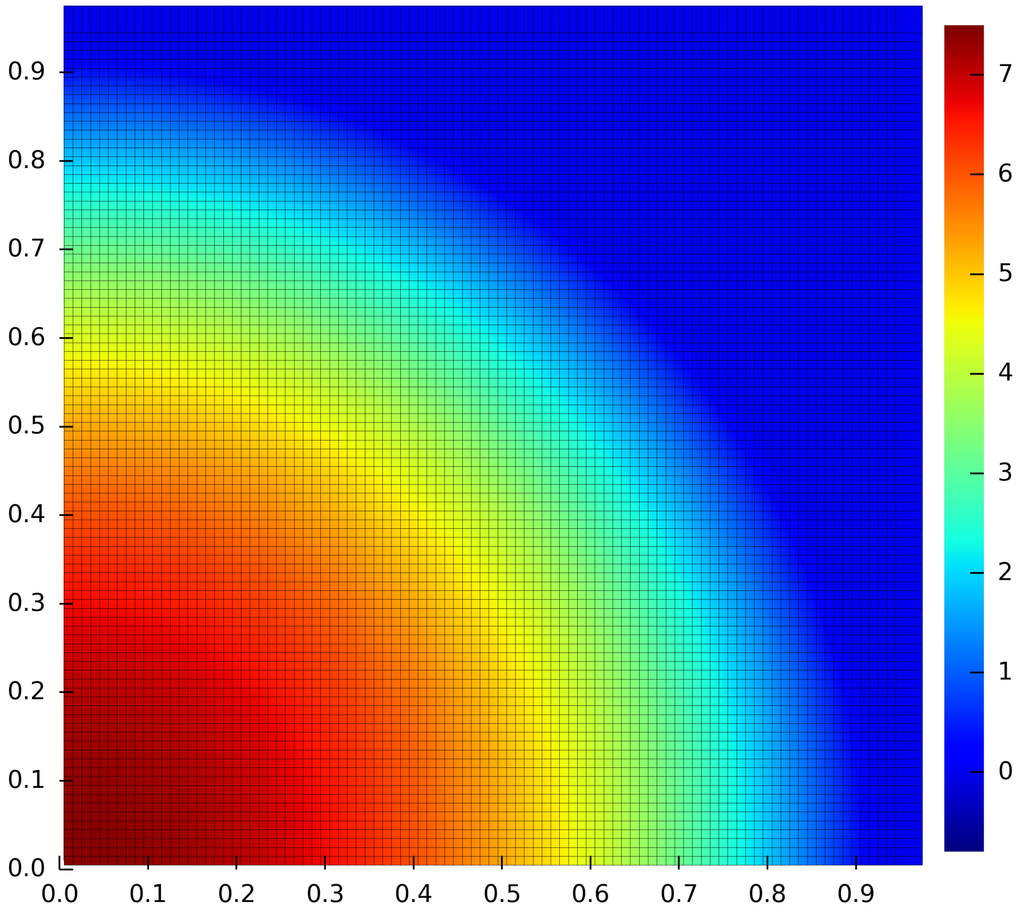

Figure 6.4: Inlet velocity contours of 3d pie-shaped wedge for $Q_{in} = 0.01$ L/s and the 97 × 97 Cartesian structured computational grid.

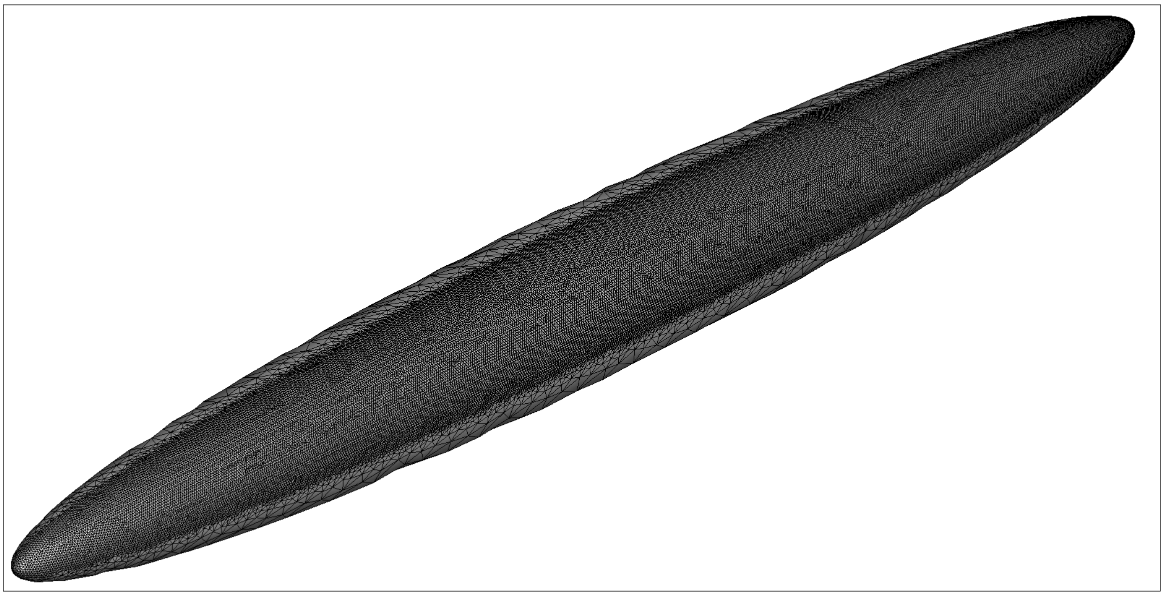

(a) Balloon dense quarter.

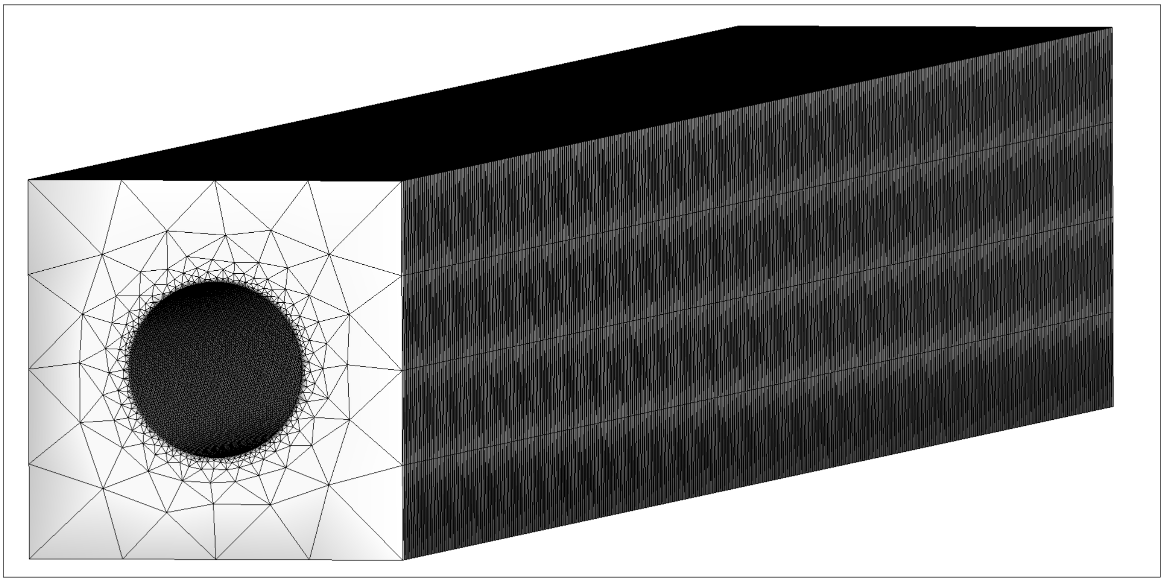

(b) Aorta surface mesh.

Figure 6.5: Surface grids of the prolate spheroid pulsating balloon and the artery.

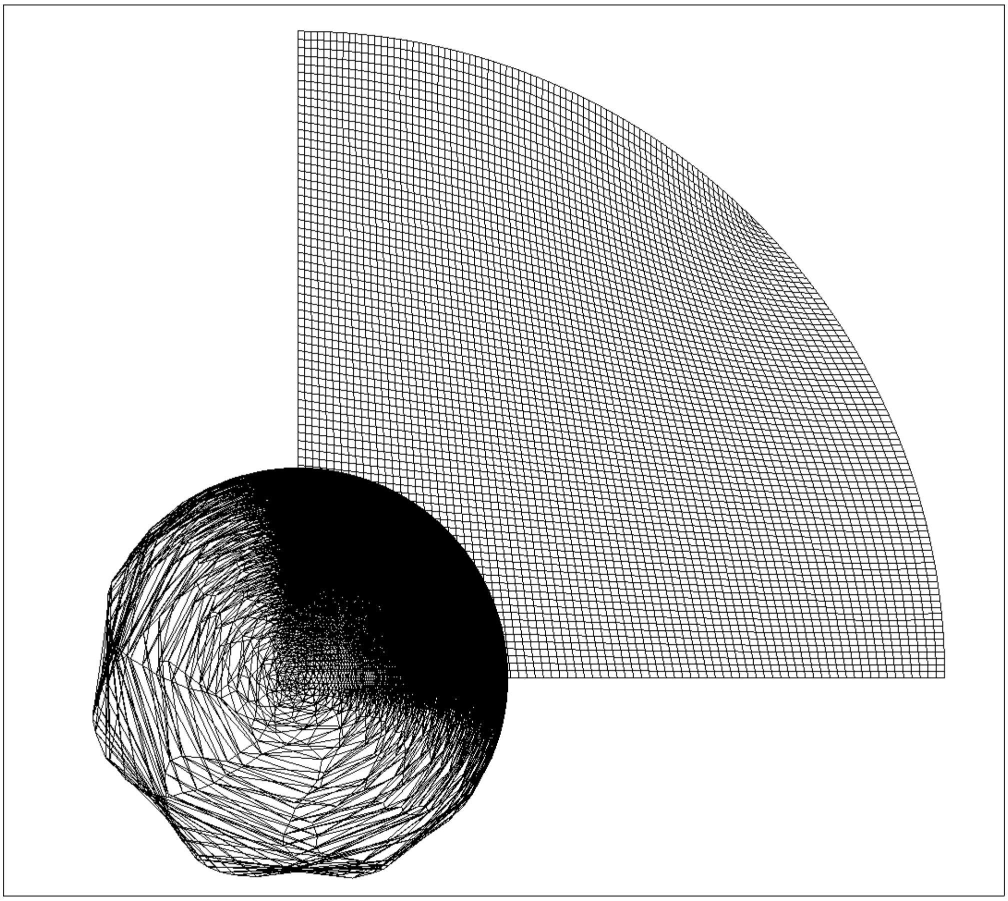

(a) Curvilinear immersion.

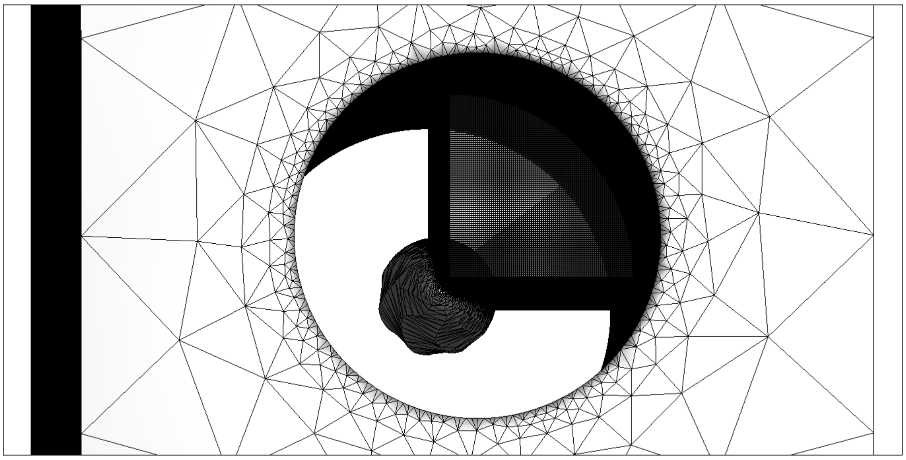

(b) Cartesian immersion.

Figure 6.6: Surface grids of prolate spheroid pulsating balloon and pipe, along with their integration in the computational domain.

Time integration is performed with steps of magnitude $\delta t = 0.00002$.

6.3 Results

The resulting velocity vectors on a plane defined by the cylinder main axis and a generator axis of the cylinder, are depicted in Figures 6.7 and 6.8.

The inlet parabolic profile at the pipe cross-section, transitions to a toroid profile around the pulsating balloon's lengthwise center, with a cross-section resembling that of the oscillating flow over the cross-section of an annular pipe [Tsa84]. Downstream of the balloon, the radial velocity component tends to restore the maximization of the longitudinal velocity profile on the pipe axis. The maximum, over the cross-section, vectors are of larger magnitude near the inlet and shorter at the balloon region, as expected by mass conservation.

Axial velocity contours are given in Figures 6.9 and 6.10. At the part of the period where the balloon volume change rate increases, the outflow volume rate increases. The maximizer of Equation (6.4) is

$$\arg\max_{t\in[0,T)} Q_{out}(t) = \frac{T}{2\pi} \arccos\left(\frac{\frac{r_{b0}}{A_b} - \sqrt{\frac{r_{b0}^2}{A_b^2} + 8}}{4} \right), \tag{6.11}$$

for which a dark red region emerges near the outflow. For the rest of the period, where the balloon volume change rate decreases, the outflow volume rate follows the same trend. For $t = 3T/4$ the longitudinal velocity near the outlet, is minimal. The low velocity region near the outer wall has smaller thickness in the region $4 \leq x \leq 10$, where the balloon is placed, due to the viscous effects in the duct between the wall and the moving surface of balloon.

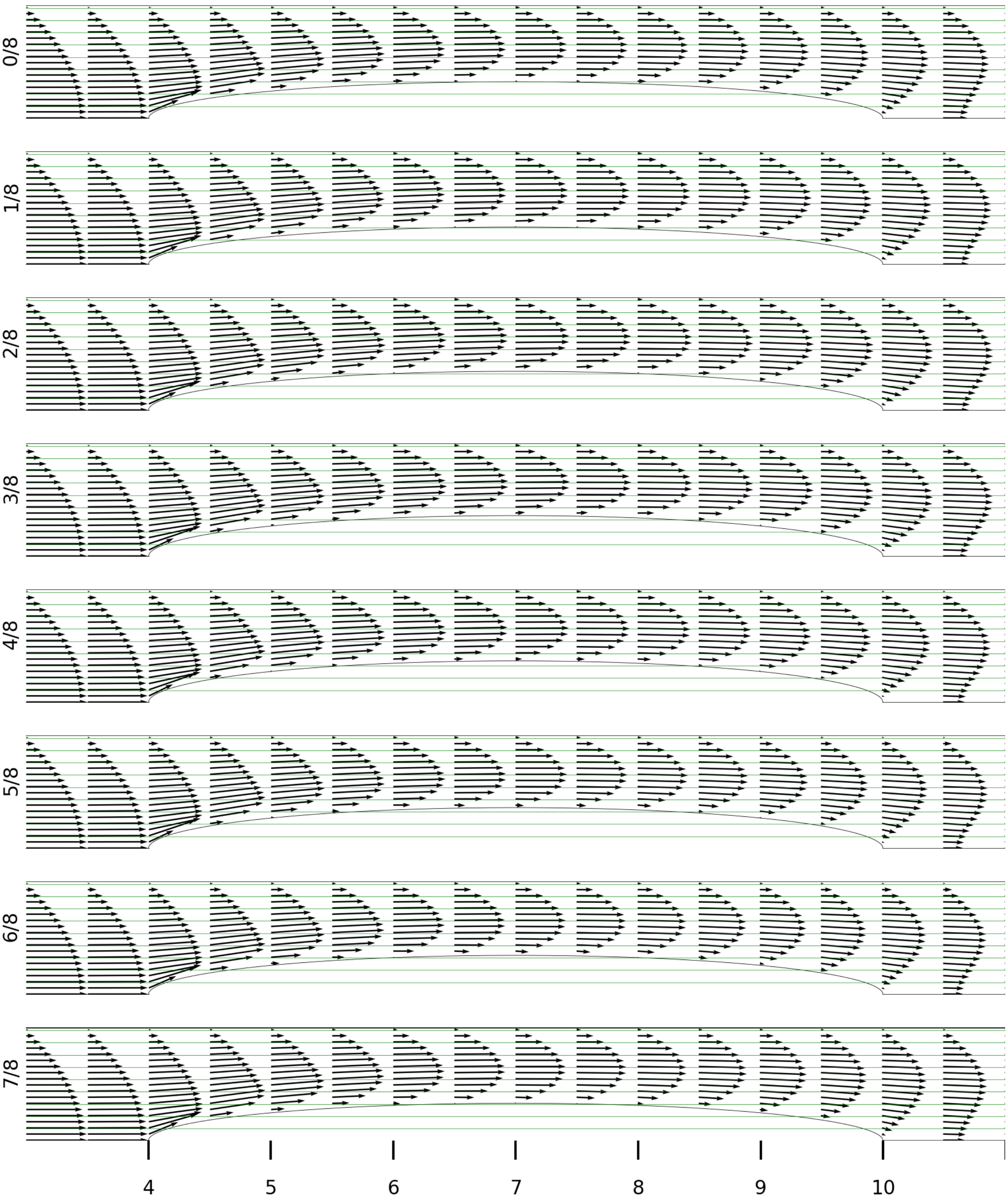

Figure 6.7: Velocity vectors on a meridional plane, for balloon pulsating according to Equation (6.2) with inlet velocity profile given by Equation (6.7), for 8 instances during the period (left side titles refer to the fraction of the period T). The inlet volume rate is $Q_{in} = 0.01$ L/s, $r_{b0} = 0.32$ cm and $A_b = 0.02$ cm.

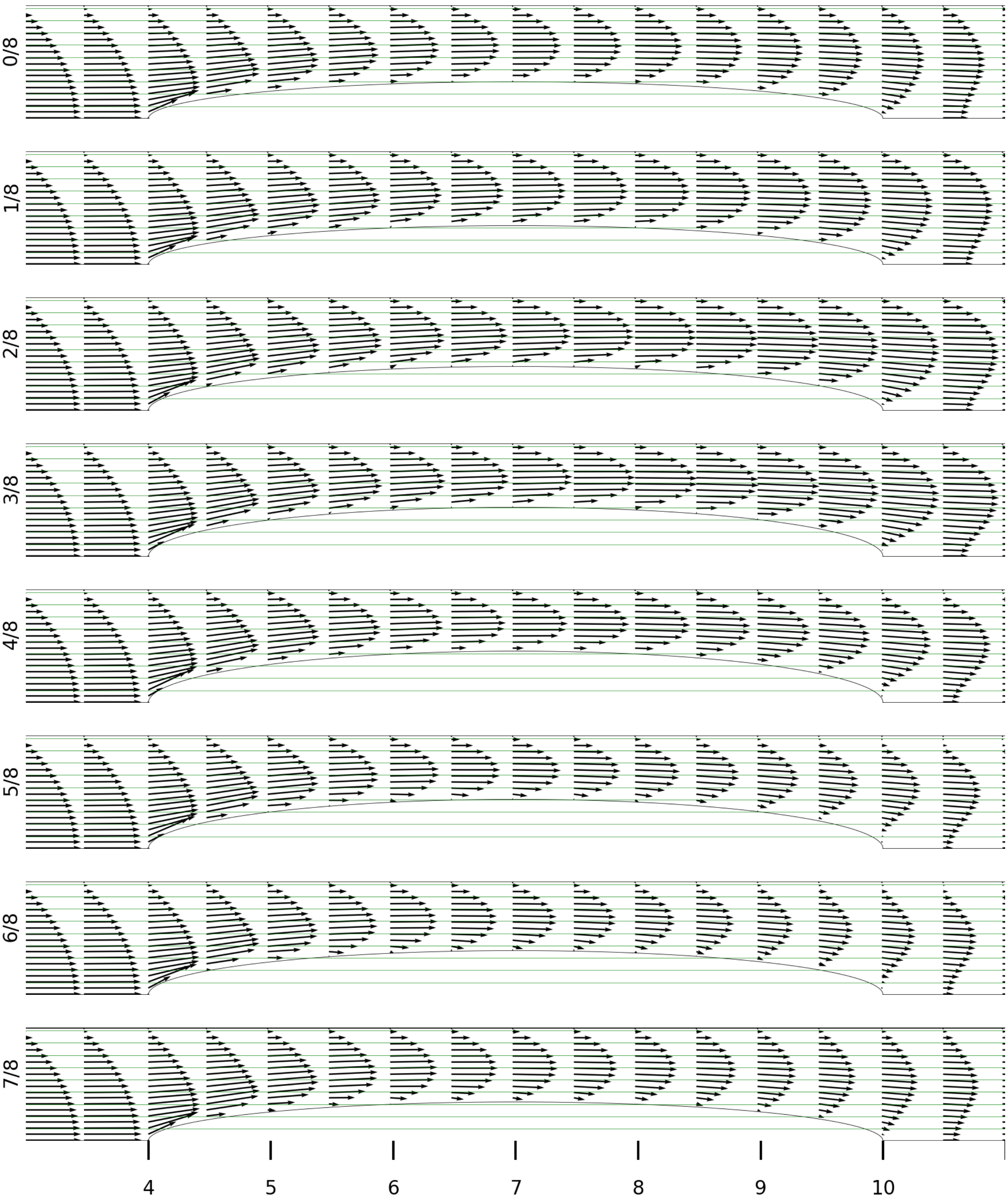

Figure 6.8: Velocity vectors on a meridional plane, for balloon pulsating according to Equation (6.2) with inlet velocity profile given by Equation (6.7), for 8 instances during the period (left side titles refer to the fraction of the period T). The inlet volume rate is $Q_{in} = 0.01$ L/s, $r_{b0} = 0.36$ cm and $A_b = 0.06$ cm.

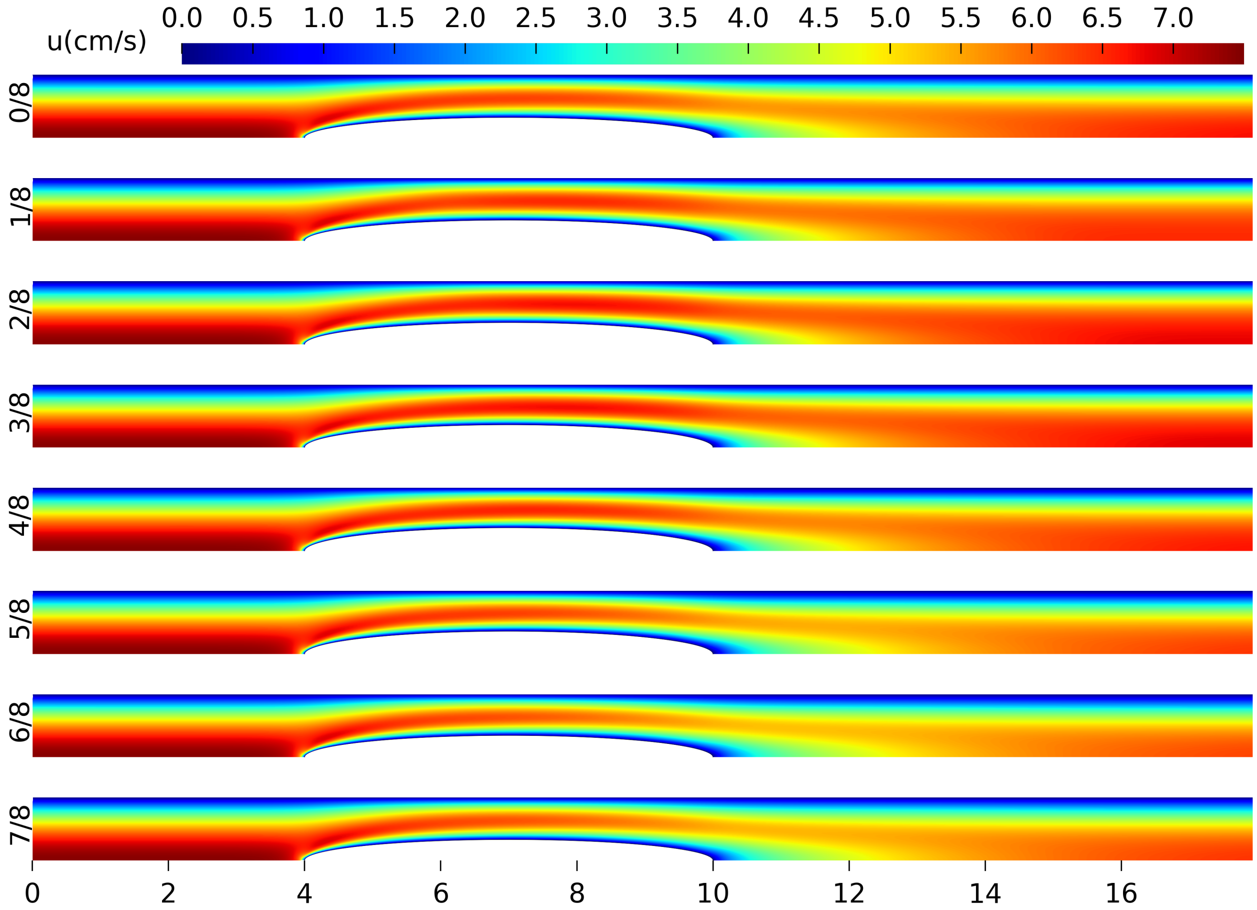

Figure 6.9: Axial velocity contours on a meridional plane, for balloon pulsating according to Equation (6.2), with inlet velocity profile given by Equation (6.7), for 8 instances during the period (left side titles refer to the fraction of the period T). The inlet volume rate is $Q_{in} = 0.01$ L/s, $r_{b0} = 0.32$ cm and $A_b = 0.02$ cm.

Radial velocity contours are given in Figures 6.11 and 6.12. At the position where the incoming fluid velocity profile attacks the balloon, a high radial velocity region is created, as the streamlines curve in order to adjust to the geometry. The length of the high radial velocity component region gets grosso modo higher values during inflation than during deflation.

Axial and radial velocity profiles for 8 instances in time and 24 axial positions are given in Figures 6.13-6.28. Downstream of the intersection of the three perpendicular ellipsoid planes of symmetry, negative radial velocity component values emerge. The radial velocity component has its maximum in space at the point where the input stream attacks the balloon and in time at $t = T/2$

$$\max_{x,t} U_r(x, 0, \theta, t) = 2.17\ cm/s.$$

The minimum in time, maximum value for the radial velocity emerges for $t = 6T/8$

$$\min_{t} \left(\max_{x} U_r(x, 0, \theta, t) \right) = 1.88\ cm/s.$$

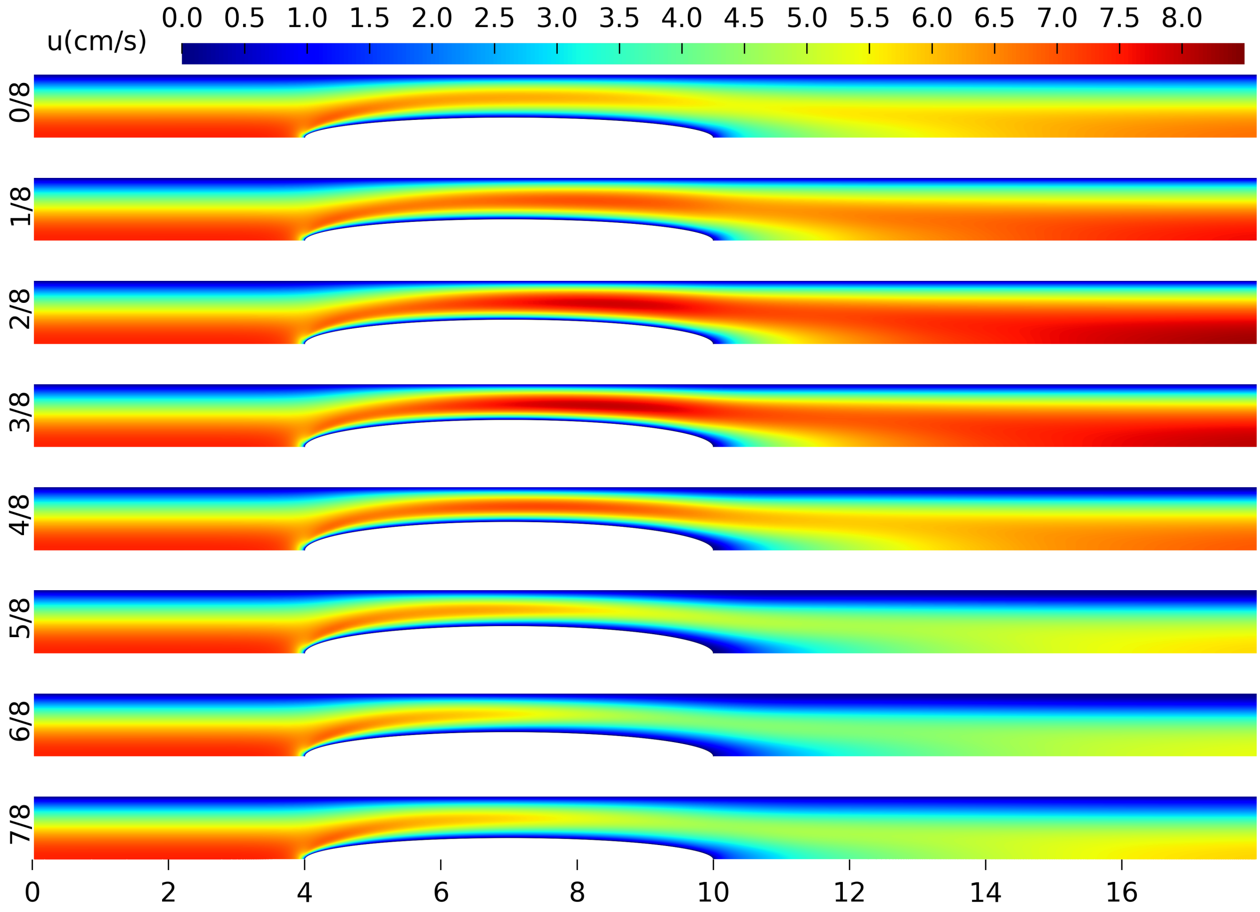

Figure 6.10: Axial velocity contours on a meridional plane, for balloon pulsating according to Equation (6.2), with inlet velocity profile given by Equation (6.7), for 8 instances during the period (left side titles refer to the fraction of the period T). The inlet volume rate is $Q_{in} = 0.01$ L/s, $r_{b0} = 0.36$ cm and $A_b = 0.06$ cm.

For $x = 15$ the maximum cross-section axial velocity is on the aorta axis.

The evolution of the outlet pressure, p_{out}, in time is given in Figure 6.29.

The mean value of the waveform of the outlet surplus pressure, with respect to the inlet, is -4.319 Pa for $Q_{in} = 0.01$ L/s, $r_{b0} = 0.32$ cm and $A_b = 0.02$ cm.

The phase shift between the maximization of the outlet flow volume rate and the pressure gradient is found to be almost independent of r_{b0} and A_b. For $Q_{in} = 0.01$ L/s, $r_{b0} = 0.32$ cm and $A_b = 0.02$ cm has the value

$$\delta\phi = 2\pi\left(\arg\max_{t\in[0,T)} p_{out}(t) - \arg\max_{t\in[0,T)} Q_{out}(t)\right) = \frac{109\pi}{100} - \arccos\left(4 - \frac{\sqrt{66}}{2}\right) = 0.57025\pi,$$

which is typical for large Womersley numbers [Zam00].

Pressure distribution contours are given in Figures 6.30 and 6.31. Output pressure rises for the late most part of balloon inflation phase and falls for the late most part of the balloon deflation phase.

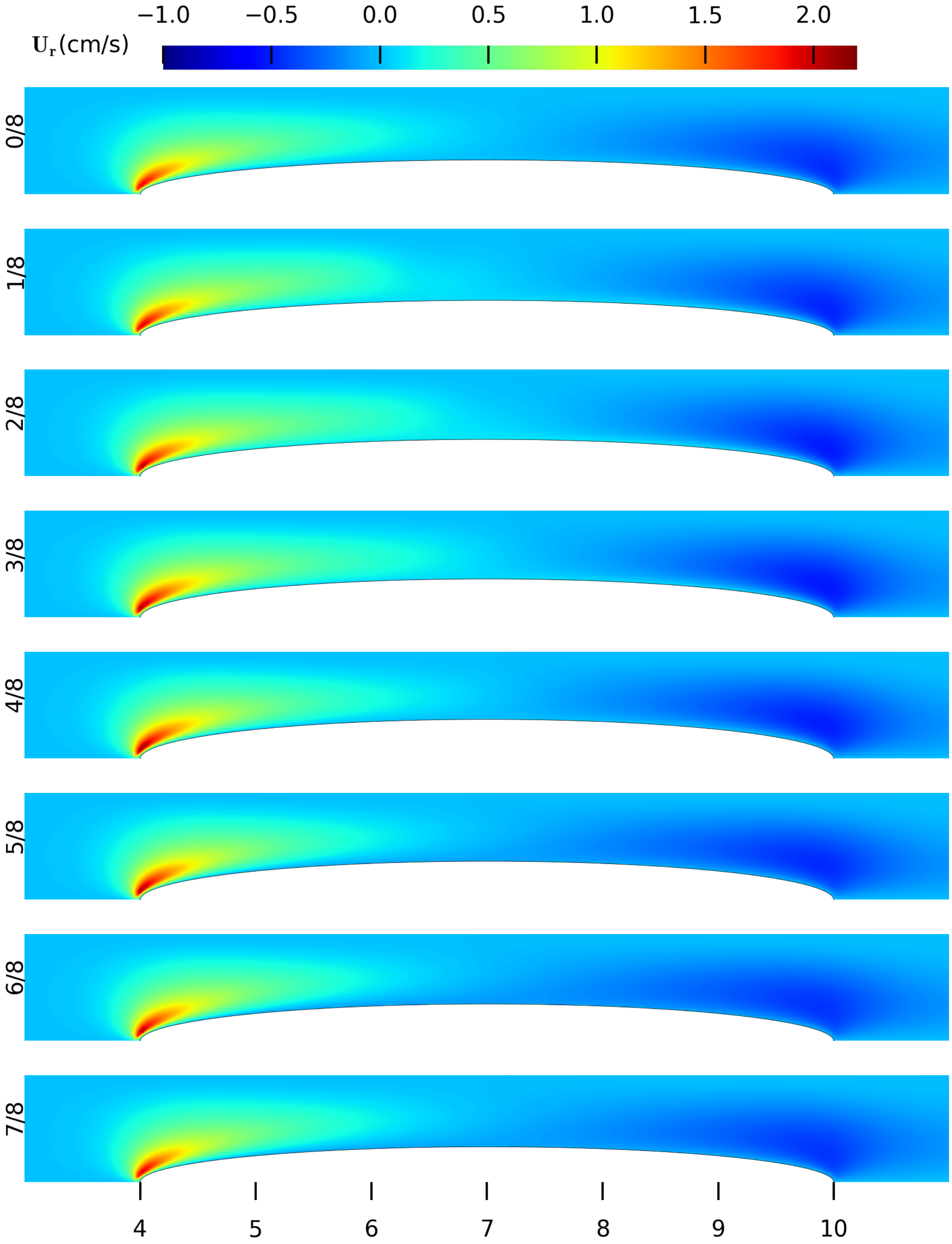

Figure 6.11: Radial velocity contours on a meridional plane, for balloon pulsating according to Equation (6.2), with inlet velocity profile given by Equation (6.7), for 8 instances during the period (left side titles refer to the fraction of the period T). The inlet volume rate is $Q_{in} = 0.01$ L/s, $r_{b0} = 0.32$ cm and $A_b = 0.02$ cm.

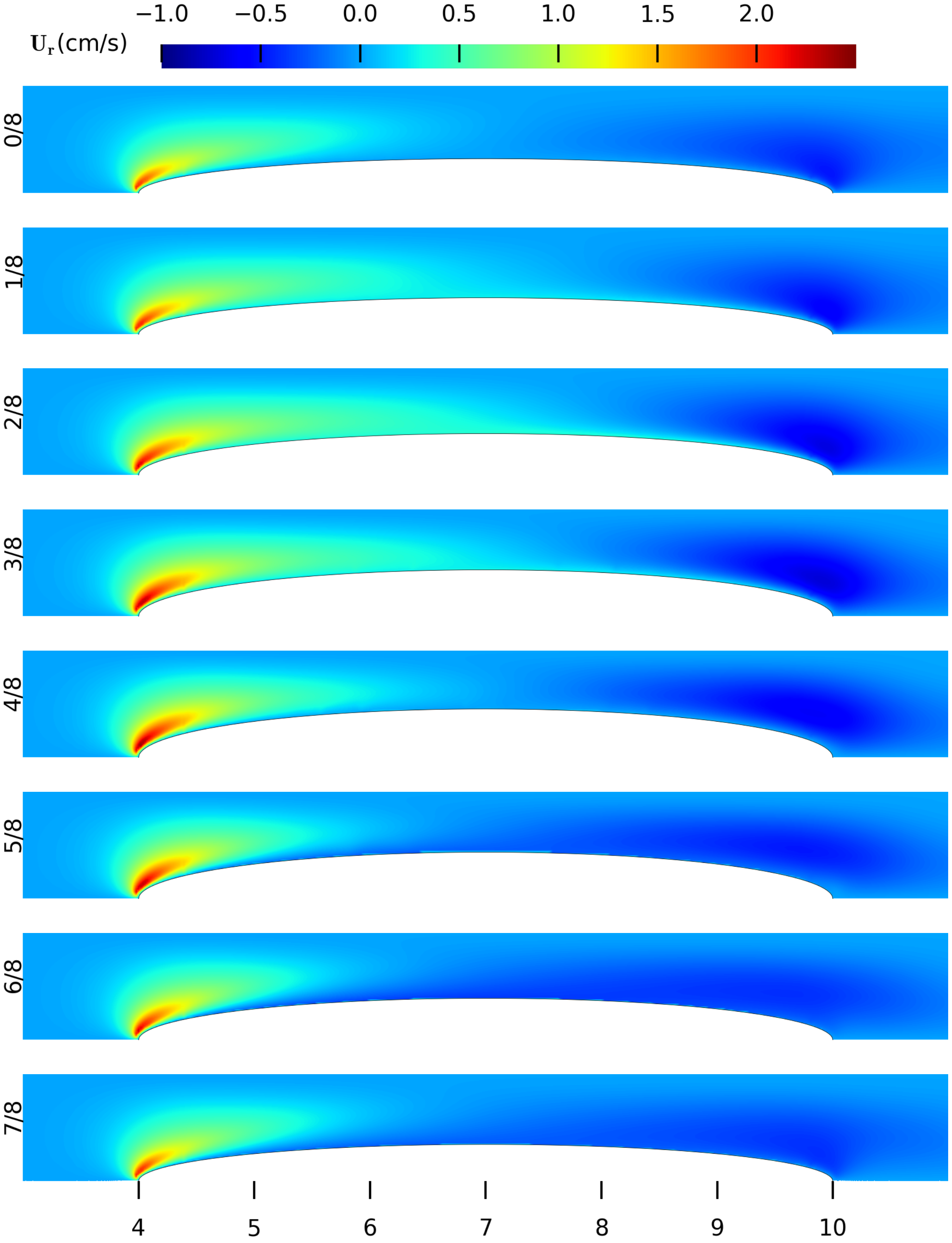

Figure 6.12: Radial velocity contours on a meridional plane, for balloon pulsating according to Equation (6.2), with inlet velocity profile given by Equation (6.7), for 8 instances during the period (left side titles refer to the fraction of the period T). The inlet volume rate is $Q_{in} = 0.01$ L/s, $r_{b0} = 0.36$ cm and $A_b = 0.06$ cm.

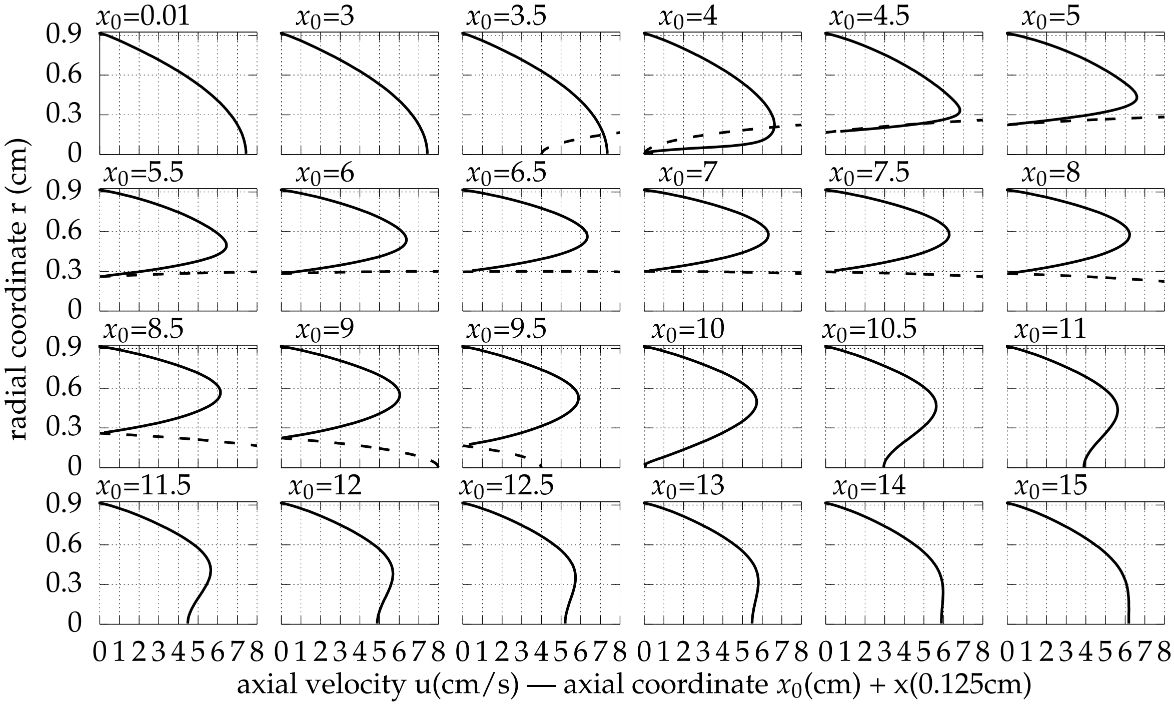

Figure 6.13: Axial velocity profiles for $t = 0T/8$ (continuous line), for $Q_{in} = 0.01$ L/s, $r_{b0} = 0.32$ cm and $A_b = 0.02$ cm. The dashed line indicates the balloon profile.

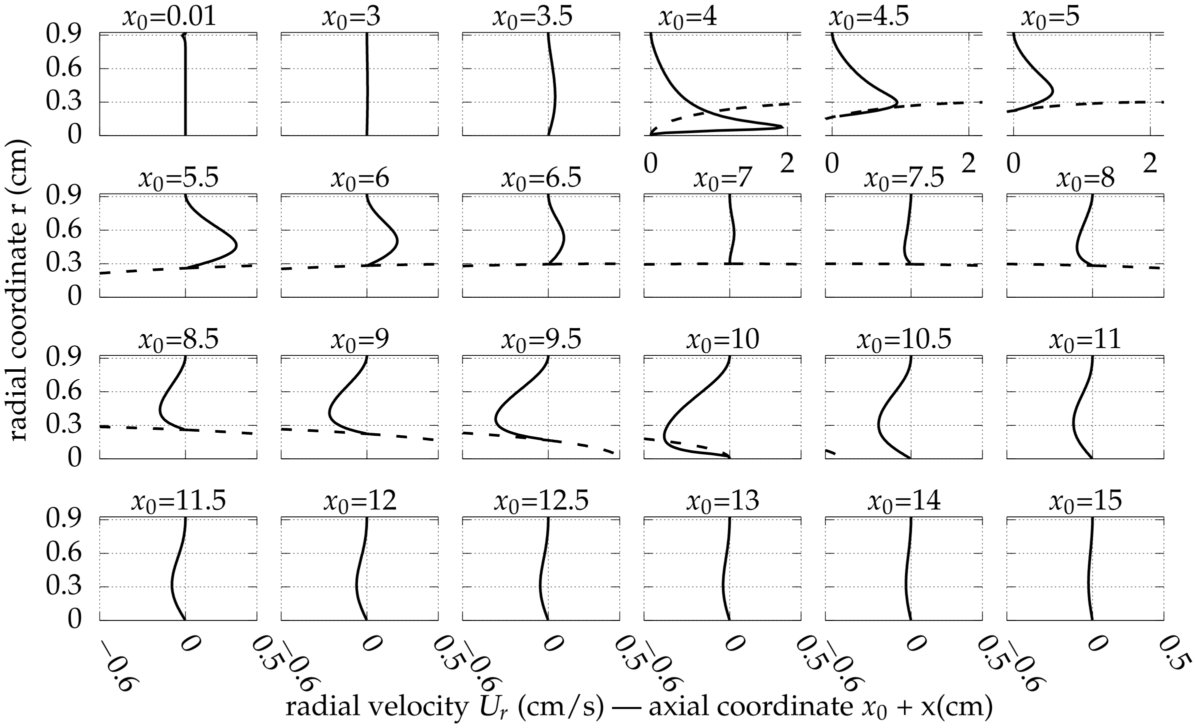

Figure 6.14: Radial velocity profiles for $t = 0T/8$ (continuous line), for $Q_{in} = 0.01$ L/s, $r_{b0} = 0.32$ cm and $A_b = 0.02$ cm. The dashed line indicates the balloon profile.

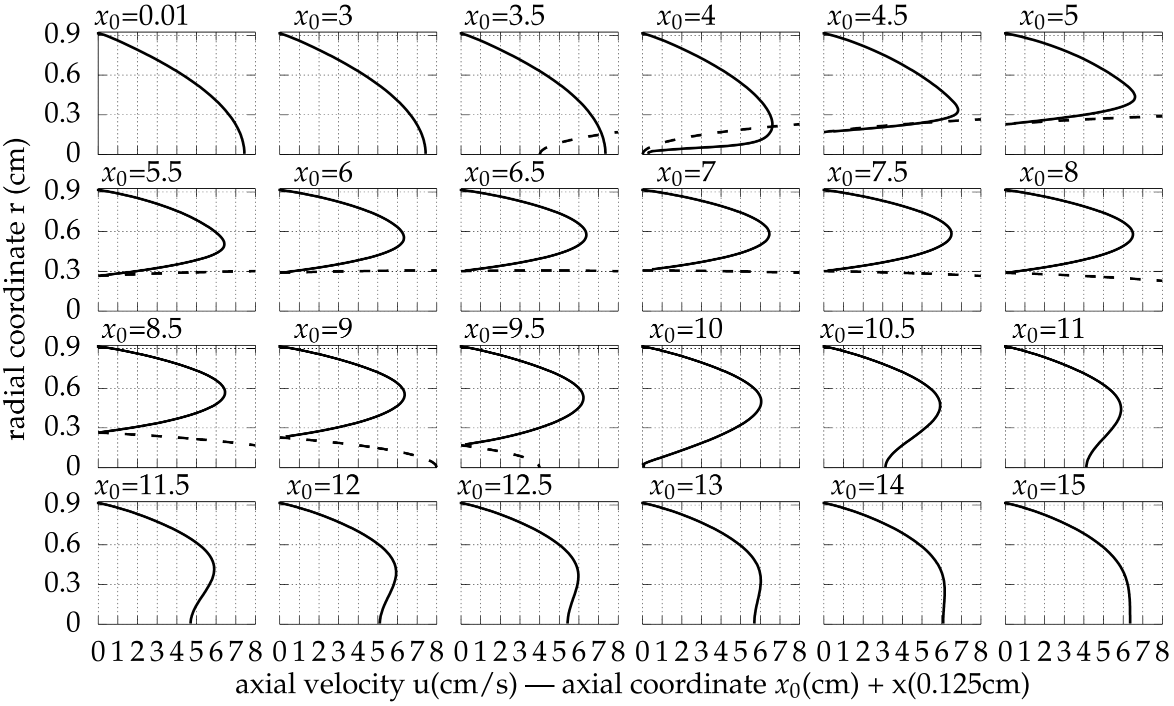

Figure 6.15: Axial velocity profiles for $t = T/8$ (continuous line), for $Q_{in} = 0.01$ L/s, $r_{b0} = 0.32$ cm and $A_b = 0.02$ cm. The dashed line indicates the balloon profile.

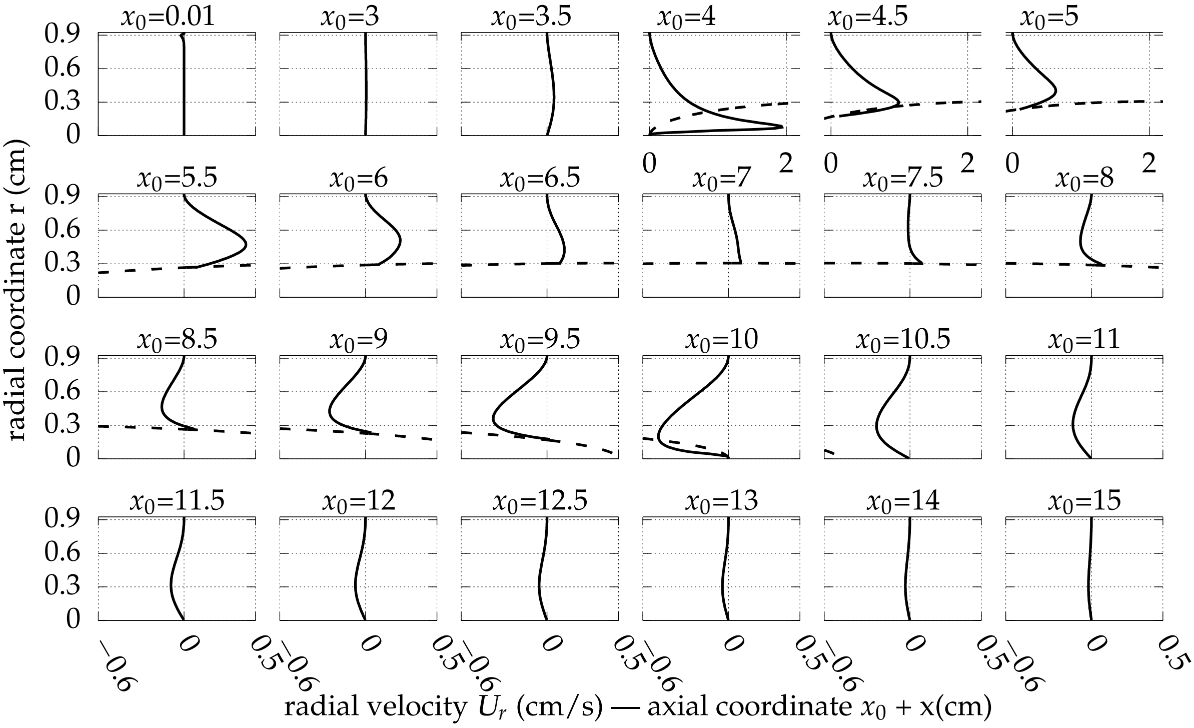

Figure 6.16: Radial velocity profiles for $t = T/8$ (continuous line), for $Q_{in} = 0.01$ L/s, $r_{b0} = 0.32$ cm and $A_b = 0.02$ cm. The dashed line indicates the balloon profile.

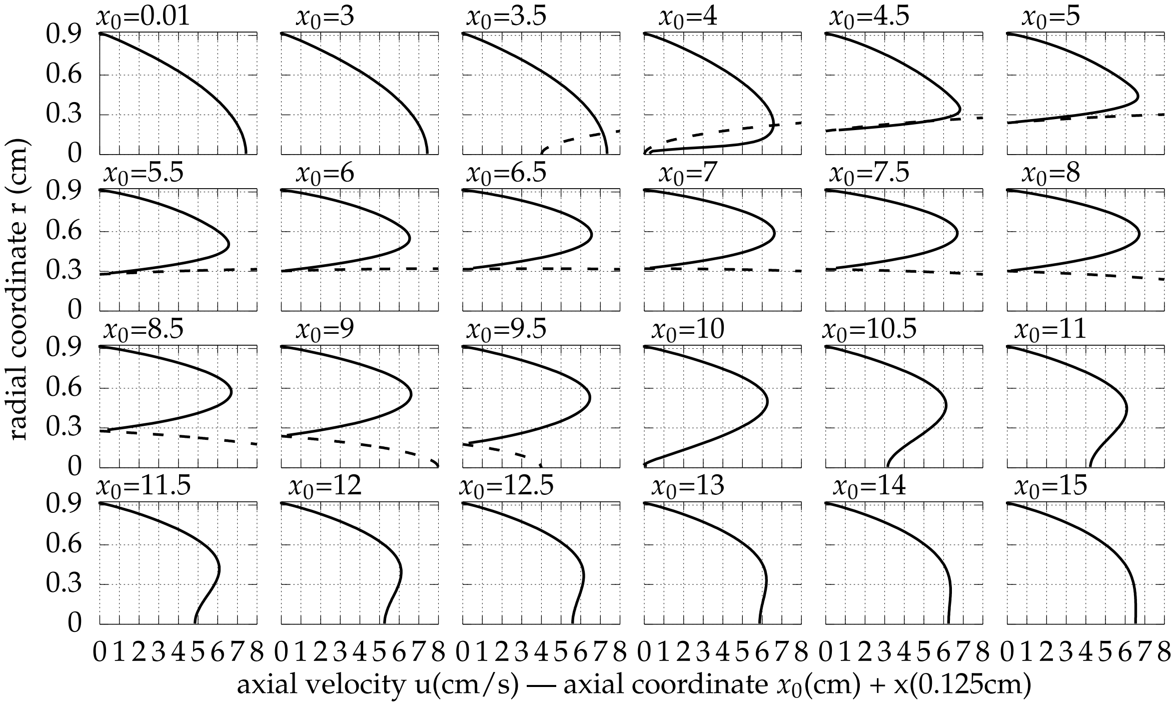

Figure 6.17: Axial velocity profiles for $t = 2T/8$ (continuous line), for $Q_{in} = 0.01$ L/s, $r_{b0} = 0.32$ cm and $A_b = 0.02$ cm. The dashed line indicates the balloon profile.

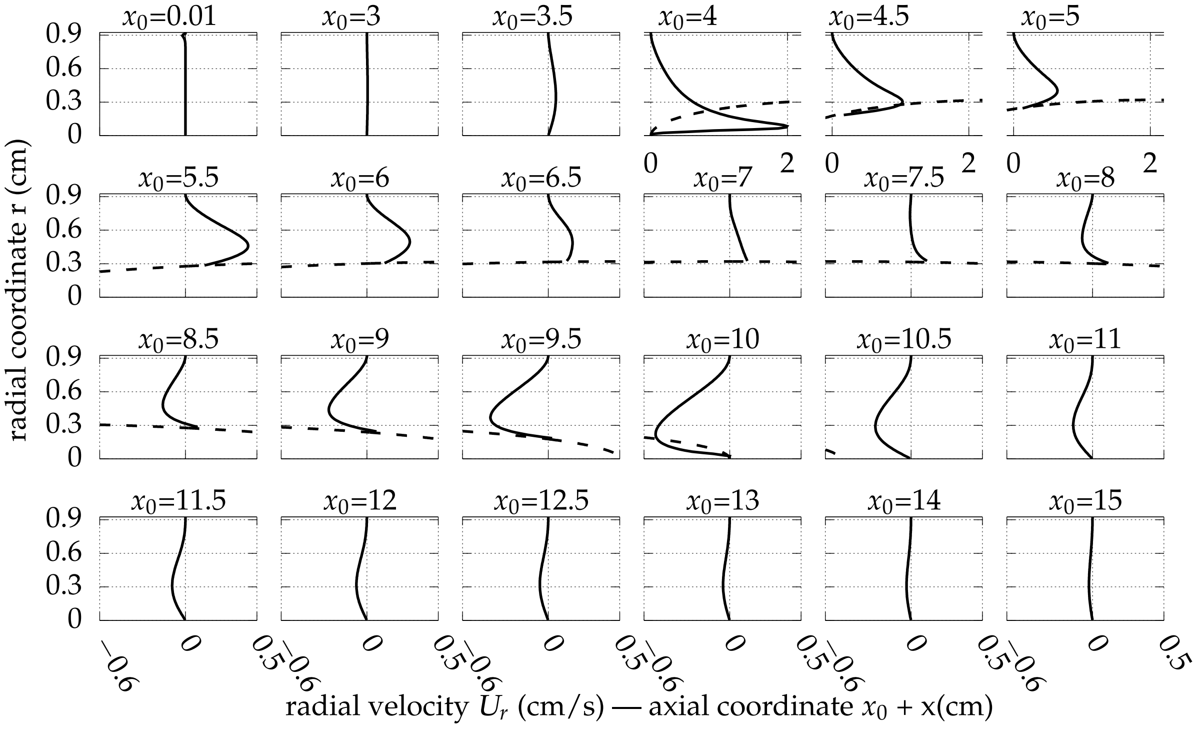

Figure 6.18: Radial velocity profiles for $t = 2T/8$ (continuous line), for $Q_{in} = 0.01$ L/s, $r_{b0} = 0.32$ cm and $A_b = 0.02$ cm. The dashed line indicates the balloon profile.

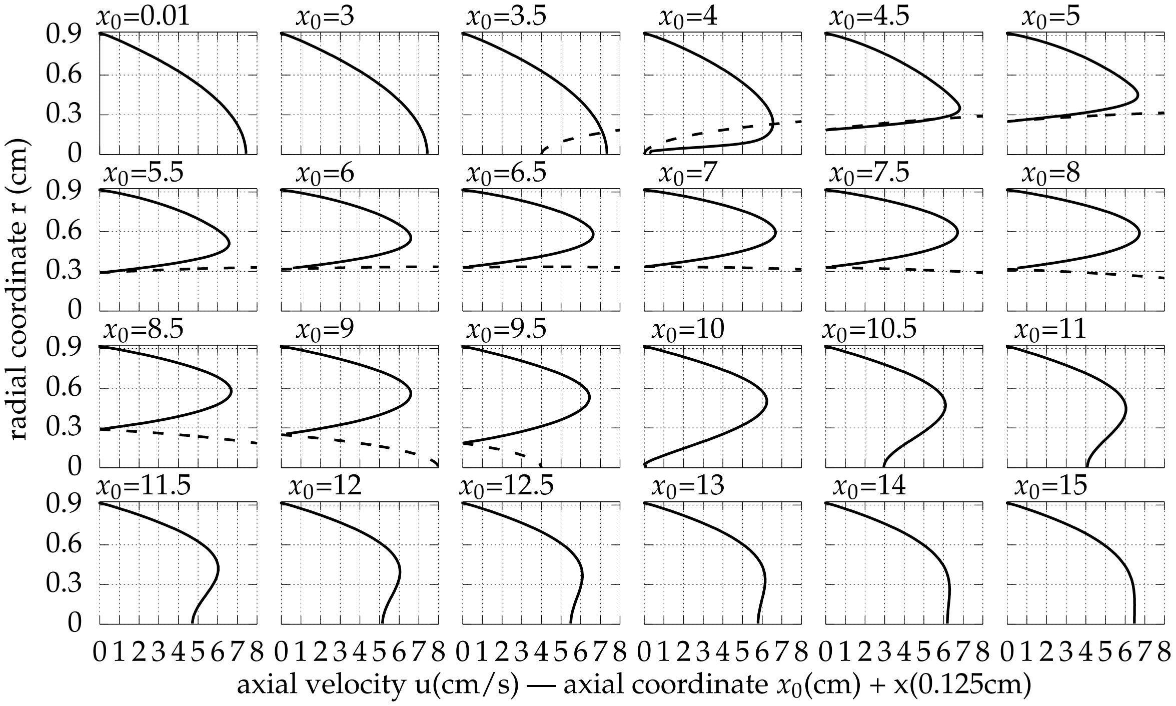

Figure 6.19: Axial velocity profiles for $t = 3T/8$ (continuous line), for $Q_{in} = 0.01$ L/s, $r_{b0} = 0.32$ cm and $A_b = 0.02$ cm. The dashed line indicates the balloon profile.

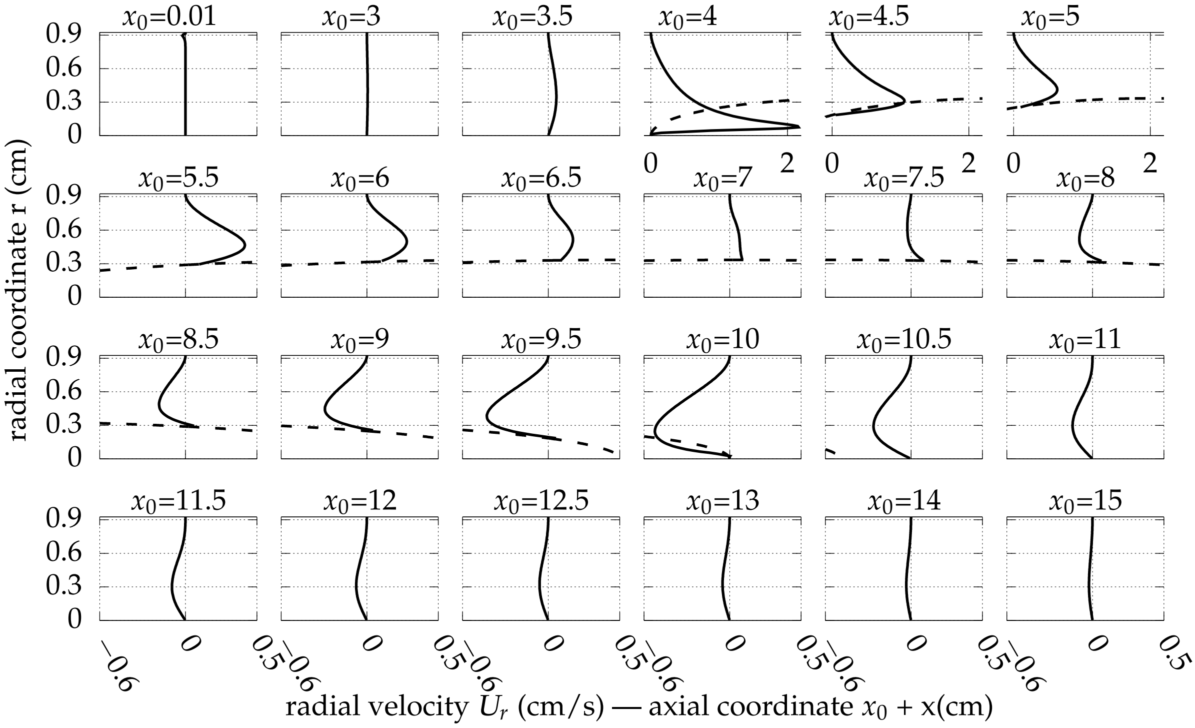

Figure 6.20: Radial velocity profiles for $t = 3T/8$ (continuous line), for $Q_{in} = 0.01$ L/s, $r_{b0} = 0.32$ cm and $A_b = 0.02$ cm. The dashed line indicates the balloon profile.

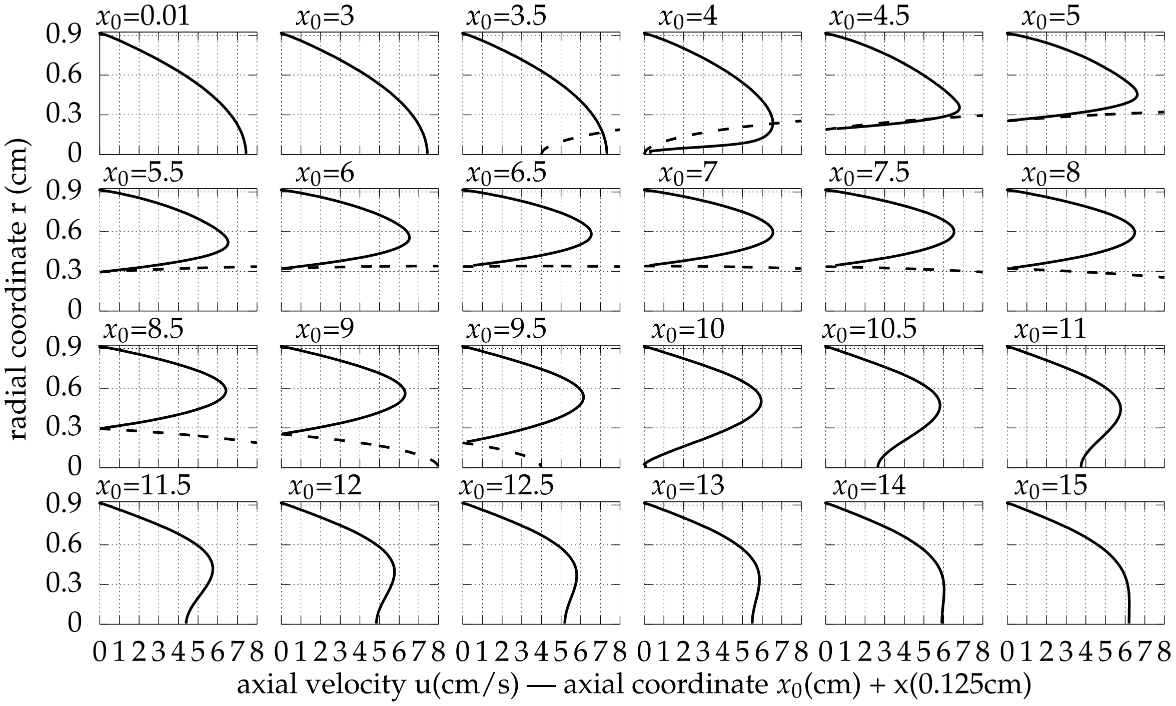

Figure 6.21: Axial velocity profiles for $t = 4T/8$ (continuous line), for $Q_{in} = 0.01$ L/s, $r_{b0} = 0.32$ cm and $A_b = 0.02$ cm. The dashed line indicates the balloon profile.

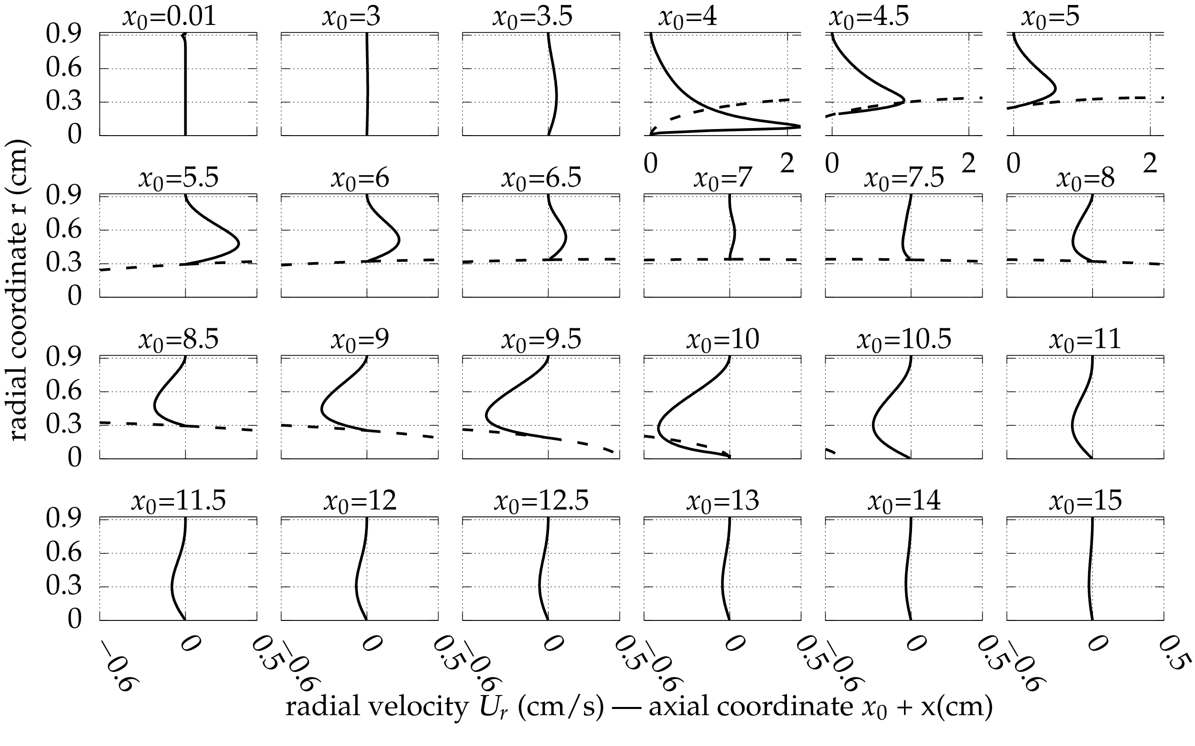

Figure 6.22: Radial velocity profiles for $t = 4T/8$ (continuous line), for $Q_{in} = 0.01$ L/s, $r_{b0} = 0.32$ cm and $A_b = 0.02$ cm. The dashed line indicates the balloon profile.

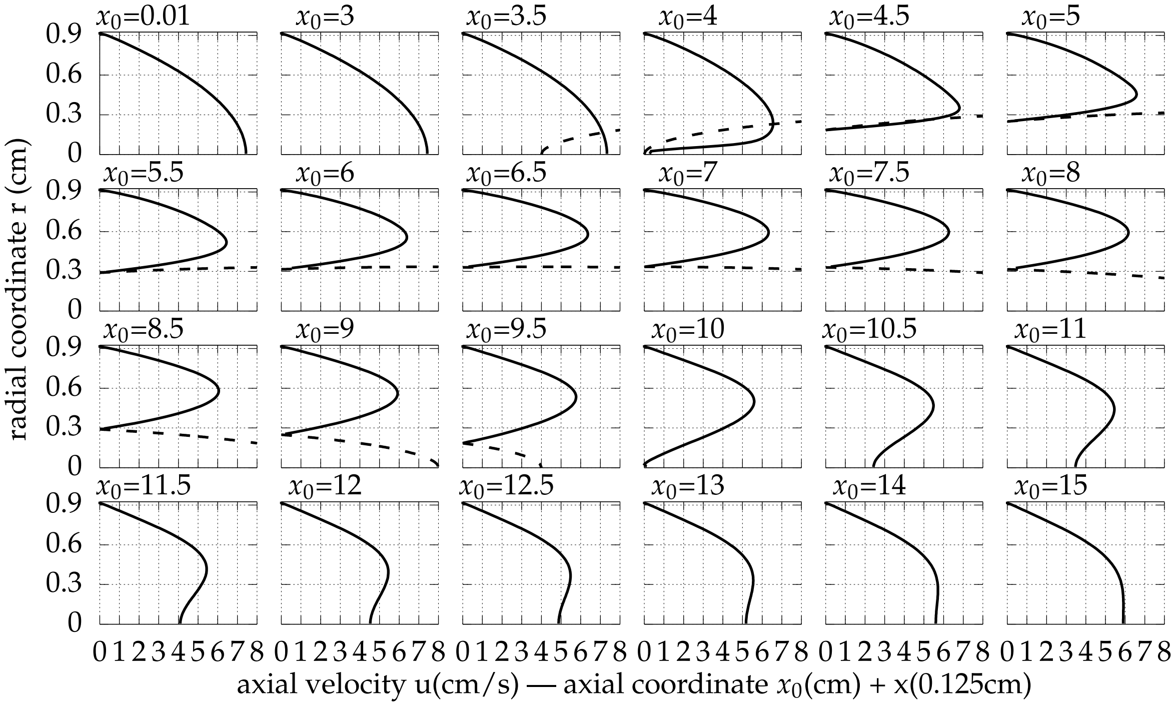

Figure 6.23: Axial velocity profiles for $t = 5T/8$ (continuous line), for $Q_{in} = 0.01$ L/s, $r_{b0} = 0.32$ cm and $A_b = 0.02$ cm. The dashed line indicates the balloon profile.

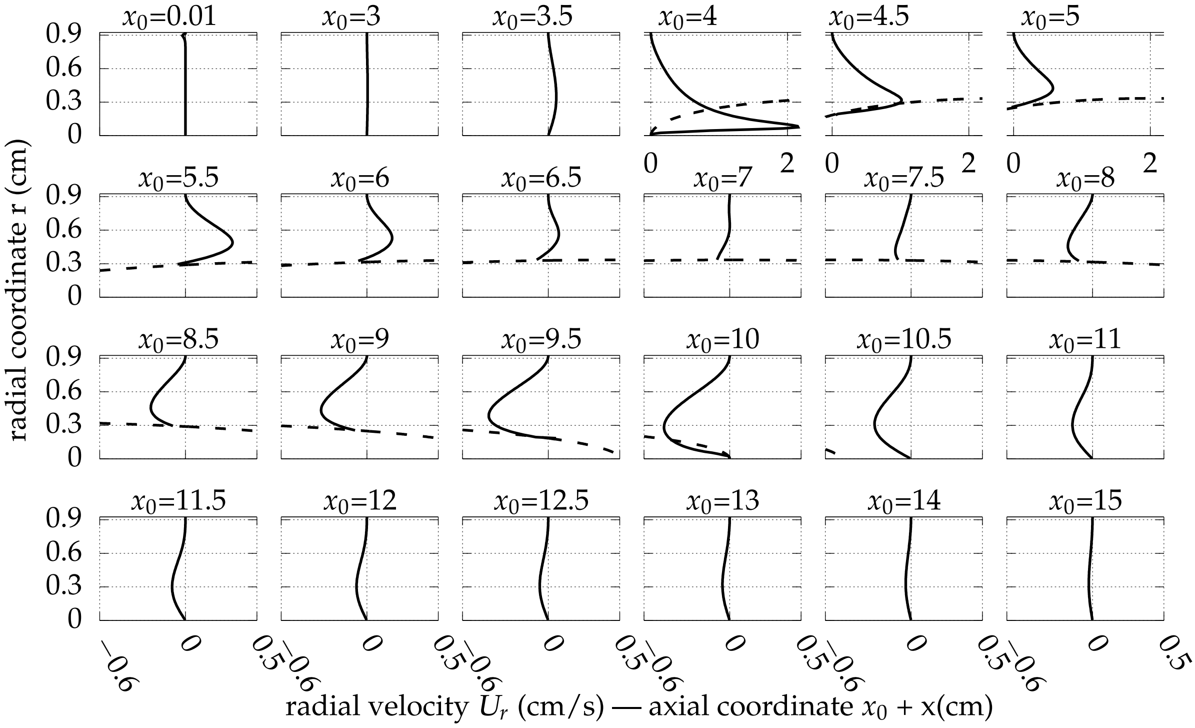

Figure 6.24: Radial velocity profiles for $t = 5T/8$ (continuous line), for $Q_{in} = 0.01$ L/s, $r_{b0} = 0.32$ cm and $A_b = 0.02$ cm. The dashed line indicates the balloon profile.

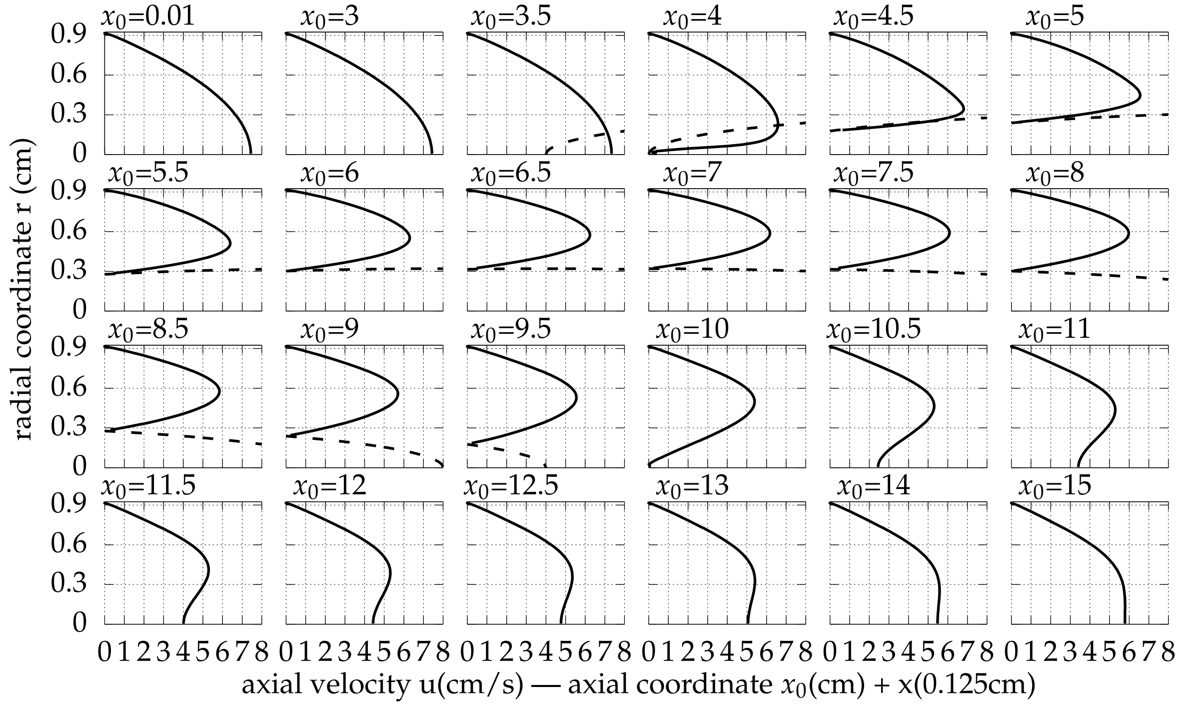

Figure 6.25: Axial velocity profiles for $t = 6T/8$ (continuous line), for $Q_{in} = 0.01$ L/s, $r_{b0} = 0.32$ cm and $A_b = 0.02$ cm. The dashed line indicates the balloon profile.

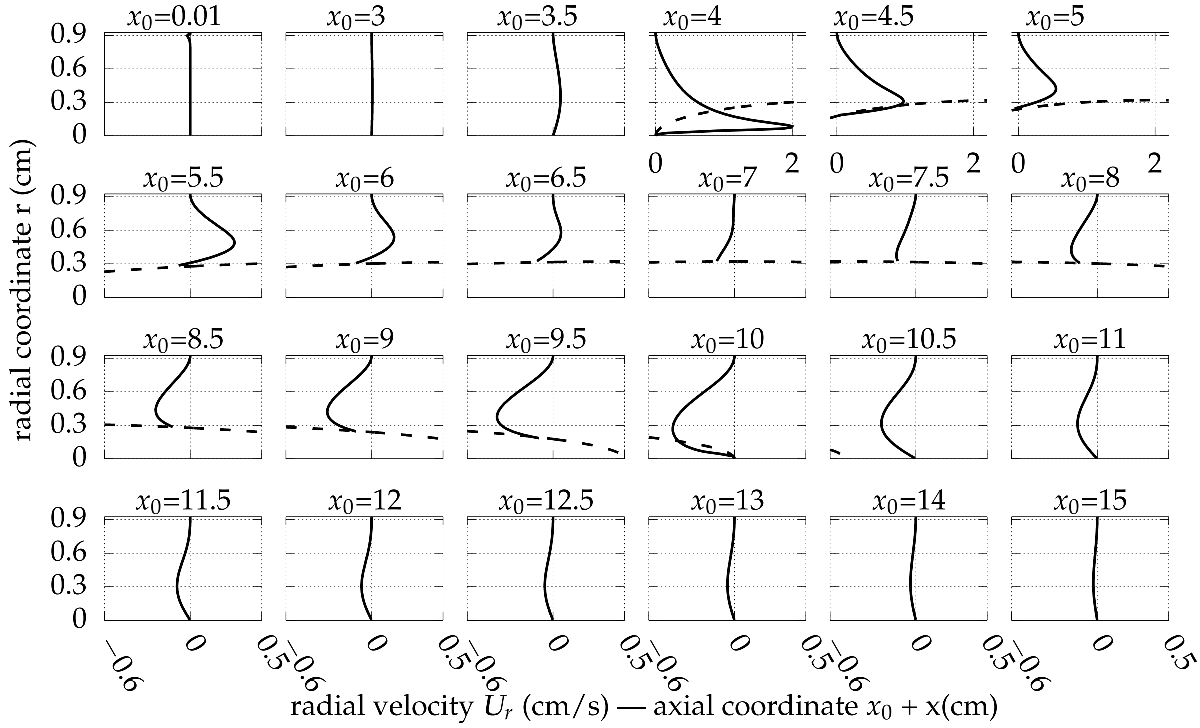

Figure 6.26: Radial velocity profiles for $t = 6T/8$ (continuous line), for $Q_{in} = 0.01$ L/s, $r_{b0} = 0.32$ cm and $A_b = 0.02$ cm. The dashed line indicates the balloon profile.

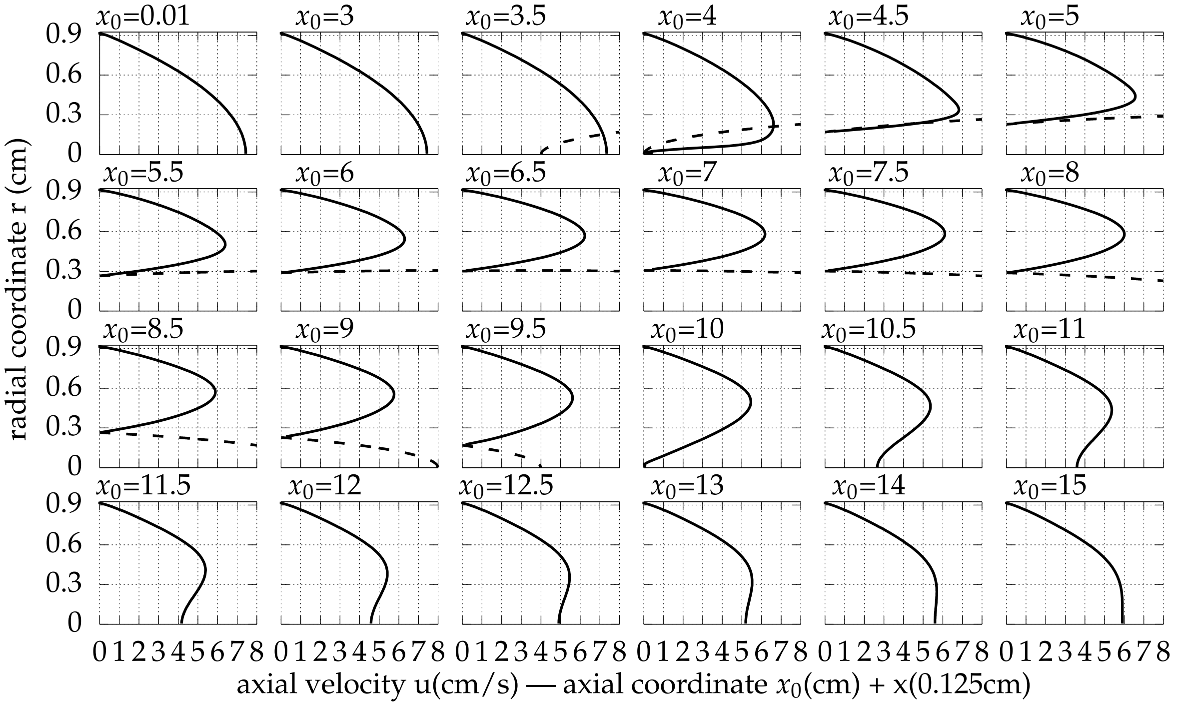

Figure 6.27: Axial velocity profiles for $t = 7T/8$ (continuous line), for $Q_{in} = 0.01$ L/s, $r_{b0} = 0.32$ cm and $A_b = 0.02$ cm. The dashed line indicates the balloon profile.

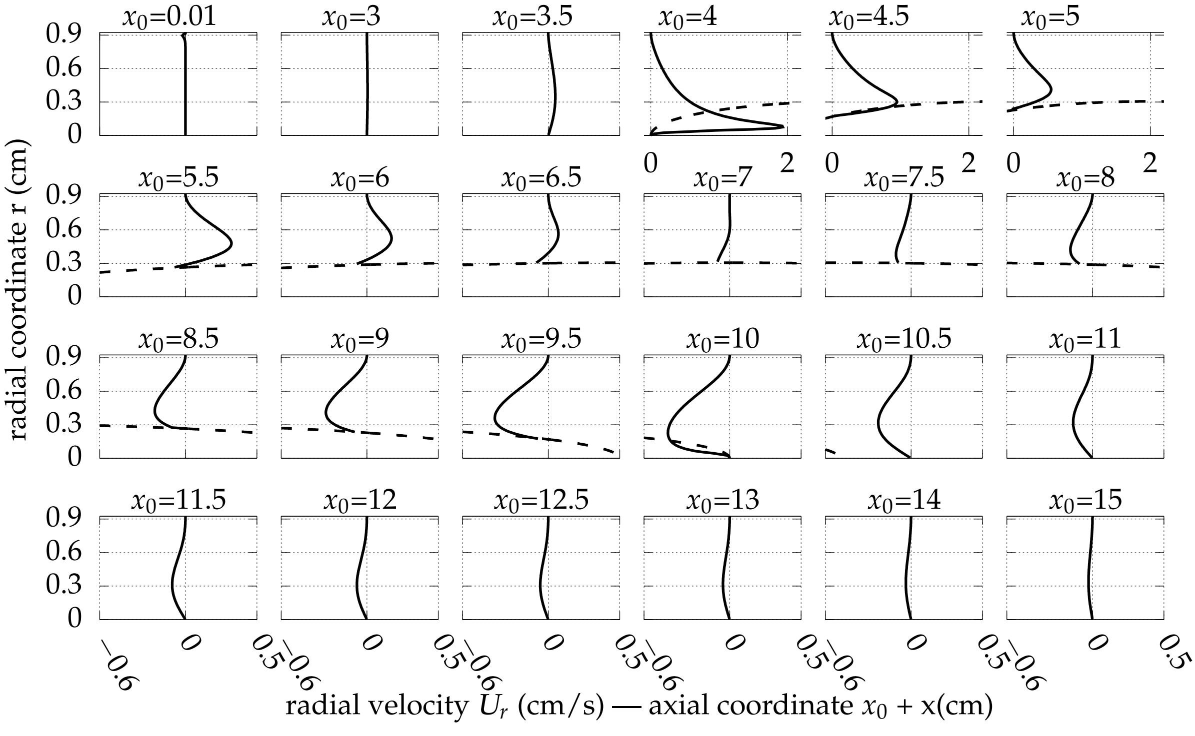

Figure 6.28: Radial velocity profiles for $t = 7T/8$ (continuous line), for $Q_{in} = 0.01$ L/s, $r_{b0} = 0.32$ cm and $A_b = 0.02$ cm. The dashed line indicates the balloon profile.

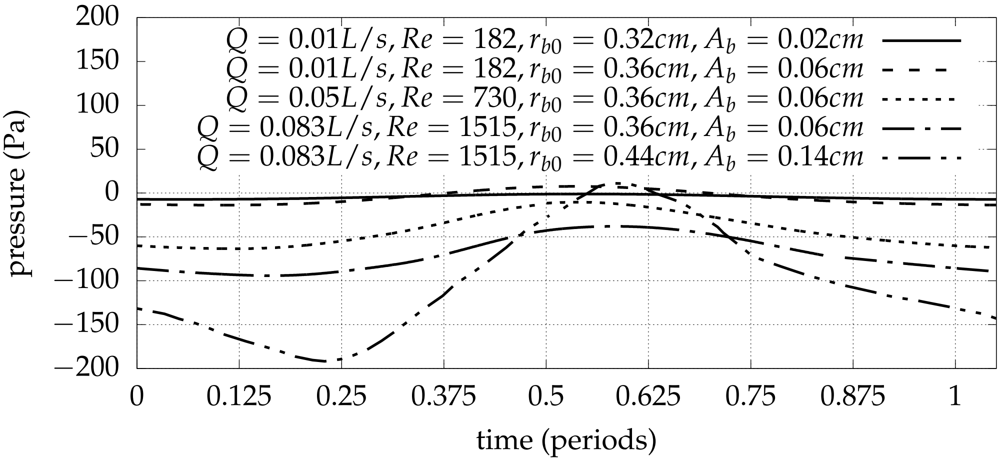

Figure 6.29: Pressure $p_{out} - p_{in}$ during a period for various values of r_{b0} and A_b.

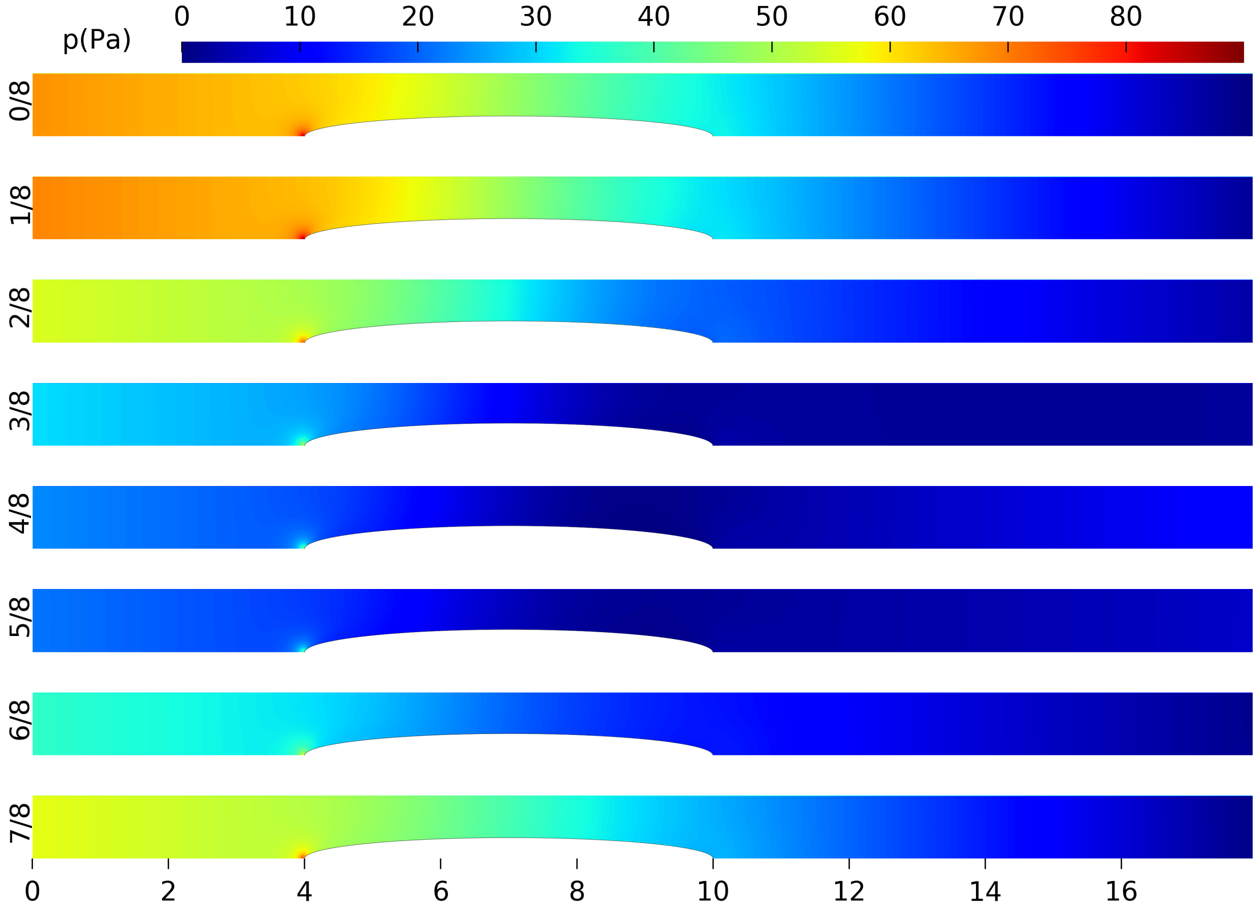

Figure 6.30: Pressure contours on a meridional plane, for balloon pulsating according to Equation (6.2), with inlet velocity profile given by Equation (6.7), for 8 instances during the period (left side titles refer to the fraction of the period T). The inlet volume rate is $Q_{in} = 0.01$ L/s, $r_{b0} = 0.32$ cm and $A_b = 0.02$ cm.

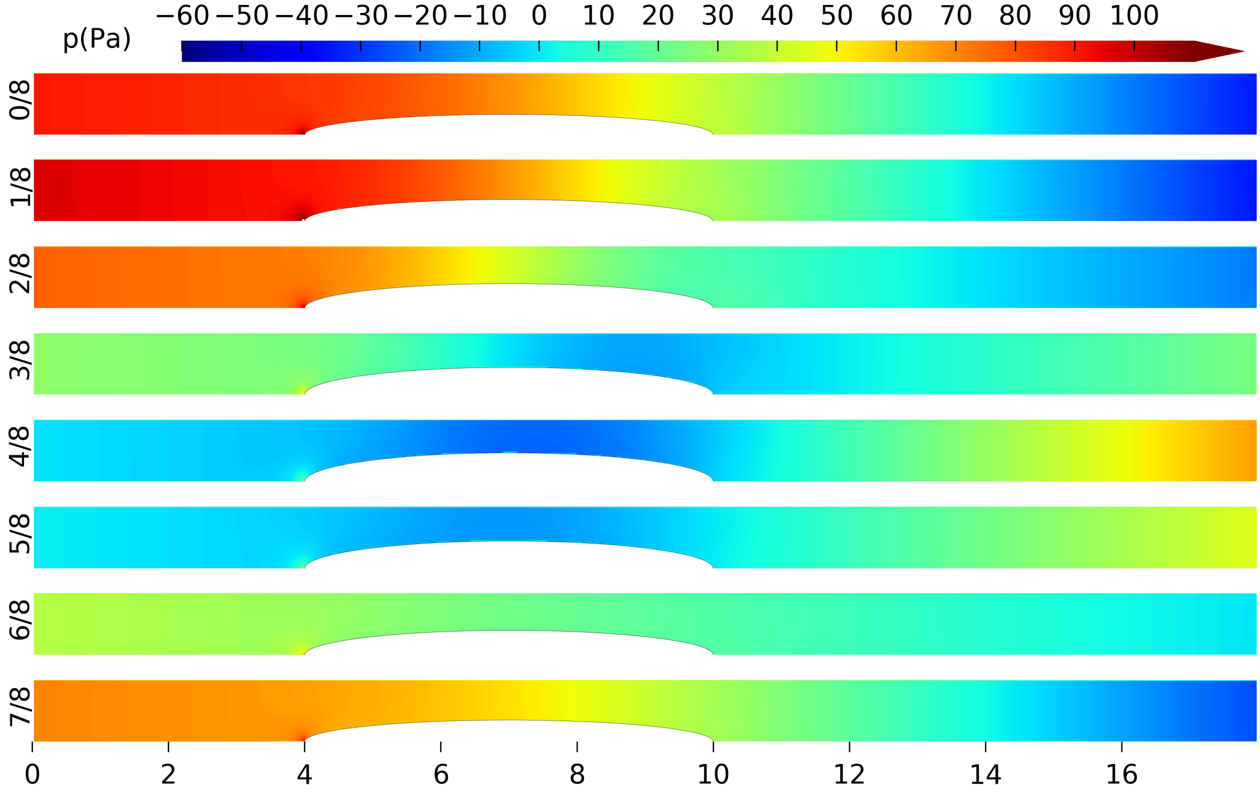

Figure 6.31: Pressure contours on a meridional plane, for balloon pulsating according to Equation (6.2), with inlet velocity profile given by Equation (6.7), for 8 instances during the period (left side titles refer to the fraction of the period T). The inlet volume rate is $Q_{in} = 0.01$ L/s, $r_{b0} = 0.36$ cm and $A_b = 0.06$ cm.

The outlet longitudinal velocity profiles are given in Figure 6.32.

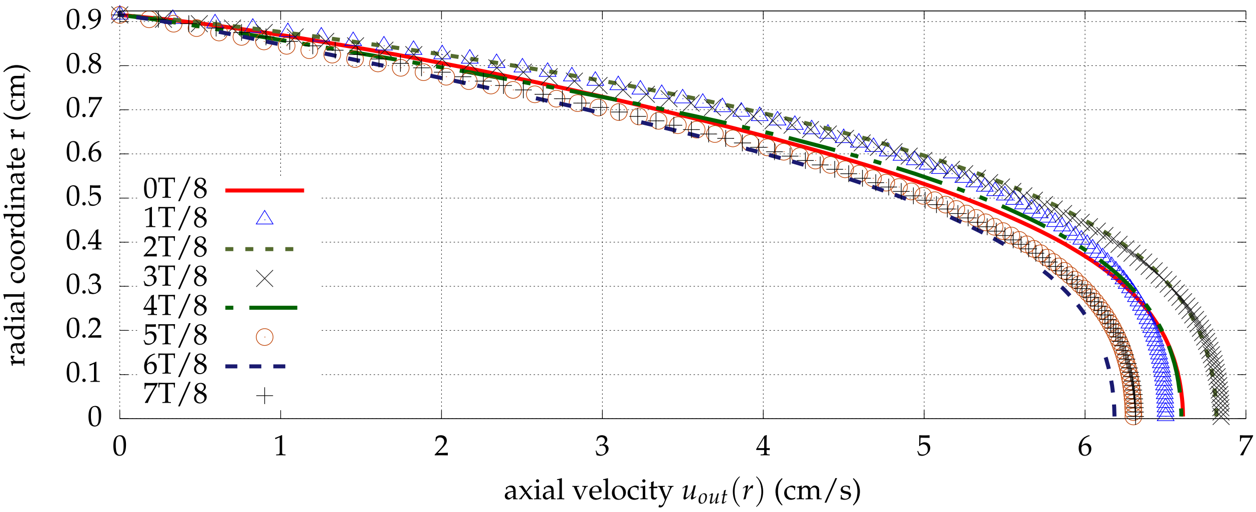

Figure 6.32: Outlet axial velocity profile $u_{out}(r)$ sampled 8 times during the period. The inlet volume rate is $Q_{in} = 0.01$ L/s, $r_{b0} = 0.32$ cm and $A_b = 0.02$ cm.

The difference of the outlet and inlet axial velocity profiles is given in Figure 6.33.

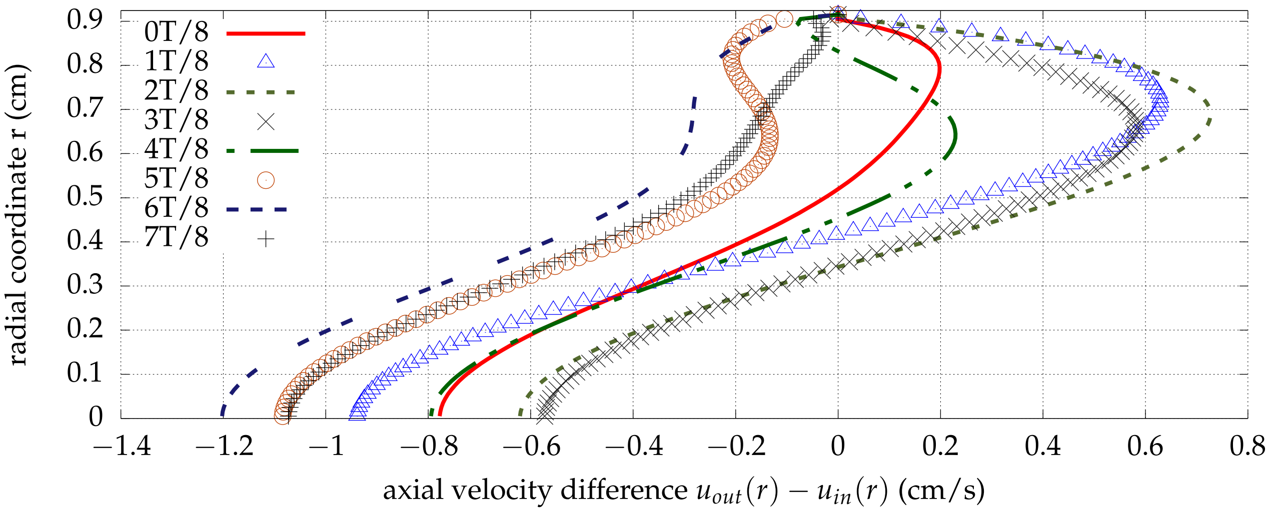

Figure 6.33: Difference between outlet axial velocity profile $u_{out}(r)$ and inlet axial velocity profile $u_{in}(r)$, sampled 8 times during the period. The inlet volume rate is $Q_{in} = 0.01$ L/s, $r_{b0} = 0.32$ cm and $A_b = 0.02$ cm.

6.4 Discussion

The flow around an intra aortic balloon pump is studied, where the pulsating closed surface membrane is spindle-shaped, with oscillating equatorial radius magnitude. The Womersley number is 11.936 which corresponds to the periodic cardiac flow in the human aorta. The mean Reynolds numbers used are 182, 730 and 1515. The lower value corresponds to inlet flow $Q_{in} = 0.01$ L/s, while the higher value corresponds to inlet volume $Q_{in} = 0.0833$ L/s, which is the average resting cardiac output for both trained and sedentary individuals [CGF19; Cif20; Hun05]. The flow fields computed via a) structured curvilinear meshes, body fitted at the vessel geometry and b) structured Cartesian meshes, considering the vessel an immersed boundary, are in good agreement.

The radial velocity field exhibits maximum intensity for $t = T/4$, triggered by the maximization of the balloon surface oscillation velocity. The most extended intensely negative region emerges for $t = 3T/8$ as the result of large balloon oscillation displacement and high flow volume rate (Figure 6.12).

The outlet pressure is not in phase with outlet velocity. As shown in Figure 6.31, for the time instances $t = 3T/4$ to $t = 5T/4$, the pressure distribution is non-monotonic with respect to the streamwise direction and gets its minimum values near the lengthwise position of the balloon center of symmetry, where the cross-section area minimizes.

For identical lower extreme position of the balloon small axis length oscillation, the amplitude of the membrane oscillation and the pressure fluctuation are positively correlated. For larger Reynolds numbers and for identical oscillations, the output pressure with respect to the inlet, gets lower values.

The enhanced importance of inertia results in significant lagging of the output pressure curve behind the flow volume rate curve [Zam05]. The phase difference between the maximum flow volume rate and the maximum outlet pressure is found to be independent of the amplitude of oscillation and the equilibrium position and to increase slightly for middle Reynolds number cases.

Because of the balloon pulsation, the vessel outlet velocity profile is not parabolic as in the inlet and the maximum axial velocity is notably lower, in comparison to the Poiseuille value corresponding to the flow rate (Figure 6.32). The high value of the nondimensional frequency parameter (11.936), which results to increased relative significance of the inertia effects leads to flattened velocity profiles around the axis, near to the outlet [Wes+19]. Downstream of the balloon, at sufficient distance from it, shear stresses are significant at the wall vicinity and are almost absent at the flow core [Kis09].

Near the outlet of the pipe, where the flow is developed, the simplified form of the Navier-Stokes equations

$$\frac{\partial^2 u}{\partial r^2} + \frac{1}{r}\frac{\partial u}{\partial r} - \frac{1}{\nu}\frac{\partial u}{\partial t} = \frac{1}{\mu}\frac{\partial p}{\partial x}, \tag{6.12}$$

is linear for the velocity profile and pressure [Nic+22]. Therefore, in cases where the steady and the time dependent pressure gradient parts coexist, they satisfy independently Equation (6.12) [Uch56; Ver60]. As shown in Figure 6.33, the effect of the pulsation of the balloon at the outlet is more intense for radii in the middle of the narrowest duct created by the inner and outer solid boundaries.

6.5 Summary

The computation of the laminar flow around an ellipsoidal expanding-contracting balloon with equal median and minor axes and with major axis at the direction of the flow, in a straight pipe of circular cross-section is conducted. The minor axis length is oscillating sinusoidally with period that of the cardiac pulse. The inflow is considered a developed Poiseuille profile. The effect on pressure of the balloon volume evolution is investigated and the corresponding pulsating flow produced is described. The flow field around the dilating-shrinking body is documented analytically.

Successive step of the current study is the use of the framework presented, augmented with fluid-structure interaction to take under consideration the compliance of the artery [Wom57]. Moreover the cardiac output pulse could be substituted for the steady inlet velocity and the IABP timing could be used to simulate the three-dimensional flow around the IABP in the human aorta.

Chapter 7

Conclusions

7.1 Thesis central points

By recapitulating central points of the thesis, the following are noted:

- The immersed boundary method (IBM) used, is recommended as adequate for the simulation of the flow manipulation, where moving rigid or deformable solid parts are involved. The solution domain discretization mesh is constant in time, hence, the demanding procedure of mesh generation is substituted by the notably less challenging goal of surface tracing. Each simulation demands less effort for the discretization part and significantly less processing time.
- Larger values of the control surface length, ceteris paribus, for the backward facing step, results to increased steadiness for the detachment location of the upper wall and higher maximum for the upper wall reattachment position location. As a consequence of this increase of the length, the longitudinal oscillation amplitude of the lower wall bubble reduces.
- Passive elastic surface means interacting with the main flow are found to be an efficient way for the recirculation control of steady and time varying flow fields. By supplying suitable external pressure and without an energy source, a membrane can suppress flow separation to a significant extend.
- Biological flows are in majority governed by constitutive equations with shear dependent coefficients. The curvilinear immersed boundary algorithm is found to give predictions of non-Newtonian behavior in accordance with those of body adapted methods.
- Analysis of peristalsis in straight peristaltic pumps, shows multi-cylinder settings to confer advantages over unimodal squeeze wave ones. Parallel and perpendicular to the wave velocity, velocity gradient fields are less intense for multi modal waves. Pumped fluids, therefore, are subjected to lower levels of shear rate and suffer shear stresses of less magnitude. Another positive feature of multimodal waves is the unidirectional longitudinal flow at the full length and width of the pump, tackling the implications of reversed flow.

- Shear thinning generalized Newtonian fluids are set in motion under lower values of reverse pressure gradient than Newtonian. Slopes of peristalsis characteristics of fluids with pseudoplastic behavior are negatively correlated with Bird-Carreau power index. Pumping of this category of fluids demands less work.
- Outlet pressure of an intra-aortic balloon pump maximizes at an approximately constant time instance during the pulsation period almost independently of the central value of the small axis length or its oscillation amplitude. For the same frequency, higher peak to peak outlet pressure is the result of the augmentation of peak to peak balloon volume.

7.2 Contribution of the dissertation

In the present dissertation we shed light on flow control in various cases of interest, using the immersed boundary method. The main contributions of this work are summarized here:

- The curvilinear immersed boundary method is applied for the prediction of flow fields with varying in time fluid volume. The fluid-structure interaction with deformable bodies is added to the algorithm. Solid response is that of an elastic membrane whose governing equation is weakly associated with Navier-Stokes equations. The procedure is implemented in steady and unsteady cases.
- Active control of a separation bubble via an oscillating surface is studied, using steady computational meshes. In addition to the role of amplitude and frequency, the longitudinal extension of the active surface is taken under consideration.
- Fluids pumped by contraction waves or by pulsation, often do not comply with linear constitutive equations. The solver is extended to include fluids following time-independent nonlinear constitutive equations such as cases of the Carreau-Yasuda rheology model.
- A way of confronting the standard issues of negative axial velocities and limitation of shear stresses in peristaltic pumping is proposed. Increasing the multitude of periods of the waveshape is investigated and found to achieve good performance in these directions.
- The pumping characteristics of peristalsis for straight pumps are presented for Newtonian and non-Newtonian fluids and for several values of the relative occlusion.
- Pulsatile flow engendered by a spheroid balloon in a cylindrical duct is modeled. Pumping performance for a range of the inflow volume rate value and balloon volume oscillation amplitude are analyzed and the flow field through the apparatus is described.

7.3 Publications

Part of the current work has been/is published as:

Recirculation control

- 9th International Conference on Experiments / Process / System Modeling / Simulation / Optimization, Athens, 7-10 July 2021
- Iosif Moulinos, Christos Manopoulos, and Sokrates Tsangaris (2022) ”Computational Analysis of Active and Passive Flow Control for Backward Facing Step”, Computation 10(1), 12: `https://doi.org/10.3390/computation10010012`

Peristalsis

- 9th International Conference on Experiments / Process / System Modeling / Simulation / Optimization, Athens, 7-10 July 2021
- 9th Panhellenic Conference on Biomedical Technology, Aristotle University of Thessaloniki, 9-11 September 2021
- Iosif Moulinos, Christos Manopoulos, and Sokrates Tsangaris (2021) ”A Computational Analysis for Active Flow and Pressure Control Using Moving Roller Peristalsis”, Computation 9(12), 144: `https://doi.org/10.3390/computation9120144`

Balloon pumping

- Iosif Moulinos, Christos Manopoulos, and Sokrates Tsangaris (2023) ”Modification of Poiseuille flow to a pulsating flow using a periodically expanding - contracting balloon”, Fluids 8(4), 129: `https://doi.org/10.3390/fluids8040129`

7.4 Future directions

Further progress on the research presented in this thesis can be made by expanding on the following topics.

- More sophisticated variants for the solid response are of interest. Three dimensional stream in interaction with a surface membrane with pressure - deformation equation of the form

  $$T_m\left(\frac{\partial^2 g(x,y,t)}{\partial x^2}+\frac{\partial^2 g(x,y,t)}{\partial y^2}\right)=-(p_e(x,y,t)-p_i(x,y,t)), \tag{7.1}$$

  allows the control in more complex flow field cases, such as the flow over a finite depth three dimensional backward facing step with frictional side walls. Research on the scheme determining the pressure on the immersed boundary surface, by extrapolating from the immersed boundary nodes or/and fluid nodes, ameliorates the accuracy of the FSI procedure. The widening of the analysis at the turbulent counterpart of the examined flow remains open.

- Natural and engineering peristaltic applications span a wide range of geometric configurations. Study of pumping in settings such as in rubbing circular cross-section elastic tube by a torus contracting ring or in rectangular cross-section elastic tube, will lead in more comprehensive understanding of the peristaltic mechanism parameters. In the $2\alpha \times 2b$ rectangular tube setting, Equation 5.5 is substituted for

$$\begin{aligned} u(x=0,y,z) = & \frac{12\alpha^2 Q}{\pi^3} \left(1 - \frac{192\alpha}{\pi^5 b} \sum_{\substack{i=2n+1,\\ n\in\mathbb{N}}}^{\infty} \frac{\tanh\left(\frac{i\pi b}{2\alpha}\right)}{i^5} \right) \\ & \cdot \sum_{\substack{i=2n+1,\\ n\in\mathbb{N}}}^{\infty} (-1)^{\frac{i-1}{2}} \left(1 - \frac{\cosh\left(\frac{i\pi z}{2\alpha}\right)}{\cosh\left(\frac{i\pi b}{2\alpha}\right)} \right) \frac{\cos\left(\frac{i\pi y}{2\alpha}\right)}{i^3}, \end{aligned} \tag{7.2}$$

  where Q is the flow volume rate.

- Optimization of flow control under suitable objective functions of interest using methods of Chapter 1 is an exciting area of further examination. Optimization arguments of importance for the flows presented are among others the membrane parameters (tensile load, external pressure), the peristalsis waveshape and the shape and position of the pulsating balloon of the IABP.

- Cylindrical coordinate form of the Navier-Stokes equations reduces the computation time of axisymmetric flows, by reducing their dimensionality and also is expected to increase the computation accuracy because of the lower error levels of the discretization in two dimensions. Pulsatile flow in the compliant human aorta is the successor of the research in the rigid aorta presented. More progress in this line of research consists the simulation of the complete human arterial system in terms of flow rate and pressure propagation, considering zero order model for the main arteries (excluding aorta).

Bibliography

[AB71] A. S. Ahuja and G. Bugliarello. A note on the compressibility of blood. *Biorheology* 7.4 (1971), pp. 199–203.

[AB99] J. Anagnostopoulos and G. Bergeles. Three-dimensional modeling of the flow and the interface surface in a continuous casting mold model. *Metallurgical and Materials Transactions B* 30.6 (1999), pp. 1095–1105.

[Ach72] E. Achenbach. Experiments on the flow past spheres at very high Reynolds numbers. *Journal of Fluid Mechanics* 54.3 (1972), pp. 565–575.

[ACS16] D. Angelidis, S. Chawdhary, and F. Sotiropoulos. Unstructured Cartesian refinement with sharp interface immersed boundary method for 3D unsteady incompressible flows. *Journal of Computational Physics* 325 (2016), pp. 272–300.

[AG09] V. G. Asouti and K. C. Giannakoglou. Aerodynamic optimization using a parallel asynchronous evolutionary algorithm controlled by strongly interacting demes. *Engineering Optimization* 41 (2009), pp. 241–257.

[AH13] A. A. Al-Habahbeh. Simulations of Newtonian and non-Newtonian flows in deformable tubes. PhD thesis. Michigan Technology University, 2013.

[Alo+18] S. Alokaily, K. Feigl, F. X. Tanner, and E. J. Windhab. Numerical Simulations of the Transport of Newtonian and Non-newtonian Fluids via Peristaltic Motion. *Applied Rheology* 28.3, 32832 (2018).

[AM05] J. Anagnostopoulos and D. Mathioulakis. Numerical Simulation and Hydrodynamic Design Optimization of a Tesla-Type Valve for Micropumps. In: *Proceedings of the 3rd IASME/WSEAS International Conference on Fluid Dynamics & Aerodynamics*. (Corfu, Greece). 2005, pp. 195–201.

[Ana07] J. Anagnostopoulos. A Cartesian grid method for the simulation of flows in complex geometries. In: *Proceedings of the International Conference on Adaptive Modeling and Simulation*. (Barcelona, Spain). Oct. 2007.

[Ana09] J. S. Anagnostopoulos. A fast numerical method for flow analysis and blade design in centrifugal pump impellers. *Computers & Fluids* 38.2 (2009), pp. 284–289.

[And95] J. Anderson. *Computational Fluid Dynamics: The Basics with Applications*. McGraw-Hill Education, 1995.

[AP00] V. Armenio and U. Piomelli. A Lagrangian Mixed Subgrid-Scale Model in Generalized Coordinates. *Flow, Turbulence and Combustion* 65 (2000), pp. 51–81.

[Arm+83] B. F. Armaly, F. Durst, J. C. F. Pereira, and B. Schnung. Experimental and theoretical investigation of backward-facing step flow. *Journal of Fluid Mechanics* 127 (1983), pp. 473–496.

[AW+10] M. Abdel-Wahab, M. Saad, J. Kynast, V. Geist, M. Sherif, G. Richardt, and R. Toelg. Comparison of Hospital Mortality With Intra-Aortic Balloon Counterpulsation Insertion Before Versus After Primary Percutaneous Coronary Intervention for Cardiogenic Shock Complicating Acute Myocardial Infarction. *The American Journal of Cardiology* 105 (2010), pp. 967–971.

[BAH87] R. Bird, R. Armstrong, and O. Hassager. *Dynamics of polymeric liquids, Volume 1: Fluid mechanics, 2nd Edition*. Wiley, 1987.

[BB16] W. F. Boron and E. L. Boulpaep. *Medical Physiology*. Elsevier, 2016.

[BBC17] A. Batikh, L. Baldas, and S. Colin. Application of active flow control on aircrafts - State of the art. In: *International Workshop on Aircraft System Technologies*. Vol. 2017. Hamburg, Germany, Feb. 2017.

[Bel58] R. Bellman. Dynamic programming and stochastic control processes. *Information and Control* 1.3 (1958), pp. 228–239.

[BGS08] I. Borazjani, L. Ge, and F. Sotiropoulos. Curvilinear immersed boundary method for simulating fluid structure interaction with complex 3D rigid bodies. *Journal of Computational Physics* 227.16 (2008), pp. 7587–7620.

[Bin+18] C. Bingham, C. Raibaudo, C. Morton, and R. Martinuzzi. Suppression of fluctuating lift on a cylinder via evolutionary algorithms: Control with interfering small cylinder. *Physics of Fluids* 30, 127104 (2018).

[Bin22] E. C. Bingham. *Fluidity and Plasticity*. International chemical series. McGraw-Hill, 1922.

[BL89] M. Berger and R. Leveque. An adaptive Cartesian mesh algorithm for the Euler equations in arbitrary geometries. In: *AIAA 9th Computational Fluid Dynamics Conference*. (Buffalo, New York). June 1989.

[BLW08] E. Braun, F. Lu, and D. Wilson. A Critical Review of Electric and Electromagnetic Flow Control Research Applied to Aerodynamics. In: *Proccedings of the 39th Plasmadynamics and Lasers Conference (23 - 26 June)*. (Seattle, Washington). American Institute of Aeronautics and Astronautics, 2008.

[Boo02] W. M. Boothby. *An introduction to differentiable manifolds and Riemannian geometry*. Academic Press, 2002.

[Bou21] E. Boujo. Second-order adjoint-based sensitivity for hydrodynamic stability and control. *Journal of Fluid Mechanics* 920, A12 (2021).

[Bou77] J. Boussinesq. *Essai Sur la Théorie des Eaux Courantes*. Paris, France: Imprimerie Nationale, 1877.

[Bro87] P. N. Brown. A Local Convergence Theory for Combined Inexact - Newton / Finite - Difference Projection Methods. *SIAM Journal on Numerical Analysis* 24.2 (1987), pp. 407–434.

[Bru15] G. Bruti. Experimental and computational investigations for the development of intra-aortic balloon pump therapy. PhD thesis. London, United Kingdom: Brunel University, 2015.

[BS90] P. N. Brown and Y. Saad. Hybrid Krylov Methods for Nonlinear Systems of Equations. *SIAM Journal on Scientific and Statistical Computing* 11.3 (1990), pp. 450–481.

[But75] J. C. Butcher. A stability property of implicit Runge-Kutta methods. *BIT Numerical Mathematics* 15 (1975), pp. 358–361.

[Cal+15] A. Calderer, X. Yang, D. Angelidis, A. Khosronejad, T. Le, S. Kang, A. Gilmanov, L. Ge, and I. Borazjani. *Virtual Flow Simulator, Version 1.0*. 2015.

[Car+16] M. V. Caruso, V. Gramigna, A. Renzulli, and G. Fragomeni. Computational analysis of aortic hemodynamics during total and partial extra-corporeal membrane oxygenation and intra-aortic balloon pump support. *Acta of Bioengineering and Biomechanics* 18.3 (2016), pp. 3–9.

[Car68] P. J. Carreau. Rheological equations from molecular network theories. PhD thesis. Madison, WI: University of Winsconsin - Madison, 1968.

[CGF19] M. V. Caruso, V. Gramigna, and G. Fragomeni. A CFD investigation of intra-aortic balloon pump assist ratio effects on aortic hemodynamics. *Biocybernetics and Biomedical Engineering* 39.1 (2019), pp. 224–233.

[Che+14] G. Chen, Q. Xiong, P. J. Morris, E. G. Paterson, A. Sergeev, and Y. C. Wang. OpenFOAM for computational fluid dynamics. *Notices of the American Mathematical Society* 61.4 (2014), pp. 354–363.

[Che+18] L. Chen, K. Asai, T. Nonomura, G. Xi, and T. Liu. A review of Backward-Facing Step (BFS) flow mechanisms, heat transfer and control. *Thermal Science and Engineering Progress* 6 (2018), pp. 194–216.

[Cho67] A. J. Chorin. A numerical method for solving incompressible viscous flow problems. *Journal of Computational Physics* 2.1 (1967), pp. 12 –26.

[Cho68] A. J. Chorin. Numerical solution of the Navier-Stokes Equations. *Mathematics of Computation* 22.104 (1968), pp. 745–762.

[Chr69] E. B. Christoffel. Über die Transformation der homogenen Differentialausdrücke zweiten Grades. *Journal für die reine und angewandte Mathematik* 94 (1869).

[Cif20] D. Cifu. *Braddom's Physical Medicine and Rehabilitation*. 6th ed. Elsevier Health Sciences, 2020.

[CK84] J. L. C. Chang and D. Kwak. On the method of pseudo compressibility for numerically solving incompressible flows. In: *22nd Aerospace Sciences Meeting*. American Institute of Aeronautics and Astronautics, 1984.

[CK90] J. R. Cash and A. H. Karp. A Variable Order Runge-Kutta Method for Initial Value Problems with Rapidly Varying Right-Hand Sides. *ACM Transactions of Mathematical Software* 16.3 (1990), pp. 201–222.

[CKS14] A. Calderer, S. Kang, and F. Sotiropoulos. Level set immersed boundary method for coupled simulation of air/water interaction with complex floating structures. *Journal of Computational Physics* 277 (2014), pp. 201–227.

[CL00] D. Calhoun and R. J. LeVeque. A Cartesian Grid Finite-Volume Method for the Advection-Diffusion Equation in Irregular Geometries. *Journal of Computational Physics* 157.1 (2000), pp. 143–180.

[CN47] J. Crank and P. Nicolson. A practical method for numerical evaluation of solutions of partial differential equations of the heat-conduction type. *Mathematical Proceedings of the Cambridge Philosophical Society* 43.1 (1947), pp. 50–67.

[CRF17] M. V. Caruso, A. Renzulli, and G. Fragomeni. Influence of IABP-Induced Abdominal Occlusions on Aortic Hemodynamics: A Patient-Specific Computational Evaluation. *ASAIO journal* 63.2 (2017), pp. 161–167.

[CS04] G. Constantinescu and K. Squires. Numerical investigations of flow over a sphere in the subcritical and supercritical regimes. *Physics of Fluids* 16.5 (2004), pp. 1449–1466.

[CS96] K. Chun and H. Sung. Control of turbulent separated flow over a backward-facing step by local forcing. *Experiments in Fluids* 21 (1996), pp. 417–426.

[CSH86] D. K. Clarke, M. D. Salas, and H. A. Hassan. Euler calculations for multielement airfoils using Cartesian grids. *AIAA Journal* 24.3 (1986), pp. 353–358.

[D'h+91] W. D. D'haeseleer, W. N. G. Hitchon, J. D. Callen, and L. Shohet. *Flux Coordinates and Magnetic Field Structure: A Guide to a Fundamental Tool of Plasma Theory*. Springer Series in Computational Physics. Springer-Verlag, 1991.

[DL+20] C. De Lazzari, B. De Lazzari, A. Iacovoni, S. Marconi, S. Papa, M. Capoccia, R. Badagliacca, and C. D. Vizza. Intra-aortic balloon counterpulsation timing: A new numerical model for programming and training in the clinical environment. *Computer Methods and Programs in Biomedicine* 194, 105537 (2020).

[DL+22] B. De Lazzari, R. Badagliacca, D. Filomena, S. Papa, C. D. Vizza, M. Capoccia, and C. De Lazzari. CARDIOSIM: The First Italian Software Platform for Simulation of the Cardiovascular System and Mechanical Circulatory and Ventilatory Support. *Bioengineering* 9.8, 383 (2022).

[Eck17] M. Eckert. Ludwig Prandtl and the growth of fluid mechanics in Germany. A century of fluid mechanics: 1870-1970. *Comptes Rendus Mécanique* 345.7 (2017), pp. 467–476.

[EN+05] A. Emami-Naeini, S. McCabe, D. de Roover, J. Ebert, and R. Kosut. Active Control of Flow Over a Backward-Facing Step. In: *Proceedings of the 44th IEEE Conference on Decision and Control*. (Seville, Spain). 2005, pp. 7366–7371.

[Fad+00] E. Fadlun, R. Verzicco, P. Orlandi, and J. Mohd-Yusof. Combined Immersed-Boundary Finite-Difference Methods for Three-Dimensional Complex Flow Simulations. *Journal of Computational Physics* 161.1 (2000), pp. 35–60.

[Fan+20] D. Fan, L. Yang, Z. Wang, M. S. Triantafyllou, and G. E. Karniadakis. Reinforcement learning for bluff body active flow control in experiments and simulations. *Proceedings of the National Academy of Sciences* 117.42 (2020), pp. 26091–26098.

[FFSR04] R. Fernández-Feria and E. Sanmiguel-Rojas. An explicit projection method for solving incompressible flows driven by a pressure difference. *Computers & Fluids* 33.3 (2004), pp. 463–483.

[FP99] J. H. Ferziger and M. Perić. *Computational Methods for Fluid Dynamics*. 2nd ed. Berlin, Germany: Springer, 1999.

[FQV09] L. Formaggia, A. Quarteroni, and A. Veneziani, eds. *Cardiovascular Mathematics: Modeling and simulation of the circulatory system*. Vol. 1. Milano, Italia: Springer-Verlag, 2009.

[GA13] N. Gautier and J.-L. Aider. Control of the separated flow downstream of a backward-facing step using visual feedback. *Proceedings of the Royal Society A: Mathematical, Physical and Engineering Sciences* 469.2160, 20130404 (2013).

[GAL21] A. L. Gregory, A. Agarwal, and J. Lasenby. An experimental investigation to model wheezing in lungs. *Royal Society Open Science* 8.2, 201951 (2021).

[Gar90] D. K. Gartling. A test problem for outflow boundary conditions - flow over a backward - facing step. *International Journal for Numerical Methods in Fluids* 11.7 (1990), pp. 953–967.

[GB98] P. L. George and H. Borouchaki. *Delaunay Triangulation and Meshing: Application to Finite Elements*. Hermès, 1998.

[Ger+91] M. Germano, U. Piomelli, P. Moin, and W. H. Cabot. A dynamic subgridscale eddy viscosity model. *Physics of Fluids A: Fluid Dynamics* 3.7 (1991), pp. 1760–1765.

[Ger86] M. Germano. A proposal for a redefinition of the turbulent stresses in the filtered Navier-Stokes equations. *The Physics of Fluids* 29.7 (1986), pp. 2323–2324.

[Gia04] K. C. Giannakoglou. *Viscous flows in turbomachines*. In Greek. Athens, Greece: National Technical University of Athens, 2004.

[GKM00] M. Gunzburger, H. Kim, and S. Manservisi. On a shape control problem for the stationary Navier-Stokes equations. *Mathematical Modelling and Numerical Analysis* 34 (2000), pp. 1233–1258.

[GLS15] A. Gilmanov, T. B. Le, and F. Sotiropoulos. A numerical approach for simulating fluid structure interaction of flexible thin shells undergoing arbitrarily large deformations in complex domains. *Journal of Computational Physics* 300 (2015), pp. 814–843.

[Gra+15a] V. Gramigna, M. V. Caruso, M. Rossi, G. Serraino, A. Renzulli, and G. Fragomeni. A numerical analysis of the aortic blood flow pattern during pulsed cardiopulmonary bypass. *Computer methods in biomechanics and biomedical engineering* 18.14 (2015), pp. 1574–1581.

[Gra+15b] G. P. Gravlee, R. F. Davis, J. Hammon, and B. Kussman. *Cardiopulmonary Bypass and Mechanical Support: Principles And Practice, 4th ed.* Philadelphia, PA: Wolters Kluwer - Lippincott Williams & Wilkins, 2015.

[Gra75] K. Graff. *Wave motion in elastic solids*. New York, NY: Dover Publications, 1975.

[GS05] A. Gilmanov and F. Sotiropoulos. A hybrid Cartesian/immersed boundary method for simulating flows with 3D, geometrically complex, moving bodies. *Journal of Computational Physics* 207.2 (2005), pp. 457–492.

[GS07] L. Ge and F. Sotiropoulos. A numerical method for solving the 3D unsteady incompressible Navier-Stokes equations in curvilinear domains with complex immersed boundaries. *Journal of Computational Physics* 225.2 (2007), pp. 1782–1809.

[GS87] P. M. Gresho and R. L. Sani. On pressure boundary conditions for the incompressible Navier-Stokes equations. *International Journal for Numerical Methods in Fluids* 7.10 (1987), pp. 1111–1145.

[GSB03] A. Gilmanov, F. Sotiropoulos, and E. Balaras. A general reconstruction algorithm for simulating flows with complex 3D immersed boundaries on Cartesian grids. *Journal of Computational Physics* 191.2 (2003), pp. 660–669.

[GTG07] E. Greitzer, C. Tan, and M. Graf. *Internal Flow: Concepts and Applications*. Cambridge Engine Technology Series. Cambridge University Press, 2007.

[Gu+19] K. Gu, Z. Guan, X. Lin, Y. Feng, J. Feng, Y. Yang, Z. Zhang, Y. Chang, Y. Ling, and F. Wan. Numerical Analysis of Aortic Hemodynamics under the Support of Venoarterial Extracorporeal Membrane Oxygenation and Intra-Aortic Balloon Pump. *Computer Methods and Programs in Biomedicine* 182, 105041 (2019).

[Gu+22] K. Gu, S. Gao, Z. Zhang, B. Ji, and Y. Chang. Hemodynamic Effect of Pulsatile on Blood Flow Distribution with VA ECMO: A Numerical Study. *Bioengineering* 9.10, 487 (2022).

[Hak00] M. Gad el Hak. *Flow Control: Passive, Active, and Reactive Flow Management*. Cambridge, England: Cambridge University Press, 2000.

[Hak01] M. Gad el Hak. *The MEMS Handbook*. Mechanical and Aerospace Engineering Series. CRC Press, 2001.

[HS18] J. M. Hill and Y. M. Stokes. A note on Navier-Stokes equations with nonorthogonal coordinates. *The ANZIAM Journal* 59.3 (2018), pp. 335–348.

[Hua01] L. Huang. Viscous flutter of a finite elastic membrane in Poiseuille flow. *Journal of Fluids and Structures* 15.7 (2001), pp. 1061–1088.

[Hun05] T.-K. Hung. Unsteady flows with moving boundaries: Pulsating blood flows and earthquake hydrodynamics. In: *Advances in Engineering Mechanics - Reflections and Outlooks*. 2005, pp. 446–473.

[HW65] F. H. Harlow and J. E. Welch. Numerical Calculation of Time - Dependent Viscous Incompressible Flow of Fluid with Free Surface. *The Physics of Fluids* 8.12 (1965), pp. 2182–2189.

[Ise09] A. Iserles. *A first course in the numerical analysis of differential equations*. 2nd ed. Cambridge Texts in Applied Mathematics. Cambridge, England: Cambridge University Press, 2009.

[IV03] G. Iaccarino and R. Verzicco. Immersed boundary technique for turbulent flow simulations. *Applied Mechanics Reviews* 56.3 (2003), pp. 331–347.

[Jef61] H. Jeffreys. *Cartesian Tensors*. Cambridge, England: Cambridge University Press, 1961.

[Jin+04] S. Jindal, L. Long, P. Plassmann, and N. Sezer Uzol. Large Eddy Simulations around a Sphere Using Unstructured Grids. In: *34th AIAA Fluid Dynamics Conference and Exhibit*. (Portland, Oregon, USA). American Institute of Aeronautics and Astronautics, 2004.

[JS71] M. Y. Jaffrin and A. H. Shapiro. Peristaltic Pumping. *Annual Review of Fluid Mechanics* 3.1 (1971), pp. 13–37.

[Kan+11] S. Kang, A. Lightbody, C. Hill, and F. Sotiropoulos. High-resolution numerical simulation of turbulence in natural waterways. *Advances in Water Resources* 34.1 (2011), pp. 98–113.

[Kan10] S. K. Kang. Numerical modeling of turbulent flows in arbitrarily complex natural streams. PhD thesis. University of Minnesota, 2010.

[Kan86] J. van Kan. A Second-Order Accurate Pressure-Correction Scheme for Viscous Incompressible Flow. *SIAM Journal on Scientific and Statistical Computing* 7.3 (1986), pp. 870–891.

[Kho+11] A. Khosronejad, S. Kang, I. Borazjani, and F. Sotiropoulos. Curvilinear immersed boundary method for simulating coupled flow and bed morphodynamic interactions due to sediment transport phenomena. *Advances in Water Resources* 34.7 (2011), pp. 829–843.

[Kia+15] E. P. Kiachagias, A. Zymaris, I. Kavvadias, D. Papadimitriou, and K. Giannakoglou. The continuous adjoint approach to the k-ϵ turbulence model for shape optimization and optimal active control of turbulent flows. *Engineering Optimization* 47.3 (2015), pp. 370–389.

[Kis09] V. Kislik. *Liquid Membranes: Principles and Applications in Chemical Separations and Wastewater Treatment*. Amsterdam, The Netherlands: Elsevier, 2009.

[KK04] D. A. Knoll and D. E. Keyes. Jacobian-free Newton-Krylov methods: a survey of approaches and applications. *Journal of Computational Physics* 193.2 (2004), pp. 357–397.

[KM14] P. Kapiris and D. Mathioulakis. Experimental study of vortical structures in a periodically perturbed flow over a backward-facing step. *International Journal of Heat and Fluid Flow* 47 (2014), pp. 101–112.

[KM85] J. Kim and P. Moin. Application of a fractional-step method to incompressible Navier-Stokes equations. *Journal of Computational Physics* 59.2 (1985), pp. 308–323.

[KR52] S. M. Karim and L. Rosenhead. The Second Coefficient of Viscosity of Liquids and Gases. *Reviews of Modern Physics* 24.2 (1952), pp. 108–116.

[KS12] S. Kang and F. Sotiropoulos. Numerical modeling of 3D turbulent free surface flow in natural waterways. *Advances in Water Resources* 40 (2012), pp. 23–36.

[KTH13] M. J. Krause, G. Thäter, and V. Heuveline. Adjoint - based fluid flow control and optimisation with lattice Boltzmann methods. *Computers & Mathematics with Applications* 65.6 (2013), pp. 945–960.

[Kut01] W. Kutta. Beitrag zur näherungsweisen Integration totaler Differentialgleichungen. *Zeitschrift für Mathematik und Physik* 46 (1901), pp. 435–453.

[Küh06] W. Kühnel. *Differential Geometry: Curves - Surfaces - Manifolds*. Student mathematical library. American Mathematical Society, 2006.

[Lat66] T. W. Latham. Fluid motion in a peristaltic pump. MA thesis. Cambridge, MA: Massachusetts Institute of Technology, 1966.

[LE88] S. Lie and F. Engel. *Theorie der Transformationsgruppen*. B. G. Teubner Verlag, 1888.

[Leo75] A. Leonard. Energy Cascade in Large-Eddy Simulations of Turbulent Fluid Flows. In: *Turbulent Diffusion in Environmental Pollution*. Ed. by F. Frenkiel and R. Munn. Vol. 18. Advances in Geophysics. Elsevier, 1975, pp. 237–248.

[LP00] M.-C. Lai and C. S. Peskin. An Immersed Boundary Method with Formal Second-Order Accuracy and Reduced Numerical Viscosity. *Journal of Computational Physics* 160.2 (2000), pp. 705–719.

[LP95] X. Y. Luo and T. J. Pedley. A Numerical Simulation of Steady Flow in a 2-D Collapsible Channel. *Journal of Fluids and Structures* 9.2 (1995), pp. 149–174.

[LP96] X. Y. Luo and T. J. Pedley. A numerical simulation of unsteady flow in a two-dimensional collapsible channel. *Journal of Fluid Mechanics* 314 (1996), pp. 191–225.

[LS12] J. Liesen and Z. Strakoš. *Krylov Subspace Methods: Principles and Analysis*. Numerical Mathematics and Scientific Computation. Oxford University Press, Oxford, 2012.

[MA10] D. Mateescu and M. Abdo. Analysis of flows past airfoils at very low Reynolds numbers. *Proceedings of The Institution of Mechanical Engineers Part G-journal of Aerospace Engineering* 224 (2010), pp. 757–775.

[Ma15] X. Ma. Experimental Investigation of Coherent Structures Generated by Active and Passive Separation Control in Turbulent Backward-Facing Step Flow. PhD thesis. University of Minnesota, 2015.

[Man+20] C. Manopoulos, G. Savva, A. Tsoukalis, G. Vasileiou, N. Rogkas, V. Spitas, and S. Tsangaris. Optimal Design in Roller Pump System Applications for Linear Infusion. *Computation* 8.2, 35 (2020).

[McD55] D. A. McDonald. The relation of pulsatile pressure to flow in arteries. *The Journal of Physiology* 127.3 (1955), pp. 533–552.

[McN+04] A. McNamara, A. Treuille, Z. Popović, and J. Stam. Fluid Control Using the Adjoint Method. *ACM Transactions on Graphics* 23.3 (2004), pp. 449–456.

[MGW08] L. A. Matthews, D. M. Greaves, and C. J. K. Williams. Numerical simulation of viscous flow interaction with an elastic membrane. *International Journal for Numerical Methods in Fluids* 57.11 (2008), pp. 1577–1602.

[MH04] T. Morioka and S. Honami. Dynamic Characteristics in a Control System of Backward Facing Step Flow by Vortex Generator Jets. In: *2nd AIAA Flow Control Conference*. (Portland, Oregon, U.S.A.). 2004.

[MI05] R. Mittal and G. Iaccarino. Immersed boundary methods. *Annual Review of Fluid Mechanics* 37.1 (2005), pp. 239–261.

[MMN22] H. Muir, L. Michael, and N. Nikiforakis. Numerical Methodologies for Magnetohydrodynamic Flow Control for Hypersonic Vehicles. In: *Active Flow and Combustion Control 2021*. Ed. by R. King and D. Peitsch. Cham, Switzerland: Springer International Publishing, 2022, pp. 336–355.

[MMnS10] D. Mateescu, M. Muñoz, and O. Scholz. Analysis of unsteady confined viscous flows with variable inflow velocity and oscillating walls. *Journal of Fluids Engineering* 132.4, 041105 (2010).

[MMT21] I. Moulinos, C. Manopoulos, and S. Tsangaris. A Computational Analysis for Active Flow and Pressure Control Using Moving Roller Peristalsis. *Computation* 9.12, 144 (2021).

[MMT22] I. Moulinos, C. Manopoulos, and S. Tsangaris. Computational Analysis of Active and Passive Flow Control for Backward Facing Step. *Computation* 10.1, 12 (2022).

[MMT23] I. Moulinos, C. Manopoulos, and S. Tsangaris. Modification of Poiseuille Flow to a Pulsating Flow Using a Periodically Expanding-Contracting Balloon. *Fluids* 8.4, 129 (2023).

[Mor+84] J. J. Moré, D. C. Sorensen, B. S. Garbow, and K. E. Hillstrom. The Minpack Project. In: *Sources and development of mathematical software*. Ed. by W. R. Cowell. Computational Mathematics. Prentice-Hall, 1984. Chap. 5, pp. 88–111.

[MR17] A. Mandawat and S. V. Rao. Percutaneous Mechanical Circulatory Support Devices in Cardiogenic Shock. *Circulation: Cardiovascular Interventions* 10.5, e004337 (2017).

[MRF95] J. Magnaudet, M. Rivero, and J. Fabre. Accelerated flows past a rigid sphere or a spherical bubble. Part 1. Steady straining flow. *Journal of Fluid Mechanics* 284 (1995), pp. 97–135.

[MS17] X. Ma and A. Schröder. Analysis of flapping motion of reattaching shear layer behind a two-dimensional backward-facing step. *Physics of Fluids* 29.11, 115104 (2017).

[MSM04] S. O. Macheret, M. N. Shneider, and R. B. Miles. Magnetohydrodynamic and Electrohydrodynamic Control of Hypersonic Flows of Weakly Ionized Plasmas. *AIAA Journal* 42.7 (2004), pp. 1378–1387.

[MT97] T. Möller and B. Trumbore. Fast, Minimum Storage Ray-Triangle Intersection. *Journal of Graphics Tools* 2.1 (1997), pp. 21–28.

[MTK62] S. D. Moulopoulos, S. Topaz, and W. J. Kolff. Diastolic balloon pumping (with carbon dioxide) in the aorta—A mechanical assistance to the failing circulation. *American Heart Journal* 63.5 (1962), pp. 669–675.

[MV01] D. Mateescu and D. A. Venditti. Unsteady confined viscous flows with oscillating walls and multiple separation regions over a downstream - facing step. *Journal of Fluids and Structures* 15.8 (2001), pp. 1187–1205.

[MY97] J. Mohd-Yusof. Combined Immersed Boundary / B-Spline Methods for Simulation of Flow in Complex Geometries. *Annual Research Briefs, Center for Turbulence Research* (1997), pp. 317–328.

[Nah12] S. Nahar. Steady and Unsteady Flow Characteristics of non-Newtonian Fluids in Deformed Elastic Tubes. PhD thesis. Swiss Federal Institute of Technology (ETH), 2012.

[Nic+22] W. W. Nichols, M. O'Rourke, E. R. Elelman, and C. E. Vlachopoulos. *McDonalds Blood Flow in Arteries: Theoretical, Experimental and Clinical Principles*. 7th ed. Boca Raton, FL: CRC Press, 2022.

[NJW10] S. Nahar, S. A. K. Jeelani, and E. J. Windhab. Steady and Unsteady Flow Characteristics of non-Newtonian Fluids in Deformed Elastic Tubes. In: *Proceedings of the 7th International Symposium on Ultrasonic Doppler Methods for Fluid mechanics and Fluid Engineering*. (Gothenburg, Sweden). Ed. by J. Wiklund, E. Levenstam Bragd, and S. Manneville. Gothenburg, Sweden: Chalmers University of Technology, 2010, pp. 61–64.

[OH12] D. M. Ouweneel and J. P. S. Henriques. Percutaneous cardiac support devices for cardiogenic shock: current indications and recommendations. *Heart* 98.16 (2012), pp. 1246–1254.

[ON04] M. S. Olufsen and A. Nadim. On deriving lumped models for blood flow and pressure in the systemic arteries. *Mathematical Biosciences & Engineering* 1.1 (2004), pp. 61–80.

[Pap+02] T. G. Papaioannou, D. S. Mathioulakis, J. N. Nanas, S. G. Tsangaris, S. F. Stamatelopoulos, and S. D. Moulopoulos. Arterial compliance is a main variable determining the effectiveness of intra-aortic balloon counterpulsation: quantitative data from an in vitro study. *Medical Engineering & Physics* 24.4 (2002).

[Pap+04] T. Papaioannou, D. Mathioulakis, K. Stamatelopoulos, E. Gialafos, J. Lekakis, J. Nanas, S. Stamatelopoulos, and S. Tsangaris. New aspects on the role of blood pressure and arterial stiffness in mechanical assistance by intra-aortic balloon pump: In-vitro data and their application in clinical practice. *Artificial Organs* 28.8 (2004), pp. 717 –727.

[Par+16] H. Parissis, V. Graham, S. Lampridis, M.-C. Lau, G. Hooks, and P. Mhandu. IABP: History - evolution - pathophysiology - indications: What we need to know. *Journal of Cardiothoracic Surgery* 11, 122 (2016).

[Pat80] S. V. Patankar. *Numerical heat transfer and fluid flow*. Series on Computational Methods in Mechanics and Thermal Science. Hemisphere Publishing Corporation (CRC Press, Taylor & Francis Group), 1980.

[Pen+11] G. Pennati, C. Corsini, D. Cosentino, T.-Y. Hsia, V. S. Luisi, G. Dubini, and F. Migliavacca. Boundary conditions of patient-specific fluid dynamics modelling of cavopulmonary connections: possible adaptation of pulmonary resistances results in a critical issue for a virtual surgical planning. *Interface Focus* 1.3 (2011), pp. 297–307.

[Pes72] C. S. Peskin. Flow patterns around heart valves: A numerical method. *Journal of Computational Physics* 10.2 (1972), pp. 252–271.

[Pin+10] A. Pinelli, I. Z. Naqavi, U. Piomelli, and J. Favier. Immersed-boundary methods for general finite-difference and finite-volume Navier-Stokes solvers. *Journal of Computational Physics* 229.24 (2010), pp. 9073 –9091.

[PM06] J. G. Proakis and D. G. Manolakis. *Digital Signal Processing*. 4th ed. Prentice Hall, 2006.

[Poi46] J. L. M. Poiseuille. Recherches expérimentales sur Ie mouvement des liquides dans les tubes de très-petits diamètres. In: vol. IX. Mémoires presentés par divers savants à l'Academie Royale des Sciences de l'Institut de France, 1846, pp. 433–544.

[Pop00] S. B. Pope. *Turbulent Flows*. Cambridge, England: Cambridge University Press, 2000.

[Pra04] L. Prandtl. Über Flüssigkeitsbewegung bei sehr kleiner Reibung. In: *Verhandlungen des III. Internationalen Mathematiker Kongresses*. (Heidelberg, Germany). Leipzig, Germany: B.G. Teubner, 1904, pp. 485–491.

[Pre+07] W. H. Press, S. A. Teukolsky, W. T. Vetterling, and B. P. Flannery. *Numerical Recipes 3rd Edition: The Art of Scientific Computing*. Cambridge University Press, 2007.

[PS05] T. Papaioannou and C. Stefanadis. Basic principles of the intraaortic balloon pump and mechanisms affecting its performance. *ASAIO Journal* 51.3 (2005), pp. 296 –300.

[PS72] S. V. Patankar and D. B. Spalding. A calculation procedure for heat, mass and momentum transfer in three-dimensional parabolic flows. *International Journal of Heat and Mass Transfer* 15.10 (1972), pp. 1787–1806.

[PT97] T. Pappou and S. Tsangaris. Development of an artificial compressibility methodology using flux vector splitting. *International Journal for Numerical Methods in Fluid Mechanics* 25.5 (1997), pp. 523–545.

[Rab+20] J. Rabault, F. Ren, W. Zhang, H. Tang, and H. Xu. Deep reinforcement learning in fluid mechanics: A promising method for both active flow control and shape optimization. *Journal of Hydrodynamics* 32.2 (2020), pp. 234–246.

[RE55] R. S. Rivlin and J. L. Ericksen. Stress-Deformation Relations for Isotropic Materials. *Journal of Rational Mechanics and Analysis* 4 (1955), pp. 323–425.

[RHT20] F. Ren, H. Hu, and H. Tang. Active flow control using machine learning: A brief review. *Journal of Hydrodynamics* 32.2 (2020), pp. 247–253.

[RK19] J. Rabault and A. Kuhnle. Accelerating deep reinforcement learning strategies of flow control through a multi-environment approach. *Physics of Fluids* 31.9, 094105 (2019).

[RKV91] M. Rosenfeld, D. Kwak, and M. Vinokur. A fractional step solution method for the unsteady incompressible Navier-Stokes equations in generalized coordinate systems. *Journal of Computational Physics* 94.1 (1991), pp. 102–137.

[RLC00] G. M. M. Ricci and T. Levi-Civita. Méthodes de calcul différentiel absolu et leurs applications. *Mathematische Annalen* 54.1 (1900), pp. 125–201.

[Rom+13] F. Romeo, M. C. Acconcia, D. Sergi, A. Romeo, S. Muscoli, S. Valente, G. F. Gensini, F. Chiarotti, and Q. Caretta. The outcome of intra - aortic balloon pump support in acute myocardial infarction complicated by cardiogenic shock according to the type of revascularization: A comprehensive meta - analysis. *American Heart Journal* 165.5 (2013), pp. 679–692.

[Ros+21] R. Rossini, S. Valente, F. Colivicchi, C. Baldi, P. Caldarola, D. Chiappetta, M. Cipriani, M. Ferlini, N. Gasparetto, R. Gilardi, S. Giubilato, M. Imazio, M. Marini, L. Roncon, F. Scotto di Uccio, A. Somaschini, C. Sorini Dini, P. Trambaiolo, T. Usmiani, M. M. Gulizia, and D. Gabrielli. ANMCO Position Paper: Role of intra-aortic balloon pump in patients with acute advanced heart failure and cardiogenic shock. *European Heart Journal Supplements* 23 (2021), pp. C204–C220.

[RRR11] R. Roy, F. Rios, and D. Riahi. Mathematical Models for Flow of Chyme during Gastrointestinal Endoscopy. *Applied Mathematics* 2.5 (2011), pp. 600–607.

[RRT21] F. Ren, J. Rabault, and H. Tang. Applying deep reinforcement learning to active flow control in weakly turbulent conditions. *Physics of Fluids* 33.3, 037121 (2021).

[RS87] J. W. Ruge and K. Stüben. Algebraic Multigrid. In: *Multigrid Methods*. Ed. by S. F. McCormick. Vol. 3. Frontiers in applied mathematics. Society for Industrial and Applied Mathematics, 1987. Chap. 4, pp. 73–130.

[Run95] C. Runge. Ueber die numerische Auflösung von Differentialgleichungen. *Mathematische Annalen* 46 (1895), pp. 167–178.

[Rut90] A. Rutherford. *Vectors, Tensors and the Basic Equations of Fluid Mechanics*. Dover Books on Mathematics. Dover Publications, 1990.

[RW19] B. Riemann and H. Weyl. *Über die Hypothesen: welche der Geometrie zu Grunde liegen*. Berlin - Heidelberg, Germany: Springer-Verlag, 1919.

[RZ10] M. P. Rumpfkeil and D. W. Zingg. The optimal control of unsteady flows with a discrete adjoint method. *Optimization and Engineering* 11 (2010), pp. 5–22.

[SA08] J. H. Spurk and N. Aksel. *Fluid Mechanics*. 2nd ed. Berlin - Heidelberg, Germany: Springer, 2008.

[Sag06] P. Sagaut. *Large eddy simulation for incompressible flows: An introduction*. 3rd ed. Scientific computation. Berlin - Heidelber, Germany: Springer-Verlag, 2006.

[SB18] R. S. Sutton and A. G. Barto. *Reinforcement Learning: An Introduction*. 2nd ed. The MIT Press, 2018.

[Sen+15] I. Senocak, M. Sandusky, R. DeLeon, D. Wade, K. Felzien, and M. Budnikova. An Immersed Boundary Geometric Preprocessor for Arbitrarily Complex Terrain and Geometry. *Journal of Atmospheric and Oceanic Technology* 32.11 (2015), pp. 2075–2087.

[SFS04] K. Sakuraba, K. Fukazawa, and M. Sano. Control of Turbulent Channel Flow over a Backward-Facing Step by Suction or Injection. *Hear Transfer* 33.8 (2004), pp. 490–504.

[Sho00] A. C. Shore. Capillaroscopy and the measurement of capillary pressure. *British Journal of Clinical Pharmacology* 50.6 (2000), pp. 501–513.

[Sim97] J. G. Simmonds. *A Brief on Tensor Analysis*. Undergraduate Texts in Mathematics. New York, NY: Springer, 1997.

[SJW69] A. H. Shapiro, M. Y. Jaffrin, and S. L. Weinberg. Peristaltic pumping with long wavelengths at low Reynolds number. *Journal of Fluid Mechanics* 37.4 (1969), pp. 799–825.

[Sma63] J. Smagorinsky. General Circulation Experiments with the Primitive Equations I. The Basic Experiment. *Monthly Weather Review* 91.3 (1963), pp. 99–164.

[Smi86] G. D. Smith. *Numerical Solution of Partial Differential Equations: Finite Difference Methods*. 3rd ed. Oxford Applied Mathematics and Computing Science Series. Oxford University Press, 1986.

[Soh88] J. L. Sohn. Evaluation of FIDAP on some classical laminar and turbulent benchmarks. *International Journal for Numerical Methods in Fluids* 8.12 (1988), pp. 1469–1490.

[SS85] L. M. Srivastava and V. P. Srivastava. Peristaltic Transport of a non-Newtonian Fluid: Applications to Vas Deferens and Small Intestine. *Annals of Biomedical Engineering* 13.2 (1985), pp. 137–153.

[SS86] Y. Saad and M. H. Schultz. GMRES: A Generalized Minimal Residual Algorithm for Solving Nonsymmetric Linear Systems. *SIAM Journal on Scientific and Statistical Computing* 7.3 (1986), pp. 856–869.

[SSJ13] A. C. Saleel, A. Shaija, and S. Jayaraj. On Simulation of Backward Facing Step Flow Using Immersed Boundary Method. *American Journal of Fluid Dynamics* 3.2 (2013), pp. 9–19.

[ST68] A. H. Sacks and E. G. Tickner. The compressibility of blood. *Biorheology* 5.4 (1968), pp. 271–274.

[Sto+15] K. Stokos, S. Vrahliotis, T. Pappou, and S. Tsangaris. Development and validation of an incompressible Navier-Stokes solver including convective heat transfer. *International Journal of Numerical Methods for Heat & Fluid Flow* 25.4 (2015), pp. 861–886.

[Sto45] G. G. Stokes. On the Theories of the Internal Friction of Fluids in Motion, and of the Equilibrium and Motion of Elastic Solids. *Transactions of Cambridge Philosophical Society* VIII (1845), pp. 287–319.

[SY14] F. Sotiropoulos and X. Yang. Immersed boundary methods for simulating fluid-structure interaction. *Progress in Aerospace Sciences* 65 (2014), pp. 1–21.

[SYR92] N. Stergiopulos, D. F. Young, and T. R. Rogge. Computer simulation of arterial flow with applications to arterial and aortic stenoses. *Journal of Biomechanics* 25.12 (1992), pp. 1477 –1488.

[Tat+09] K. Tatsumi, Y. Matsunaga, Y. Miwa, and K. Nakabe. Numerical study on fluid-flow characteristics of peristaltic pump. *Progress in Computational Fluid Dynamics* 9.3-5 (2009), pp. 176–182.

[TF03] Y.-H. Tseng and Y.-H. Ferziger. A ghost-cell immersed boundary method for flow in complex geometry. *Journal of Computational Physics* 192.2 (2003), pp. 593–623.

[Thi+12] H. Thiele, U. Zeymer, F.-J. Neumann, M. Ferenc, H.-G. Olbrich, J. Hausleiter, G. Richardt, M. Hennersdorf, K. Empen, G. Fuernau, S. Desch, I. Eitel, R. Hambrecht, J. Fuhrmann, M. Böhm, H. Ebelt, S. Schneider, G. Schuler, and K. Werdan. Intraaortic Balloon Support for Myocardial Infarction with Cardiogenic Shock. *New England Journal of Medicine* 367.14 (2012), pp. 1287–1296.

[TP00] S. Tsangaris and T. Pappou. Flow investigation in deformable arteries. *Intra and Extracorporeal Cardiovascular Fluid Dynamics* 33.8 (2000). Ed. by P. Verdonck and K. Perktold, pp. 291–332.

[TPP10] J. Tihon, V. Penkavova, and M. Pantzali. The effect of inlet pulsations on the backward-facing step flow. *European Journal of Mechanics - B/Fluids* 29.3 (2010), pp. 224–235.

[Tri88] D. Tritton. *Physical Fluid Dynamics*. Oxford Science Publications. Clarendon Press, 1988.

[Tro+12] X. Trompoukis, V. Asouti, I. Kampolis, and K. Giannakoglou. Chapter 17 - CUDA Implementation of Vertex-Centered, Finite Volume CFD Methods on Unstructured Grids with Flow Control Applications. In: *GPU Computing Gems Jade Edition*. Ed. by W.-m. W. Hwu. Applications of GPU Computing Series. Cambridge, MA: Morgan Kaufmann, 2012, pp. 207–223.

[TS88] S. Tsangaris and N. Stergiopulos. The inverse Womersley problem for pulsatile flow in a straight rigid tube. *Journal of Biomechanics* 21.3 (1988), pp. 263–266.

[Tsa05] S. Tsangaris. *Fluid mechanics*. In Greek. Symeon, 2005.

[Tsa84] S. Tsangaris. Oscillatory flow of an incompressible, viscous fluid in a straight annular pipe. *Journal de Mécanique Théorique et Appliquée* 3.3 (1984), pp. 467–478.

[Tse+12] K. M. Tse, R. Chang, H. P. Lee, S. P. Lim, S. K. Venkatesh, and P. Ho. A computational fluid dynamics study on geometrical influence of the aorta on haemodynamics. *European Journal of Cardio-Thoracic Surgery* 43.4 (2012), pp. 829–838.

[Tsu+14] Y.-Y. Tsui, D.-C. Guo, S.-H. Chen, and S.-W. Lin. Pumping Flow in a Channel With a Peristaltic Wall. *ASME Journal of Fluids Engineering* 136.2, 021202 (2014).

[TVI14] M. de Tullio, R. Verzicco, and G. Iaccarino. Immersed Boundary Technique for Large - Eddy - Simulation. Von Karman Institute Lecture Series (2014), pp. 1–97.

[Uch56] S. Uchida. The pulsating viscous flow superposed on the steady laminar motion of incompressible fluid in a circular pipe. *Zeitschrift für Angewandte Mathematik und Physik (ZAMP)* 7.5 (1956), pp. 403–422.

[Ver60] P. Verma. The Pulsating Viscous Flow Superposed on the Steady Laminar Motion of Incompressible Fluid in a Tube of Elliptic Section. *Proceedings of the National Institute of Sciences of India, Part A* 26.3 (1960), pp. 282–297.

[Vfs] *VFS - WIND Virtual Flow Simulator*. https://safl-cfd-lab.github.io/VFS-Wind/.

[Vie69] J. Viecelli. A method for including arbitrary external boundaries in the MAC incompressible fluid computing technique. *Journal of Computational Physics* 4.4 (1969), pp. 543–551.

[Vin+22] R. Vinuesa, O. Lehmkuhl, A. Lozano-Durn, and J. Rabault. Flow Control in Wings and Discovery of Novel Approaches via Deep Reinforcement Learning. *Fluids* 7.2, 62 (2022).

[VPT12] S. Vrahliotis, T. Pappou, and S. Tsangaris. Artificial Compressibility 3-D Navier-Stokes Solver for Unsteady Incompressible Flows with Hybrid Grids. *Engineering Applications of Computational Fluid Mechanics* 6.2 (2012), pp. 248–270.

[VSG21] Y. Vrionis, K. Samouchos, and K. Giannakoglou. Topology optimization in fluid mechanics using continuous adjoint and the cut-cell method. *Computers & Mathematics with Applications* 97 (2021), pp. 286–297.

[Wes+19] N. Westerhof, N. Stergiopulos, M. Noble, and B. Westerhof. *Snapshots of Hemodynamics: An Aid for Clinical Research and Graduate Education*. Cham, Switzerland: Springer, 2019.

[Wes+69] N. Westerhof, F. Bosman, C. J. De Vries, and A. Noordergraaf. Analog studies of the human systemic arterial tree. *Journal of Biomechanics* 2.2 (1969), pp. 121 –143.

[WES71] S. L. Weinberg, E. C. Eckstein, and A. H. Shapiro. An experimental study of peristaltic pumping. *Journal of Fluid Mechanics* 49.3 (1971), pp. 461–479.

[WF18] J. Wang and L. Feng. *Flow Control Techniques and Applications*. Cambridge Aerospace Series. Cambridge, England: Cambridge University Press, 2018.

[Whi06] F. M. White. *Viscous Fluid Flow*. McGraw-Hill international edition. McGraw-Hill, 2006.

[WL16] B. Wang and H. Li. POD analysis of flow over a backward-facing step forced by right-angle-shaped plasma actuator. *SpringerPlus* 5.1, 795 (2016).

[Wom55] J. R. Womersley. Method for the calculation of velocity, rate of flow and viscous drag in arteries when the pressure gradient is known. *The Journal of Physiology* 127.3 (1955), pp. 553–563.

[Wom57] J. Womersley. *An Elastic Tube Theory of Pulse Transmission and Oscillatory Flow in Mammalian Arteries*. WADC technical report TR 56-614. 1957.

[Xie+21] Y. Xie, D. Yang, H. Yu, K. Wang, and Q. Xie. Development of Intra-Aortic Balloon Pump with Vascular Stent and Vitro Simulation Verification. In: *2021 IEEE 9th International Conference on Bioinformatics and Computational Biology (ICBCB)*. 2021, pp. 174–179.

[YAC81] K. Yasuda, R. C. Armstrong, and R. E. Cohen. Shear flow properties of concentrated solutions of linear and star branched polystyrenes. *Rheologica Acta* 20.2 (1981), pp. 163–178.

[Yan+15] X. Yang, F. Sotiropoulos, R. Conzemius, J. Wachtler, and M. Strong. Large-eddy simulation of turbulent flow past wind turbines/farms: The Virtual Wind Simulator (VWiS). *Wind Energy* 18.12 (2015), pp. 2025–2045.

[Yan+21] D. Yang, S. He, L. Shen, and X. Luo. Large eddy simulation coupled with immersed boundary method for turbulent flows over a backward facing step. *Proceedings of the Institution of Mechanical Engineers, Part C: Journal of Mechanical Engineering Science* 235.15 (2021), pp. 2705–2714.

[YB19] M. Yousefzadeh and I. Battiato. High order ghost-cell immersed boundary method for generalized boundary conditions. *International Journal of Heat and Mass Transfer* 137 (2019), pp. 585–598.

[YHP94] H. Q. Yang, S. D. Habchi, and A. J. Przekwas. General strong conservation formulation of Navier-Stokes equations in nonorthogonal curvilinear coordinates. *AIAA Journal* 32.5 (1994), pp. 936–941.

[YM08] D. You and P. Moin. Active control of flow separation over an airfoil using synthetic jets. *Journal of Fluids and Structures* 24.8 (2008), pp. 1349–1357.

[Zam00] M. M. Zamir. *The physics of pulsatile flow.* Biological Physics Series. New York, NY: AIP Press / Springer, 2000.

[Zam05] M. Zamir. *The Physics of Coronary Blood Flow*. Biological and Medical Physics, Biomedical Engineering series. New York, NY: AIP Press / Springer, 2005.

[Zam16] M. M. Zamir. *Hemo-Dynamics*. Biological and Medical Physics, Biomedical Engineering. Cham, Switzerland: AIP Press / Springer, 2016.

[Zho+14] X. Zhou, X. Liang, G. Zhao, Y. Su, and Y. Wang. A New Computational Fluid Dynamics Method for In-Depth Investigation of Flow Dynamics in Roller Pump Systems. *Artificial Organs* 38.7 (2014), E106–E117.

[Zym+13] A. Zymaris, D. Papadimitriou, E. M. Papoutsis-Kiachagias, K. C. Giannakoglou, and C. Othmer. The continuous adjoint method as a guide for the design of flow control systems based on jets. *Engineering Computations: International Journal for Computer-Aided Engineering* 30.4 (2013), pp. 494–520.

Εθνικό Μετσόβιο Πολυτεχνείο

Σχολή Μηχανολόγων Μηχανικών

Τομέας Ρευστών

Εργαστήριο Βιορευστομηχανικής και Βιοϊατρικής Τεχνολογίας

Υπολογιστική Προσομοίωση Ελέγχου Ροών με τη Μέθοδο του Εμβαπτισμένου Ορίου

Διδακτορική διατριβή
Εκτενής περίληψη

Ιωσήφ Κ. Μουλίνος

Επιβλέπων: Σωκράτης Τσαγγάρης
Ομ. Καθηγητής ΕΜΠ

Αθήνα 2022

Εθνικό Μετσόβιο Πολυτεχνείο
Σχολή Μηχανολόγων Μηχανικών
Τομέας Ρευστών
Εργαστήριο Βιορευστομηχανικής και Βιοϊατρικής Τεχνολογίας

Υπολογιστική προσομοίωση ελέγχου ροών με τη μέθοδο του εμβαπτισμένου ορίου

Διδακτορική διατριβή

Ιωσήφ Κ. Μουλίνος

Επιβλέπων: Σωκράτης Τσαγγάρης, Ομ. Καθηγητής,
Σχολή Μηχανολόγων Μηχανικών ΕΜΠ

Εξεταστική επιτροπή:

1. Σπυρίδων Βουτσινάς, Καθηγητής, Σχολή Μηχανολόγων Μηχανικών ΕΜΠ,
   Μέλος της Τριμελούς Συμβουλευτικής Επιτροπής
2. Ιωάννης Αναγνωστόπουλος, Καθηγητής, Σχολή Μηχανολόγων Μηχανικών ΕΜΠ,
   Μέλος της Τριμελούς Συμβουλευτικής Επιτροπής
3. Δημήτριος Μαθιουλάκης, Καθηγητής, Σχολή Μηχανολόγων Μηχανικών ΕΜΠ
4. Κυριάκος Γιαννάκογλου, Καθηγητής, Σχολή Μηχανολόγων Μηχανικών ΕΜΠ
5. Δημήτριος Μπούρης, Καθηγητής, Σχολή Μηχανολόγων Μηχανικών ΕΜΠ
6. Βασίλειος Ριζιώτης, Αναπληρωτής Καθηγητής, Σχολή Μηχανολόγων Μηχανικών ΕΜΠ
7. Χρήστος Μανόπουλος, Επίκουρος Καθηγητής, Σχολή Μηχανολόγων Μηχανικών ΕΜΠ

Αθήνα 2022

Υπολογιστική προσομοίωση ελέγχου ροών με τη μέθοδο του εμβαπτισμένου ορίου

Ιωσήφ Κ. Μουλίνος

Διδακτορική διατριβή

Επιβλέπων: Σωκράτης Τσαγγάρης, Ομ. Καθηγητής ΕΜΠ

Περίληψη

Ο έλεγχος ροής αποτελεί την απώτερη εφαρμογή της ρευστοδυναμικής. Μη παραμορφώσιμα και παραμορφώσιμα κινούμενα στερεά μέρη χρησιμοποιούνται σε πληθώρα τεχνικών ρύθμισης των παραμέτρων και των χαρακτηριστικών της ροής. Η υπολογιστική πρόλεξη ροών που εμπίπτουν σε αυτή την κατηγορία, μέσω κλασσικών μεθόδων με προσαρμογή στο σώμα, απαιτεί την επαναγένεση του υπολογιστικού πλέγματος για κάθε νέο βήμα στο πεδίο του διακριτού χρόνου. Στον αντίποδα, οι μέθοδοι εμβαπτισμένου ορίου επιτυγχάνουν ολοκλήρωση στο χρόνο των εξισώσεων ροής για μεταβαλλόμενη στον χρόνο γεωμετρία χωρίου ρευστού, χρησιμοποιώντας αμετάβλητο υποκείμενο πλέγμα κατά τον υπολογισμό.

Στην προσέγγιση δομημένου πλέγματος, η κλάση των γεωμετρικών πεδίων στα οποία το πλέγμα είναι προσαρμόσιμο, επεκτείνεται σημαντικά για την οικογένεια των καμπυλόγραμμων πλεγμάτων εν συγκρίσει με εκείνη των Καρτεσιανών. Η προσαρμογή του υποκείμενου πλέγματος στο σταθερό τμήμα του ορίου του πεδίου ρευστού είναι επιθυμητό χαρακτηριστικό καθώς επιτρέπει την άμεση επιβολή των οριακών συνθηκών, επιτυγχάνοντας μειωμένη πολυπλοκότητα της διαδικασίας. Το προκύπτον σχήμα σε αυτή την περίπτωση παρουσιάζει επίσης αυξημένη ακρίβεια για μεθόδους εμβαπτισμένου ορίου που εφαρμόζουν σχήματα προσέγγισης στις εμβαπτισμένες επιφάνειες.

Στην παρούσα διατριβή εφαρμόζεται δομημένη, καμπυλόγραμμη μέθοδος εμβαπτισμένου ορίου, επεκτεταμένη με χαρακτηριστικά αλληλεπίδρασης ρευστού-παραμορφώσιμου στερεού, για την ανάλυση του ελέγχου ροής με μία πλειάδα τεχνικών:

- Μόνιμη και μη μόνιμη αποκολλημένη ροή σε αλληλεπίδραση με ενεργά και παθητικά κινούμενες επιφάνειες
- Περισταλτική κίνηση γενικευμένων Νευτώνειων ρευστών
- Παλμική ροή από διογκούμενο - συρρικνούμενο μπαλόνι.

Η έρευνα προσανατολίζεται στην κατεύθυνση των ερωτήσεων:

- Πώς μπορεί να μειωθεί το μήκος της αποκολλημένης ροής, μέσω ενός κινούμενου τμήματος της επιφάνειας πάνω από την οποία το οριακό στρώμα είναι αποκολλημένο;
- Πόσο αποδοτικός είναι ο έλεγχος της ανακυκλοφορίας μέσω παθητικής μεμβράνης;
- Ποια είναι η επίδραση της ταχύτητας, του πλάτους και του πλήθους κορυφών του περισταλτικού κύματος στην αποδοτικότητα μεταφοράς;
- Πώς συμπεριφέρονται κατά την περίσταλση τα διατμητικά λεπτυνόμενα ρευστά σε σύγκριση με τα Νευτώνεια ρευστά;
- Πώς επηρεάζει το πλάτος ταλάντωσης της μεμβράνης την πίεση εξόδου αντλίας μπαλονιού;
- Ποιοι παράγοντες καθορίζουν την διαφορά φάσης μεταξύ των κυμάτων ρυθμού αλλαγής όγκου του μπαλονιού και πίεσης εξόδου;

Η μέθοδος εμβαπτισμένου ορίου που χρησιμοποιήθηκε προτείνεται ως κατάλληλη για την προσομοίωση των μεθόδων χειραγώγησης της ροής που μελετώνται. Η πρόλεξη με την μέθοδο εμβαπτισμένου ορίου, κατόπιν επέκτασης για γενικευμένα Νευτώνεια ρευστά, εμφανίζει υψηλό βαθμό σύμπτωσης με τα αποτελέσματα που λαμβάνονται από προσομοίωση με τις κλασσικές μεθόδους. Εισάγεται η ελαστική μεμβράνη για τον έλεγχο της αποκολλημένης ροής και αναλύεται η αλληλεπίδραση ρευστού - στερεού της μόνιμης και της μη μόνιμης ροής με το παθητικό μέσο. Παραμετρική διερεύνηση του πλήθους των αντιγράφων του κύματος συστολής για ευθύγραμμη περισταλτική αντλία αναδεικνύει τα πλεονεκτήματα της πολυκύλινδρης διάταξης. Ευάριθμα ρευστά ενδιαφέροντος, όπως το αίμα είναι μη Νευτώνεια. Ερευνάται η επίδραση της συμπεριφοράς διατμητικής λέπτυνσης στις χαρακτηριστικές άντλησης. Παρουσιάζεται η απόδοση ως προς την πίεση εξόδου και το χρονομεταβλητό πεδίο ροής για άντληση μέσω μπαλονιού σε ευθύγραμμη αρτηρία.

Λέξεις κλειδιά: Υπολογιστική ρευστοδυναμική, Εξισώσεις Navier-Stokes, Καμπυλόγραμμη μέθοδος εμβαπτισμένου ορίου, Αλληλεπίδραση ρευστού - στερεού, Ενεργός - παθητικός έλεγχος ροής, Γενικευμένο καμπυλόγραμμο σύστημα συντεταγμένων, Ελαστική μεμβράνη, Περίσταλση, Μη Νευτώνεια ρευστά, Παλμική ροή, Ενδοαορτική αντλία μπαλονιού, Αντιώθηση, Βιοϊατρική τεχνολογία

Περιεχόμενα

Κεφάλαιο 1

Εισαγωγή

1.1 Έλεγχος ροής

Ο έλεγχος ροής είναι ένας κλάδος της ρευστοδυναμικής ο οποίος προσελκύει έντονα το ενδιαφέρον των ερευνητών λόγω της πληθώρας και της σημασίας των εφαρμογών του. Η εργασία του Prandtl που παρουσιάστηκε στο τρίτο διεθνές συνέδριο μαθηματικών το 1904, εισάγοντας το οριακό στρώμα και τον έλεγχό του, ήταν μία τομή στο γνωστικό αυτό πεδίο [Pra04; Eck17]. Μείζονες στόχους του ελέγχου της ροής αποτελούν ο καθορισμός της παροχής όγκου, η μείωση της οπισθέλκουσας, η ενίσχυση της άνωσης, η αύξηση της ανάμιξης, η καταστολή του θορύβου και ο καθορισμός της πίεσης. Οι μέθοδοι ελέγχου σκοπεύουν συνήθως στην καταστολή ή την πρόκληση της αποκόλλησης της ροής, τον χωρικό προσδιορισμό της μετάβασης από γραμμική σε τυρβώδη ροή και το θετικό ή αρνητικό κέρδος που προστίθεται στην τύρβη [Hak01]. Για την επιβολή των ζητούμενων συνθηκών, εφαρμόζεται ενεργός, παθητικός ή αντιδραστικός έλεγχος. Πληθώρα τεχνικών ελέγχου ροής έχουν εφαρμοστεί, όπως εμφύσηση-αναρρόφηση ροής, γεννήτορες στροβίλων, μεμβράνες, πτερύγια, πηγές θερμότητας και ηλεκτρομαγνητικά πεδία [WF18; BBC17; MMN22; Hak00; Sto+15; BLW08; MSM04].

Βελτιστοποίηση του ελέγχου έχει προταθεί μέσω υπολογισμού παραγώγων ευαισθησίας, δηλαδή της συζυγούς μεθόδου [GKM00; Kia+15; Zym+13; McN+04; KTH13; Bou21; RZ10] ή με χρήση στοχαστικών μεθόδων όπως οι εξελικτικοί αλγόριθμοι [Bin+18; AG09; Tro+12].

Για την εύρεση του μέγιστου κέρδους, για δεδομένο στόχο χαρακτηριστικών της ροής, έχουν ακόμα εφαρμοστεί αλγόριθμοι μηχανικής μάθησης. Στο πλαίσιο της βαθιάς μάθησης με ενίσχυση [SB18] η μεγιστοποίηση σταθμισμένης ανταμοιβής λαμβάνεται ως

$$v^*(s) = \max_{\pi} \lim_{T\to\infty} \mathbb{E}_{\pi}\left[\sum_{k=0}^{T} \gamma^k R_{t+k+1} \,\middle|\, S_t = s\right], \forall s \in S, \tag{1.1}$$

όπου v^* είναι η βέλτιστη αμοιβή, π είναι η πολιτική του δικτύου, δηλαδή η πιθανότητα πραγματοποίησης κάποιας ενέργειας σε δεδομένη κατάσταση, R_{t+k+1} είναι η αμοιβή στο βήμα $t+k+1$, S_t είναι η παρούσα κατάσταση, και S είναι το σύνολο των καταστάσεων οι οποίες συχνά λαμβάνονται ως καταστάσεις διαδικασίας αποφάσεων Markov [RK19; Rab+20; RHT20; Fan+20; RRT21; Vin+22]. Για την επίλυση της εξίσωσης 1.1 εφαρμόζεται Bellman αποσύνθεση.

1.2 Η μέθοδος εμβαπτισμένου ορίου

Η μέθοδος εμβαπτισμένου ορίου εισήχθη από τον Viecelli [Vie69] για τη διαχείριση του υγρού ορίου ως ελεύθερη επιφάνεια στην οποία ασκείται πίεση. Λίγο αργότερα, ο Peskin χρησιμοποίησε τη νέα ιδέα για τον υπολογισμό της ροής γύρω από καρδιακές βαλβίδες [Pes72]. Βασική ιδέα της μεθόδου είναι η περιγραφή της δυναμικής του ρευστού με αποσύζευξη του ορίου του χωρίου ρευστού από το υπολογιστικό πλέγμα [TVI14]. Στο μοντέλο του εμβαπτισμένου ορίου, δεν υφίσταται η απαίτηση επαναγέννησης του πλέγματος για την διακριτοποίηση του πεδίου ροής, που ανακύπτει σε περιπτώσεις ύπαρξης κινουμένων σωμάτων.

Κρίσιμο και χαρακτηριστικό σημείο της μεθόδου είναι ο τρόπος με τον οποίο λαμβάνονται υπόψιν οι οριακές συνθήκες στην εμβαπτισμένη επιφάνεια. Μία από τις προταθείσες τεχνικές επιβολής των συνθηκών αποτελεί η τροποποίηση των εξισώσεων με την προσθήκη εξωτερικής δύναμης που περιγράφει την παρουσία του ορίου [LP00; MY97; Fad+00]. Ένας εναλλακτικός τρόπος της μεθόδου συνεχούς δύναμης είναι η διακριτή δύναμη που εφαρμόζεται απευθείας στις διακριτοποιημένες εξισώσεις για να αναπαραστήσει το εμβαπτισμένο σώμα. Για να αποφευχθεί η διάχυση της εξωτερικής δύναμης σε πολλαπλούς γειτονικούς οριακούς κόμβους, έχουν αναπτυχθεί προσεγγίσεις κατά τις οποίες η δύναμη εφαρμόζεται απευθείας στο όριο. Με τη μέθοδο τεμνομένων κυψελών ανασχηματίζονται τα υπολογιστικά κελιά τα οποία τέμνονται από την εμβαπτισμένη επιφάνεια. Σε περίπτωση που το κέντρο του κελιού βρίσκεται στην περιοχή του ρευστού, το κελί διατηρείται, περικεκομμένο στο τμήμα του που βρίσκεται στο χωρίο ρευστού. Ειδάλλως, το κελί απορροφάται από τα γειτνιάζοντα με αυτό κελιά [CSH86; CL00; VSG21]. Η μέθοδος εικονικών κελιών (ghost-cell) λαμβάνει υπόψιν τους στερεούς κόμβους που γειτνιάζουν με το ρευστό. Οι τιμές που επιβάλλονται στους κόμβους είναι τέτοιες ώστε οι προκύπτουσες τιμές από παρεμβολή στην εμβαπτισμένη επιφάνεια, να είναι οι ζητούμενες [IV03; TF03; YB19]. Οι υβριδικές Καρτεσιανές/εμβαπτισμένου ορίου μέθοδοι ορίζουν τις τιμές των μεταβλητών στους κόμβους ρευστού που παράκεινται σε κόμβους στερεού, παρεμβάλλοντας μεταξύ των τιμών του εμβαπτισμένου ορίου και των αντιδιαμετρικών, ως προς τον κόμβο ενδιαφέροντος, κόμβων ρευστού [Fad+00; GS05; SY14].

Κεφάλαιο 2

Διέπουσες εξισώσεις

2.1 Γενικευμένα Νευτώνεια ρευστά

Εξετάζονται χρονικά αμετάβλητα, μη Νευτώνεια ρευστά με συντακτική εξίσωση της μορφής γενικευμένου ρευστού Rivlin-Ericksen. Η συνεκτικότητα που εξαρτάται από τον ρυθμό διάτμησης, δίνεται ως

$$\sigma(\boldsymbol{v}) = -p\boldsymbol{I} + 2\mu(\dot{\gamma})\boldsymbol{D}, \tag{2.1}$$

όπου $\boldsymbol{D}$ είναι ο τανυστής ρυθμού παραμόρφωσης ($2\boldsymbol{D}$ είναι ο πρώτος τανυστής Rivlin-Ericksen) και $\dot{\gamma}$ είναι ο ρυθμός διάτμησης (δηλ. η δεύτερη νόρμα του ρυθμού παραμόρφωσης):

$$\begin{aligned} \dot{\gamma} =& \sqrt{2(\boldsymbol{D} : \boldsymbol{D})} = \sqrt{2tr(\boldsymbol{D}^2)} \\ =& \sqrt{2\left(\frac{\partial u}{\partial x}\right)^2 + 2\left(\frac{\partial \mathrm{v}}{\partial y}\right)^2 + 2\left(\frac{\partial w}{\partial z}\right)^2 + \left(\frac{\partial u}{\partial y} + \frac{\partial \mathrm{v}}{\partial x}\right)^2 + \left(\frac{\partial u}{\partial z} + \frac{\partial w}{\partial x}\right)^2 + \left(\frac{\partial w}{\partial y} + \frac{\partial \mathrm{v}}{\partial z}\right)^2}. \end{aligned} \tag{2.2}$$

Το σύμβολο : αναπαριστά το διπλό εσωτερικό γινόμενο μεταξύ δυάδων και δυαδικών.

Υποθέτοντας δυναμική συνεκτικότητα εξαρτώμενη από τον ρυθμό διάτμησης, οι εξισώσεις Navier-Stokes ασυμπίεστης ροής, για την κλάση των γενικευμένων Νευτώνειων ρευστών με ρεολογική εξίσωση κατάστασης όπως η εξίσωση (2.1) είναι

$$\rho\frac{\partial \boldsymbol{u}}{\partial t} + \rho(\boldsymbol{u} \cdot \nabla)\boldsymbol{u} = \rho\boldsymbol{g} - \nabla p + \nabla \cdot (2\mu(\dot{\gamma})\boldsymbol{D}). \tag{2.3}$$

Εξετάζεται η κατηγορία των γενικευμένων Νευτώνειων ρευστών που χαρακτηρίζεται από ρεολογία που προβλέπεται από την εξίσωση Bird-Carreau για την δυναμική συνεκτικότητα που είναι συνάρτηση του ρυθμού παραμόρφωσης:

$$\mu(\dot{\gamma}) = \mu_{\text{inf}} + (\mu_0 - \mu_{\text{inf}})(1 + (\lambda\dot{\gamma})^2)^{\frac{n-1}{2}}. \tag{2.4}$$

Στην παραπάνω εξίσωση, μ_{inf} είναι η συνεκτικότητα για άπειρο ρυθμό διάτμησης, μ_0 είναι η συνεκτικότητα για μηδενικό ρυθμό διάτμησης, λ είναι ο χρόνος χαλάρωσης και n είναι ο εκθέτης Bird-Carreau. Ρευστά με $n < 1$ εμφανίζουν συμπεριφορά διατμητικής λέπτυνσης ή ψευδοπλαστική συμπεριφορά, ενώ τιμές $n > 1$ δείχνουν διατμητική πάχυνση ή διασταλτική συμπεριφορά. Ρευστά με $n = 1$ εκφυλίζονται σε Νευτώνεια.

2.2 Το γενικευμένο καμπυλόγραμμο σύστημα συντεταγμένων

Ένα καμπυλόγραμμο σύστημα συντεταγμένων είναι ένας χάρτης συντεταγμένων στη διαφορίσιμη πολλαπλότητα E^n (Ευκλείδειος χώρος n διαστάσεων) που είναι ισομορφικός με τον Καρτεσιανό χάρτη συντεταγμένων στην πολλαπλότητα.

Εισάγεται η ένα προς ένα διαφορίσιμη απεικόνιση από τον $\mathbb{R}^3$ στον $\mathbb{R}^3$: $(x, y, z) \rightarrow (\xi, \eta, \zeta)$. Οι τιμές των συναρτήσεων (ξ, η, ζ) καλούνται καμπυλόγραμμες συντεταγμένες του σημείου με Καρτεσιανές συντεταγμένες (x, y, z) στον Ευκλείδειο χώρο.

Θεωρούμε τη συναλλοίωτη βάση που αλλάζει ανάλογα με την αλλαγή των αξόνων $(\boldsymbol{g}_1, \boldsymbol{g}_2, \boldsymbol{g}_3)$ και την ανταλλοίωτη που αλλάζει αντιστρόφως ανάλογα με τους άξονες $(\boldsymbol{g}^1, \boldsymbol{g}^2, \boldsymbol{g}^3)$, αντίστοιχα. Οι παραπάνω βάσεις λαμβάνονται ως

$$\begin{aligned}
\boldsymbol{g}_1 =& \frac{\partial \boldsymbol{x}}{\partial \xi} = \left(\frac{\partial x}{\partial \xi}, \frac{\partial y}{\partial \xi}, \frac{\partial z}{\partial \xi}\right) = (x_\xi, y_\xi, z_\xi) \\
\boldsymbol{g}_2 =& \frac{\partial \boldsymbol{x}}{\partial \eta} = \left(\frac{\partial x}{\partial \eta}, \frac{\partial y}{\partial \eta}, \frac{\partial z}{\partial \eta}\right) = (x_\eta, y_\eta, z_\eta) \\
\boldsymbol{g}_3 =& \frac{\partial \boldsymbol{x}}{\partial \zeta} = \left(\frac{\partial x}{\partial \zeta}, \frac{\partial y}{\partial \zeta}, \frac{\partial z}{\partial \zeta}\right) = (x_\zeta, y_\zeta, z_\zeta)
\end{aligned} \tag{2.5}$$

$$\begin{aligned}
\boldsymbol{g}^1 =& \nabla \xi = \left(\frac{\partial \xi}{\partial x}, \frac{\partial \xi}{\partial y}, \frac{\partial \xi}{\partial z}\right) = (\xi_x, \xi_y, \xi_z) \\
\boldsymbol{g}^2 =& \nabla \eta = \left(\frac{\partial \eta}{\partial x}, \frac{\partial \eta}{\partial y}, \frac{\partial \eta}{\partial z}\right) = (\eta_x, \eta_y, \eta_z) \\
\boldsymbol{g}^3 =& \nabla \zeta = \left(\frac{\partial \zeta}{\partial x}, \frac{\partial \zeta}{\partial y}, \frac{\partial \zeta}{\partial z}\right) = (\zeta_x, \zeta_y, \zeta_z).
\end{aligned} \tag{2.6}$$

Η συναλλοίωτη βάση αποτελείται από τα διανύσματα $\boldsymbol{g}_i$ που εφάπτονται στην αντίστοιχη γραμμή πλέγματος ξ^i και η ανταλλοίωτη βάση αποτελείται από τα διανύσματα $\boldsymbol{g}^i$ που είναι κάθετα σε γραμμές σταθερού ξ^i, αντίστοιχα. Με σκοπό να χρησιμοποιήσουμε τον συμβολισμό του Einstein μετονομάζουμε την τριάδα (x, y, z) σε $(x_1, x_2, x_3) = \boldsymbol{r}$ και την τριάδα (ξ, η, ζ) σε (ξ^1, ξ^2, ξ^3). Συνεπώς η τελευταία βάση μπορεί να γραφεί συνοπτικότερα ως

$$\boldsymbol{g}_i = \frac{\partial \boldsymbol{r}}{\partial \xi^i} = \left(\frac{\partial x_1}{\partial \xi^i}, \frac{\partial x_2}{\partial \xi^i}, \frac{\partial x_3}{\partial \xi^i}\right) \tag{2.7}$$

$$\boldsymbol{g}^i = \nabla \xi^i = \left(\frac{\partial \xi^i}{\partial x_1}, \frac{\partial \xi^i}{\partial x_2}, \frac{\partial \xi^i}{\partial x_3}\right). \tag{2.8}$$

Εξ' ορισμού του τελεστή βαθμίδας, λαμβάνεται για τη συνάρτηση ξ^i

$$d\xi^i = \nabla \xi^i \cdot d\boldsymbol{r} \tag{2.9}$$

και επειδή $\boldsymbol{r} = \boldsymbol{r}(\xi^1, \xi^2, \xi^3)$, από τον κανόνα της αλυσίδας έπεται ότι

$$d\boldsymbol{r} = \frac{\partial \boldsymbol{r}}{\partial \xi^j} d\xi^j = \boldsymbol{g}_j d\xi^j. \tag{2.10}$$

Συνακόλουθα, από την εξίσωση 2.9 λαμβάνεται

$$d\xi^i = \nabla \xi^i \cdot \boldsymbol{g}_j d\xi^j. \tag{2.11}$$

Συμπεραίνεται ότι

$$\begin{aligned}
\nabla \xi^i \cdot \boldsymbol{g}_j &= \delta^i_j \\
\boldsymbol{g}^i \cdot \boldsymbol{g}_j &= \delta^i_j.
\end{aligned} \tag{2.12}$$

Συνάγεται ότι οι δύο βάσεις είναι αντίστροφες και για να παραχθούν τα διανύσματα $\boldsymbol{g}^i$ από τα $\boldsymbol{g}_i$ χρησιμοποιούμε τους μετασχηματισμούς

$$\boldsymbol{g}^1 = \frac{\boldsymbol{g}_2 \times \boldsymbol{g}_3}{\boldsymbol{g}_1 \cdot (\boldsymbol{g}_2 \times \boldsymbol{g}_3)}, \ \boldsymbol{g}^2 = \frac{\boldsymbol{g}_3 \times \boldsymbol{g}_1}{\boldsymbol{g}_2 \cdot (\boldsymbol{g}_3 \times \boldsymbol{g}_1)}, \ \boldsymbol{g}^3 = \frac{\boldsymbol{g}_1 \times \boldsymbol{g}_2}{\boldsymbol{g}_3 \cdot (\boldsymbol{g}_1 \times \boldsymbol{g}_2)} \tag{2.13}$$

και τούμπαλιν

$$\boldsymbol{g}_1=\frac{\boldsymbol{g}^2\times\boldsymbol{g}^3}{\boldsymbol{g}^1\cdot(\boldsymbol{g}^2\times\boldsymbol{g}^3)},\ \boldsymbol{g}_2=\frac{\boldsymbol{g}^3\times\boldsymbol{g}^1}{\boldsymbol{g}^2\cdot(\boldsymbol{g}^3\times\boldsymbol{g}^1)},\ \boldsymbol{g}_3=\frac{\boldsymbol{g}^1\times\boldsymbol{g}^2}{\boldsymbol{g}^3\cdot(\boldsymbol{g}^1\times\boldsymbol{g}^2)}. \tag{2.14}$$

Ένα διάνυσμα $\boldsymbol{a}$ εκφράζεται ως προς την Καρτεσιανή βάση $(\boldsymbol{x}_1,\boldsymbol{x}_2,\boldsymbol{x}_3)$ ως

$$\boldsymbol{a}=a_{x_1}\boldsymbol{x}_1+a_{x_2}\boldsymbol{x}_2+a_{x_3}\boldsymbol{x}_3,$$

ενώ ως προς τη βάση $(\boldsymbol{g}_1,\boldsymbol{g}_2,\boldsymbol{g}_3)$ ως

$$\boldsymbol{a}=A^1\boldsymbol{g}_1+A^2\boldsymbol{g}_2+A^3\boldsymbol{g}_3. \tag{2.15}$$

Οι συνιστώσες του διανύσματος που γράφεται σε συναλλοίωτη βάση είναι ανταλλοίωτες. Στον αντίποδα η έκφραση για την ανταλλοίωτη βάση $(\boldsymbol{g}^1,\boldsymbol{g}^2,\boldsymbol{g}^3)$ είναι

$$\boldsymbol{a}=A_1\boldsymbol{g}^1+A_2\boldsymbol{g}^2+A_3\boldsymbol{g}^3, \tag{2.16}$$

δηλαδή περιλαμβάνει συναλλοίωτες συνιστώσες.

Χρησιμοποιώντας την εξίσωση 2.12 λαμβάνεται η σχέση μεταξύ των ανταλλοίωτων και των Καρτεσιανών συντεταγμένων ως

$$\begin{aligned}A^i=&\boldsymbol{g}^i\cdot a_{x_j}\boldsymbol{x}_j\\ =&\left(\frac{\partial\xi^i}{\partial x_1},\frac{\partial\xi^i}{\partial x_2},\frac{\partial\xi^i}{\partial x_3}\right)\cdot(1,0,0)a_{x_1}+\left(\frac{\partial\xi^i}{\partial x_1},\frac{\partial\xi^i}{\partial x_2},\frac{\partial\xi^i}{\partial x_3}\right)\cdot(0,1,0)a_{x_2}\\ &+\left(\frac{\partial\xi^i}{\partial x_1},\frac{\partial\xi^i}{\partial x_2},\frac{\partial\xi^i}{\partial x_3}\right)\cdot(0,0,1)a_{x_3}\\ =&\frac{\partial\xi^i}{\partial x_1}a_{x_1}+\frac{\partial\xi^i}{\partial x_2}a_{x_2}+\frac{\partial\xi^i}{\partial x_3}a_{x_3}\\ =&\frac{\partial\xi^i}{\partial x_j}a_{x_j}\qquad .\end{aligned} \tag{2.17}$$

Κατά τον ίδιο τρόπο, οι Καρτεσιανές συνιστώσες δίνονται ως συνάρτηση των ανταλλοίωτων ως

$$a_{x_i}=\frac{\partial x_j}{\partial\xi^i}A^j. \tag{2.18}$$

Το στοιχείο όγκου σε καμπυλόγραμμες συντεταγμένες είναι

$$dV=\left|\frac{\partial(x_1,x_2,x_3)}{\partial(\xi^1,\xi^2,\xi^3)}\right|d\xi^1d\xi^2d\xi^3. \tag{2.19}$$

Ο Ιακωβιανός πίνακας είναι

$$\frac{\partial(x_1,x_2,x_3)}{\partial(\xi^1,\xi^2,\xi^3)} \tag{2.20}$$

και η ορίζουσά του έχει τη μορφή

$$J=\left|\frac{\partial(x_1,x_2,x_3)}{\partial(\xi^1,\xi^2,\xi^3)}\right|=\begin{bmatrix}\frac{\partial x_1}{\partial\xi^1}&\frac{\partial x_1}{\partial\xi^2}&\frac{\partial x_1}{\partial\xi^3}\\ \frac{\partial x_2}{\partial\xi^1}&\frac{\partial x_2}{\partial\xi^2}&\frac{\partial x_2}{\partial\xi^3}\\ \frac{\partial x_3}{\partial\xi^1}&\frac{\partial x_3}{\partial\xi^2}&\frac{\partial x_3}{\partial\xi^3}\end{bmatrix}=\boldsymbol{g}_1\cdot(\boldsymbol{g}_2\times\boldsymbol{g}_3). \tag{2.21}$$

2.3 Ο μετρικός τανυστής

Υποθέτοντας την αναλλοίωτη βάση $\boldsymbol{e}_1 = (1,0,0), \boldsymbol{e}_2 = (0,1,0), \boldsymbol{e}_3 = (0,0,1)$ του Καρτεσιανού συστήματος συντεταγμένων, η απόσταση μεταξύ των σημείων P και Q με συντεταγμένες x_i και $x_i + dx_i$ είναι ds

$$ds^2 = \sum_{i=1}^{3} dx_i dx_i. \tag{2.22}$$

Μπορούμε να γράψουμε το διαφορικό του x_i ως

$$dx_k = \frac{\partial x_k}{\partial \xi^i} d\xi^i \tag{2.23}$$

και η εξίσωση για το ds γίνεται

$$ds^2 = \sum_{k=1}^{3} \left(\frac{\partial x_k}{\partial \xi^i} d\xi^i \right) \left(\frac{\partial x_k}{\partial \xi^j} d\xi^j \right) = g_{ij} d\xi^i d\xi^j. \tag{2.24}$$

Η ποσότητα

$$g_{ij} = \sum_{k=1}^{3} \frac{\partial x_k}{\partial \xi^i} \frac{\partial x_k}{\partial \xi^j} = \boldsymbol{g}_i \cdot \boldsymbol{g}_j \tag{2.25}$$

που εμφανίζεται στο δεξί μέλος, ονομάζεται μετρικός τανυστής και είναι ο συντελεστής αναλογίας μεταξύ των διαφορικών των καμπυλόγραμμων συντεταγμένων και του μήκους.

2.4 Συνοχή Riemann - συναλλοίωτη παράγωγος

Για ένα διανυσματικό πεδίο $\boldsymbol{Y}$ η μερική παράγωγος ως προς την i-οστή συντεταγμένη είναι

$$\boldsymbol{Y}_{,i} = Y^j_{,i} \boldsymbol{g}_j + Y^j \boldsymbol{g}_{j,i}. \tag{2.26}$$

Ένα διανυσματικό πεδίο αναπτύσσεται ως

$$\boldsymbol{X} = X^\mu \frac{\partial}{\partial x^\mu}, \tag{2.27}$$

για X^μ λείες συναρτήσεις στην πολλαπλότητα M.

Υποθέτοντας τα διαφορίσιμα διανυσματικά πεδία $\boldsymbol{X}, \boldsymbol{Y}$, μία συνοχή ή συναλλοίωτη παράγωγος, σε πολλαπλότητα Riemann M εφοδιασμένη με τη μετρική h, είναι μία απεικόνιση $(\boldsymbol{X}, \boldsymbol{Y}) \mapsto \nabla_{\boldsymbol{X}} \boldsymbol{Y}$ που ικανοποιεί τα ακόλουθα αξιώματα

- Προσεθετικότητα στην κατεύθυνση $\nabla_{\boldsymbol{X}_1 + \boldsymbol{X}_2} \boldsymbol{Y} = \nabla_{\boldsymbol{X}_1} \boldsymbol{Y} + \nabla_{\boldsymbol{X}_2} \boldsymbol{Y}$
- Γραμμικότητα στην κατεύθυνση $\nabla_{f\boldsymbol{X}} \boldsymbol{Y} = f \cdot \nabla_{\boldsymbol{X}} \boldsymbol{Y}$
- Προσεθετικότητα στο διαφοριζόμενο πεδίο $\nabla_{\boldsymbol{X}} (\boldsymbol{Y}_1 + \boldsymbol{Y}_2) = \nabla_{\boldsymbol{X}} \boldsymbol{Y}_1 + \nabla_{\boldsymbol{X}} \boldsymbol{Y}_2$
- Κανόνας γινομένου στο διαφοριζόμενο πεδίο $\nabla_{\boldsymbol{X}} (f\boldsymbol{Y}) = f \cdot \nabla_{\boldsymbol{X}} \boldsymbol{Y} + \nabla_{\boldsymbol{X}} f \cdot \boldsymbol{Y}$

Εάν επιπρόσθετα ισχύουν τα δύο ακόλουθα αξιώματα, για διανυσματικό πεδίο $\boldsymbol{Z}$, προκύπτει συνοχή Riemann ή Levi-Civita

- Συμβατότητα με την μετρική $\nabla_{\boldsymbol{X}}\, h(\boldsymbol{Y}, \boldsymbol{Z}) = h(\nabla_{\boldsymbol{X}} \boldsymbol{Y}, \boldsymbol{Z}) + h(\boldsymbol{Y}, \nabla_{\boldsymbol{X}} \boldsymbol{Z})$
- Συμμετρία - μηδενική στρέψη $\nabla_{\boldsymbol{X}} \boldsymbol{Y} - \nabla_{\boldsymbol{Y}} \boldsymbol{X} = [\boldsymbol{X}, \boldsymbol{Y}]$,

όπου η αγκύλη Lie ορίζεται ως $[\boldsymbol{X},\boldsymbol{Y}](f) = \boldsymbol{X}(\boldsymbol{Y}(f)) - \boldsymbol{Y}(\boldsymbol{X}(f))$ και $f : M \to \mathbb{R}$ είναι διαφορίσιμη συνάρτηση.

Από τον κανόνα του γινομένου, για $\boldsymbol{X} = \boldsymbol{g}_i$

$$\nabla_{\boldsymbol{X}}\boldsymbol{Y} = \nabla_{\boldsymbol{g}_i}(Y^j\boldsymbol{g}_j) = \frac{\partial Y^j}{\partial \xi^i}\boldsymbol{g}_j + Y^j\frac{\partial \boldsymbol{g}_j}{\partial \xi^i}. \tag{2.28}$$

Ή παράγωγος $\boldsymbol{g}_{i,j}$ είναι

$$\boldsymbol{g}_{i,j} = \Gamma^1_{ij}\,\boldsymbol{g}_1 + \Gamma^2_{ij}\,\boldsymbol{g}_2 + \dots + \Gamma^n_{ij}\,\boldsymbol{g}_n = \Gamma^k_{ij}\,\boldsymbol{g}_k, \tag{2.29}$$

όπου η ποσότητα Γ^k_{ij} ονομάζεται σύμβολο Christoffel και λόγω της συμμετρίας $g_{i,j} = g_{j,i}$, έπεται ότι $\Gamma^k_{ij} = \Gamma^k_{ji}$. Αντικαθιστώντας στην εξίσωση 2.28, λαμβάνεται

$$\boldsymbol{Y}_{,i} = Y^j_{,i}\,\boldsymbol{g}_j + Y^j\Gamma^k_{ij}\boldsymbol{g}_k = (Y^k_{,i} + \Gamma^k_{ij}Y^j)\boldsymbol{g}_k, \tag{2.30}$$

όπου η ποσότητα $Y^k_{,i} + \Gamma^k_{ij}Y^j$ καλείται συναλλοίωτη παράγωγος του Y^k και συμβολίζεται ως $\nabla_i Y^k$. Πολλαπλασιάζοντας εσωτερικά την εξίσωση 2.29 με $\boldsymbol{g}^p$, προκύπτει

$$\boldsymbol{g}^p\boldsymbol{g}_{i,j} = \Gamma^k_{ij}\,\boldsymbol{g}^p \cdot \boldsymbol{g}_k = \Gamma^k_{ij}\delta^p_k = \Gamma^p_{ij}. \tag{2.31}$$

2.5 Διαφορικοί τελεστές σε καμπυλόγραμμες συντεταγμένες

Ο τελεστής del σε καμπυλόγραμμες συντεταγμένες είναι

$$\nabla = \boldsymbol{g}^i\frac{\partial}{\partial \xi^i}. \tag{2.32}$$

Η απόκλιση διανυσματικού πεδίου $\boldsymbol{Y}$ είναι το εσωτερικό γινόμενο του τελεστή del με το $\boldsymbol{Y}$ i.e.

$$\begin{aligned}\nabla \cdot \boldsymbol{Y} =& \boldsymbol{g}^i \cdot \frac{\partial (Y^j\boldsymbol{g}_j)}{\partial \xi^i} = \boldsymbol{g}^i \cdot \boldsymbol{g}_j \nabla_i Y^j \\ =& \nabla_i Y^i = Y^i_{,i} + \Gamma^i_{ij}Y^j.\end{aligned} \tag{2.33}$$

Για τα σύμβολα Christoffel ισχύει η σχέση

$$\Gamma^i_{ij} = J^{-1}J_{,i}. \tag{2.34}$$

Χρήση της σχέσης 2.34 δίνει

$$\begin{aligned}\nabla \cdot \boldsymbol{Y} =& Y^i_{,i} + \Gamma^i_{ij}Y^j = Y^i_{,i} + J_{,j}J^{-1}Y^j \\ =& Y^i_{,i} + J_{,i}J^{-1}Y^i = J^{-1}(JY^i)_{,i} = \frac{1}{J}(J\boldsymbol{g}^i \cdot \boldsymbol{Y})_{,i}.\end{aligned} \tag{2.35}$$

Όμοια, για τον τελεστή βαθμίδας εφαρμοσμένο σε βαθμωτό πεδίο

$$\nabla\phi = \boldsymbol{g}^j\frac{\partial \phi}{\partial \xi^j} = \frac{1}{J}\frac{\partial}{\partial \xi^j}(J\boldsymbol{g}^j\phi). \tag{2.36}$$

Συνεπώς, ο τελεστής Laplace λαμβάνεται στη μορφή

$$\nabla^2\phi = \frac{1}{J}\frac{\partial}{\partial \xi^j}\left(J\boldsymbol{g}^j \cdot \boldsymbol{g}^k\frac{\partial \phi}{\partial \xi^k}\right). \tag{2.37}$$

2.6 Εξισώσεις Navier-Stokes σε καμπυλόγραμμα συστήματα συντεταγμένων

Η εξίσωση συνέχειας σε διαφορική μορφή δίνεται ως

$$\frac{\partial \rho}{\partial t} + div(\rho \boldsymbol{u}) = 0. \tag{2.38}$$

και υποθέτοντας ότι η ροή είναι ασυμπίεστη, δηλαδή ότι οι μετάβολες στην πυκνότητα, σε ολόκληρο το πεδίο ροής είναι μικρές, η εξίσωση συνέχειας γίνεται

$$div(\rho \boldsymbol{u}) = div(\boldsymbol{u}) = 0. \tag{2.39}$$

Επομένως συνδυάζοντας τα αποτελέσματα της ενότητας 2.5 με την εξίσωση 2.39 προκύπτει ότι για την εξίσωση συνέχειας η ανταλλοίωτη μορφή δεικτών είναι

$$\frac{1}{J}\frac{\partial}{\partial \xi^j}(J\mathrm{U}^j) = 0 \tag{2.40}$$

και χρησιμοποιώντας τους διαφορικούς τελεστές σε καμπυλόγραμμες συντεταγμένες στην εξίσωση (2.3), η εξίσωση ορμής είναι

$$\rho \frac{\partial \left(J\mathrm{U}^k\right)}{\partial t} + \rho \frac{\partial \xi^k}{\partial x_i}\frac{\partial}{\partial \xi^j}(J\, \mathrm{U}^j u_i) = -\frac{\partial \xi^k}{\partial x_i}\frac{\partial}{\partial \xi^j}\left(J\, \frac{\partial \xi^j}{\partial x_i} p\right) + \frac{\partial \xi^k}{\partial x_i}\frac{\partial}{\partial \xi^j}\left(J\, \mu(\dot{\gamma}) g^{jm}\frac{\partial u_i}{\partial \xi^m}\right). \tag{2.41}$$

Υποθέτοντας δυναμική συνεκτικότητα ανεξάρτητη από τον ρυθμό διάτμησης

$$\frac{\partial \left(J\mathrm{U}^k\right)}{\partial t} + \frac{\partial \xi^k}{\partial x_i}\frac{\partial}{\partial \xi^j}(J\, \mathrm{U}^j u_i) = -\frac{\partial \xi^k}{\partial x_i}\frac{\partial}{\partial \xi^j}\left(J\, \frac{\partial \xi^j}{\partial x_i}\frac{p}{\rho}\right) + \nu \frac{\partial \xi^k}{\partial x_i}\frac{\partial}{\partial \xi^j}\left(J\, g^{jm}\frac{\partial u_i}{\partial \xi^m}\right). \tag{2.42}$$

2.7 Εξίσωση κίνησης ελαστικής μεμβράνης

Η δυναμική της ελαστικής μεμβράνης προβλέπεται από την ακόλουθη εξίσωση, υπό τις υποθέσεις μικρών μετατοπίσεων και μικρής αδράνειας

$$T_m \frac{\partial^2 g(x,t)}{\partial x^2} = -(p_e(x,t) - p_i(x,t)), \quad \left|\frac{\partial g(x,t)}{\partial x}\right| \ll 1, \;\; b\rho_0 \to 0, \;\; 0 \le x \le l. \tag{2.43}$$

Στην παραπάνω εξίσωση, T_m είναι η σταθερή τάση της μεμβράνης (δύναμη ανά μονάδα πλάτους), $p_e(x,t)$ είναι η πίεση που ασκείται στην αρνητική της πλευρά και $p_i(x,t)$ είναι η πίεση που ασκείται στη θετική της πλευρά, b είναι το πάχος της μεμβράνης και ρ_0 είναι η πυκνότητά της. Υποθέτοντας γνωστές συναρτήσεις θέσης, $c_0(t), c_l(t)$, για τα άκρα της μεμβράνης της μορφής

$$\begin{aligned} g(0,t) &= c_0(t) \\ g(l,t) &= c_l(t), \end{aligned} \tag{2.44}$$

ορίζεται πρόβλημα συνοριακών τιμών με οριακές συνθήκες Dirichlet για τη μορφή της μεμβράνης $g(x,t)$.

Κεφάλαιο 3

Αριθμητικές μέθοδοι για την επίλυση των ΜΔΕ

Οι μέθοδοι εμβαπτισμένου ορίου [Pes72] παρουσιάζουν το πλεονέκτημα της προσομοίωσης της ροής γύρω από κινούμενα σώματα, παραμορφώσιμες κατασκευές και σχήματα πολύπλοκης γεωμετρίας, χρησιμοποιώντας μόνιμα υποκείμενα υπολογιστικά πλέγματα περιορισμένης πολυπλοκότητας, συνοδευόμενα από μία διαδικασία διαχείρισης του κινούμενου ή του παραμορφώσιμου ή του σύνθετου τμήματος των διεπιφανειών στερεού-ρευστού. Γεωμετρίες στερεού αυτού του είδους αναπαρίστανται από την αντίστοιχη κλειστή επιφάνεια του εξωτερικού τους ορίου που στις Καρτεσιανές-εμβαπτισμένου ορίου μεθόδους συχνά ψηφιδώνεται με τρίγωνα [GS05; GB98]. Στις παραλλαγές της παραπάνω κατηγορίας, κάθε επιπρόσθετη περιοχή στερεού που λαμβάνεται ως εμβαπτισμένο σώμα, επιφέρει αρχική επιβάρυνση για τριγωνοποίηση του ορίου και για ανίχνευση της διεπιφάνειας (ενότητα 3.1). Επιπλέον, αυξάνει την πολυπλοκότητα της επιβολής των οριακών συνθηκών επ` αυτής και του υπολογισμού ποσοτήτων ενδιαφέροντος στο όριό της. Συνεπώς είναι επιθυμητή η ελαχιστοποίηση του τμήματος της στερεής περιοχής που θεωρείται εμβαπτισμένο όριο. Στοχεύοντας εκεί, ο βαθμός προσαρμογής του υποκείμενου πλέγματος στο χωρίο ρευστού, αποτελεί κρίσιμο παράγοντα. Στην παρούσα διατριβή εφαρμόζεται η μέθοδος εμβαπτισμένου ορίου όπως διατυπώνεται από τους Ge και Sotiropoulos [GS07]. Καμπυλόγραμμο ογκικό δομημένο πλέγμα προσαρμόζεται σε επιφάνεια που περικλείει το χωρίο ρευστού καθ' όλη τη χρονική διάρκεια της κίνησης. Το σύνολο των καμπυλόγραμμων πλεγμάτων προσφέρει πολύ υψηλότερη δυνατότητα προσαρμογής εν συγκρίσει με το Καρτεσιανό σύνολο.

3.1 Κατηγοριοποίηση των κόμβων του υπολογιστικού πλέγματος

Οι κόμβοι του υποκείμενου πλέγματος κατηγοριοποιούνται ως στερεού, εμβαπτισμένου ορίου και ρευστού [BGS08]. Για κάθε εμβαπτισμένο σώμα, αρχικά δημιουργείται ένα πλαίσιο οριοθέτησης. Όλοι οι κόμβοι εξωτερικά του πλαισίου κατηγοριοποιούνται ως κόμβοι ρευστού. Για τα υπόλοιπα σημεία του υποκείμενου πλέγματος, με σκοπό την επιτάχυνση της διαδικασίας, το πλαίσιο οριοθέτησης διαιρείται σε $n_i \times n_j \times n_k$ ορθογώνια τμήματα για x, y, z καρτεσιανές κατευθύνσεις αντίστοιχα. Κάθε τμήμα λαμβάνει σημαία "άδειο" ή "γεμάτο", βάσει του εάν υπάρχουν στοιχεία του επιφανειακού πλέγματος εντός του τμήματος. Για επιφανειακό πλέγμα με N τριγωνικά στοιχεία, η υποδιαδικασία που για την απλοϊκή προσέγγιση (χωρίς διαίρεση του χωρίου σε ορθογώνια τμήματα) επαναλαμβάνεται N κύκλους για κάθε σημείο του υποκείμενου πλέγματος, επαναλαμβάνεται προσεγγιστικά $\frac{N}{n_i \times n_j}$ κύκλους.

Τελικά, κάθε κόμβος με σημαία "ρευστού" ελέγχεται για το εάν υπάρχει στη γειτονιά του κόμβος "στερεού". Εάν υπάρχει, ο κόμβος "ρευστού" σημαίνεται ως κόμβος "εμβαπτισμένου ορίου".

Οι εξισώσεις ροής επιλύονται σε κάθε κόμβο στο χωρίο ρευστού με σημαία "ρευστού".

3.2 Διακριτοποίηση εξισώσεων Navier-Stokes σε καμπυλόγραμμο πλέγμα

Οι αδιάστατες εξισώσεις Navier-Stokes (2.40) και (2.41), εκφράζονται σε καμπυλόγραμμο σύστημα συντεταγμένων $\boldsymbol{\xi} = \{\xi^1, \xi^2, \xi^3\}$. Για τη διακριτοποίηση στο καμπυλόγραμμο πλέγμα, οι μεταβλητές της ροής (u_1, u_2, u_3, p) ορίζονται στα κέντρα των κελιών ενώ οι μεταβλητές (U^1, U^2, U^3) ορίζονται στα κέντρα των όψεων των υπολογιστικών κυψελών οδηγώντας σε ομόθετη/μη ομόθετη προσέγγιση. Οι εξισώσεις ορμής επιλύονται στα κέντρα επιφανειών, χρησιμοποιώντας τιμές για τους συναγωγικούς και τους συνεκτικούς όρους που προκύπτουν από παρεμβολή στα κέντρα των κελιών. Συνεπώς, η εκτίμηση των συναλλοίωτων παραγώγων των διανυσμάτων βάσης, δηλαδή τα σύμβολα Christoffel, αποφεύγεται, οδηγώντας σε μείωση του υπολογιστικού κόστους [GS07].

Για τις τιμές της ταχύτητας σε κόμβο με σημαία εμβαπτισμένου ορίου, P, λαμβάνεται η κάθετος από το P στην εμβαπτισμένη επιφάνεια, η οποία την τέμνει στο σημείο C. Επεκτείνοντας την ημιευθεία CP, βρίσκεται το πρώτο σημείο τομής με τρίγωνο σημείων με σημαία ρευστού, το σημείο A. Η ταχύτητα του P προκύπτει ως γραμμικός συνδυασμός μεταξύ των τιμών των σημείων C και A [GS05] (σχήμα 3.1).

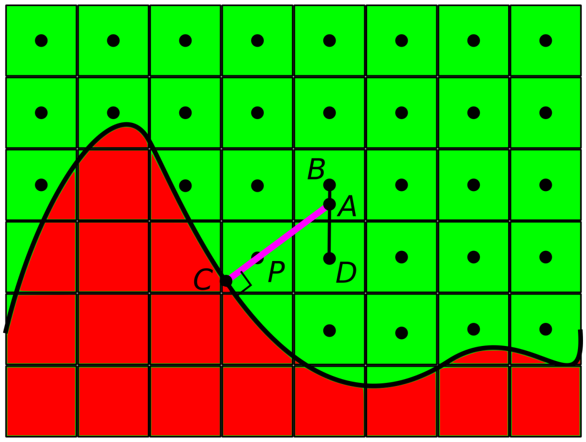

Σχήμα 3.1: Ικανοποίηση της οριακής συνθήκης σε κόμβο εμβαπτισμένου ορίου P. Η ταχύτητα του P προσεγγίζεται μέσω γραμμικής παρεμβολής μεταξύ της ταχύτητας του πλησιέστερου στοιχείου C της εμβαπτισμένης επιφάνειας και του σημείου A. Το σημείο A εντοπίζεται επεκτείνοντας την ημιευθεία CP και βρίσκοντας το πλησιέστερο στο P σημείο τομής με τρίγωνο που σχηματίζεται από κόμβους ρευστού. Το παράδειγμα εμφανίζεται σε δύο διαστάσεις χάριν εποπτείας, συνεπώς το τρίγωνο των κόμβων ρευστού αναπαρίσταται από το ευθύγραμμο τμήμα BD.

Η χρονική ολοκλήρωση του συστήματος των εξισώσεων πραγματοποιείται μέσω σχήματος δεύτερης τάξης Crank-Nicolson της μορφής [CN47; CKS14]

$$J\frac{\mathbf{U}^m - \mathbf{U}^n}{\Delta t} = 0.5 \cdot \mathbf{F}(\mathbf{U}^m, \mathbf{u}^m) + 0.5 \cdot \mathbf{F}(\mathbf{U}^n, \mathbf{u}^n) + \mathbf{G}(p^n). \tag{3.1}$$

Ο υπερδείκτης (m) χρησιμοποιείται για την αναφορά στο πεδίο ταχύτητας που προκύπτει από την επίλυση των εξισώσεων ορμής και πριν το βήμα προβολής για την επίλυση της εξίσωσης της συνέχειας, ενώ ο υπερδείκτης (n) αναφέρεται στο τελευταίο χρονικό βήμα στο οποίο η ροή έχει ήδη πλήρως υπολογιστεί.

Το πεδίο πίεσης υπολογίζεται έτσι ώστε να ικανοποιείται ο περιορισμός της ασυμπίεστης ροής. Για τον σκοπό αυτό λαμβάνεται η απόκλιση της εξίσωσης (2.41) και χρησιμοποιείται η εξίσωση (2.40) ώστε να ληφθεί η συνθήκη που απαιτείται να πληροί το πεδίο διόρθωσης πίεσης

$$\phi^{n+1} = \frac{p^{n+1}}{\rho} - \frac{p^n}{\rho}, \tag{3.2}$$

που οδηγεί σε μηδενική απόκλιση του πεδίου ταχύτητας στο επόμενο χρονικό βήμα [PS72]. Ο υπερδείκτης $(n+1)$ αναφέρεται στο επόμενο χρονικό βήμα, εκείνο δηλαδή στο οποίο αποσκοπεί ο υπολογισμός.

Βάσει της γραμμικότητας του τελεστή που ενεργεί στην πίεση και χρησιμοποιώντας την εξίσωση (2.35), προκύπτει η εξίσωση Poisson για τη διόρθωση στο πεδίο πίεσης [Kan+11]

$$\frac{1}{\Delta t}\frac{\partial (J^2 \mathbf{g}^j \cdot \mathrm{U}^{i,m} \mathbf{g}_i)}{\partial \xi^j} = -\frac{\partial}{\partial \xi^i}\left(J\mathbf{g}^i \cdot \frac{\partial \xi^k}{\partial x_l}\frac{\partial}{\partial \xi^j}\left(J\frac{\partial \xi^j}{\partial x_l}\phi^{n+1}\mathbf{g}_k \right)\right). \tag{3.3}$$

Οι διακριτοποιημένες εξισώσεις ορμής εισάγονται σε Newton επαναληπτικό επιλύτη για μη γραμμικά συστήματα, που χρησιμοποιεί περιοχή εμπιστοσύνης [Mor+84]. Τα προκύπτοντα γραμμικά συστήματα επιλύονται με τη μέθοδο του γενικευμένου ελαχιστικού υπολοίπου [Kan10; SS86; KK04] με προσταθεροποιητή Jacobi.

Η μέθοδος GMRES χρησιμοποιείται και για την επίλυση του γραμμικού συστήματος για τις διορθώσεις πίεσης που ανακύπτει από τη διακριτοποίηση της εξίσωσης Poisson (εξίσωση (3.3)) στο υποκείμενο πλέγμα [GS07], χρησιμοποιώντας την αλγεβρική πολυπλεγματική μέθοδο ως προσταθεροποιητή [RS87].

Η εφαρμογή της μεθόδου εμβαπτισμένου ορίου και η επίλυση των εξισώσεων Navier-Stokes πραγματοποιούνται με το λογισμικό Virtual Flow Simulator [Cal+15; Vfs].

3.3 Ακίνητη σφαίρα σε στρωτό και σε τυρβώδες ρεύμα ρευστού

Σφαίρα μοναδιαίας διαμέτρου τοποθετείται σε ρεύμα μοναδιαίας ταχύτητας σε αριθμό Reynolds 100. Το μη δομημένο, επιφανειακό πλέγμα που τη διακριτοποιεί αποτελείται από $236,321$ κόμβους και $472,638$ τριγωνικά στοιχεία. Το υποκείμενο δομημένο, Καρτεσιανό πλέγμα αποτελείται από $294 \times 244 \times 244$ στις κατευθύνσεις x (διεύθυνση της ροής), y και z αντίστοιχα. Εκτείνεται στην περιοχή $15D \times 10D \times 10D$, όπου D είναι η διάμετρος της σφαίρας. Οι κόμβοι του πλέγματος κατανέμονται με διάστημα $\delta\phi$ ως:

$$\delta\phi = \begin{cases} 0.02D, & |\phi - \phi_c| < 1.46D \\ 0.04D, & 1.46D < |\phi - \phi_c| < 1.92D \\ 0.08D, & 1.92D < |\phi - \phi_c|, \end{cases}$$

όπου $\phi \in \{x, y, z\}$ και ϕ_c είναι η συντεταγμένη του κέντρου της σφαίρας. Το πεδίο διαμήκους ταχύτητας και οι ισοϋψείς πίεσης για αριθμό Reynolds 100 παρουσιάζονται στο σχήμα 3.2.

Το μήκος της φυσαλίδας ανακυκλοφορίας κατάντι της σφαίρας αναφέρεται στον πίνακα 3.1.

Πίνακας 3.1: Μήκος ανακυκλοφορίας και γωνία αποκόλλησης για σφαίρα σε ελεύθερο ρεύμα σε αριθμό Reynolds 100. Σύγκριση με αποτελέσματα των [ACS16], [MRF95] και [VPT12].

Μετρική	Παρόντα αποτελέσματα	Angelidis et al. [ACS16]	Magnaudet et al. [MRF95]	Vrachliotis et al. [VPT12]
Μήκος ανακυκλοφορίας	0.85D	0.88D	0.88D	0.87D
Γωνία αποκόλλησης	126.1°	126.2°	126.1°	-

Ο συντελεστής πίεσης που υπολογίζεται γύρω από τη σφαίρα

$$C_p = \frac{P - P_\infty}{\frac{1}{2}\rho V_\infty^2} \tag{3.4}$$

παρουσιάζεται στο σχήμα 3.3.

Ακολουθώντας μία γραμμή έρευνας για υπερκρίσιμη τυρβώδη ροή γύρω από σφαίρα [Ach72; CS04; Jin+04], μελετάται η εν λόγω ροή για αριθμό Reynolds $1,140,000$, προλέγοντας την τύρβη με τη μέθοδο προσομοίωσης μεγάλων

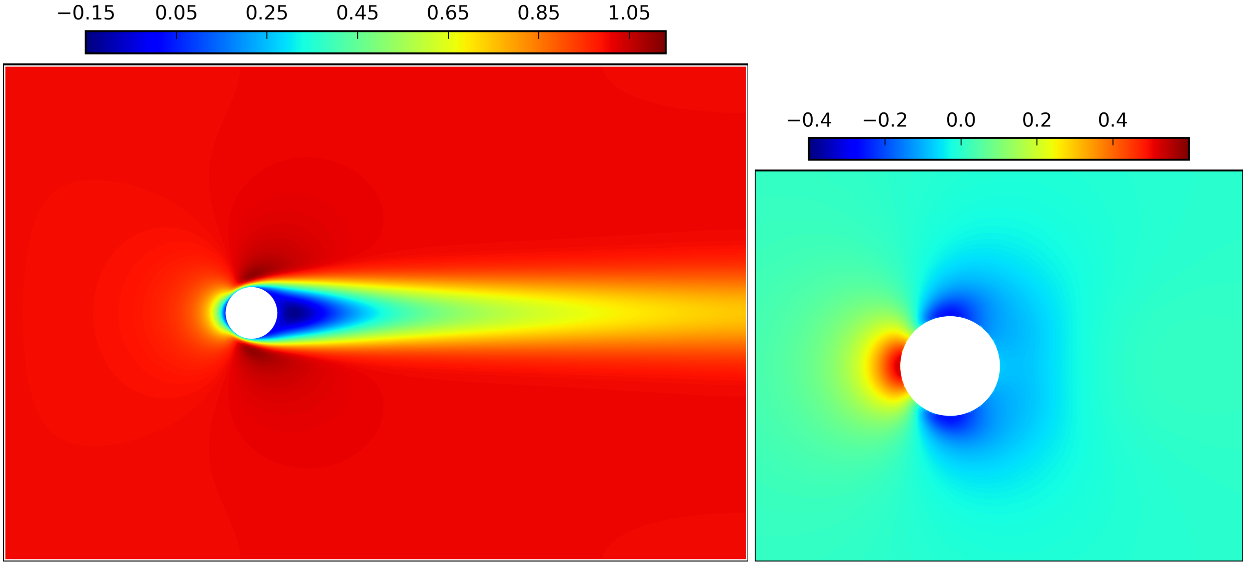

(α′) Το πεδίο διαμήκους ταχύτητας γύρω από σφαίρα για αριθμό Reynolds 100.

(β′) Το πεδίο πίεσης γύρω από σφαίρα για αριθμό Reynolds 100.

Σχήμα 3.2: Ισοϋψείς παραμέτρων ροής γύρω από σφαίρα μοναδιαίας διαμέτρου για αριθμό Reynolds 100.

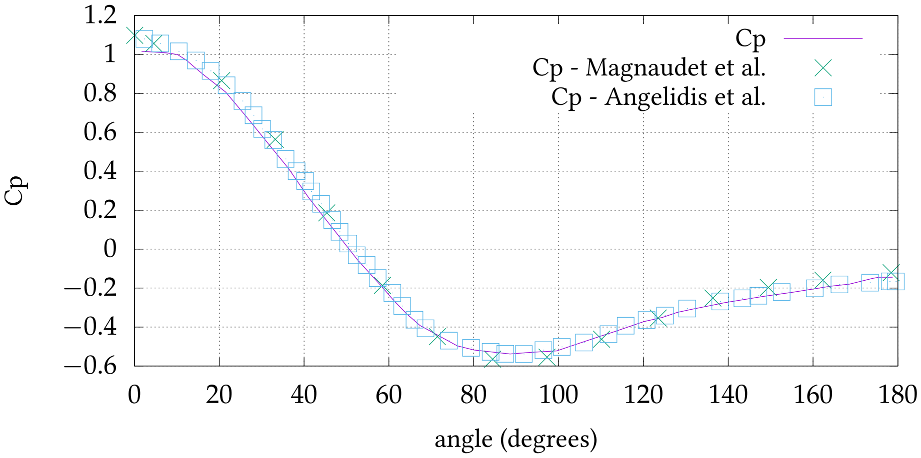

Σχήμα 3.3: Συντελεστής πίεσης C_p για σφαίρα σε αριθμό Reynolds 100. Σύγκριση με αποτελέσματα των [MRF95] και [ACS16].

δινών σε συνδυασμό με το μοντέλο Smagorinsky υποπλεγματικής κλίμακας (SGS) [Sma63]. Χρησιμοποιείται το υποκείμενο και το επιφανειακό πλέγμα που χρησιμοποιήθηκαν για την περίπτωση της στρωτής ροής. Ο συντελεστής πίεσης (εξίσωση (3.4)) παρουσιάζεται στο σχήμα 3.4. Οι τιμές που υπολογίζονται κατάντι του σημείου αποκόλλησης δεν συμπίπτουν με τις προκύπτουσες από πειραματικές μετρήσεις. Η μετάβαση από στρωτή σε τυρβώδη ροή στην περιοχή έναρξης της φυσαλλίδας, μπορεί να επηρεάσει τη ροή κατάντι του σημείου αποκόλλησης. Η δυσχέρεια του μοντέλου τύρβης να προσομοιώσει την περίπλοκη διαδικασία μετάβασης του οριακού στρώματος είναι πιθανός παράγοντας της απόκλισης των υπολογιστικών αποτελεσμάτων από τις μετρηθείσες ποσότητες [CS04].

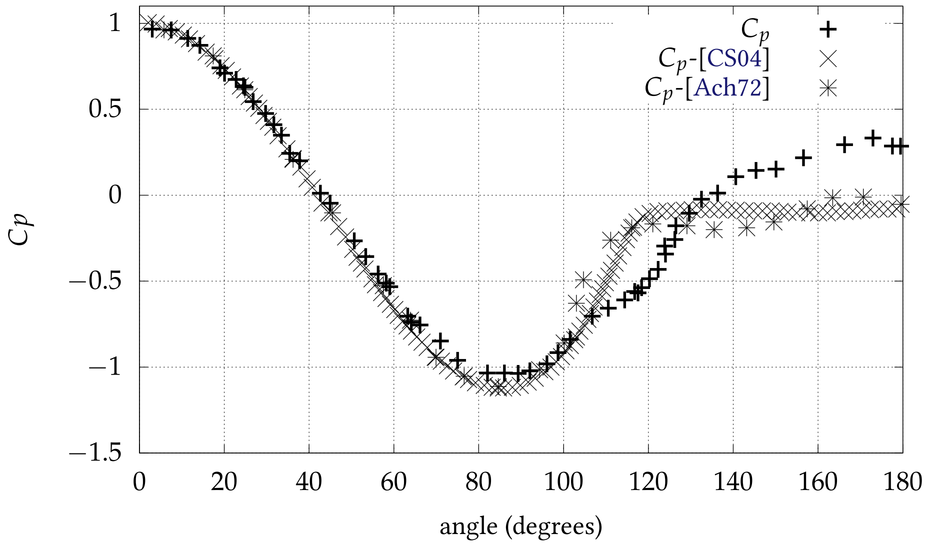

Σχήμα 3.4: Συντελεστής πίεσης C_p για σφαίρα σε αριθμό Reynolds $1,140,000$. Σύγκριση με αποτελέσματα των [CS04] και [Ach72]

.

3.4 Εξίσωση κίνησης μεμβράνης

Το πρόβλημα συνοριακών τιμών της ενότητας 2.7 επιλύεται με χρήση της μεθόδου βολής. Η ολοκλήρωση της διαφορικής εξίσωσης ξεκινάει στο ένα άκρο, υποθέτοντας την τιμή της παραγώγου στο ίδιο σημείο. Εφαρμόζοντας τη μέθοδο Newton-Raphson βρίσκεται η ορθή τιμή της παραγώγου στο όριο από όπου εκκινεί η ολοκλήρωση, στοχεύοντας στην ικανοποίηση της οριακής συνθήκης στο όριο όπου η ολοκλήρωση περαιώνεται [Pre+07].

Για την ολοκλήρωση της δεύτερης τάξης συνήθους διαφορικής εξίσωσης που παράγεται από την εξίσωση (2.43) για δεδομένο χρονικό σημείο $t = t_0$, εφαρμόζεται μετασχηματισμός σε σύστημα ΣΔΕ πρώτης τάξης με τη μορφή

$$\begin{aligned} \frac{dg(x,t_0)}{dx} &= y_1 \\ \frac{dy_1}{dx} &= \frac{-(p_e(x,t_0) - p_i(x,t_0))}{T_m} = f_1(x). \end{aligned} \tag{3.5}$$

Το ζεύγος των ΣΔΕ επιλύεται με τη μέθοδο Cash-Karp [CK90] συνδυάζοντας μεθόδους Runge-Kutta με κοινά ενδιάμεσα σημεία για κάθε βήμα. Για διαφορική εξίσωση της μορφής

$$\frac{dy(x)}{dx} = f(x, y(x)) \tag{3.6}$$

υπολογίζονται οι κλίσεις

$$k_i = hf(x_n + \alpha_i h, y_n + \sum_{j=1}^{RK-order} b_{i,j} k_j), \;\; i \in \{1, .., RK - order\}, \tag{3.7}$$

όπου h είναι το προσαρμοζόμενο βήμα. Ένα βήμα ολοκλήρωσης δίνεται ως

$$y(x_{n+1}, t_0) = y_1 + \sum_{i=1}^{RK-order} c_i k_i. \tag{3.8}$$

Οι συντελεστές a_i, $b_{i,j}$, c_i συνοψίζονται στον αντίστοιχο πίνακα Butcher.

Για κάθε ΣΔΕ, υπολογίζεται η διαφορά στις εκτιμήσεις μέσω των πέμπτου και τετάρτου βαθμού μεθόδους Runge-Kutta για το $y(x_{n+1}, t_0)$

$$e = y_5(x_{n+1}, t_0) - y_4(x_{n+1}, t_0), \tag{3.9}$$

όπου $y_5(x_{n+1}, t_0)$ και $y_4(x_{n+1}, t_0)$ είναι οι εκτιμήσεις για το $y(x_{n+1}, t_0)$ με τις μεθόδους Runge-Kutta πέμπτης και τέταρτης τάξης αντίστοιχα. Όταν το μέγιστο σφάλμα των ΣΔΕ

$$em_{i,x_s=x_0} = \max_{eq\, \in\, ODE\ system} e_{i,x_s=x_0}, \tag{3.10}$$

είναι μικρότερο από κατάλληλα επιλεγμένη ανοχή (tol), το βήμα i που αρχίζει στη θέση $x_s = x_0$ θεωρείται επιτυχές. Ειδάλλως το $em_{i,x_s=x_0}$ χρησιμοποιείται για τον προσδιορισμό του μεγέθους βήματος ($h_{i+1,x_s=x_0}$) για την επανάληψη $i+1$ στο διάστημα που αρχίζει στο $x_s = x_0$

$$h_{i+1,x_s=x_0} = \max\left(0.9 \cdot h_{i,x_s=x_0} \cdot \left(\frac{em_{i,x_s=x_0}}{tol}\right)^{-\frac{1}{5}}, \frac{h_{i,x_s=x_0}}{10}\right), \ em_{i,x_s=x_0} > tol. \tag{3.11}$$

Το πρώτο όρισμα της συνάρτησης max αποσκοπεί στην εξασφάλιση σφάλματος πλησίον της τιμής $em_{i,x_s=x_0} = 0.9 \cdot tol$. Το δεύτερο αποτελεί εχέγγυο ότι η τιμή του επόμενου βήματος θα είναι τουλάχιστον δεδομένο κλάσμα της προηγούμενης ($h_{i,x_s=x_0}$).

Εάν το μέγιστο σφάλμα ενός συμπληρωμένου βήματος (που ξεκινάει στο $x_s = x_0$ και περαιώνεται στο $x_e = x_0 + h_{i,x_s=x_0}$) προκύπτει μικρότερο από τεθειμένο κατώφλι th, η εναρκτήρια τιμή του επόμενου βήματος ολοκλήρωσης τίθεται διπλάσια της προηγούμενης

$$h_{0,x_s=x_0+h_{i,x_s=x_0}} = 2 \cdot h_{i,x_s=x_0}, \quad em_{i,x_s=x_0} < th. \tag{3.12}$$

Δυνάμει των προσαρμογών του βήματος ολοκλήρωσης, επιτυγχάνεται η ζητούμενη ακρίβεια ακόμα και σε απαιτητικά διαστήματα, χωρίς να επιμηκύνεται η διαδικασία σε σχετικά ομαλότερες περιοχές.

3.5 Σύζευξη εξισώσεων ροής - μεμβράνης

Εξετάζεται η αλληλεπίδραση ρευστού - στερεού (ΑΡΣ) μεταξύ της κύριας ροής και ελαστικής μεμβράνης. Οι εξισώσεις δυναμικής του ρευστού συζεύγνυνται ασθενώς με το πρόβλημα οριακών τιμών της εξίσωσης κίνησης μεμβράνης (εξίσωση (2.43)) με τον περιορισμό των οριακών συνθηκών που ορίζονται από την εξίσωση (2.44). Κατόπιν του υπολογισμού του πεδίου ροής προσδιορίζεται η νέα επιφάνεια της μεμβράνης.

Για την ικανοποίηση του περιορισμού μη εξάχνωσης, την μη ύπαρξη κόμβου στερεού που σε διαδοχικό χρονικό βήμα να μετατρέπεται σε κόμβο ρευστού χωρίς ενδιάμεσα να λάβει τη σημαία κόμβου εμβαπτισμένου ορίου, εφαρμόζεται δυαδική αναζήτηση ώστε να επιλεγεί κατάλληλο χρονικό βήμα ολοκλήρωσης.

Κεφάλαιο 4

Έλεγχος αποκολλημένης ροής σε απότομη διεύρυνση

4.1 Εισαγωγή

Εξετάζεται η εσωτερική μόνιμη και μη μόνιμη περιοδική ροή μέσω απότομης διεύρυνσης (λόγος διεύρυνσης 2), για χαμηλούς αριθμούς Reynolds ($Re = 400$, $Re = 800$). Ένα τμήμα του κάτω τοιχώματος της απότομης διεύρυνσης ταλαντώνεται με την συχνότητα της μη μόνιμης ροής. Ερευνάται η επίδραση της συχνότητας, του πλάτους ταλάντωσης και του μήκους της ταλαντούμενης επιφάνειας. Με κατάλληλη ρύθμιση του ενεργού ελέγχου, μειώνονται τα μήκη ανακυκλοφορίας και για ποσοστό της περιόδου δεν εμφανίζεται ζώνη αρνητικών ταχυτήτων στο άνω τοίχωμα. Επιπρόσθετα, αντικαθιστώντας την προκαθορισμένα κινούμενη επιφάνεια από μεμβράνη που αποκρίνεται στην ασκούμενη επί αυτής πίεση, εξετάζεται η αλληλεπίδραση υγρού-στερεού. Προκύπτει ότι επιλέγοντας κατάλληλες τιμές για τις παραμέτρους της μεμβράνης, όπως η τάση της και η ασκούμενη επ' αυτής εξωτερική πίεση, εξαλείφεται η φυσαλίδα αποκόλλησης της ροής στο άνω τοίχωμα, ενώ η φυσαλλίδα στο κάτω τοίχωμα συρρικνώνεται σημαντικά στη μόνιμη και τη μη μόνιμη περίπτωση. Επιπρόσθετα, για τη μεταβαλλόμενη στον χρόνο περίπτωση, η διακύμανση του μήκους της περιοχής ανάστροφης ροής στο κάτω τοίχωμα περιορίζεται σημαντικά. Τα αποτελέσματα της μελέτης βρίσκουν εφαρμογή σε εσωτερικές και εξωτερικές ροές όπου συμβαίνει αποκόλληση.

4.2 Περιγραφή του προβλήματος

Η γεωμετρία του προβλήματος στο επίπεδο x-y φαίνεται στο σχήμα 4.1.

Ακολουθώντας μεγάλο τμήμα της υφιστάμενης έρευνας [Arm+83; KM85; Gar90; Soh88; PT97], εξετάζεται απότομη διεύρυνση με λόγο διεύρυνσης δύο, $H/(H-h_s) = 2$, μήκος ανάντι της μονόπλευρης απότομης διεύρυνσης $l_0 = 2H$ και μήκος κατάντι της διεύρυνσης $L - l_0 = 30H$.

Οι οριακές συνθήκες Dirichlet για την ταχύτητα στην είσοδο ($x = -l_0$) δίνονται ως [Gar90; MMnS10]

$$u(x=-l_0,y,t) = \mathrm{U}_0(1-\alpha sin(\omega t))6(y-h_s)\frac{H-y}{(H-h_s)^2}, \;\; \mathrm{v}(x=-l_0,y,t) = 0, \;\; y \in [h_s, H], \qquad (4.1)$$

όπου $\alpha \mathrm{U}_0$ είναι το πλάτος ταλάντωσης της ταχύτητας εισόδου, u, v είναι η διαμήκης και η εγκάρσια Καρτεσιανή συνιστώσα της ταχύτητας αντίστοιχα, ω είναι οι γωνιακή συχνότητα της ταλάντωσης και t είναι ο χρόνος. Στην

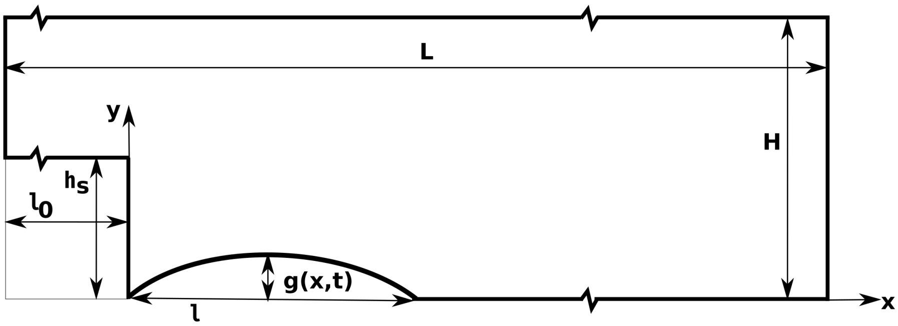

Σχήμα 4.1: Μονόπλευρη απότομη διεύρυνση με κινούμενο τμήμα μήκους l του κάτω τοιχώματος. Η είσοδος βρίσκεται τη θέση $x = -l_0$ και η έξοδος στη θέση $x = L - l_0$.

έξοδο ($x = L - l_0$) εφαρμόζονται οι οριακές συνθήκες Neumann

$$\left.\frac{\partial \psi}{\partial x}\right|_{x=L-l_0} = 0, \ \ \psi \in \{u, \mathrm{v}\}. \tag{4.2}$$

Εξετάζουμε δύο περιπτώσεις για τη συνάρτηση $g(x,t)$ της θέσης του κινούμενου τμήματος του κάτω τοιχώματος μήκους l.

α) Εξαναγκασμένη κίνηση με συχνότητα ίση με της εισερχόμενης ροής, σύμφωνα με την εξίσωση [MV01]

$$g(x,t) = Acos(\omega t)sin(\frac{\pi x}{l}), \ \ 0 \leq x \leq l, \tag{4.3}$$

όπου A είναι το πλάτος της ταλάντωσης και l είναι το μήκος του ταλαντούμενου τμήματος του κάτω τοιχώματος.

β) Αλληλεπίδραση υγρού - στερεού μεταξύ της ροής και του κινούμενου τμήματος του κάτω τοιχώματος που θεωρείται ελαστική μεμβράνη. Η κατασκευή αποκρίνεται στη ροή σύμφωνα με την εξίσωση μεμβράνης, με την υπόθεση μικρών μετατοπίσεων και μικρής αδράνειας (εξίσωση (2.43)). Η εξίσωση κίνησης της μεμβράνης περιορίζεται από τις οριακές συνθήκες στα άκρα της κατά τη φορά της ροής ($x = 0$ και $x = l$) που επιβάλλουν μηδενική μετακίνηση, $y = 0$

$$g(0,t) = g(l,t) = 0. \tag{4.4}$$

Σε κάθε τοίχωμα S_w, περιλαμβανομένου του εμβαπτισμένου ορίου, εφαρμόζονται συνθήκες μη ολίσθησης. Αδιαστατοποίηση των γεωμετρικών ποσοτήτων και των ποσοτήτων ροής πραγματοποιείται με το H για το μήκος, με το U_0 για την ταχύτητα, με την ποσότητα $\rho {\mathrm{U}_0}^2$ για την πίεση και με την ποσότητα $H\rho {\mathrm{U}_0}^2$ για την τάση της μεμβράνης T_m. Στη συνέχεια, θεωρείται η αδιάστατη εκδοχή των εμφανιζόμενων μεταβλητών, διατηρώντας το σύμβολο έκαστης φυσικής ποσότητας

$$H = 1, \ \ l_0 = 2, \ \ L = 32, \ \ u(x = -2, y = 0.75, z, t = 0) = 1.5 \ \ \kappa\lambda\pi.$$

Εφεξής θεωρούμε το αδιάστατο πρόβλημα και όλες οι αναφερόμενες μεταβλητές είναι κανονικοποιημένες.

4.3 Μόνιμη ροή

Στον πίνακα 4.1, παρουσιάζονται τα χαρακτηριστικά μήκη ανακυκλοφορίας, για τη μόνιμη περίπτωση πάνω από απότομη διεύρυνση, για αριθμό Reynolds 800. Τα αποτελέσματα της πιστοποίησης της μεθόδου βρίσκονται σε στενή συμφωνία με τα αποτελέσματα που λαμβάνονται από μεθόδους που προσαρμόζονται στο σώμα. Για αριθμό Reynolds

400 και $l_0 = 2$, βρίσκεται η επανακόλληση κάτω τοιχώματος στη θέση $x = 4.065$ και δεν βρίσκεται αποκόλληση της ροής στο άνω τοίχωμα.

Πίνακας 4.1: Θέση της αποκόλλησης και της επανακόλλησης του άνω τοιχώματος και μήκος ανακυκλοφορίας για απότομη διεύρυνση σε μόνιμη, παραβολικού προφίλ ροή, με αριθμό Reynolds 800, χωρίς έλεγχο. Σύγκριση με αποτελέσματα από μεθόδους προσαρμοσμένες στο όριο (body fitted).

	$l_0 = 0$				$l_0 = 2$	
	Εμβ. όριο	[MV01]	[Gar90]	[Soh88]	Εμβ. όριο	[MV01]
Πυκνότητα πλέγματος	2019 × 121	1201 × 241	600 × 30		3025 × 182	2193 × 401
Αποκόλληση άνω τοιχ.	4.82	4.85	4.85	-	4.4	4.66
Επανακόλληση άνω τοιχ.	10.46	10.47	10.48	-	10.38	10.31
Επανακόλληση κάτω τοιχ.	6.06	6.09	6.1	5.8	5.61	5.9

4.4 Έλεγχος της μόνιμης ροής χρησιμοποιώντας ελαστική μεμβράνη

Το τμήμα του απαραμόρφωτου κάτω τοιχώματος με το ανάντι άκρο στη θέση της απότομης διεύρυνσης και με μήκος $l = 10$, αντικαθίσταται από ελαστική μεμβράνη με τάση $T_m = 55$. Η περιβάλλουσα πίεση που ασκείται στην εξωτερική πλευρά της μεμβράνης λαμβάνεται σταθερή και ομοιόμορφη με τιμή $p_e(x,t) = p_e = 0.525$. Η τιμή επιλέγεται ούτως, ώστε να διατηρείται η παραμόρφωση της μεμβράνης σε μικρές και θετικές τιμές και η εξωτερική πίεση να είναι εγγύς των τιμών της εσωτερικής πίεσης που ασκείται από την ροή.

Λόγω της αδράνειας του ρευστού, η διεύρυνση της κύριας δέσμης της ροής κατάντι της θέσης της απότομης διεύρυνσης του αγωγού, δεν είναι άμεση όπως δηλώνεται από τις ισοϋψείς της διαμήκους ταχύτητας του σχήματος 4.2. Η δέσμη του ρευστού πλατύνεται κατάντι της απότομης διεύρυνσης και εμφανίζει μέγιστη ένταση πλάτυνσης στην περιοχή $2 \leq x \leq 3.5$.

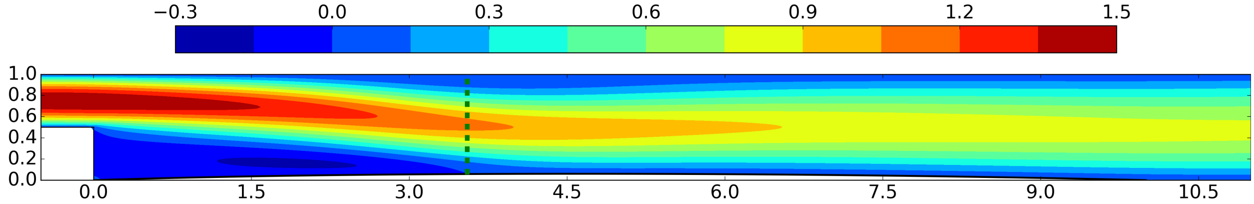

Σχήμα 4.2: Απότομη διεύρυνση με σταθερό προφίλ ταχύτητας εισόδου, με τμήμα ελέγχου μήκους $l = 10$ ελαστικής μεμβράνης στο κάτω τοίχωμα με $T_m = 55$ και $p_e = 0.525$. Διάγραμμα ισογραμμών της διαμήκους ταχύτητας για $-0.5 \leq x \leq 11$. Η θέση επανακόλλησης κάτω τοιχώματος σημαίνεται από την διακεκομμένη γραμμή.

Οι κλειστές γραμμές στο κάτω τοίχωμα εκτείνονται έως τη θέση $x = 3.55$, μειώνοντας κατά 12.7% το μήκος αποκόλλησης άνευ ελέγχου με εύρος 4.065 (ενότητα 4.3). Η αποκόλληση άνω τοιχώματος εξαλείφεται. Λόγω της χαμηλής ταχύτητας του ρευστού κάτω από τη ροή εισόδου, στη φυσαλίδα του κάτω τοιχώματος, η καμπυλότητα των γραμμών ροής είναι μικρή. Κατά συνέπεια, η κατανομή πίεσης είναι σχεδόν ομοιόμορφη για κάθε διατομή (σχήμα 4.3) [GTG07]. Στην περιοχή $2.9 \leq x \leq 5.3$ οι γραμμές ροής στρέφουν τα κοίλα προς τα άνω. Η πίεση αυξάνει στη διεύθυνση της ροής κατάντι της απότομης διεύρυνσης, ως αποτέλεσμα της συνδυασμένης εφαρμογής της εξίσωσης της ορμής και της εξίσωσης της συνέχειας και λαμβάνει τη μέγιστη τιμή της πλησίον της θέσης όπου η περιοχή ανακυκλοφορίας κάτω τοιχώματος απισχνάται [SA08]. Κατάντι αυτής της θέσης, η πίεση μειώνεται κατά τη διεύθυνση της ροής συνεπεία της δράσης της συνεκτικότητας.

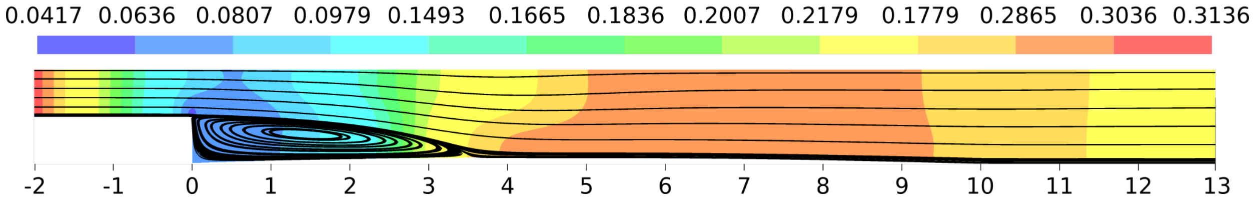

Σχήμα 4.3: Ισογραμμές πίεσης και γραμμές ροής για απότομη διεύρυνση με τμήμα ελέγχου ελαστικής μεμβράνης στο κάτω τοίχωμα, μήκους $l = 10$ με $T_m = 55$ και $p_e = 0.525$, για σταθερή ροή εισόδου με $Re = 400$, για $-2 \leq x \leq 13$.

4.5 Μη μόνιμη περιοδική ροή

Υπολογίζεται η περιοδική ροή με ταχύτητα εισόδου όπως ορίστηκε στην ενότητα 4.2. Ακολουθώντας υπάρχουσα έρευνα [MMnS10], το πλάτος της ταλαντούμενης ροής λαμβάνεται ως $\alpha = 0.05$ και η αντίστοιχη συχνότητα της ροής λαμβάνεται ως $\omega = 0.05$.

Οι θέσεις αποκόλλησης και επανακόλλησης για μη μόνιμη ροή, άνευ ελέγχου, παρουσιάζονται στο σχήμα 4.4.

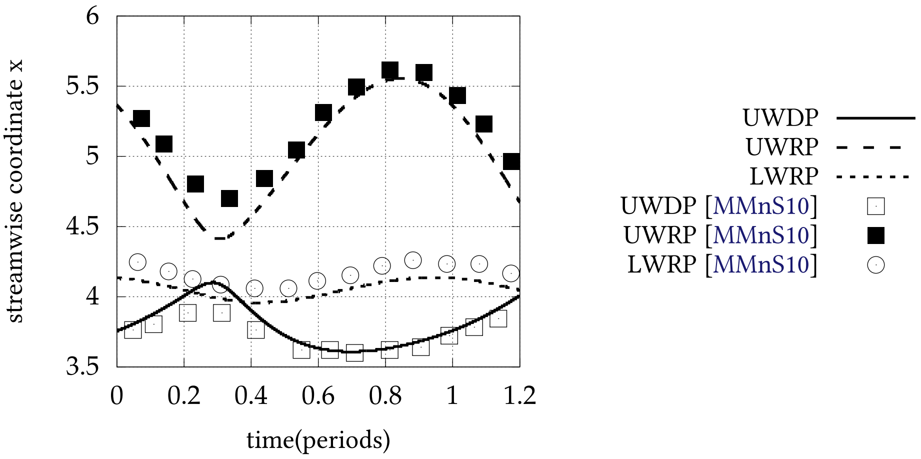

Σχήμα 4.4: Θέση αποκόλλησης άνω τοιχώματος (UWDP) και θέσεις επανακόλλησης άνω και κάτω τοιχώματος (UWRP, LWRP) για μη μόνιμη, περιοδική ροή εισόδου με $\alpha = 0.05$, $\omega = 0.05$ και $Re = 400$, άνευ ελέγχου ($A = 0$). Παρουσιάζεται σύγκριση με αποτελέσματα των Mateescu κ.α. [MMnS10].

4.6 Ενεργός έλεγχος μη μόνιμης περιοδικής ροής

Στοχεύοντας στον έλεγχο της ροής της ενότητας 4.5, το τμήμα του κάτω τοιχώματος κατάντι της θέσης της απότομης διεύρυνσης με μήκος l, εξαναγκάζεται σε ημιτονοειδή κίνηση που ακολουθεί την εξίσωση (4.3). Η εξέλιξη στο χρόνο των θέσεων αποκόλλησης και επανακόλλησης παρουσιάζεται στο σχήμα 4.5, για πλάτος $A = 0.2$, συχνότητα $\omega = 0.05$ και μήκος $l = 10$.

Η σημαντική βύθιση του κάτω τοιχώματος στο μέσο της περιόδου ελαττώνει την κλίση της στάσιμης γραμμής του κάτω τοιχώματος και αυξάνει το μήκος της. Συνεπώς, ωθεί το σημείο επανακόλλησης του κάτω τοιχώματος κατάντι. Αντίθετα, η μέγιστη θετική μετατόπιση της ταλαντούμενης επιφάνειας του κάτω τοιχώματος αυξάνει την κλίση και μειώνει το μήκος της γραμμής ανακοπής, προκαλώντας την ανάντι μετατόπιση της θέσης επανακόλλησης του κάτω τοιχώματος. Η αναστροφή ροής στο άνω τοίχωμα εμφανίζεται πιο απομακρυσμένα από τη θέση της απότομης διεύρυνσης και επιμηκύνεται καθώς η επιφάνεια ελέγχου κινείται κατάντι. Στο δεύτερο μισό της περιόδου, όπου η επιφάνεια ελέγχου κινείται άνω και η ταχύτητα εισόδου αυξάνεται, απαλείφεται ταχέως η φυσαλίδα άνω τοιχώματος. Ως συνέπεια του σημαντικού πλάτους ταλάντωσης της επιφάνειας ελέγχου ($A = 0.2$), που είναι το ένα πέμπτο της διατομής του διευρυμένου αγωγού, η ροή είναι προσκολλημένη στο άνω τοίχωμα κατά το μισό της περιόδου.

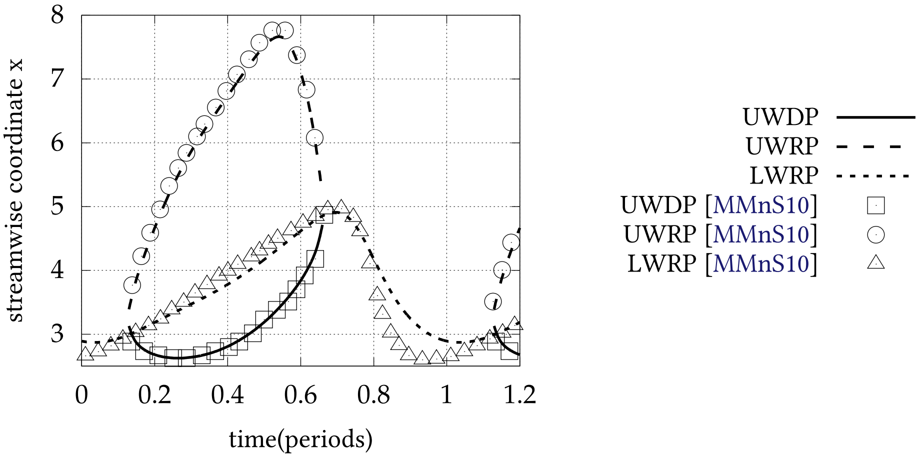

Σχήμα 4.5: Θέση αποκόλλησης άνω τοιχώματος (UWDP) και θέσεις επανακόλλησης άνω και κάτω τοιχώματος (UWRP, LWRP) για μη μόνιμη περιοδική ροή είσοδου με $\alpha = 0.05$ and $Re = 400$ και ταλαντούμενο τμήμα του κάτω τοιχώματος με $\omega = 0.05$, $A = 0.2$, $l = 10$. Παρουσιάζεται σύγκριση με αποτελέσματα των Mateescu κ.α. [MMnS10].

4.7 Παθητικός έλεγχος μη μόνιμης, περιοδικής ροής μέσω ελαστικής μεμβράνης

Σκοπεύοντας στον έλεγχο της ροής που υπολογίστηκε στην ενότητα 4.5, χρησιμοποιείται ελαστική μεμβράνη που ακολουθεί την εξίσωση (2.43) με τάση $T_m = 55$ και σταθερή και ομοιόμορφη επιβαλλόμενη πίεση ασκούμενη στην εξωτερική πλευρά, $p_e(x,t) = p_e = 0.55$. Όπως για τη μόνιμη περίπτωση, οι παράμετροι T_m και p_e επιλέγονται έτσι ώστε η μέγιστη παραμόρφωση της μεμβράνης να διατηρείται σε χαμηλό επίπεδο ($\max_{x,t} g(x,t) < 0.1$) καθ' όλη την περίοδο. Επιπλέον αντικειμενικοί σκοποί που οδηγούν στις τιμές των παραμέτρων, είναι η εξωτερική πίεση να είναι ίδιας τάξης μεγέθους με την πίεση που ασκείται από τη ροή και η διατοιχωματική πίεση $p_e - p_i(x,t)$ να είναι θετική.

Η αλληλεπίδραση της ροής με την ελαστική μεμβράνη οδηγεί στην πλήρη καταστολή της ανακυκλοφορίας άνω τοιχώματος, όπως φαίνεται στα προφίλ ταχύτητας του σχήματος 4.6. Διακρίνεται ακόμα ότι το πλάτος ταλάντωσης της επιφάνειας ελέγχου περιορίζεται συγκριτικά με το πλάτος ενεργού ελέγχου της προηγούμενης ενότητας.

Όπως παρατηρείται στο σχήμα 4.7, το μήκος της ζώνης αποκόλλησης κάτω τοιχώματος συρρικνώνεται σημαντικά (14.3%). Η από κορυφή σε κορυφή διακύμανση τιμής 0.18 για την άνευ ελέγχου περίπτωση, πέφτει στην τιμή 0.14 για την περίπτωση παθητικού ελέγχου, δηλαδή σημειώνεται μείωση 22.2%.

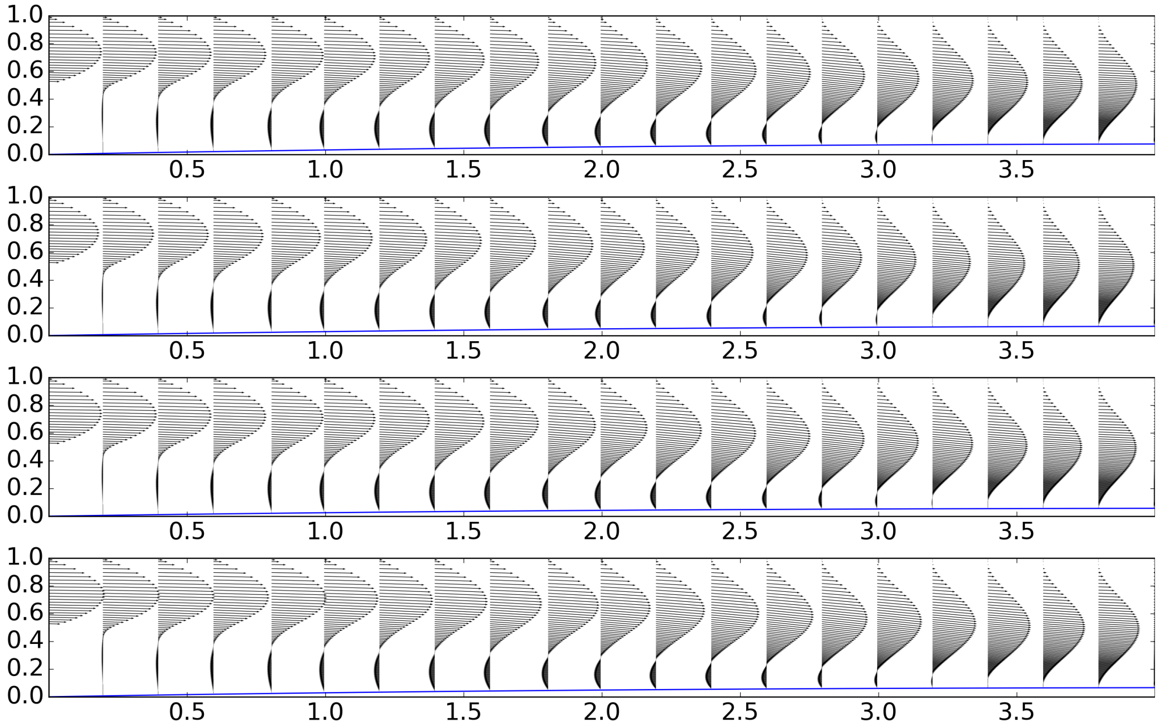

Σχήμα 4.6: Υπολογισμένα πεδία ταχυτήτων για $t = 0$, $t = T/4$, $t = T/2$, $t = 3T/4$, αντίστοιχα, κατά τη διάρκεια μίας περιόδου εισόδου T, για αλληλεπίδραση ρευστού - στερεού της ροής με μεμβράνη με $T_m = 55$ και $p_e = 0.55$. Η είσοδος (εξίσωση 4.1) ταλαντώνεται με $\alpha = 0.05$ και $\omega = 0.05$. Ο αριθμός Reynolds είναι 400.

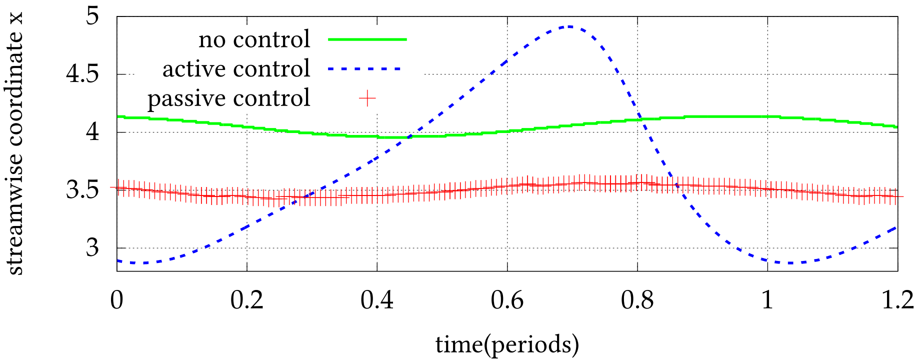

Σχήμα 4.7: Θέση επανακόλλησης κάτω τοιχώματος (LWRP) κατά τη διάρκεια μίας περιόδου της περιοδικής ροής πάνω από απότομη διεύρυνση που ελέγχεται από ελαστική μεμβράνη με $l = 10$, $T_m = 55$ και $p_e = 0.55$. Η είσοδος ορίζεται από την εξίσωση (4.1) με $\alpha = 0.05$ και $\omega = 0.05$. Σύγκριση με αποτελέσματα άνευ ελέγχου και με ενεργό έλεγχο.

Κεφάλαιο 5

Περίσταλση

5.1 Εισαγωγή

Περισταλτική κίνηση εμφανίζεται σε πολλές φυσιολογικές, ιατρικές, φαρμακευτικές και βιομηχανικές διαδικασίες. Ο έλεγχος της παροχής όγκου ρευστού και της πίεσης είναι κρίσιμος για εφαρμογές άντλησης, όπως η έγχυση ενδοφλέβιων φαρμάκων, η μετάγγιση αίματος κλπ. Στην παρούσα μελέτη, παρουσιάζεται προσομοίωση της περισταλτικής ροής στην οποία η έμφραξη υλοποιείται από ζεύγη κυλίνδρων που συμπιέζουν παραμορφώσιμο κανάλι, συνδεδεμένο με δεξαμενή ρευστού σταθερής πίεσης. Το είδος αυτό ροής απαντάται ως στρωτή ροή, κατά συνέπεια ο υπολογισμός έλαβε χώρα σε τέτοιες συνθήκες. Ερευνάται η επίδραση του αριθμού και της ταχύτητας των κυλίνδρων, όπως και του διακένου μεταξύ του ζεύγους των κυλίνδρων. Μελετάται περίσταλση μη Νευτώνειων ρευστών και εξετάζεται η επίδραση της συμπεριφοράς διατμητικής λέπτυνσης στην άντληση. Η παροχή όγκου ρευστού βρίσκεται να αυξάνεται με την αύξηση του αριθμού κυλίνδρων ή της σχετικής έμφραξης. Μείωση στον εκθέτη Bird-Carreau έχει ως συνέπεια μικρή μείωση στην απόδοση μεταφοράς. Υπολογίζεται η χαρακτηριστική της άντλησης, δηλαδή η επαγόμενη πίεση ως συνάρτηση της παροχής όγκου ρευστού. Ισχυρή θετική συσχέτιση υπάρχει ανάμεσα στην σχετική έμφραξη και την επαγόμενη πίεση. Η συμπεριφορά αραίωσης υπό διάτμηση μειώνει σημαντικά την αναπτυσσόμενη πίεση εν συγκρίσει με τη Νευτώνεια απόκριση. Γίνεται σύγκριση με υπάρχοντα υπολογιστικά αποτελέσματα [AH13] που λαμβάνονται με τον προσαρμοζόμενο στο σώμα (body-fitted) αλγόριθμο OpenFOAM [Che+14]. Η πιστοποίηση της καμπυλόγραμμης μεθόδου εμβαπτισμένου ορίου για μη Νευτώνεια ρευστά έχει ικανοποιητικά αποτελέσματα, καθώς παρατηρείται συμφωνία, με όμοια απεικόνιση των τάσεων της ροής σε συνάρτηση με τις παραμέτρους.

5.2 Γεωμετρία

Για την προσομοίωση του παραμορφώσιμου καναλιού χρησιμοποιείται διδιάστατο, συμμετρικό μοντέλο, που παρουσιάζεται στο σχήμα 5.1. Ο ελαστικός σωλήνας συμπιέζεται από δύο αντικρυστά κυλινδρικά κύματα που κινούνται οριζόντια με ταχύτητα c. Το ημιύψος του απαραμόρφωτου καναλιού λαμβάνεται ως $H = 10$ mm, όπως του ανθρώπινου οισοφάγου. Η ακτίνα του κυκλικού τομέα του ρόλλερ είναι $r = 30$ mm (όπως στα πειράματα που παρουσιάζονται από τη [Nah12]). Το ελάχιστο ύψος του παραμορφωμένου καναλιού λαμβάνει τιμές ανάλογα με το πλάτος συμπίεσης.

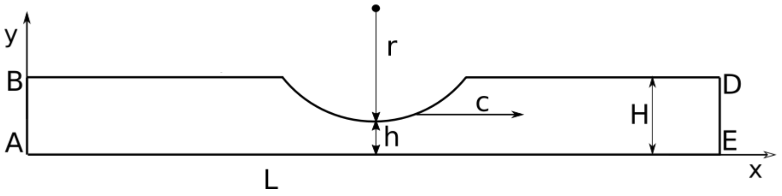

Σχήμα 5.1: Γεωμετρία του διδιάστατου υπολογιστικού χωρίου για περισταλτική αντλία. Ο κατοπτρισμός του σχήματος ως προς τον άξονα x και η εξώθηση ως προς τον άξονα z αποδίδει την γεωμετρία της πλήρους αντλίας.

5.3 Μαθηματική περιγραφή

Ακολουθώντας έρευνα των Nahar κ.α. [NJW10] και του Al-Hababheh [AH13], η πυκνότητα του αντλούμενου ρευστού λαμβάνεται ως $\rho = 1000\ \mathrm{kg/m^3}$ και η ρεολογία του προβλέπεται από την εξίσωση Bird-Carreau [Car68; BAH87] (εξίσωση (2.4))

$$\mu(\dot{\gamma}) = \mu_{\text{inf}} + (\mu_0 - \mu_{\text{inf}})(1 + (\lambda\dot{\gamma})^2)^{\frac{n-1}{2}}. \tag{5.1}$$

Οι τιμές των σταθερών λαμβάνονται ως $\mu_{\text{inf}} = 0$, $\mu_0 = 0.1452\ \mathrm{Pa \cdot s}$, $\lambda = 20\ \mathrm{s}$ και $n \leq 1$.

Στην κεντρική γραμμή ορίζονται οριακές συνθήκες συμμετρίας, δηλαδή η κάθετη βαθμίδα της αξονικής ταχύτητας και η εγκάρσια ταχύτητα τίθενται μηδενικές:

$$\left.\frac{\partial u}{\partial y}\right|_{y=0} = 0, \;\; \mathrm{v}(x, y = 0) = 0, \tag{5.2}$$

όπου η u είναι η κατά τη φορά της ροής συνιστώσα της ταχύτητας και v η κάθετη συνιστώσα της ταχύτητας. Επί του άνω παραμορφώσιμου τοιχώματος ορίζεται συνθήκη μη ολίσθησης.

$$\phi(\text{wall}) = \phi_{\text{wall}}, \;\; \phi \in \{u, \mathrm{v}\}, \tag{5.3}$$

όπου ϕ_{wall} είναι η συνιστώσα ταχύτητας του τοιχώματος.

Στις ενότητες 5.4-5.5, η οριακή συνθήκη για το αριστερό και το δεξί άκρο του σωλήνα-διατομές AB και DE στο σχήμα 5.1, αντίστοιχα-είναι η περιοδική συνθήκη για τις συνιστώσες ταχύτητας:

$$\phi(x = 0, y) = \phi(x = L, y), \;\; \phi \in \{u, \mathrm{v}\}. \tag{5.4}$$

Για την ενότητα 5.6, στη διατομή AB του σχήματος 5.1, η επιβαλλόμενη οριακή συνθήκη είναι παραβολικού προφίλ ταχυτήτων:

$$u(x = 0, y) = u_{max}\left(1 - \left(\frac{y}{H}\right)^2\right), \;\; \mathrm{v}(x = 0, y) = 0, \tag{5.5}$$

όπου u_{max} είναι η μέγιστη ταχύτητα του παραβολικού προφίλ στον άξονα $y = 0$. Στην διατομή εξόδου DE, για $x = L$, τίθεται μηδενική κάθετη βαθμίδα ταχύτητας

$$\left.\frac{\partial \phi}{\partial x}\right|_{x=L} = 0, \;\; \phi \in \{u, \mathrm{v}\}. \tag{5.6}$$

Πραγματοποιήθηκε μελέτη ανεξαρτησίας πλέγματος χρησιμοποιώντας ένα αδρό Καρτεσιανό πλέγμα (451 × 52 κόμβων) και ένα πυκνότερο (1041 × 102 κόμβων) για την αντλία των 180 mm. Ανάλογης πυκνότητας πλέγματα εφαρμόστηκαν για την αντλία των 90 mm. Η μέγιστη διαφορά στην αξονική ταχύτητα για τα δύο πλέγματα είναι μικρότερη από 0.25%. Η μέγιστη διαμέριση του πυκνού πλέγματος είναι 0.1 mm. Λόγω της χρήσης τριδιάστατου αλγορίθμου επίλυσης, λαμβάνεται μικρό βάθος πεδίου με συνθήκες ολίσθησης στις οριακές επιφάνειες της τρίτης διάστασης. Η εμβαπτισμένη επιφάνεια του κυλίνδρου τριγωνοποιείται με 3104 κόμβους που παράγουν 6204 στοιχεία με απόσταση των κόμβων που φράσσεται άνω από το μέγεθος 0.2 mm.

Το σύστημα συντεταγμένων που εμφανίζεται στο σχήμα 5.1 προσαρτάται στον κύλινδρο και ορίζεται ως κινούμενο σύστημα αναφοράς. Η προσομοίωση έλαβε χώρα σε αυτό το κινούμενο σύστημα αναφοράς. Συνεπώς, ο κύλινδρος μένει ακίνητος, ενώ η επιφάνεια $y = H$ κινείται με ταχύτητα $\boldsymbol{v} = (-c, 0)$, οπότε προσομοιώνεται ένα σταθερό πεδίο ροής. Στο υπολογισμένο πεδίο ροής προστίθεται ομοιόμορφα η ταχύτητα του κυλίνδρου $\boldsymbol{v} = (c, 0)$ ούτως ώστε να επιστρέψουμε στο εργαστηριακό πλαίσιο αναφοράς.

Η σχετική έμφραξη (RO) ορίζεται ως ο λόγος της διείσδυσης ζεύγους κυλίνδρων στον παραμορφώσιμο σωλήνα προς το ύψος του απαραμόρφωτου καναλιού

$$RO = \frac{H - h}{H}. \tag{5.7}$$

Το πεδίο ροής για ταχύτητα ρόλλερ $c = 5$ mm/s και ημιδιάκενο $h = 4$ mm παρουσιάζεται στο σχήμα 5.2 ενώ το πεδίο πίεσης στο σχήμα 5.3.

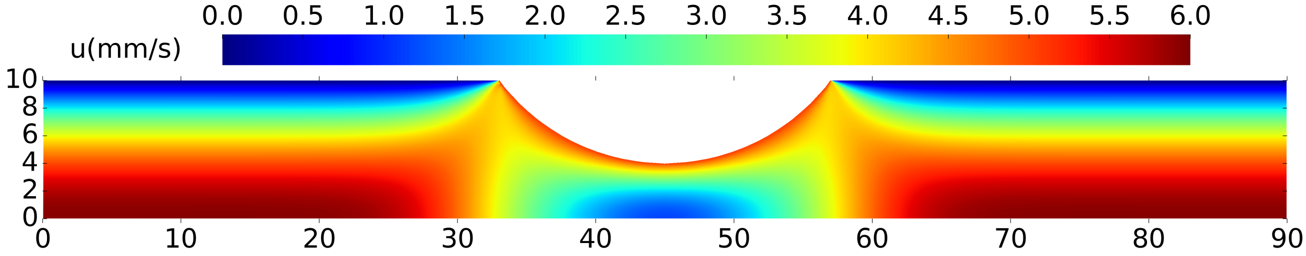

Σχήμα 5.2: Ισοεπιφάνειες αξονικής ταχύτητας για 1 ρόλλερ, $c = 5$ mm/s, $L = 90$ mm, $RO = 0.6$ και $n = 1$.

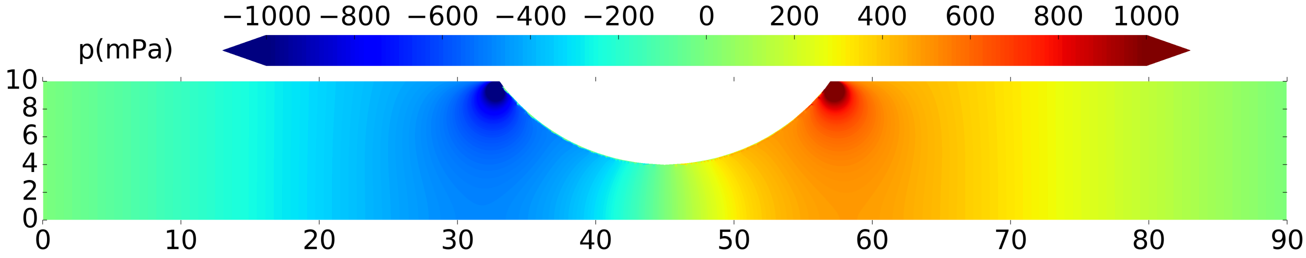

Σχήμα 5.3: Ισοεπιφάνειες πίεσης για 1 ρόλλερ, $c = 5$ mm/s, $L = 90$ mm, $RO = 0.6$ και $n = 1$.

Η απόδοση μεταφοράς (TE) ορίζεται ως η παροχή όγκου του ρευστού προς την ταχύτητα του κύματος και το ύψος του πλήρους καναλιού

$$TE = \frac{\dot{V}}{c \cdot 2H}. \tag{5.8}$$

5.4 Μη Νευτώνεια ρευστά

Καθώς μειώνεται ο εκθέτης Bird-Carreau, η επίδραση του κινούμενου ρόλλερ στην αξονική ταχύτητα πλησίον του διαμήκους άξονα συμμετρίας ($y = 0.05$ mm) γίνεται ασθενέστερη˙ δηλαδή, κοντά στον άξονα, η κατά μήκος καμπύλη της διαμήκους ταχύτητας παρουσιάζει εμφανώς μικρότερη διακύμανση, όπως φαίνεται στο σχήμα 5.4. Λεπτομερέστερα, μακριά από τη θέση του ρόλλερ, η ταχύτητα μειώνεται, ενώ στη θέση του ρόλλερ, αυξάνεται.

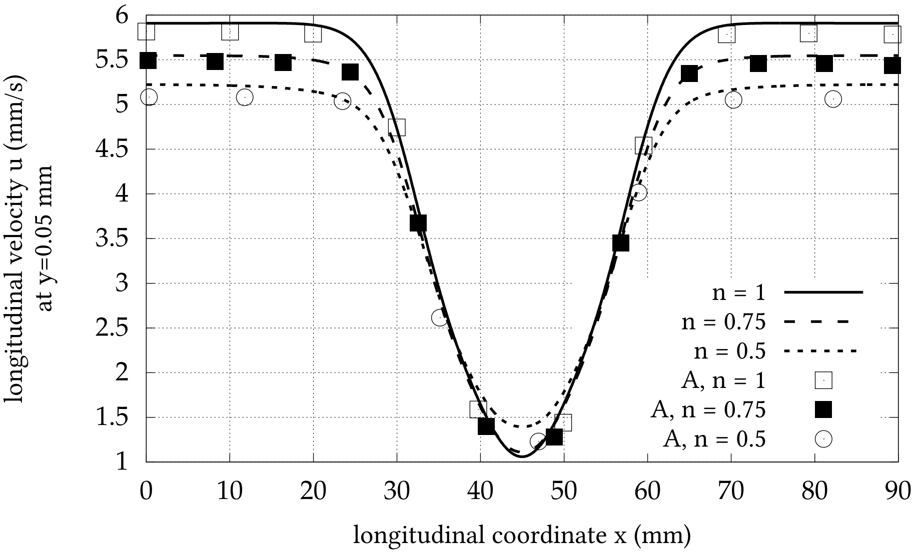

Σχήμα 5.4: Κατά μήκος ταχύτητα κοντά στον κεντρικό άξονα της αντλίας ($y = 0.05$ mm) για Νευτώνεια και μη Νευτώνεια ρευστά, $c = 5$ mm/s, $RO = 0.6$ και έναν κύλινδρο. Παρουσιάζεται σύγκριση με αποτελέσματα από μέθοδο προσαρμοσμένη στο σώμα (A: Δεδομένα από το [AH13]).

Πίνακας 5.1: Απόδοση μεταφοράς (TE) για διάφορες συνθήκες άντλησης και μήκος αντλίας $L = 90$ mm. Σύγκριση με υπάρχοντα αποτελέσματα [AH13].

$n = 1$, $RO = 0.6$		$c = 5$ mm/s, $n = 1$			$c = 10$ mm/s, $n = 1$		$c = 5$ mm/s, $RO = 0.6$		
c (mm/s)	TE (%)	RO	TE (%)	TE (%) [AH13]	RO	TE (%)	n	TE (%)	TE (%) [AH13]
2.5	78.8	0.8	95.6	95	0.6	78.8	1	78.4	78
5	78.4	0.6	78.4	78	0.2	28.6	0.75	77.5	77
10	78.8	0.2	28.4	28			0.5	77.1	76

5.5 Πολλαπλά ρόλλερ

Τα διανύσματα ταχύτητας για αντλίες ενός, δύο και τριών ρόλλερ με $L = 180$ mm παρουσιάζονται στο σχήμα 5.5. Η αξονική ταχύτητα εμφανίζει μέγιστη τιμή πλησίον του x άξονα μακριά από το ρόλλερ και λαμβάνει την ελάχιστη τιμή της υπό τον κύλινδρο. Για την περίπτωση ενός κυλίνδρου, η αξονική ταχύτητα υπό το ρόλλερ (82 mm $\leq x \leq$ 98 mm) και πλησίον του διαμήκους άξονα συμμετρίας ($y = 0.05$ mm) είναι αρνητική, δημιουργώντας ζώνη ανακυκλοφορίας. Για πολλαπλά ρόλλερ, δεν εμφανίζεται αρνητική αξονική ταχύτητα.

Τα ακρότατα της εγκάρσιας ταχύτητας βρίσκονται στο ανάντι και το κατάντι όριο του συρμού των ρόλλερ, για όλες τις περιπτώσεις. Η συμπεριφορά αυτή ερμηνεύεται από την εκκένωση χώρου που συμβαίνει για τη διέλευση του συρμού των ρόλλερ (π.χ. για $x = 114.5$ mm για δύο ρόλλερ) και την πλήρωση του κενού χώρου που καταλείπεται από την αναχώρηση του συρμού των ρόλλερ π.χ. στη θέση $x = 65.5$ mm για δύο ρόλλερ).

Η πίεση λαμβάνει την ελάχιστη τιμή της στο ανάντι όριο του συρμού των ρόλλερ, τη θέση $\inf_x\{w^{-1}(x)\}$, όπου $w(x)$ είναι η κυματομορφή περίσταλσης και την υψηλότερη τιμή της στο κατάντι όριο του συρμού των ρόλλερ, τη θέση $\sup_x\{w^{-1}(x)\}$. Επιπλέον, η συνάρτηση της πίεσης κατά μήκος των ρόλλερ είναι μονότονη, ενώ τα μέγιστα και

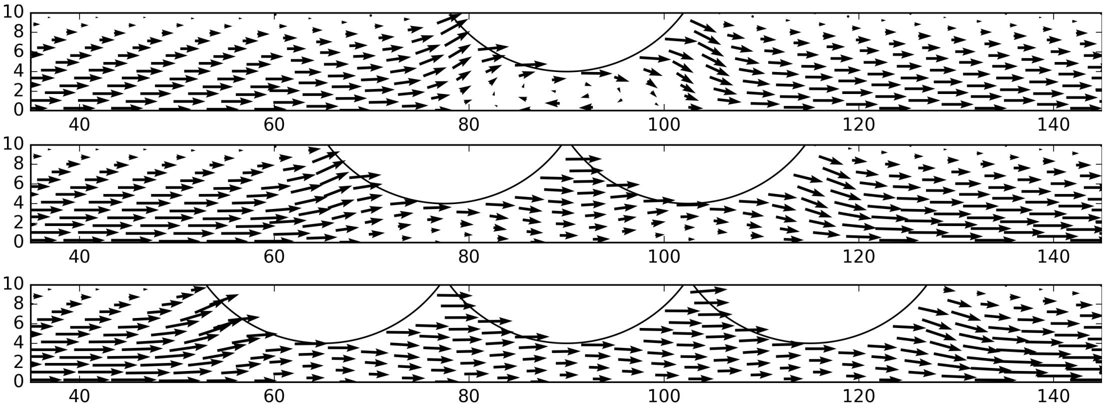

Σχήμα 5.5: Διανύσματα ταχύτητας για 1, 2 και 3 ρόλλερ, $c = 5$ mm/s, $L = 180$ mm, $RO = 0.6$ και $n = 1$.

τα ελάχιστα έχουν τιμές πρακτικά ανεξάρτητες από τον αριθμό των κυλίνδρων. Η μέγιστη τιμή του ρυθμού διάτμησης πλησίον του άξονα συμμετρίας είναι σημαντικά υψηλότερη για ένα ρόλλερ (0.98 s^{-1}) από ότι για περισσότερα (0.75 s^{-1} για δύο και 0.68 s^{-1} για τρία). Όπως φαίνεται στον πίνακα 5.2, η απόδοση μεταφοράς αυξάνει υπογραμμικά καθώς ο αριθμός των διαδοχικών ρόλλερ αυξάνει.

Πίνακας 5.2: Απόδοση μεταφοράς για πολλαπλά συνεχόμενα ρόλλερ, μήκος αντλίας $L = 180$ mm, $c = 5$ mm/s, $RO = 0.6$ και $n = 1$.

Πλήθος ρόλλερ	**1**	**2**	**3**
Απόδοση μεταφοράς TE (%)	60	78	87

5.6 Χαρακτηριστικές περισταλτικής αντλίας

Προσομοιώσαμε τη ροή παραβολικού προφίλ ταχύτητας εισόδου (εξίσωση (5.5)) μέσω της γεωμετρίας της αντλίας με ένα ρόλλερ. Ως εκ τούτου, υπολογίσαμε την αύξηση πίεσης που επάγεται από την παρουσία της κυματομορφής του ρόλλερ. Για υψηλότερη εισερχόμενη παροχή όγκου ρευστού, η αύξηση πίεσης μειώνεται. Η πτώση πίεσης μέσω του ελαστικού καναλιού εκατέρωθεν του ρόλλερ μειώνεται, καθώς μειώνεται η εισερχόμενη παροχή ρευστού. Η αύξηση πίεσης κατά μήκος του ρόλλερ αυξάνει δραστικά καθώς ο εισερχόμενος όγκος ρευστού ελαττώνεται.

Η χαρακτηριστική καμπύλη της περισταλτικής αντλίας δίνεται στα σχήματα 5.6 και 5.7 για την περίπτωση αντλίας ενός ρόλλερ, με μήκος $L = 90$ mm και ταχύτητα ρόλλερ $c = 5$ mm/s και για δύο διαφορετικές τιμές του διακένου μεταξύ των ρόλλερ και του εκθέτη Bird-Carreau. Οι χαρακτηριστικές είναι κατά προσέγγιση ευθείες γραμμές με αρνητική κλίση. Η εφαπτομένη της γωνίας της χαρακτηριστικής με τον οριζόντιο άξονα συσχετίζεται αρνητικά με την σχετική έμφραξη. Η επίδραση στη ροή, της διείσδυσης του ρόλλερ είναι μεγαλύτερη όταν είναι βαθύτερη, δηλαδή όταν το ημιδιάκενο είναι μικρότερο. Για δεδομένη ροή όγκου, η μέγιστη πίεση που αναπτύσσεται στη ροή είναι προσεγγιστικά έξι φορές υψηλότερη για $RO = 0.8$ από ότι για $RO = 0.6$. Για σταθερή πίεση, η σχετική έμφραξη και η παροχή όγκου ρευστού συσχετίζονται θετικά. Για διατμητικά λεπτυνόμενα ρευστά, η κλίση των χαρακτηριστικών αυξάνει σε μεγάλο βαθμό, δηλαδή η δυνατότητα άντλησης μειώνεται σημαντικά. Χαρακτηριστικά, για ρευστό με εκθέτη $n = 0.5$, η δυνητική πίεση κατάθλιψης μειώνεται μία τάξη μεγέθους εν συγκρίσει με την αντίστοιχη τιμή για Νευτώνειο ρευστό. Η μέγιστη δυνητική παροχή όγκου ρευστού επίσης μειώνεται για διατμητικά λεπτυνόμενα ρευστά.

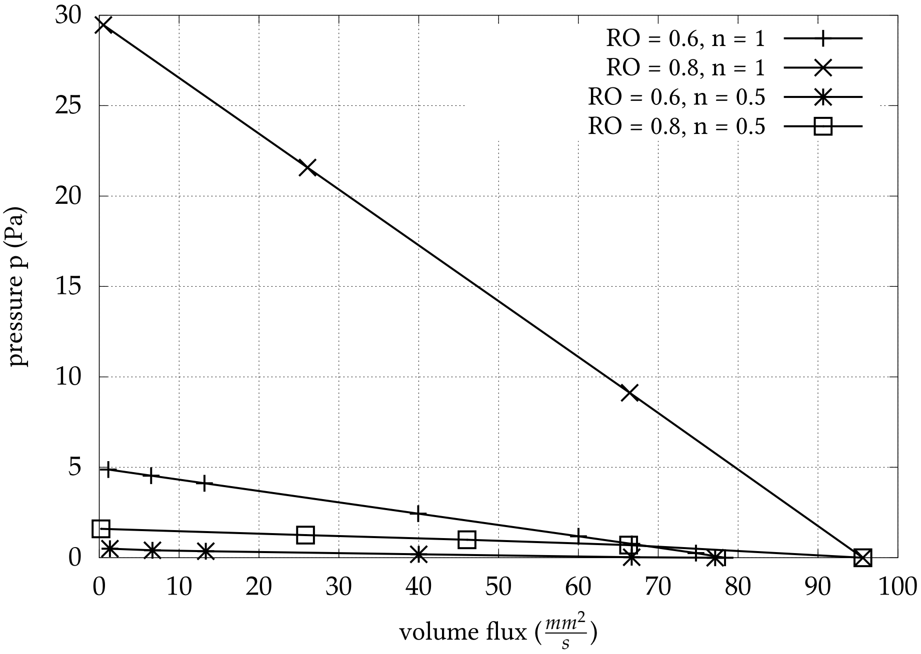

Σχήμα 5.6: Χαρακτηριστικές περίσταλσης για περισταλτικές αντλίες μήκους 90 mm και ενός ρόλλερ, που κινείται με $c = 5$ mm/s, χρησιμοποιώντας γραμμική κλίμακα για την πίεση.

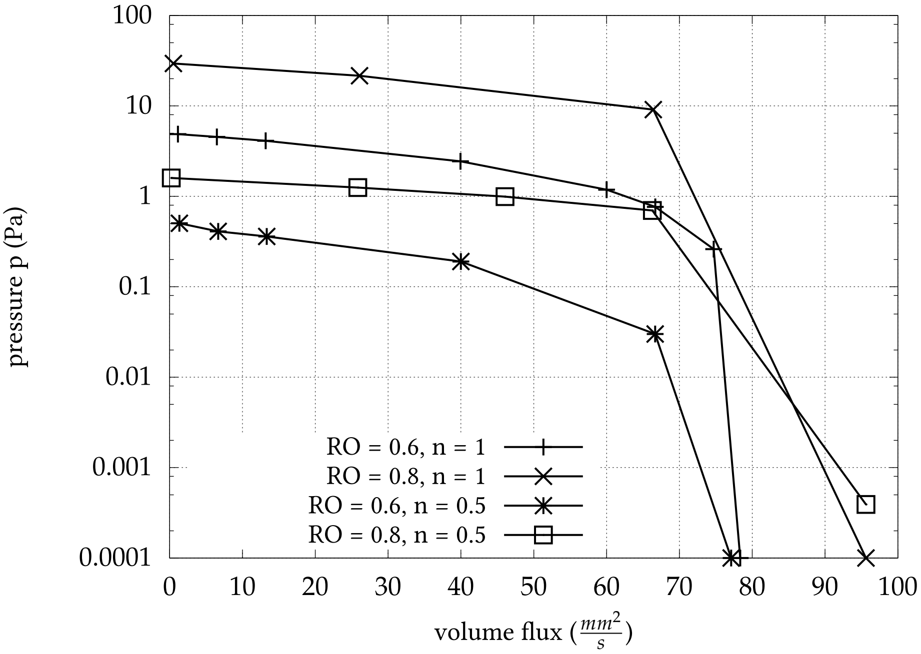

Σχήμα 5.7: Χαρακτηριστικές περίσταλσης για περισταλτικές αντλίες μήκους 90 mm και ενός ρόλλερ, που κινείται με $c = 5$ mm/s, χρησιμοποιώντας λογαριθμική κλίμακα για την πίεση.

Κεφάλαιο 6

Παλμική ροή με άντληση ασκού

6.1 Εισαγωγή

Αντλίες ασκού χρησιμοποιούνται για την υποβοήθηση της καρδιακής λειτουργίας σε περιπτώσεις οξέως εμφράγματος του μυοκαρδίου, κοιλιακής αρρυθμίας, καρδιογενούς σοκ, ασταθούς στηθάγχης, ανθεκτικής κοιλιακής ανεπάρκειας ή εγχείρησης καρδιάς. Η παλμική αντιώθηση μέσω αύξησης της διαστολικής πίεσης και μείωσης της συστολικής πίεσης, αυξάνει τη στεφανιαία αιμάτωση και υποβοηθεί την καρδιά να αντλεί περισσότερο αίμα σε κάθε σφύξη. Στην παρούσα μελέτη εξετάζεται αντλία μπαλονιού που μεταβάλλει την ροή Poiseuille σε ευθύγραμμο κυκλικό αγωγό. Το μπαλόνι είναι σφαιροειδούς σχήματος ενώ το μήκος ελάσσονος άξονα, που είναι κάθετος στη διεύθυνση της ροής, μεταβάλλεται στον χρόνο ακολουθώντας ημιτονοειδή νόμο. Η εισερχόμενη παροχή όγκου ρευστού είναι σταθερή ενώ ο όγκος ρευστού που εξέρχεται του αγωγού μεταβάλλεται στον χρόνο λόγω της παρουσίας της αντλίας ασκού. Η διαφορά πίεσης εκατέρωθεν του σφύζοντος ασκού παρουσιάζει σημαντική διαφορά φάσης ακολουθώντας την κυματομορφή παροχής όγκου για συχνότητα πάλμωσης 60 σφύξεων ανά λεπτό. Παρουσιάζεται το πλήρες πεδίο ροής γύρω από το μπαλόνι άντλησης.

6.2 Μεθοδολογία

Σκαρίφημα της αντλίας παρουσιάζεται στο σχήμα 6.1. Το αγγείο που περιέχει την ενδοαορτική αντλία μπαλονιού, μοντελοποιείται ως ευθύγραμμος αγωγός κυκλικής διατομής. Η ακτίνα της αρτηρίας είναι r_a, και το μήκος της είναι l_a.

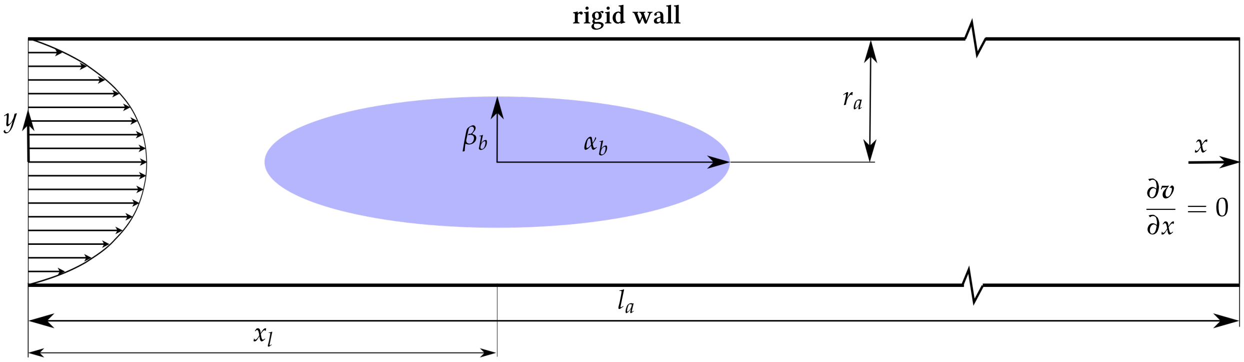

Σχήμα 6.1: Σχήμα του σφαιροειδούς μπαλονιού και της ομοαξονικής περιβάλλουσας αρτηρίας.

Το μπαλόνι έχει σχήμα ωοειδούς ελλειψοειδούς εκ περιστροφής. Ο μέγιστος άξονάς του ταυτίζεται με τον άξονα συμμετρίας της αρτηρίας και το μέσον του κείται στη διαμήκη θέση x_l. Η επιφάνεια του ασκού σε Καρτεσιανές συντεταγμένες ακολουθεί την εξίσωση

$$\frac{(x-x_l)^2}{{\alpha_b}^2}+\frac{y^2}{{\beta_b}^2(t)}+\frac{z^2}{{\gamma_b}^2(t)}=1,\ \ |x-x_l|\leq a_b, \tag{6.1}$$

όπου $\alpha_b > \beta_b = \gamma_b$ είναι οι αντίστοιχοι ημιάξονες. Το μήκος του μείζονος ημιάξονα είναι σταθερό στο χρόνο ενώ η ισημερινή ακτίνα μεταβάλλεται στον χρόνο σύμφωνα με τον συνημιτονοειδή νόμο

$$\beta_b(t)=\gamma_b(t)=r_{b0}-A_b cos\left(\frac{2\pi}{T}t\right), \tag{6.2}$$

όπου T είναι η περίοδος της ταλάντωσης.

Συνεπώς ο όγκος του ρευστού στην έξοδο, δηλαδή η παροχή όγκου της παλλόμενης ροής, είναι

$$Q_{out}(t)=Q_{in}(t)+\frac{dV(t)}{dt}=Q_{in}(t)+\frac{8}{3}\cdot\alpha_b\cdot\frac{A_b\pi^2}{T}\left(2\cdot r_{b0}\cdot sin\left(\frac{2\pi}{T}t\right)-A_b\cdot sin\left(\frac{4\pi}{T}t\right)\right). \tag{6.3}$$

Οι τιμές που λαμβάνονται για τα γεωμετρικά μεγέθη της αντλίας δίνονται στον πίνακα 6.1.

Πίνακας 6.1: Τιμές των γεωμετρικών ποσοτήτων της προσομοίωσης.

Ποσότητα	**Τιμή (cm)**
r_a	0.925
l_a	18 (for $Q_{in} = 0.01L/s$), 40 (for $Q_{in} > 0.01L/s$)
α_b	3
r_{b0}	0.32, 0.36, 0.44
A_b	0.02, 0.06, 0.14
x_l	7

Οι ιδιότητες του ρευστού για την προσομοίωση παρουσιάζονται στον πίνακα 6.2.

Πίνακας 6.2: Τιμές των ιδιοτήτων ρευστού στο σύστημα μονάδων CGS.

Ποσότητα	**Τιμή**
δυναμική συνεκτικότητα μ	0.04 $g/(cm\cdot s)$
πυκνότητα ρ	1.06 g/cm^3

Για περίοδο $T = 1s$, ο αριθμός Womersley [Wom55] της παλλόμενης ροής είναι

$$\alpha = r_\alpha\sqrt{\frac{\omega}{\nu}}=11.936, \tag{6.4}$$

όπου $\omega=\dfrac{2\pi}{T}$ είναι η γωνιακή συχνότητα της ταλάντωσης του μπαλονιού.

Εισάγοντας κυλινδρικές συντεταγμένες (x, r, θ) για την αξονική, την ακτινική και την εφαπτωμενική συνιστώσα αντίστοιχα, η ταχύτητα εκφράζεται ως (u, U_r, U_θ), όπου U_r είναι η ακτινική συνιστώσα της ταχύτητας και U_θ είναι η περιφερειακή συνιστώσα της ταχύτητας.

Στο εσωτερικό στερεό όριο, δηλαδή στην επιφάνεια του ασκού, καθορίζεται η ακτινική συνιστώσα της ταχύτητας ως

$$\mathrm{U}_r\left(x,r,\theta,t \,\middle|\, \frac{(x-x_l)^2}{{\alpha_b}^2}+\frac{r^2}{{\beta_b}^2(t)}=1\ ,\ \ |x-x_l|\leq a_b\right)=\frac{\partial r(x,t)}{\partial t}=\sqrt{a_b^2-(x-x_l)^2}\cdot\frac{2\pi A_b}{\alpha_b T}sin\left(\frac{2\pi}{T}t\right), \tag{6.5}$$

ενώ οι λοιπές συνιστώσες τίθενται μηδενικές. Στο εξωτερικό όριο του υπολογιστικού χωρίου εφαρμόζονται μεικτές οριακές συνθήκες. Στην είσοδο, η αξονική ταχύτητα είναι μη μηδενική και ακολουθεί παραβολικό προφίλ ενώ οι λοιπές συνιστώσες είναι μηδενικές

$$u(x=0,r,\theta,t)=\frac{Q_{in}}{\pi {r_a}^2}2\left(1-\frac{y^2+z^2}{{r_a}^2}\right). \tag{6.6}$$

Στο τοίχωμα του αγγείου, τίθεται συνθήκη μη ολίσθησης, ενώ στο κατάντι άκρο του, επιβάλλεται μηδενική διαμήκης παράγωγος της ταχύτητας. Αξιοποιώντας τη συμμετρία της γεωμετρίας και του πεδίου ροής και λαμβάνοντας υπόψιν τη δομή του αλγορίθμου επίλυσης, εξετάζεται ένα τέταρτο της γεωμετρίας κυλίνδρου. Στα δύο διαμήκη επίπεδα επιβάλλονται συνθήκες συμμετρίας δηλαδή σταθερή μεσημβρινή ταχύτητα ως προς την αζιμουθιακή κατεύθυνση και μηδενική περιφερειακή ταχύτητα. Η ροή του αίματος σε μεγάλες αρτηρίες μπορεί να θεωρηθεί Νευτώνεια [FQV09], συνεπώς επιλύονται οι εξισώσεις ροής (2.40) και (2.42) σε καμπυλόγραμμο και Καρτεσιανό υποκείμενο πλέγμα.

6.3 Αποτελέσματα και Συζήτηση

Τα προκύπτοντα διανύσματα ταχύτητας σε επίπεδο που ορίζεται από τον κεντρικό άξονα του κυλίνδρου και έναν γεννήτορά του, απεικονίζονται στο σχήμα 6.2. Το παραβολικό προφίλ στη διατομή εισόδου της αρτηρίας, μεταβαίνει σε τοροειδές γύρω από το διάμηκες κέντρο της παλλόμενης μεμβράνης, με διατομή που ομοιάζει στο προφίλ ταχύτητας σε διατομή δακτυλιοειδούς αγωγού σε ταλαντούμενη ροή [Tsa84]. Η ακτινική συνιστώσα της ταχύτητας τείνει να αποκαταστήσει τη μεγιστοποίηση της αξονικής ταχύτητας στον άξονα του αγωγού, κατάντι του μπαλονιού. Τα μέγιστα, επάνω στη διατομή, διανύσματα έχουν μεγαλύτερο μέτρο πλησίον της εισόδου και μικρότερο στην περιοχή του ασκού, όπως αναμένεται από τη διατήρηση της μάζας.

Ισοϋψείς της αξονικής ταχύτητας δίνονται στο σχήμα 6.3. Στο τμήμα της περιόδου όπου αυξάνει ο ρυθμός αλλαγής του όγκου του μπαλονιού, αυξάνει και η εξερχόμενη παροχή όγκου ρευστού. Ο μεγιστοποιητής της εξίσωσης (6.3) είναι

$$\underset{t\in[0,T)}{\arg\max}\, Q_{out}(t)=\frac{T}{2\pi}\arccos\left(\frac{\frac{r_{b0}}{A_b}-\sqrt{\frac{r_{b0}^2}{A_b^2}+8}}{4}\right), \tag{6.7}$$

στην οποία χρονική στιγμή εμφανίζεται βαθειά κόκκινη περιοχή στην έξοδο του αγωγού. Για το υπόλοιπο του χρόνου όπου ο ρυθμός αλλαγής όγκου του μπαλονιού μειώνεται, ο ρυθμός εξόδου όγκου ρευστού ακολουθεί την ίδια τάση. Για $t=3T/4$ η διαμήκης ταχύτητας πλησίον της εξόδου ελαχιστοποιείται. Η περιοχή χαμηλών ταχυτήτων πλησίον του εξωτερικού τοιχώματος έχει μικρότερο πάχος στην περιοχή $4\leq x\leq 10$ όπου είναι τοποθετημένο το μπαλόνι, λόγω των συνεκτικών φαινομένων στον αγωγό μεταξύ του τοιχώματος και της μεμβράνης.

Ισογραμμές της κατανομής πίεσης δίνονται στο σχήμα 6.4. Η πίεση εξόδου αυξάνεται για το ύστερο, μέγιστο τμήμα της φάσης διόγκωσης και μειώνεται για το ύστερο, μέγιστο τμήμα της φάσης συρρίκνωσης. Η συνάρτηση της πίεσης εξόδου, p_{out}, με τον χρόνο, δίνεται στο σχήμα 6.5.

Η μέση τιμή της κυματομορφής του πλεονάσματος πίεσης εξόδου εν σχέσει με την πίεση εισόδου, είναι -4.319 Pa για $Q_{in}=0.01$ L/s, $r_{b0}=0.32$ cm και $A_b=0.02$ cm. Για ταυτόσημη χαμηλή ακραία θέση της ταλάντωσης για τον μικρό άξονα του ασκού, το πλάτος της ταλάντωσης του μπαλονιού και η διακύμανση της πίεσης συσχετίζονται θετικά.

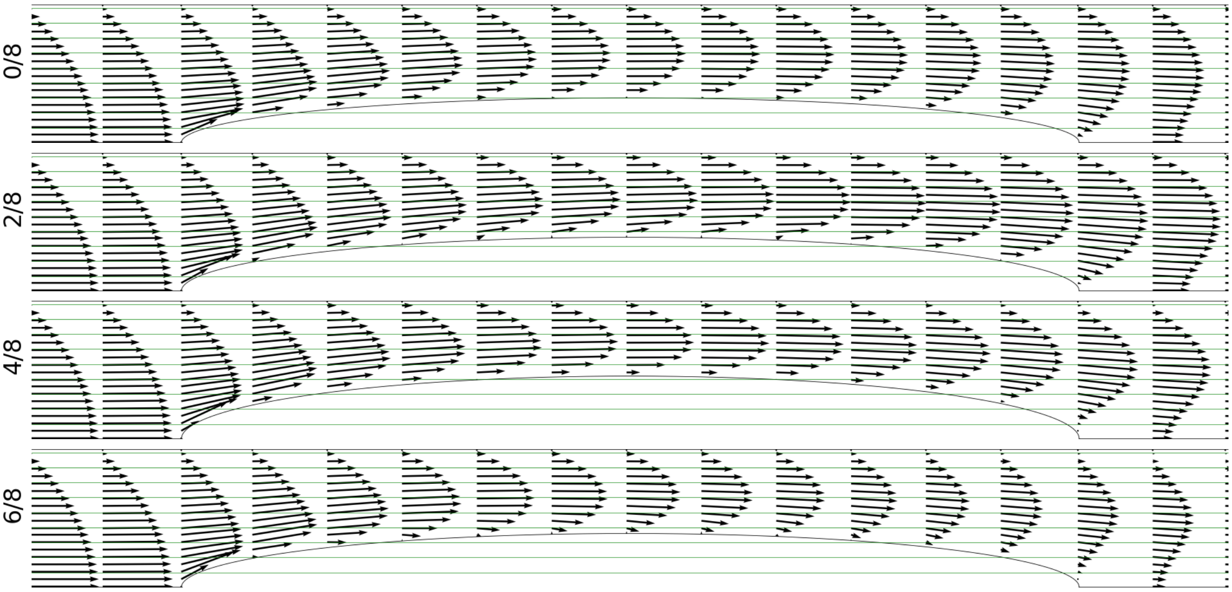

Σχήμα 6.2: Διανύσματα ταχύτητας σε μεσημβρινή όψη, για ασκό παλλόμενο σύμφωνα με την εξίσωση (6.2) με προφίλ ταχύτητας εισόδου που δίνεται από την εξίσωση (6.6), για 4 στιγμιότυπα κατά τη διάρκεια της περιόδου (οι τίτλοι στο αριστερό μέρος του σχήματος αναφέρονται στο κλάσμα της περιόδου T). Η εισερχόμενη παροχή όγκου είναι $Q_{in} = 0.01$ L/s, $r_{b0} = 0.36$ cm και $A_b = 0.06$ cm.

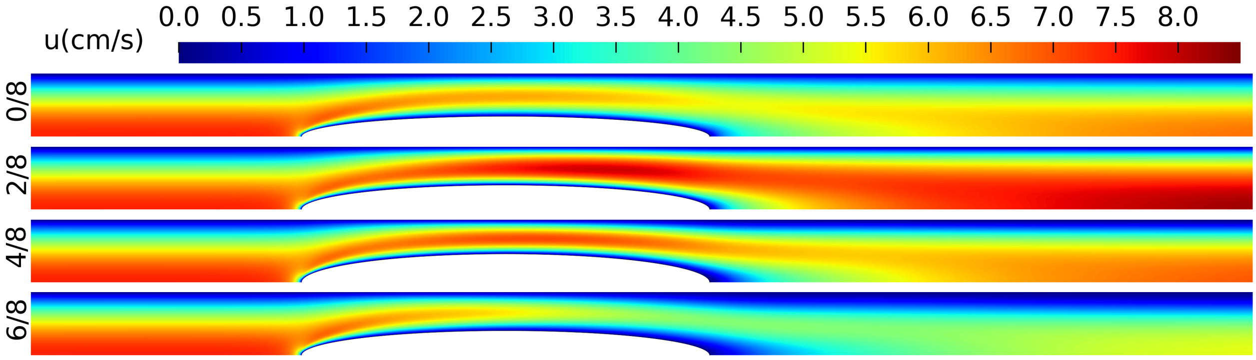

Σχήμα 6.3: Ισογραμμές αξονικής ταχύτητας σε μεσημβρινή όψη, για ασκό παλλόμενο σύμφωνα με την εξίσωση (6.2) με προφίλ ταχύτητας εισόδου που δίνεται από την εξίσωση (6.6), για 4 στιγμιότυπα κατά τη διάρκεια της περιόδου (οι τίτλοι στο αριστερό μέρος του σχήματος αναφέρονται στο κλάσμα της περιόδου T). Η εισερχόμενη παροχή όγκου είναι $Q_{in} = 0.01$ L/s, $r_{b0} = 0.36$ cm και $A_b = 0.06$ cm.

Για μεγαλύτερους αριθμούς Reynolds και ταυτόσημες ταλαντώσεις, η πίεση εξόδου ως προς την είσοδο, λαμβάνει χαμηλότερες τιμές. Η διαφορά φάσης μεγιστοποίησης της εξερχόμενης παροχής όγκου ρευστού και μεγιστοποίησης της πίεσης εξόδου για $Q_{in} = 0.01$ L/s, $r_{b0} = 0.32$ cm and $A_b = 0.02$ cm είναι

$$\delta\phi = 2\pi \left(\underset{t\in[0,T)}{\arg\max}\, p_{out}(t) - \underset{t\in[0,T)}{\arg\max}\, Q_{out}(t) \right) = \frac{109\pi}{100} - \arccos\left(4 - \frac{\sqrt{66}}{2}\right) = 0.57025\pi.$$

Η παρούσα τιμή του $\delta\phi$ είναι χαρακτηριστική για διαφορά φάσης μεταξύ της κλίσης πίεσης και της παροχής όγκου ρευστού για μεγάλους αριθμούς Womersley [Zam00].

Η ενισχυμένη επίδραση της αδράνειας έχει ως συνέπεια σημαντική υστέρηση της καμπύλης πίεσης εν σχέσει με

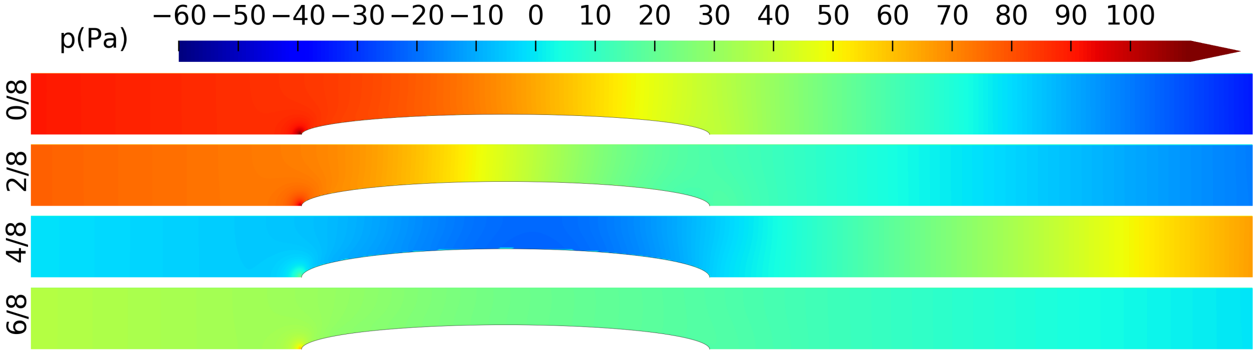

Σχήμα 6.4: Ισογραμμές πίεσης σε μεσημβρινή όψη, για ασκό παλλόμενο σύμφωνα με την εξίσωση (6.2) με προφίλ ταχύτητας εισόδου που δίνεται από την εξίσωση (6.6), για 4 στιγμιότυπα κατά τη διάρκεια της περιόδου (οι τίτλοι στο αριστερό μέρος του σχήματος αναφέρονται στο κλάσμα της περιόδου T). Η εισερχόμενη παροχή όγκου είναι $Q_{in} = 0.01$ L/s, $r_{b0} = 0.36$ cm και $A_b = 0.06$ cm.

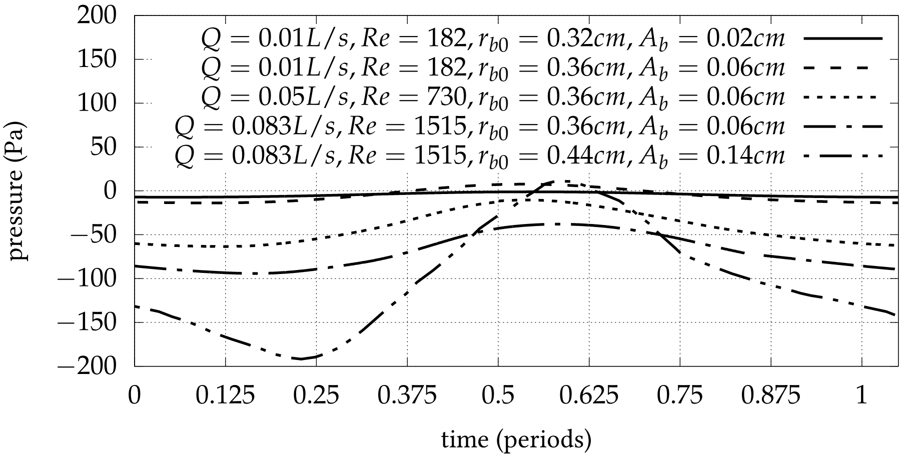

Σχήμα 6.5: Πίεση $p_{out} - p_{in}$ κατά τη διάρκεια της περιόδου για διάφορες τιμές των r_{b0} και A_b.

την καμπύλη του ρυθμού παροχής όγκου [Zam05]. Η διαφορά φάσης μεταξύ του μέγιστου ρυθμού παροχής όγκου ρευστού στην έξοδο της αρτηρίας και της μέγιστης πίεσης εξόδου, βρίσκεται να είναι σχεδόν ανεξάρτητη από το πλάτος της ταλάντωσης και τη θέση ισορροπίας και να αυξάνεται σε μικρό βαθμό με αύξηση του αριθμού Reynolds.

Τα προφίλ διαμήκους ταχύτητας εξόδου δίνονται στο σχήμα 6.6. Λόγω της πάλμωσης του ασκού, το προφίλ ταχύτητας στην έξοδο του αγγείου δεν είναι παραβολικό όπως στην εισόδο. Η μέγιστη αξονική ταχύτητα υπολείπεται σημαντικά σε σχέση με τη αντίστοιχη τιμή Poiseuille. Η υψηλή τιμή της αδιάστατης παραμέτρου συχνότητας (11.936) που έχει ως αποτέλεσμα αυξημένη σχετική σημασία της αδράνειας, οδηγεί σε πεπλατυσμένα προφίλ ταχύτητας περί τον άξονα του αγωγού πλησίον της εξόδου [Wes+19]. Κατάντι του μπαλονιού, σε ικανή απόσταση από αυτό, οι διατμητικές τάσεις έχουν επίδραση στη γειτονιά του τοιχώματος και είναι σχεδόν μηδενικές στον πυρήνα της ροής [Kis09].

Η διαφορά των προφίλ αξονικής ταχύτητας εξόδου και εισόδου δίνεται στο σχήμα 6.7. Η επίδραση της πάλμωσης του μπαλονιού στην έξοδο, είναι εντονότερη σε ακτίνες περί το μέσο του στενότατου αγωγού που διαμορφώνεται από το εσωτερικό και το εξωτερικό όριο.

Πλησίον της εξόδου του αγωγού, όπου η ροή είναι αναπτυγμένη, η απλουστευμένη μορφή των εξισώσεων Navier-

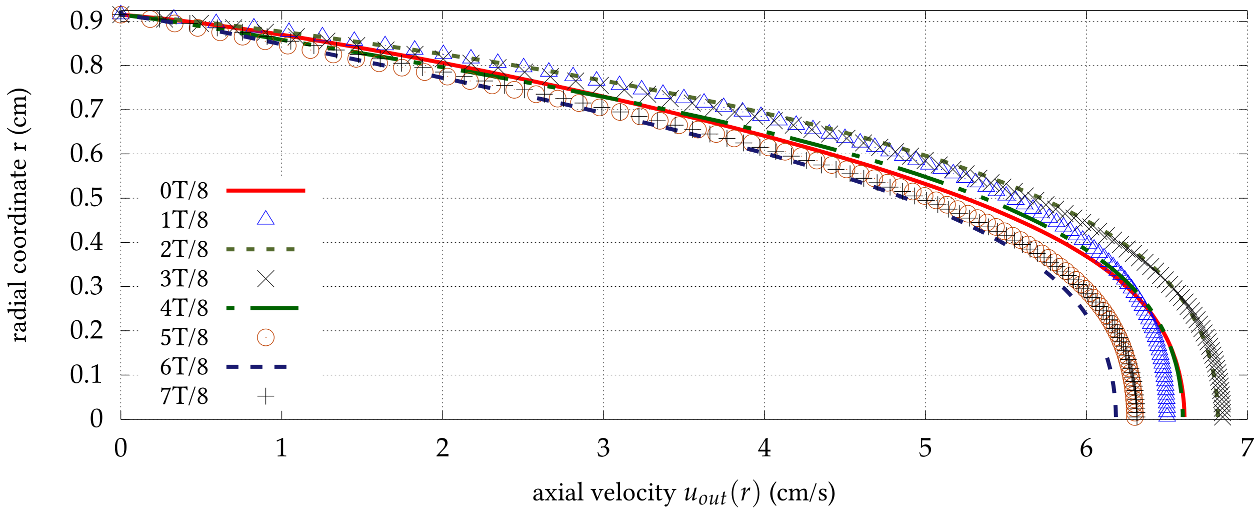

Σχήμα 6.6: Προφίλ ταχύτητας εξόδου $u_{out}(r)$ δειγματοληπτημένα 8 ισαπέχουσες χρονικές στιγμές στην περίοδο. Η εισερχόμενη παροχή όγκου είναι $Q_{in} = 0.01$ L/s, $r_{b0} = 0.32$ cm και $A_b = 0.02$ cm.

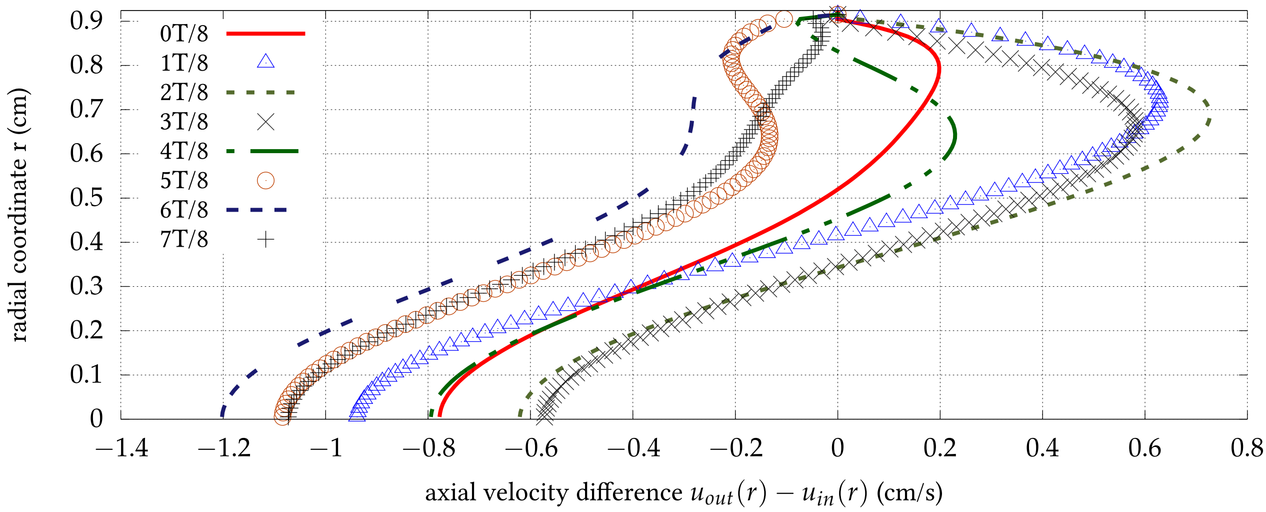

Σχήμα 6.7: Διαφορά προφίλ αξονικής ταχύτητας εξόδου $u_{out}(r)$ και προφίλ ταχύτητας εισόδου $u_{in}(r)$, δειγματοληπτημένη 8 ισαπέχουσες στιγμές κατά τη διάρκεια της περιόδου, για $Q_{in} = 0.01$ L/s, $r_{b0} = 0.32$ cm και $A_b = 0.02$ cm.

Stokes

$$\frac{\partial^2 u}{\partial r^2} + \frac{1}{r}\frac{\partial u}{\partial r} - \frac{1}{\nu}\frac{\partial u}{\partial t} = \frac{1}{\mu}\frac{\partial p}{\partial x}, \tag{6.8}$$

είναι γραμμική για το προφίλ διαμήκους ταχύτητας και την πίεση [Nic+22]. Κατά συνέπεια, στις περιπτώσεις που η μόνιμη και η μεταβαλλόμενη στο χρόνο κλίση πίεσης συνυπάρχουν, ικανοποιούν ανεξάρτητα την εξίσωση (6.8) [Uch56; Ver60].

Κεφάλαιο 7

Συμπεράσματα

7.1 Κεντρικά σημεία της διατριβής

Ανακεφαλαιώνοντας τα βασικά συμπεράσματα της εργασίας, σημειώνονται τα ακόλουθα:

- Η μέθοδος εμβαπτισμένου ορίου που χρησιμοποιήθηκε, προτείνεται ως κατάλληλη για την προσομοίωση της χειραγώγησης ροής, όπου εμπλέκονται κινούμενα μη παραμορφώσιμα και παραμορφώσιμα στερεά τμήματα. Το πλέγμα διακριτοποίησης του χωρίου επίλυσης είναι σταθερό στον χρόνο, συνεπώς η απαιτητική διαδικασία της γένεσης πλέγματος αντικαθίσταται από τον αξιοσημείωτα πιο ευπρόσιτο στόχο της ανίχνευσης επιφάνειας. Κάθε προσομοίωση απαιτεί λιγότερη προσπάθεια για τη διακριτοποίηση και σημαντικά λιγότερο χρόνο επεξεργασίας.

- Για μεγαλύτερες τιμές του μήκους της επιφάνειας ελέγχου, με σταθερές τις λοιπές παραμέτρους για την απότομη διεύρυνση εμφανίζεται μεγαλύτερη σταθερότητα της θέσης αποκόλλησης του άνω τοιχώματος και μεγαλύτερη μέγιστη τιμή της θέσης επανακόλλησης άνω τοιχώματος. Ως συνέπεια της αύξησης του μήκους, μειώνεται το πλάτος της διαμήκους ταλάντωσης της φυσαλλίδας κάτω τοιχώματος.

- Ο έλεγχος της ανακυκλοφορίας του μόνιμου και του χρονομεταβλητού πεδίου ροής μέσω παθητικής ελαστικής επιφάνειας σε αλληλεπίδραση με την κύρια ροή, βρίσκεται να είναι αποδοτικός. Παρέχοντας κατάλληλη εξωτερική πίεση και απουσία πηγής ενέργειας, η μεμβράνη μπορεί να καταστείλει την αποκόλληση της ροής σε σημαντικό βαθμό.

- Οι βιολογικές ροές συχνά διέπονται από συντακτικές εξισώσεις με συντελεστές εξαρτώμενους από τον ρυθμό διάτμησης. Η καμπυλόγραμμη μέθοδος εμβαπτισμένου ορίου δείχνεται να προβλέπει τη μη Νευτώνεια συμπεριφορά σε συμφωνία με τις μεθόδους που προσαρμόζονται στο σώμα.

- Η ανάλυση των ευθύγραμμων περισταλτικών αντλιών υποστηρίζει ότι οι πολυκύλινδρες διατάξεις εμφανίζουν πλεονεκτήματα ως προς εκείνες όπου το κύμα συμπίεσης είναι μονοτροπικό. Παράλληλα και κάθετα στην κυματική ταχύτητα, τα πεδία κλίσης ταχύτητας είναι λιγότερο έντονα για πολυτροπικά κύματα. Συνεπώς, τα αντλούμενα ρευστά υποβάλλονται σε χαμηλότερα επίπεδα ρυθμού διάτμησης και υφίστανται χαμηλότερες διατμητικές τάσεις. Επιπλέον θετικό χαρακτηριστικό των πολυτροπικών κυμάτων αποτελεί η διαμήκης κίνηση σε μία κατεύθυνση σε όλο το μήκος της αντλίας όπου αποφεύγονται οι επιπλοκές της οπισθορροής.

- Διατμητικά λεπτυνόμενα γενικευμένα Νευτώνεια ρευστά τίθενται σε κίνηση κάτω από χαμηλότερες τιμές ανάστροφης βαθμίδας πίεσης από ότι τα Νευτώνεια. Η κλίση των χαρακτηριστικών περίσταλσης των ρευστών που εμφανίζουν ψευδοπλαστική συμπεριφορά συσχετίζονται αρνητικά με τον εκθέτη Bird-Carreau. Η άντληση ρευστών αυτής της κατηγορίας απαιτεί λιγότερο παρεχόμενο έργο.

- Η πίεση εξόδου ενδοαορτικής αντλίας μπαλονιού μεγιστοποιείται σε προσεγγιστικά σταθερή χρονική στιγμή κατά τη διάρκεια της περιόδου πάλμωσης σχεδόν ανεξάρτητα από την κεντρική τιμή του μήκους του ελάσσωνος άξονα ή το πλάτος ταλάντωσής του. Για σταθερή συχνότητα, αύξηση του όγκου του μπαλονιού από κορυφή σε κορυφή συνεπάγεται υψηλότερη τιμή πίεσης εξόδου από κορυφή σε κορυφή.

7.2 Συμβολή της διατριβής

Στην παρούσα διατριβή ερευνήθηκε ο έλεγχος της ροής σε περιπτώσεις ενδιαφέροντος με χρήση της μεθόδου εμβαπτισμένου ορίου. Η κύρια συνεισφορά της εργασίας συνοψίζεται εδώ:

- Εφαρμόζεται η καμπυλόγραμμη μέθοδος εμβαπτισμένου ορίου για την πρόβλεψη πεδίων ροής με χρονομεταβαλλόμενο όγκο ρευστού. Στον αλγόριθμο της μεθόδου προστέθηκε η αλληλεπίδραση ρευστού-στερεού με παραμορφώσιμα σώματα. Η απόκριση του στερεού αντιστοιχεί σε ελαστική μεμβράνη της οποίας η εξίσωση κίνησης συνδέεται ασθενώς με τις εξισώσεις Navier-Stokes. Η διαδικασία εφαρμόζεται για μόνιμες και μη μόνιμες περιπτώσεις.
- Μελετάται ο ενεργός έλεγχος φυσαλλίδας αποκόλλησης μέσω ταλαντούμενης επιφάνειας, χρησιμοποιώντας σταθερά υπολογιστικά πλέγματα. Επιπρόσθετα με την επίδραση του πλάτους και της συχνότητας εξετάζεται η διαμήκης επέκταση της ενεργού επιφάνειας.
- Ρευστά που αντλούνται μέσω κυμάτων συστολής η μέσω πάλμωσης, συχνά δεν περιγράφονται με γραμμικές συντακτικές εξισώσεις. Ο επιλύτης επεκτείνεται ώστε να συμπεριληφθούν ρευστά που ακολουθούν χρονικά ανεξάρτητες, μη γραμμικές καταστατικές εξισώσεις, όπως περιπτώσεις του ρεολογικού μοντέλου Carreau-Yasuda.
- Προτείνεται τρόπος αντιμετώπισης των θεμάτων των αρνητικών αξονικών ταχυτήτων και της οριοθέτησης των διατμητικών τάσεων στην περισταλτική άντληση. Εξετάζεται η αύξηση της πολλαπλότητας των περιόδων του κύματος και βρίσκεται να επιτυγχάνει καλά αποτελέσματα σε αυτές τις κατευθύνσεις.
- Παρουσιάζονται οι χαρακτηριστικές περισταλτικής άντλησης για ευθύγραμμες αντλίες για Νευτώνεια και μη Νευτώνεια ρευστά και για διάφορες τιμές της σχετικής έμφραξης.
- Μοντελοποιείται η παλμική ροή που διαμορφώνεται από σφύζον σφαιροειδές μπαλόνι σε κυλινδρικό αγωγό. Η επίδοση άντλησης αναλύεται για ένα εύρος τιμών του ρυθμού εισερχόμενου όγκου και του πλάτους ταλάντωσης του όγκου του μπαλονιού και περιγράφεται το πεδίο ροής διαμέσου της διάταξης.

Βιβλιογραφία

[Ach72] E. Achenbach. Experiments on the flow past spheres at very high Reynolds numbers. *Journal of Fluid Mechanics* 54.3 (1972), σσ. 565–575.

[ACS16] D. Angelidis, S. Chawdhary και F. Sotiropoulos. Unstructured Cartesian refinement with sharp interface immersed boundary method for 3D unsteady incompressible flows. *Journal of Computational Physics* 325 (2016), σσ. 272–300.

[AG09] V. G. Asouti και K. C. Giannakoglou. Aerodynamic optimization using a parallel asynchronous evolutionary algorithm controlled by strongly interacting demes. *Engineering Optimization* 41 (2009), σσ. 241–257.

[AH13] A. A. Al-Habahbeh. Simulations of Newtonian and non-Newtonian flows in deformable tubes. Διδακτορική διατρ. Michigan Technology University, 2013.

[Arm+83] B. F. Armaly, F. Durst, J. C. F. Pereira και B. Schönung. Experimental and theoretical investigation of backward-facing step flow. *Journal of Fluid Mechanics* 127 (1983), σσ. 473–496.

[BAH87] R. Bird, R. Armstrong και O. Hassager. *Dynamics of polymeric liquids, Volume 1: Fluid mechanics, 2nd Edition.* Wiley, 1987.

[BBC17] A. Batikh, L. Baldas και S. Colin. Application of active flow control on aircrafts - State of the art. Στο: *International Workshop on Aircraft System Technologies.* Τόμ. 2017. Hamburg, Germany, Φεβ. 2017.

[BGS08] I. Borazjani, L. Ge και F. Sotiropoulos. Curvilinear immersed boundary method for simulating fluid structure interaction with complex 3D rigid bodies. *Journal of Computational Physics* 227.16 (2008), σσ. 7587–7620.

[Bin+18] C. Bingham, C. Raibaudo, C. Morton και R. Martinuzzi. Suppression of fluctuating lift on a cylinder via evolutionary algorithms: Control with interfering small cylinder. *Physics of Fluids* 30, 127104 (2018).

[BLW08] E. Braun, F. Lu και D. Wilson. A Critical Review of Electric and Electromagnetic Flow Control Research Applied to Aerodynamics. Στο: *Proccedings of the 39th Plasmadynamics and Lasers Conference (23 - 26 June).* (Seattle, Washington). American Institute of Aeronautics και Astronautics, 2008.

[Bou21] E. Boujo. Second-order adjoint-based sensitivity for hydrodynamic stability and control. *Journal of Fluid Mechanics* 920, A12 (2021).

[Cal+15] A. Calderer, X. Yang, D. Angelidis, A. Khosronejad, T. Le, S. Kang, A. Gilmanov, L. Ge και I. Borazjani. *Virtual Flow Simulator, Version 1.0.* 2015.

[Car68] P. J. Carreau. Rheological equations from molecular network theories. Διδακτορική διατρ. Madison, WI: University of Winsconsin - Madison, 1968.

[Che+14] G. Chen, Q. Xiong, P. J. Morris, E. G. Paterson, A. Sergeev και Y. C. Wang. OpenFOAM for computational fluid dynamics. *Notices of the American Mathematical Society* 61.4 (2014), σσ. 354–363.

[CK90] J. R. Cash και A. H. Karp. A Variable Order Runge-Kutta Method for Initial Value Problems with Rapidly Varying Right-Hand Sides. *ACM Transactions of Mathematical Software* 16.3 (1990), σσ. 201–222.

[CKS14] A. Calderer, S. Kang και F. Sotiropoulos. Level set immersed boundary method for coupled simulation of air/water interaction with complex floating structures. *Journal of Computational Physics* 277 (2014), σσ. 201–227.

[CL00] D. Calhoun και R. J. LeVeque. A Cartesian Grid Finite-Volume Method for the Advection-Diffusion Equation in Irregular Geometries. *Journal of Computational Physics* 157.1 (2000), σσ. 143–180.

[CN47] J. Crank και P. Nicolson. A practical method for numerical evaluation of solutions of partial differential equations of the heat-conduction type. *Mathematical Proceedings of the Cambridge Philosophical Society* 43.1 (1947), σσ. 50–67.

[CS04] G. Constantinescu και K. Squires. Numerical investigations of flow over a sphere in the subcritical and supercritical regimes. *Physics of Fluids* 16.5 (2004), σσ. 1449–1466.

[CSH86] D. K. Clarke, M. D. Salas και H. A. Hassan. Euler calculations for multielement airfoils using Cartesian grids. *AIAA Journal* 24.3 (1986), σσ. 353–358.

[Eck17] M. Eckert. Ludwig Prandtl and the growth of fluid mechanics in Germany. A century of fluid mechanics: 1870-1970. *Comptes Rendus Mécanique* 345.7 (2017), σσ. 467–476.

[Fad+00] E. Fadlun, R. Verzicco, P. Orlandi και J. Mohd-Yusof. Combined Immersed-Boundary Finite-Difference Methods for Three-Dimensional Complex Flow Simulations. *Journal of Computational Physics* 161.1 (2000), σσ. 35–60.

[Fan+20] D. Fan, L. Yang, Z. Wang, M. S. Triantafyllou και G. E. Karniadakis. Reinforcement learning for bluff body active flow control in experiments and simulations. *Proceedings of the National Academy of Sciences* 117.42 (2020), σσ. 26091–26098.

[FQV09] L. Formaggia, A. Quarteroni και A. Veneziani, επιμελητές. *Cardiovascular Mathematics: Modeling and simulation of the circulatory system.* Τόμ. 1. Milano, Italia: Springer-Verlag, 2009.

[Gar90] D. K. Gartling. A test problem for outflow boundary conditions - flow over a backward - facing step. *International Journal for Numerical Methods in Fluids* 11.7 (1990), σσ. 953–967.

[GB98] P. L. George και H. Borouchaki. *Delaunay Triangulation and Meshing: Application to Finite Elements.* Hermès, 1998.

[GKM00] M. Gunzburger, H. Kim και S. Manservisi. On a shape control problem for the stationary Navier-Stokes equations. *Mathematical Modelling and Numerical Analysis* 34 (2000), σσ. 1233–1258.

[GS05] A. Gilmanov και F. Sotiropoulos. A hybrid Cartesian/immersed boundary method for simulating flows with 3D, geometrically complex, moving bodies. *Journal of Computational Physics* 207.2 (2005), σσ. 457–492.

[GS07] L. Ge και F. Sotiropoulos. A numerical method for solving the 3D unsteady incompressible Navier-Stokes equations in curvilinear domains with complex immersed boundaries. *Journal of Computational Physics* 225.2 (2007), σσ. 1782–1809.

[GTG07] E. Greitzer, C. Tan και M. Graf. *Internal Flow: Concepts and Applications.* Cambridge Engine Technology Series. Cambridge University Press, 2007.

[Hak00] M. Gad el Hak. *Flow Control: Passive, Active, and Reactive Flow Management.* Cambridge, England: Cambridge University Press, 2000.

[Hak01] M. Gad el Hak. *The MEMS Handbook.* Mechanical and Aerospace Engineering Series. CRC Press, 2001.

[IV03] G. Iaccarino και R. Verzicco. Immersed boundary technique for turbulent flow simulations. *Applied Mechanics Reviews* 56.3 (2003), σσ. 331–347.

[Jin+04] S. Jindal, L. Long, P. Plassmann και N. Sezer Uzol. Large Eddy Simulations around a Sphere Using Unstructured Grids. Στο: *34th AIAA Fluid Dynamics Conference and Exhibit.* (Portland, Oregon, USA). American Institute of Aeronautics και Astronautics, 2004.

[Kan+11] S. Kang, A. Lightbody, C. Hill και F. Sotiropoulos. High-resolution numerical simulation of turbulence in natural waterways. *Advances in Water Resources* 34.1 (2011), σσ. 98–113.

[Kan10] S. K. Kang. Numerical modeling of turbulent flows in arbitrarily complex natural streams. Διδακτορική διατρ. University of Minnesota, 2010.

[Kia+15] E. P. Kiachagias, A. Zymaris, I. Kavvadias, D. Papadimitriou και K. Giannakoglou. The continuous adjoint approach to the k-ϵ turbulence model for shape optimization and optimal active control of turbulent flows. *Engineering Optimization* 47.3 (2015), σσ. 370–389.

[Kis09] V. Kislik. *Liquid Membranes: Principles and Applications in Chemical Separations and Wastewater Treatment.* Amsterdam, The Netherlands: Elsevier, 2009.

[KK04] D. A. Knoll και D. E. Keyes. Jacobian-free Newton-Krylov methods: a survey of approaches and applications. *Journal of Computational Physics* 193.2 (2004), σσ. 357–397.

[KM85] J. Kim και P. Moin. Application of a fractional-step method to incompressible Navier-Stokes equations. *Journal of Computational Physics* 59.2 (1985), σσ. 308–323.

[KTH13] M. J. Krause, G. Thäter και V. Heuveline. Adjoint - based fluid flow control and optimisation with lattice Boltzmann methods. *Computers & Mathematics with Applications* 65.6 (2013), σσ. 945–960.

[LP00] M.-C. Lai και C. S. Peskin. An Immersed Boundary Method with Formal Second-Order Accuracy and Reduced Numerical Viscosity. *Journal of Computational Physics* 160.2 (2000), σσ. 705–719.

[McN+04] A. McNamara, A. Treuille, Z. Popović και J. Stam. Fluid Control Using the Adjoint Method. *ACM Transactions on Graphics* 23.3 (2004), σσ. 449–456.

[MMN22] H. Muir, L. Michael και N. Nikiforakis. Numerical Methodologies for Magnetohydrodynamic Flow Control for Hypersonic Vehicles. Στο: *Active Flow and Combustion Control 2021.* Επιμέλεια υπό R. King και D. Peitsch. Cham, Switzerland: Springer International Publishing, 2022, σσ. 336–355.

[MMnS10] D. Mateescu, M. Muñoz και O. Scholz. Analysis of unsteady confined viscous flows with variable inflow velocity and oscillating walls. *Journal of Fluids Engineering* 132.4, 041105 (2010).

[Mor+84] J. J. Moré, D. C. Sorensen, B. S. Garbow και K. E. Hillstrom. The Minpack Project. Στο: *Sources and development of mathematical software.* Επιμελεια υπό W. R. Cowell. Computational Mathematics. Prentice-Hall, 1984. Κεφ. 5, σσ. 88–111.

[MRF95] J. Magnaudet, M. Rivero και J. Fabre. Accelerated flows past a rigid sphere or a spherical bubble. Part 1. Steady straining flow. *Journal of Fluid Mechanics* 284 (1995), σσ. 97–135.

[MSM04] S. O. Macheret, M. N. Shneider και R. B. Miles. Magnetohydrodynamic and Electrohydrodynamic Control of Hypersonic Flows of Weakly Ionized Plasmas. *AIAA Journal* 42.7 (2004), σσ. 1378–1387.

[MV01] D. Mateescu και D. A. Venditti. Unsteady confined viscous flows with oscillating walls and multiple separation regions over a downstream - facing step. *Journal of Fluids and Structures* 15.8 (2001), σσ. 1187–1205.

[MY97] J. Mohd-Yusof. Combined Immersed Boundary / B-Spline Methods for Simulation of Flow in Complex Geometries. *Annual Research Briefs, Center for Turbulence Research* (1997), σσ. 317–328.

[Nah12] S. Nahar. Steady and Unsteady Flow Characteristics of non-Newtonian Fluids in Deformed Elastic Tubes. Διδακτορική διατρ. Swiss Federal Institute of Technology (ETH), 2012.

[Nic+22] W. W. Nichols, M. O'Rourke, E. R. Elelman και C. E. Vlachopoulos. *McDonald's Blood Flow in Arteries: Theoretical, Experimental and Clinical Principles.* 7η έκδοση. Boca Raton, FL: CRC Press, 2022.

[NJW10] S. Nahar, S. A. K. Jeelani και E. J. Windhab. Steady and Unsteady Flow Characteristics of non-Newtonian Fluids in Deformed Elastic Tubes. Στο: *Proceedings of the 7th International Symposium on Ultrasonic Doppler Methods for Fluid mechanics and Fluid Engineering.* (Gothenburg, Sweden). Επιμέλεια υπό J. Wiklund, E. Levenstam Bragd και S. Manneville. Gothenburg, Sweden: Chalmers University of Technology, 2010, σσ. 61–64.

[Pes72] C. S. Peskin. Flow patterns around heart valves: A numerical method. *Journal of Computational Physics* 10.2 (1972), σσ. 252–271.

[Pra04] L. Prandtl. Über Flüssigkeitsbewegung bei sehr kleiner Reibung. Στο: *Verhandlungen des III. Internationalen Mathematiker Kongresses.* (Heidelberg, Germany). Leipzig, Germany: B.G. Teubner, 1904, σσ. 485–491.

[Pre+07] W. H. Press, S. A. Teukolsky, W. T. Vetterling και B. P. Flannery. *Numerical Recipes 3rd Edition: The Art of Scientific Computing.* Cambridge University Press, 2007.

[PS72] S. V. Patankar και D. B. Spalding. A calculation procedure for heat, mass and momentum transfer in three-dimensional parabolic flows. *International Journal of Heat and Mass Transfer* 15.10 (1972), σσ. 1787–1806.

[PT97] T. Pappou και S. Tsangaris. Development of an artificial compressibility methodology using flux vector splitting. *International Journal for Numerical Methods in Fluid Mechanics* 25.5 (1997), σσ. 523–545.

[Rab+20] J. Rabault, F. Ren, W. Zhang, H. Tang και H. Xu. Deep reinforcement learning in fluid mechanics: A promising method for both active flow control and shape optimization. *Journal of Hydrodynamics* 32.2 (2020), σσ. 234–246.

[RHT20] F. Ren, H. Hu και H. Tang. Active flow control using machine learning: A brief review. *Journal of Hydrodynamics* 32.2 (2020), σσ. 247–253.

[RK19] J. Rabault και A. Kuhnle. Accelerating deep reinforcement learning strategies of flow control through a multi-environment approach. *Physics of Fluids* 31.9, 094105 (2019).

[RRT21] F. Ren, J. Rabault και H. Tang. Applying deep reinforcement learning to active flow control in weakly turbulent conditions. *Physics of Fluids* 33.3, 037121 (2021).

[RS87] J. W. Ruge και K. Stüben. Algebraic Multigrid. Στο: *Multigrid Methods.* Επιμέλεια υπό S. F. McCormick. Τόμ. 3. Frontiers in applied mathematics. Society for Industrial και Applied Mathematics, 1987. Κεφ. 4, σσ. 73–130.

[RZ10] M. P. Rumpfkeil και D. W. Zingg. The optimal control of unsteady flows with a discrete adjoint method. *Optimization and Engineering* 11 (2010), σσ. 5–22.

[SA08] J. H. Spurk και N. Aksel. *Fluid Mechanics.* 2η έκδοση. Berlin - Heidelberg, Germany: Springer, 2008.

[SB18] R. S. Sutton και A. G. Barto. *Reinforcement Learning: An Introduction.* 2η έκδοση. The MIT Press, 2018.

[Sma63] J. Smagorinsky. General Circulation Experiments with the Primitive Equations I. The Basic Experiment. *Monthly Weather Review* 91.3 (1963), σσ. 99–164.

[Soh88] J. L. Sohn. Evaluation of FIDAP on some classical laminar and turbulent benchmarks. *International Journal for Numerical Methods in Fluids* 8.12 (1988), σσ. 1469–1490.

[SS86] Y. Saad και M. H. Schultz. GMRES: A Generalized Minimal Residual Algorithm for Solving Nonsymmetric Linear Systems. *SIAM Journal on Scientific and Statistical Computing* 7.3 (1986), σσ. 856–869.

[Sto+15] K. Stokos, S. Vrahliotis, T. Pappou και S. Tsangaris. Development and validation of an incompressible Navier-Stokes solver including convective heat transfer. *International Journal of Numerical Methods for Heat & Fluid Flow* 25.4 (2015), σσ. 861–886.

[SY14] F. Sotiropoulos και X. Yang. Immersed boundary methods for simulating fluid-structure interaction. *Progress in Aerospace Sciences* 65 (2014), σσ. 1–21.

[TF03] Y.-H. Tseng και Y.-H. Ferziger. A ghost-cell immersed boundary method for flow in complex geometry. *Journal of Computational Physics* 192.2 (2003), σσ. 593–623.

[Tro+12] X. Trompoukis, V. Asouti, I. Kampolis και K. Giannakoglou. Chapter 17 - CUDA Implementation of Vertex-Centered, Finite Volume CFD Methods on Unstructured Grids with Flow Control Applications. Στο: *GPU Computing Gems Jade Edition*. Επιμέλεια υπό W.-m. W. Hwu. Applications of GPU Computing Series. Cambridge, MA: Morgan Kaufmann, 2012, σσ. 207–223.

[Tsa84] S. Tsangaris. Oscillatory flow of an incompressible, viscous fluid in a straight annular pipe. *Journal de Mécanique Théorique et Appliquée* 3.3 (1984), σσ. 467–478.

[TVI14] M. de Tullio, R. Verzicco και G. Iaccarino. Immersed Boundary Technique for Large - Eddy - Simulation. Von Karman Institute Lecture Series (2014), σσ. 1–97.

[Uch56] S. Uchida. The pulsating viscous flow superposed on the steady laminar motion of incompressible fluid in a circular pipe. *Zeitschrift für Angewandte Mathematik und Physik (ZAMP)* 7.5 (1956), σσ. 403–422.

[Ver60] P. Verma. The Pulsating Viscous Flow Superposed on the Steady Laminar Motion of Incompressible Fluid in a Tube of Elliptic Section. *Proceedings of the National Institute of Sciences of India, Part A* 26.3 (1960), σσ. 282–297.

[Vfs] *VFS - WIND Virtual Flow Simulator*. https://safl-cfd-lab.github.io/VFS-Wind/.

[Vie69] J. Viecelli. A method for including arbitrary external boundaries in the MAC incompressible fluid computing technique. *Journal of Computational Physics* 4.4 (1969), σσ. 543–551.

[Vin+22] R. Vinuesa, O. Lehmkuhl, A. Lozano-Durán και J. Rabault. Flow Control in Wings and Discovery of Novel Approaches via Deep Reinforcement Learning. *Fluids* 7.2, 62 (2022).

[VPT12] S. Vrahliotis, T. Pappou και S. Tsangaris. Artificial Compressibility 3-D Navier-Stokes Solver for Unsteady Incompressible Flows with Hybrid Grids. *Engineering Applications of Computational Fluid Mechanics* 6.2 (2012), σσ. 248–270.

[VSG21] Y. Vrionis, K. Samouchos και K. Giannakoglou. Topology optimization in fluid mechanics using continuous adjoint and the cut-cell method. *Computers & Mathematics with Applications* 97 (2021), σσ. 286–297.

[Wes+19] N. Westerhof, N. Stergiopulos, M. Noble και B. Westerhof. *Snapshots of Hemodynamics: An Aid for Clinical Research and Graduate Education*. Cham, Switzerland: Springer, 2019.

[WF18] J. Wang και L. Feng. *Flow Control Techniques and Applications*. Cambridge Aerospace Series. Cambridge, England: Cambridge University Press, 2018.

[Wom55] J. R. Womersley. Method for the calculation of velocity, rate of flow and viscous drag in arteries when the pressure gradient is known. *The Journal of Physiology* 127.3 (1955), σσ. 553–563.

[YB19] M. Yousefzadeh και I. Battiato. High order ghost-cell immersed boundary method for generalized boundary conditions. *International Journal of Heat and Mass Transfer* 137 (2019), σσ. 585–598.

[Zam00] M. M. Zamir. *The physics of pulsatile flow.* Biological Physics Series. New York, NY: AIP Press / Springer, 2000.

[Zam05] M. Zamir. *The Physics of Coronary Blood Flow.* Biological and Medical Physics, Biomedical Engineering series. New York, NY: AIP Press / Springer, 2005.

[Zym+13] A. Zymaris, D. Papadimitriou, E. M. Papoutsis-Kiachagias, K. C. Giannakoglou και C. Othmer. The continuous adjoint method as a guide for the design of flow control systems based on jets. *Engineering Computations: International Journal for Computer-Aided Engineering* 30.4 (2013), σσ. 494–520.